

High Temperature Electromagnetic Acoustic Transducer for Guided Wave Testing

A thesis submitted for the degree of Doctor of
Philosophy

by
Maria Kogia

School of Electronic and Computer Engineering
Brunel University
January 2017

Abstract

This research focuses on the theoretical analysis, development and experimental evaluation of a water cooled Electromagnetic Acoustic Transducer (EMAT) specifically designed for high-temperature Guided Wave Testing (GWT). Its novel design and detailed calculation of its optimum operating conditions resulted in its effectiveness at high temperatures for both short (500°C) and long-term inspection (250°C).

All the steps followed for the theoretical and experimental investigation of the limitations of the existing technology and the development of a probe that can overcome these boundaries are presented. Finite Element Analysis (FEA) was performed for the optimization of the EMAT design and estimation of its ultrasonic and thermal properties at room and high temperatures over time. The wave mode purity profile of the Periodic Permanent Magnet (PPM) EMAT was theoretically studied as well as the effect of temperature rise on its ultrasonic performance. Thermal and Computational Fluid Dynamics (CFD) analysis was accomplished for the EMAT design optimization and calculation of its optimum operating conditions.

The experimental validation of the theoretical study was also accomplished. The novel water cooled EMAT was developed and experimentally evaluated regarding its ultrasonic and thermal response at room and high temperatures. An empirical method for the enhancement of EMAT performance and its SNR was established. The wave mode purity characteristics of PPM EMAT were experimentally investigated via Laser vibrometry tests, which agreed with FEA results. The impedance analysis and ultrasonic evaluation of the EMAT at both room and high temperatures against various operating conditions were linked and compared to the results obtained from the ultrasonic, thermal and fluid FEA. In all cases, the experimental study is in good agreement with the theoretical results.

Contents

High Temperature Electromagnetic Acoustic Transducer for Guided Wave Testing	1
Abstract.....	2
List of Figures.....	6
List of Tables	10
Acknowledgements.....	11
Declarations	12
Nomenclature.....	13
Chapter 1.....	17
Introduction.....	17
1.1 Motivation.....	17
1.2 Aim	19
1.3. Specific Objectives	19
1.4. Summary of Methodology Used.....	20
1.5. Thesis Outline	21
1.6. Contributions to Knowledge	22
1.7. List of Publications	23
Chapter 2.....	25
Literature Review.....	25
2.1 Introduction.....	25
2.2 NDT Techniques for High-Temperature Inspection	25
2.3 Guided Wave Testing	29
2.4 Piezoelectric Transducers for GWT.....	30
2.5 EMATs.....	32
2.6 Summary	37
Chapter 3.....	38
Theoretical Background for the Design of High-Temperature EMAT.....	38
3.1 Introduction.....	38
3.2 Guided Waves.....	38
3.2.1 Introduction.....	38
3.2.2 Guided Waves Physics.....	40

3.2.3 Temperature Rise Effect	45
3.3 EMAT Transduction	46
3.3.1 Lorentz Force	47
3.3.2 Magnetization Force	49
3.3.3 Magnetostriction	50
3.4 EMAT Reception	51
3.5 EMAT Designs	52
3.6 Electromagnetic Losses	56
3.6.1 Skin Effect	56
3.6.2 Impedance – Electrical Circuit.....	58
3.6.3 Lift-off.....	63
3.7 Temperature Effect	64
3.8 Summary	67
Chapter 4.....	68
Numerical Simulation of High Temperature EMAT	68
4.1 Introduction.....	68
4.2 Wave Propagation FEA	68
4.2.1 FEA Model Overview	68
4.2.2 FEA Model Implementation	70
4.2.3 FEA Results and Discussion.....	76
4.3 Transient Thermal Simulations.....	84
4.4 CFD Analysis.....	89
4.4.1 Water Cooled EMAT for Inspection.....	89
4.4.2 Oil Cooled EMAT for Inspection	92
4.4.3 Water Cooled EMAT for Long Term Inspection.....	94
4.4.4 Summary	96
Chapter 5.....	98
Design and Characterization of Water Cooled EMAT	98
5.1 Introduction.....	98
5.2 Existing Technology	98
5.2.1 Room Temperature Ultrasonic Evaluation.....	98
5.2.2 High-Temperature Ultrasonic Evaluation	103
5.3 Water Cooled EMAT for High-Temperature GWT.....	106
5.3.1 EMAT Design.....	106
5.3.2 Impedance Analysis	107
5.3.3 Wave Mode Purity Characterization.....	112

5.3.4 Room Temperature Ultrasonic Evaluation.....	126
5.3.5 Summary	129
Chapter 6.....	131
High Temperature Experiments	131
6.1 Introduction.....	131
6.2 High-Temperature Experiments – Short Term Exposure	131
6.2.1 Experimental Set-up.....	131
6.2.2 EMAT Performance against Material of Specimen	133
6.2.3 Lift-off Limitations	137
6.2.4 Power Requirements	140
6.3 High-Temperature Experiments – Long Term Exposure.....	142
6.4 Summary	147
Chapter 7.....	149
Conclusions and Recommendation for Future Work.....	149
7.1 Thesis Review	149
7.2 Thesis Findings	151
7.2.1 EMAT model for room and high temperatures.....	151
7.2.2 EMAT thermal and CFD model.....	153
7.2.3 Limitations of existing GWT EMATs - Mechanism for SNR enhancement.....	154
7.2.4 Experimental validation of model - Wave mode purity of PPM EMAT	155
7.2.5 Water cooled PPM EMAT – Room temperature characterization.....	155
7.2.6 Water cooled PPM EMAT – High-temperature performance	156
7.3 Suggestions for Future Work	157
References.....	159

List of Figures

3.1	Schematic of Lamb wave propagation in an isotropic plate	42
3.2	Dispersion curves of a 3mm thick steel plate	44
3.3	EMAT coil (a) spiral (b) racetrack (c) meander (d) butterfly	52
3.4	EMAT designs (a) spiral EMAT (b) racetrack EMAT (c) meander EMAT d) butterfly EMAT	53
3.5	PPM EMAT	54
3.6	Equivalent electric circuit of EMAT coil	58
3.7	Equivalent electric circuit of (a) EMAT transmitter and sample (b) sample and EMAT receiver	60
3.8	Electric circuit (a) EMAT/specimen transformer connection (b) autotransformer connection (c) autotransformer connection without parasitic capacitance	62
4.1	Dispersion curves of a 3mm thick 316L stainless steel plate	72
4.2	(a) Comsol FEA model configuration (b) EMAT configuration	75
4.3	(a) Excitation/eddy current distribution at 11 μ sec (b) Magnetic flux distribution (MSP)	77
4.4	Schematic of coordinate system and displacement orientation	
4.5	Y and Z displacement at 0° angle	78
4.6	Displacement of S_0 wave mode at a) x, b) y and c) z axis	79
4.7	Displacement measured at 97 μ sec a) x, b) y and c) z axis	79
4.8	Eddy current density against temperature rise	80
4.9	(a) Y displacement against temperature rise (b) Displacement at 0° angle at 500°C (c) Out – of – plane displacement at room temperature and 500°C (zoom)	80
4.10	Displacement of S_0 wave mode at a) x, b) y and c) z axis	82

4.11	Displacement measured at 97 μ sec a) x, b) y and c) z axis	82
4.12	Thermal EMAT model (a) entire EMAT design (b) cooling chamber (c) coil structure	85
4.13	Temperature gradient of alumina encapsulated coil (a) 0.75mm alumina thickness (b) 1mm alumina thickness	86
4.14	Optimum ceramic thickness graph	87
4.15	Temperature gradient of Kapton and alumina encapsulated coil (a) 0.75mm alumina thickness (b) 1mm alumina thickness	88
4.16	(a) EMAT temperature against coolant flow velocity (b) EMAT temperature against coolant temperature	90
4.17	Water cooled EMAT (a) temperature gradient of EMAT components at 500°C (b) temperature of EMAT components against temperature rise	91
4.18	Temperature gradient of EMAT at 250°C after (a) 1min (b) 15mins (c) 30mins (d) coil and magnets temperature against operating time	95
5.1	(a) Signal received from defect-free area without shielding (b) Signal received from defect without shielding	99
5.2	(a) Signal received from defect-free area with shielding (b) Signal received from defect with shielding	100
5.3	Room temperature PPM EMAT: Amplitude against lift-off	100
5.4	Room temperature PPM EMAT: Amplitude against power	101
5.5	High temperature experimental set-up (a) EMATs attached upon specimen (b) electrical instrumentation – RITEC (c) thermal instrumentation	102
5.6	Signal received at (a) room temperature (b) 60°C (c) 100°C (d) 180°C	103
5.7	Room temperature PPM EMAT: Amplitude against temperature rise	104
5.8	(a) EMAT design (b) EMAT prototype	105
5.9	(a) Constantan coil (b) Alumina & Kapton encapsulated coil (in mm)	106
5.10	Resistance against temperature rise	111
5.11	Inductance against temperature rise	111

5.12	Capacitance against temperature rise	111
5.13	Dispersion curves (a) phase velocity of 1.5 mm thick stainless steel plate (b) group velocity of 1.5 mm thick stainless steel plate (c) phase velocity of 0.5 mm thick stainless steel plate (d) group velocity of 0.5 mm thick stainless steel plate	113
5.14	(a) Experimental setup of vibrometry tests (b) zoom in EMAT and scanning area	114
5.15	Wave mode purity for 3mm stainless steel plate. Displacement in (a) x axis (b) y axis (c) z axis at 59 μ sec (d) x axis (e) y axis (f) z axis at 97 μ sec	115
5.16	Displacement at 180° in 3mm thick stainless steel plate in (a) all axis (b) x-axis (c) y-axis (d) z axis	116
5.17	Displacement generated in 1.5mm thick stainless steel plate in (a) x axis (b) y axis (c) z axis received at 58 μ sec (d) x axis (e) y axis (f) z axis received 97 μ sec (g) x axis (h) y axis (i) z axis received 111 μ sec	118
5.18	Displacement generated in 0.5mm thick stainless steel plate in (a) x axis (b) y axis (c) z axis received at 58 μ sec (d) x axis (e) y axis (f) z axis received 97 μ sec (g) x axis (h) y axis (i) z axis received 111 μ sec	119
5.19	Displacement at 0° in 1.5mm thick stainless steel plate in (a) all axis (b) x axis (c) y axis (d) z axis	120
5.20	Displacement at 0° in 0.5mm thick stainless steel plate in (a) all axis (b) x axis (c) y axis (d) z axis	120
5.21	FEA results for wave propagation in 3mm thick mild steel plate in (a) x-axis (b) y-axis (c) z-axis received at 56 μ sec and (d) x-axis (e) y-axis (f) z-axis received at 93 μ sec	122
5.22	Displacement at 0° in 3mm thick mild steel plate in (a) all axis (b) x-axis (c) y-axis (d) z axis	123
5.23	Vibrometry results. Displacement generated in 3mm thick mild steel plate in (a) x-axis (b) y-axis (c) z-axis received at 56 μ sec (d) x-axis (e) y-axis (f) z-axis received at 93 μ sec	124
5.24	Signal received from (a) room temperature EMAT on stainless steel (b) water cooled EMAT on stainless steel (c) water cooled EMAT on mild steel (d) amplitude difference	126
5.25	Water cooled EMAT – Amplitude against lift-off	127
5.26	Water cooled EMAT – Amplitude against power	128

6.1	Experimental setup for high-temperature experiments	131
6.2	Thermal picture of the experimental setup used for the heating up of the specimen (500°C)	132
6.3	Signal received from both EMATs on mild steel at (a) room temperature (b) 250°C (c) 500°C (d) amplitude against temperature	133
6.4	Signal received from both EMATs on stainless steel at (a) room temperature (b) 250°C (c) 500°C (d) amplitude against temperature	134
6.5	Temperature of EMAT components: measured and estimated values	136
6.6	Nd-Fe-B EMAT: Amplitude against lift-off at high temperatures	137
6.7	SmCo EMAT: Amplitude against lift-off at high temperatures	138
6.8	Nd-Fe-B EMAT: Amplitude against power input at high temperatures on (a) mild steel (b) stainless steel	140
6.9	SmCo EMAT: Amplitude against power input at high temperatures on (a) mild steel (b) stainless steel	141
6.10	Thermal photo of experimental setup for the EMAT evaluation about long-term inspection at 250°C	142
6.11	Nd-Fe-B EMAT: Amplitude over time at 250°C	142
6.12	Nd-Fe-B EMAT: Impedance over time at 250°C (a) Magnitude (b) Phase	143
6.13	Nd-Fe-B EMAT: Signal received at 250°C after (a) 1min (b) 3 hours operation	144
6.14	SmCo EMAT: Amplitude over time at 250°C	144
6.15	SmCo EMAT: Amplitude over time at 250°C and 350°C	145
6.16	SmCo EMAT: Impedance over time at 250°C	145
6.17	SmCo EMAT: Signal received at 350°C after (a) 1min (b) 3 hours operation	145

List of Tables

4.1	Dispersion curves – Wave modes at 256kHz	72
4.2	Dispersion curves – Phase Velocity	73
4.3	Dispersion curves – Group Velocity	73
4.4	Material properties over temperature rise	74
4.5	Thermal properties of EMAT based on transient thermal analysis	89
4.6	Temperature of oil cooled EMAT against flow velocity and oil temperature	93
5.1	Preliminary EMAT impedance analysis	107
5.2	EMAT impedance against material properties of specimen	107
5.3	EMAT impedance against lift-off	107
5.4	Parasitic capacitance between EMAT and specimen	109
5.5	Phase and group velocity against plate thickness at 256kHz	117

Acknowledgements

I would like to express my deepest gratitude to Prof. Tat-Hean Gan for his excellent guidance, support and rigorous supervision given to me throughout all this work. I would like to sincerely thank him for giving me the opportunity to be part of the Brunel Innovation Centre (BIC) and The Welding Institute (TWI), where I was instilled in research in pioneering and niche technologies. I am also grateful to Prof. Balachandran Wamadeva for his valuable advice and numerous scientific conversations that given me the enthusiasm and drive needed for the refinement of my research and the completion of my studies.

All my gratitude goes to all the members of BIC, NDT department of TWI and Plant Integrity for their help and cooperation. I am indebted to Dr. Vassilis Kappatos for his stimulating and fruitful scientific discussions that not only have been enlightening for me but also enjoyable. I also want to express my appreciation to Dr. Makis Livadas, Dr. Bhavin Engineer, and Dr. Alex Haig for their invaluable help and advice in the theoretical analysis and experimental part of this thesis, without them this research would probably have not materialized.

I would also like to thank all those who made this arduous scientific journey also a delightful time with their friendship. Nothing of this would have ever happened without the support and love of my family. Heartfelt thanks to my Mitera, Patera, Kleopatra, and George who were next to me all these years despite the distance.

Declarations

The work presented in this thesis is my original research. Wherever contributions of others are involved, every effort is made to indicate this clearly, with due reference to the literature, and acknowledgment of collaborative research and discussions. The work was done under the guidance of Prof. Tat-Hean Gan and Prof. Balachandran Wamadeva at the Department of Department of Electronic and Computer Engineering, in Brunel University London, during the period of November 2013 and October 2016.

No part of this work has been previously submitted to Brunel University London, nor any other academic institution, for admission to a higher degree. Some of the work has appeared in the forms of publications, and those are listed on the List of publications section.

Nomenclature

\times	Vector product
∇	Vector differential operator
∇^2	Laplace operator
A	Arbitrary initial values, unit area (m^2), Magnetic Vector Potential (V s/m)
A_0	Zero order Axisymmetric Lamb wave mode
AE	Acoustic Emission
Al	Aluminium
B	Arbitrary initial values, magnetic field (T)
B_{dyn}	Dynamic magnetic field (T)
BNC	Bayonet Neil Concelman
B_{st}	Static magnetic field (T)
C	Stiffness tensor (Pa)
CFD	Computational Fluid Dynamics
c_g	Group velocity (m/s)
c_L	Longitudinal velocity (m/s)
c_p	Phase velocity (m/s)
C_p	EMAT parasitic capacitance (F)
c_s	Shear velocity (m/s)
Cu	Copper
C_w	Parasitic capacitance between EMAT and specimen (F)
d	Piezo strain coefficient (m/V), skin depth (m)
D	Electric displacement (C/m^2)
d_c	Coil wire diameter/thickness
D_p	Magnets pitch (m)
D^T	Magnetostriction matrix
E	Electric field (V/m)
e	Electron charge (C)
EC	Eddy Current
EMAT	Electromagnetic Acoustic Transducer
E_z	Electric field at z-depth (V/m)
E_{z0}	Electric field at the surface of specimen (V/m)
f	Frequency (Hz)

FEA	Finite Element Analysis
FEM	Finite Element Method
F_L	Lorentz force (N)
$F_{L_stainless\ steel}$	Lorentz force in stainless steel (N)
F_{L_steel}	Lorentz force in steel (N)
g	Piezoelectric voltage coefficient (V/m)
G	Lift-off (m)
GWT	Guided Wave Testing
H	Magnetic field strength (A/m)
J	Current density (A/m ²)
J_e	Eddy current density (A/m ²)
J_{exc}	Excitation current density (A/m ²)
j_z	Eddy current density in z-axis (A/m ²)
j_{z0}	Eddy current density in z axis (amplitude) (A/m ²)
k	Thickness shear coupling factor
k_L	Longitudinal wavenumber vector (1/m)
k_S	Shear wavenumber vector (1/m)
k_y	Through thickness wavenumber (1/m)
l	Integer
L	Length (m)
L_{coil}	EMAT self-inductance (H)
LDV	Laser Doppler Vibrometry
L_{eq}	EMAT equivalent inductance (H)
L_{lcoil}	Coil inductance primary leakage (H)
L_m	Eddy current inductance (H)
M	Magnetization (N), mutual inductance (H)
m	Electron mass (Kg)
MFC	Macro-Fiber Composite
M_n	Normal to surface component of Magnetization (N)
MOT	Maximum Operating Temperature (°C)
MPT	Magnetostrictive Patch Transducers
MSP	Magnetic Scalar Potential (V s/m)
n	Unit vector normal to sample surface
NDT	Non-Destructive Testing
n_e	Electron density (electrons /m ³)

N_i	Ion density (ions/m ³)
P	Polarisation (C/m ²)
PCB	Printed Circuit Board
PPM	Periodic Permanent Magnet
PZT	Lead Zirconate Titanate
Q	Charge (C)
q	Charge (C)
R	Electrical resistance (Ω)
R_0	Electrical resistance at room temperature (Ω)
R_{coil}	EMAT resistance – coil (Ω)
S_0	Zero order Symmetric Lamb wave mode
SH	Shear Horizontal
S^H	Elastic compliance matrix measured under constant magnetic field
SH ₀	Zero order Shear Horizontal wave mode
SHM	Structural Health Monitoring
Si	Silicon
SiO ₂	Silicon dioxide
Sn	Tin
SNR	Signal to Noise Ratio (dB)
t	Time (s)
T	Temperature ($^{\circ}$ C)
t_c	Alumina thickness (m)
t_k	Kapton thickness (m)
t_{max_coil}	Time needed for coil temperature to maximize (s)
$t_{max_magnets}$	Time needed for magnets temperature to maximize (s)
t_{norm_coil}	Normalized time for coil temperature to reach its maximum (s)
$t_{norm_magnets}$	Normalized time for magnets temperature to reach its maximum (s)
ToF	Time of Flight (s)
t_p	Thickness (m)
u	Displacement (m)
UT	Ultrasonic Testing
ν	Poisson ratio, velocity (m/s)
V	Scalar potential
v_e	Mean velocity of electron (m/s)
v_i	Ion velocity (m/s)

W	Width (m)
x	Spatial coordinate
z	Spatial coordinate
Z_{coil}	EMAT impedance – magnitude (Ω)
Z_i	Ion charge (C)
Z_{sample}	Sample impedance (Ω)
α	Linear coefficient of expansion (m/m $^{\circ}$ C), temperature coefficient of resistance (1/ $^{\circ}$ C)
ΔT	Temperature increase ($^{\circ}$ C)
E	Young's modulus (Pa)
ϵ_0	Relative permittivity of free space (F/m)
ϵ_r	Relative permittivity (F/m)
E_{TH}	Young's modulus at room temperature (Pa)
θ_{coil}	EMAT impedance – phase ($^{\circ}$)
λ, μ	Lamé constants
μ_0	Magnetic permeability of free space (H/m)
μ^{σ}	Permeability at constant stress (H/m)
ρ	Density (Kg/m ³)
ρ_q	Charge density (C/m ³)
ρ_r	Sample resistivity (Ω m)
ρ_{TH}	Density at room temperature (Kg/m ³)
σ	Electric conductivity (S/m)
σ_s	Stress tensor (Pa)
τ	Mean time of electron-ion collision (s)
φ	Compressional scalar potential
φ_0	Arbitrary initial value (amplitude)
Ψ	Vector potential
Ψ_0	Arbitrary initial value (amplitude)
ω	Angular frequency (rad/s)
ω_R	Resonant angular frequency (rad/s)
ϵ_s	Strain tensor

Chapter 1

Introduction

1.1 Motivation

In nuclear, solar thermal and oil industry, critical components operate under hostile conditions. Pipelines, tanks, pressure vessels and absorber tubes carrying flammable liquids can suffer from creep, thermomechanical fatigue and hot corrosion due to high temperatures [1-4]. This can result in the appearance of an internal or surface defect on them, which can lead to the shutdown of the plant, economic damage and in some cases to severe hazard for human life as well. The structural assessment of these components is of high importance since defects can be detected, localised and sized in early stage before an irreversible failure of the structure occurs. Non-Destructive Testing (NDT) can be employed for structural monitoring or inspection of structures operating at high temperature.

NDT is an interdisciplinary subject that has been widely applied to industrial environments for the structural assessment of components of various shapes and sizes without causing any further damage to them [5-7]. The operating conditions, access, size and structural complexity of the object under inspection limits the number of NDT techniques that can be efficiently employed. Acoustic Emission (AE), Eddy Current (EC), Laser Ultrasonic, Interferometry, Thermography and Guided Wave Testing (GWT) have been used at high temperatures, with shortcomings [8-13]. The sensitivity to noise and vibrations, instrumentation complexity, high cost and achieving qualitative results are some of their drawbacks. The high-temperature performance of the sensors or transducers used can limit the efficiency of the technique used.

GWT is commonly used for the inspection or monitoring of large structures from single point [14-15]. Long pipelines, large tanks and buried pipes carrying flammable fluids are usually inspected with the use of GWT, due to their size and limited number of access points. Guided waves can

propagate large distances without significant attenuation; however, their wave velocity depends on both the geometry of the specimen and the excitation frequency – a phenomenon called dispersion, which complicates the interpretation of signals [15-18]. Shear Horizontal (SH_0) or T(0,1) is not dispersive and cannot propagate in liquids, simplifying signal interpretation and online inspection of structures containing liquids. GWT can also be used for the inspection of high-temperature structures, like absorber tubes whose length can reach 12 meters and operate up to 500°C [2]. However, its efficiency is limited by the high-temperature performance of the transducers.

The dominant technology of transducers for GWT is piezoelectric. They have high signal to noise ratio, are easy to use, have low cost and small size and do not require high driving voltages. However, they demand physical contact with the specimen either by means of coupling medium between them and the specimen or of large force exerted on them (dry coupling) [19]. As a result, moving structures or components under vacuum cannot be inspected by piezoelectric transducers. Since the first high-temperature piezoelectric transducer appeared in 1940 several piezoelectric materials have been tested at high temperatures [20-22]. PZT is the most widely used material, operating efficiently up to 200°C. Piezoelectric transducers can thermally decompose and lose oxygen at high temperatures [20-22]. The duration of exposure to high temperatures can significantly influence transducers properties. PZTs' performance degrades greatly over time at high temperatures making it unsuitable for that particular target temperature of 500°C. When the Maximum Operating Temperature (MOT) of PZTs is exceeded, the transducers permanently lose their piezoelectric property and require costly replacement.

Electromagnetic Acoustic Transducers (EMATs) are non-contact transducers, have simple design and can be used with GWT to inspect long, moving structures, high-temperature objects or structures under vacuum. Therefore, they can potentially be employed for the inspection of absorber tubes, which are long stainless steel pipes inside glass envelope under vacuum [2]. They can excite/receive all types of wave (bulk, Rayleigh and Lamb) and require neither a viscous couplant nor a large force exerted to excite SH waves in the specimen [23-27]. They are not subject to skin effect and can be employed for the inspection of any electrically conductive material. They are more efficient on ferromagnetic specimens. However, they are power demanding and their

ultrasonic performance varies with the material properties of the specimen. Their ultrasonic response is also lower than PZTs' – inspected lengths with EMATs are an order of magnitude smaller.

To date, high-temperature EMATs have been developed only for thickness measurements on metal blocks. The already reported high-temperature EMAT technology is not suitable for GWT [231-235]. An EMAT that can be used in GWT and withstand high temperatures for both inspection and monitoring is still required to be designed and tested and it is the subject of the study reported in this thesis. This EMAT can be employed in oil and gas industry for high-temperature GWT inspection of long pipelines or tanks which carry flammable liquids and their structural integrity assessment is of great importance. The high-temperature GWT of moving or under vacuum structures, like absorber tubes, can also be accomplished with the use of this EMAT.

1.2. Aim

The development of novel EMAT for high-temperature GWT for both short and long-term thermal exposure is the aim of this study. The limitations of the current EMAT technology for GWT at high temperatures (100°C-500°C) are needed to be experimentally investigated and surpassed by the new GWT EMAT. The transducer is designed to exceed the boundaries and MOT of existing technology and operate up to 500°C for short period of time and at lower temperatures over longer time periods. Finite Element Analysis (FEA) for the calculation of the effect of temperature rise on EMAT ultrasonic performance and its thermal properties and the estimation of the optimum EMAT design has been performed. The experimental characterisation, ultrasonic and thermal evaluation of the transducer at both normal and extreme operating conditions are the final targets of this research.

1.3. Specific Objectives

This research aimed to meet the aforementioned targets by materialising the following objectives.

- Identification of potential and constraints existing GWT EMAT technology experiences at high temperatures.
- Coupled electromagnetic/mechanical FEA model for the qualitative estimation of temperature effect on the ultrasonic performance of EMAT.
- Thermal and Computational Fluid Dynamics (CFD) FEA for optimum material selection, EMAT design and operating conditions at elevated temperatures.
- Establishment of an empirical method for the enhancement of Signal to Noise Ratio (SNR) of the signal received of EMATs and improvement of their defect detection capabilities.
- EMAT development and experimental investigation of its impedance profile against various operating parameters and its wave mode purity characteristics via vibrometry tests.
- Experimental comparison of the ultrasonic performance of novel EMAT at ambient temperature to that of existing room temperature EMAT for GWT.
- Thorough experimental evaluation of ultrasonic potential and limitations and thermal properties of new EMAT at high temperatures against various operating conditions for both short and long-term thermal exposure.

1.4. Summary of Methodology Used

This research focuses on the theoretical analysis and development of an SH EMAT for GWT at high temperatures (above 100°C) for both inspection and monitoring. A Periodic Permanent Magnet (PPM) EMAT was designed to operate efficiently up to 500°C for inspection and 250°C for continuous monitoring, for potential deployment on absorber tubes. Thermal and CFD FEA were performed for material selection, optimisation of EMAT design and calculation of its optimum operating conditions. FEA of the ultrasonic response of the PPM EMAT transmitter was carried out and experimentally validated by means of vibrometry analysis on both steel and stainless steel at room temperature. Experimental impedance analysis of the transducer at both room and high temperature was also accomplished and correlated to the final ultrasonic results obtained when the EMAT was experimentally evaluated regarding its GWT performance at room and high temperatures.

1.5. Thesis Outline

The skeleton of the thesis is presented below. The first three Chapters summarise the research on EMAT technology that has been performed already, mainly focusing on EMATs for GWT and high temperatures, and introduces the main novelties of this study compared to the existing. The next three Chapters present the theoretical analysis performed for the designing of a novel EMAT for GWT at high temperatures and the experimental methodology followed for the ultrasonic characterisation and evaluation of the final EMAT prototype. A detailed description of the contributions of this study can be found in the following five Chapters.

Chapter 2 gives an overview of the NDT techniques that have been successfully employed at high temperatures, with emphasis given on GWT. The advances of piezoelectric transducer technology for GWT and more especially their high-temperature performance are also summarised. A literature review on EMAT technology and more particularly, on EMATs for high-temperature applications and GWT is also presented.

In *Chapter 3* the operating principles of guided waves and EMATs are described. The basic theory of guided waves, their wave propagation mechanisms, dispersion nature and the effect of temperature rise on the guided wave propagation and the physics governing the excitation and the reception of ultrasound by EMATs are presented and emphasis is given on both Lorentz and magnetostriction mechanism. The effect of temperature on EMAT performance is also analysed in this Chapter. The electrical circuit of EMAT, its impedance and their relationship with temperature rise are also highlighted in this section.

The theoretical analysis performed for the identification of the optimum EMAT design for GWT at high temperatures is presented in *Chapter 4*. The ultrasonic response of PPM EMAT transmitter on stainless steel plate and the guided wave propagation at both room and high temperatures was analysed via FEA. Also, the results obtained from thermal and CFD FEA in regards to material selection, optimum EMAT design and operating conditions are presented in this Chapter. Part of this Chapter is the basis of an article published in Applied Sciences [P2].

The results obtained from preliminary high-temperature experiments with the existing EMAT technology designed for GWT at room temperature are cited in *Chapter 5* and can be used as a benchmark for the novel high-temperature EMAT. An empirical approach regarding the SNR enhancement of the signal received from PPM EMAT at room temperature and its correlation to the electrical properties of EMATs against the specimen are also analysed in this Chapter. The wave purity characterisation of the new EMAT prototype via vibrometry tests and the results obtained from its impedance analysis at room and high temperature are also summarised. Parts of this Chapter are the basis of an article published in Applied Sciences [P2] and another article published in Sensors [P1].

Chapter 6 describes the experimental procedure followed for the ultrasonic evaluation of the new EMAT design against high temperatures. The experimental setup and results collected from the GWT of steel and stainless steel plates with the use of the new EMATs up to 500°C for short period of time and 250°C over time are presented in details. Parts of this Chapter and Chapter 4 are the material of an article published in Sensors [P1].

Finally, the conclusions of this study are summarised in *Chapter 7* and further work is also suggested.

1.6. Contributions to Knowledge

This study managed to shed light on various questions regarding EMAT technology and GWT at both ambient and high-temperature environment, as they are listed below.

- A shielding technique for the enhancement of the SNR of the signal received by PPM EMAT was established and theoretically analysed.
- FEA model calculating the ultrasonic response of PPM EMAT at both room and high temperatures was accomplished and can be utilised further for qualitative estimation of the ultrasonic properties of other EMAT configurations at high temperatures.

- Thermal and CFD models determining the thermal properties of EMAT were developed and experimentally validated; they can provide valuable information regarding the thermal response of EMAT designs operating under hostile conditions.
- An experimental investigation concerning the wave purity characteristics of PPM EMAT was also performed, rendering critical and fundamental information about the GWT performance of this EMAT configuration. It was proved that PPM EMAT exhibits poor wave mode purity capabilities.
- A novel, water cooled EMAT for GWT operating efficiently up to 500°C for short time period and 250°C over time was developed and thoroughly evaluated against various operating conditions.

1.7. List of Publications

- [P1] M. Kogia, T.H. Gan, W. Balachandran, M. Livadas, V. Kappatos, I. Szabo, A. Mohimi, A. Round. High-Temperature Shear Horizontal Electromagnetic Acoustic Transducer for Guided Wave Inspection. *Sensors* **2016**, *16*, 582-597.
- [P2] M. Kogia, L. Cheng, A. Mohimi, V. Kappatos, T.H. Gan, W. Balachandran, C. Selcuk. Electromagnetic Acoustic Transducer Applied to High-Temperature Plates for Potential Use in the Solar Thermal Industry. *Applied Sciences* **2015**, *5*, 1715-1734.
- [P3] M. Papaalias, L. Cheng, M. Kogia, A. Mohimi, V. Kappatos, C. Selcuk, L. Constantinou, C.Q. G. Muñoz, F.P. G. Marquez, T.H. Gan. Inspection and Structural Health Monitoring Techniques for Concentrated Solar Power Plants. *Renewable Energy* **2016**, *85*, 1178-191.
- [P4] L. Cheng, M. Kogia, A. Mohimi, V. Kappatos, C. Selcuk, T.H. Gan. Crack characterisation using invariable feature extraction in stainless steel specimen used for absorber tubes of CSP applications via EMATs. *Renewable Energy* **2017**, *101*, 771-781
- [P5] M. Kogia, T.H. Gan, W. Balachandran, M. Livadas, B. Engineer. Wave mode purity analysis of water cooled PPM EMAT. *IEEE Sensors* [submitted]

- [P6] M. Kogia, T.H. Gan, W. Balachandran, M. Livadas. Water cooled EMAT for long term inspection at high temperatures. *Metals* [submitted]
- [P7] M. Kogia, L. Cheng, A. Mohimi, V. Kappatos, T.H. Gan, W. Balachandran, C. Selcuk. An Experimental Investigation of Electromagnetic Acoustic Transducers Applied to High-Temperature Plates for Potential Use in Solar Thermal Industry. *Proceedings of the 6th International Conference on Emerging Technologies in Nondestructive Testing (ETNDT6)*. Brussels, Belgium. 27- 29 May 2015.
- [P8] M. Kogia, A. Mohimi, C. Liang, V. Kappatos, C. Selcuk, T.H. Gan. Electromagnetic Acoustic Transducer for the inspection of Jointed Solar Thermal Tubes. *In Proceedings of the 1st Young Professionals International Conference*. Budapest, Hungary. 17–20 September 2014

Chapter 2

Literature Review

2.1 Introduction

This Chapter briefly presents the operating principles of the main NDT techniques that have been successfully deployed at high temperatures and their limitations. GWT is highlighted and a literature review on GWT transducers and more particularly, on EMATs and their potential on GWT and high-temperature applications is also given.

2.2 NDT Techniques for High-Temperature Inspection

There are several NDT techniques that can be applied for the inspection or monitoring of structures operating at elevated temperatures. AE, Optical Inspection techniques, EC, Thermography, Laser Ultrasonic and Ultrasonic Testing (UT) can successfully be employed at least up to 300°C.

AE is the class of phenomena whereby transient elastic waves are generated by the rapid release of energy from a localized source or sources within a material, or the transient elastic wave(s) so generated. The initiation or propagation of a structural deformation/discontinuity in specimen generates elastic waves that can be received by transducers that are attached to the surface of the specimen. The interpretation and feature extraction of the signal received can lead to the detection and localization of a defect [28]. AE has been widely deployed for the Structural Health Monitoring (SHM) of bridges, nuclear reactors, engines and aerospace metallic structures since real-time information regarding the structural integrity of the specimen can be obtained [28-34]. AE transducers have been employed at high temperatures as well [35-41]; piezoelectric transducers, like Yttrium Calcium Oxyborate and Aluminium Nitride, have been successfully used in AE up to 700°C and 1200°C respectively [8, 42]. Nevertheless, AE is greatly sensitive to background noise and gives qualitative results [43]; recent advances show that this problem has

been partially tackled [43-46]. However, real-time de-noising and interpretation of the signal received from complicating structures is still a non-trivial task [34].

Optical inspection methods are non-contact NDT techniques that assess the structural integrity of the specimen by comparing its current state to a reference signal. A laser beam illuminates a large area of the specimen and the electromagnetic response of the latter is collected and compared to the initial laser beam characteristics. Both signals are of the same frequency and any difference in the distance they travel results in their phase difference, which is used for the construction of a pattern image of the specimen. Shearography, Holographic and Photothermal Interferometry and Digital Image Correlation have often been employed for surface defect detection [11, 47-54]. Holographic Interferometry and Digital Image Correlation have been successfully used for the structural assessment of high-temperature structures (up to 1600°C) like, turbines blade [55-57]. However, their instrumentation is complicating and are mainly utilised for laboratory tests. Specially trained personnel is also needed.

EC is a non-contact technique that can be employed for the inspection of any electrically conductive material regardless of its magnetic properties. EC probes comprise a coil that carries alternating current. A dynamic magnetic field is produced all around the coil, which induces eddy current on the surface of specimen that is underneath the coil in good proximity. When the magnetic and/or the electrical properties of the specimen alter or a defect exists on the surface of the specimen, the eddy current distribution on the surface of the specimen differs and causes an alteration in the impedance of the EC receiver. EC has been widely employed for pitting detection on metals, weld inspection and defect sizing [58-64]. It has been also employed at high temperatures up to 500°C [65, 66]. There are commercial high-temperature EC probes operating up to 280°C and 380°C (continuously) [67, 68]. Urayama et al. have also developed and preliminarily tested a dual EMAT/EC probe for high-temperature monitoring (300°C) of pipe wall thinning [69]. However, it can only be utilized on electrically conductive materials for surface and subsurface defects, since it is subject to skin effect [70]. Also, EC scanning of large structures can be greatly time-consuming.

Thermography monitors the temperature gradient on the surface of the specimen. As the structure under inspection is heated up, it emits infrared energy which can be captured by infrared camera. The radiation emitted by the specimen is directly related to its temperature and emissivity. If any internal or surface discontinuities are present, the temperature gradient of the specimen alters. Hence, the thermal imaging of the specimen can provide valuable information regarding its structural integrity [71]. Large areas can be inspected or monitored online, since thermography is a non-contact technique. Infrared thermography has been widely employed for the non-destructive testing of concrete structures, bridges and composites [71-74] and the inspection of high-temperature structures [12]. Commercial infrared cameras operating up to 3000°C are available and suitable for the inspection of industrial furnaces, heaters and boilers [75, 76]. Nevertheless, thermography cannot be used efficiently when the access on the surface of the specimen is limited and it is time-consuming for the inspection of large structures [77].

Lasers can generate ultrasound by means of either thermal expansion or ablation. In the former case, the laser beam heats up a small area on the surface of the specimen; if the temperature on this area exceeds the melting point of the specimen, thermal expansion occurs and some material is evaporated resulting in the generation of ultrasound [78-81]. In ablation regime, plasma is generated in the area the laser beam points at and it contributes to ultrasound generation due to its expansion [78-81]. Lasers produce short pulses of high power signals and therefore the energy introduced to the specimen results in broadband ultrasound with dominant high-frequency content. The ultrasound can be detected by lasers [54] or any other technology of ultrasonic transducers [91-95]. Lasers have been employed for crack sizing, wall thickness measurements and elastic properties estimation up to 1000°C [82-85]. Laser/EMATs setups have been reported in the literature for non-contact generation/reception of ultrasound at both room [86-93] and various high temperatures up to 1300°C [10, 94-101]. In all cases, the ultrasound is generated by lasers and is detected by EMATs. Laser ultrasonic has a small and adjustable footprint. Therefore, it can be used for the inspection of irregular surfaces and samples of small and complex geometry [102]. It induces high-frequency ultrasound to the specimen and thus very small defects can be detected as well [78-81]. However, its setup is complex and it is mainly used for laboratory tests [78-81].

UT is an established NDT technique that can be categorized into conventional UT where bulk waves propagate in the structure and GWT in which guided waves are of interest. The geometry of the specimen, the wave propagation mechanisms and the specifications of the application determine the technique that should be applied. Bulk waves propagate in infinite structures and their velocity depends only on the material properties of the specimen. Shear and longitudinal waves propagate inside the specimen and their velocity is independent of frequency. Conventional UT is mainly used for thickness measurements, weld inspection and defect sizing [103-114], while it is time-consuming when scanning of large structures is needed. Guided waves derive from the interaction of bulk waves with the boundaries of the specimen; reflection, refraction and mode conversion between shear and longitudinal waves occur. Guided waves can be divided into Rayleigh and Lamb waves in terms of the wave propagation mechanism; the former propagate at the boundaries while the latter travel between the boundaries of the specimen. Guided waves can propagate large distances without significant attenuation and their velocity is dependent on the material properties and the geometry of the specimen and frequency. A phenomenon called dispersion which complicates the interpretation of the signals received [14-17]. GWT is used for the inspection or monitoring of large structures from a single point and therefore it has been widely employed for pipeline and tank inspection in nuclear, solar, oil and gas industries [2, 115-121]. Conventional UT and GWT can also be used for the inspection of high-temperature structures, but their efficiency is limited by the high-temperature performance of the transducers [122, 123].

Piezoelectric, Macro Fiber Composite (MFC) and EMAT are the main three types of GWT transducers. The first two share similar operating principles, since they experience mechanical deformations when electrical energy is applied to them resulting in the vibration of the specimen and the generation of ultrasound, and vice versa [19, 124]. Nevertheless, only piezoelectric transducers have been reported for their successful deployment at high temperatures [21]. EMATs are non-contact transducers that have been used at both conventional UT and GWT and can efficiently substitute piezoelectric technology in challenging applications like inspection of moving or under vacuum structures or at high temperatures [95, 125].

A more detailed overview of GWT as well as a brief literature review of piezoelectric and mainly EMAT transducers follow.

2.3 Guided Wave Testing

In nuclear, solar, oil, gas and petrochemical industries there are meters of pipelines carrying inflammable liquids that operate under hostile conditions like high pressure and high temperatures. They are likely to suffer from corrosion, creep and fatigue. Defects like cracks and corrosion can appear on these structures and result in their structural failure and even in life hazard. Regular inspections regarding their structural integrity are therefore needed. A considerable number of these pipelines is insulated and thus any insulation removal required for their inspection can be significantly costly. In some cases, buried pipelines need to be also assessed regarding their structural integrity, however, the access to these pipes is limited and their excavation is expensive. Pressure vessels, tanks, absorber tubes and rail-rods are also large structures that require either monitoring or regular inspections. An NDT technique that has been widely employed in the aforementioned applications and has managed to tackle the above problems is GWT.

Guided waves are low-frequency ultrasonic waves that can propagate either at the boundaries of a structure or within them. They can travel long distances without great attenuation making them attractive for the inspection of large structures. Insulation removal is required only in few small areas where the transducers are to be employed; structures of tens of meters of length can be inspected from a single point, since GWT systems usually operate in a pulse-echo configuration. Since 1957, when Worlton [16, 126] experimentally investigated the use of Lamb waves in GWT, many a researcher have studied Lamb and Rayleigh waves; especially from the 1970s onwards, Viktorov [14], Doyle and Scala [127], Silk and Bainton [128], Bottger *et al.* [129], Rose [130] and Mohr and Holler [131] researched the potential of guided waves in the structural assessment of planar and tubular structures. During 1990s Cawley and Alleyne studied the interaction of Lamb waves with defects and optimized Lamb wave inspection [15-19, 132, 133]. Their research has set the foundations for the production of the first commercial GWT system [116]. To date, there are three commercial GWT systems available from Plant Integrity Ltd (wholly owned subsidiary of

TWI) [134], Guided Ultrasonics Ltd [135] and MKC NDT [136]. The first two systems make use of piezoelectric transducers and technology that has been patented by Cawley *et al.* in 1994 [116], while the third system uses magnetostrictive transducers. Guided Ultrasonics Ltd has also developed a high-temperature GWT system (High-Temperature Wavemaker Pipe Screening System) that can operate up to 240°C for inspection purposes with the use of PZT transducers and Plant Integrity Ltd has also launched a GWT system (Teletest) for high-temperature inspection up to 250°C and monitoring up to 200°C that again make use of high-temperature PZT transducers.

The SNR of the signal received at room and high temperatures, the wave mode purity characteristics, the length of inspection and the defect detection probabilities of GWT system vary for different applications due to the physics of guided waves, but also to the ultrasonic characteristics of the transducers used. The following subsection analyses the GWT potential of the two main technologies of GWT transducers and presents their capabilities at room and high temperatures.

2.4 Piezoelectric Transducers for GWT

The dominant GWT transducers are piezoelectric. They are easy to use, have low cost and small size and do not require high driving voltages but do need physical contact with the specimen [19]. A coupling medium (water-based gel) is usually applied on the surface of the structure under inspection so that the ultrasound will be efficiently introduced to it [19]. Alternatively, a large force is exerted upon the transducer so that the latter will be in full contact with the specimen while the piezo-crystal will not break as well; so-called dry-coupled piezoelectric transducer [19]. As a result, moving structures or components under vacuum cannot be inspected by this technology of transducers, while specially designed couplants and transducers withstanding high temperatures are required for high-temperature inspection or monitoring.

The phenomenon of piezoelectricity was firstly reported by Pierre and Jacques Curie in 1880 and refers to the ability of piezoelectric crystals to generate an electric field when external stress is applied to them (receiver), and conversely, to exhibit a mechanical deformation when they

experience an electric field (actuator) [20]. Quartz was the first natural piezoelectric material that has been studied, but synthetic ferroelectric materials exhibit larger piezoelectric properties than those of natural elements [20]. In more details, piezoelectric crystals have no center of symmetry along their piezoelectric axes; they are composed of randomly oriented dipoles with no net polarization. When a relatively large electric field is applied to a piezoelectric material, its dipoles get aligned to the orientation of the external electric field and they maintain this alignment even in its absence. This procedure is called poling and results in the polarization of the material, which can be described as the charge per unit area.

Polarization and subsequently ultrasonic efficiency of a piezoelectric material are directly affected by the piezoelectric, dielectric and elastic properties of the material. The main three parameters that influence the ultrasonic performance of a piezoelectric element or transducer are the piezoelectric voltage (g) and the piezo strain (d) coefficients and the thickness shear coupling factor (k). Their values can render an indication of the GWT potential of a piezoelectric material and thus they can be utilized as criteria for the material selection of a piezoelectric GWT transducer.

Curie temperature is another essential criterion for the selection of suitable high-temperature piezoelectric transducer. As temperature increases, the kinetic energy of the dipoles increases and leads them to lose their alignment. Consequently, a significant drop in the piezoelectric activity of the material occurs. Especially when temperature exceeds the Curie temperature of the material, the dipoles lose permanently their polarization and therefore extra poling is required when the material is cooled down. The electromechanical properties of the piezo-crystal also alter with temperature rise. The MOT of piezoelectric elements is usually chosen to be half of its Curie temperature.

At high temperatures, and especially at low frequencies, some piezoelectric materials are subjected to pyroelectric effect; charge drifts interfere with the piezoelectrically induced charges and the material exhibits electrical moment even in the absence of an external electric field. Thermal expansion can also contribute to a further drop in the piezoelectric activity of the material due to the increase of its volume. Another fundamental limitation that can rise at elevated temperatures is phase transition which can alter the piezoelectric properties of the material and turn the element to a nonpiezoelectric phase. Twinning can also occur at elevated temperatures in both ferroic and

ferroelastic materials like Quartz and SiO₂. Some compositions can also become chemically unstable at high temperatures and can experience oxygen loss and even decomposition; therefore, they cannot be exposed to high-temperature environment for long time periods. Unlike inspection, the piezoelectric properties and subsequently the ultrasonic performance of PZT degrade greatly over time at elevated temperatures, making it unsuitable for monitoring. Hence, careful study of the relationship of the piezoelectric properties of piezoelectric materials with temperature is needed for the design of a high-temperature piezoelectric transducer.

Since the first high-temperature piezoelectric transducer appeared in 1940, several piezoelectric materials have been tested at high temperatures [13, 20-22, 42, 123, 137-151]. Lead Zirconate Titanate (PZT) is the most widely used material, operating efficiently up to 250°C. It has been extensively used in accelerometers, hydrophones, AE sensors and UT and GWT transducers [20]. Bismuth Titanate is commercially available and has been used in accelerometers operating up to 400°C, however, its electromechanical properties, d and g , are lower than those of PZT; making it a moderately attractive high-temperature piezoelectric material [20]. Lithium Niobate possesses Curie temperature of 1150°C and its electromechanical properties are relatively high, since they are slightly smaller than those of PZT. It is an ideal candidate for the development of accelerometers and UT and GWT transducers [20]. However, its resistivity is a limiting factor especially at temperatures higher than 650° [20]. It also suffers from pyroelectricity and oxygen loss at 600°C and it can start decomposing at 300°C [20]. Lanthanum Titanate, Aluminium Nitride and Langasite possess high Curie temperature, however, their piezoelectric coefficients are considered to be low for the manufacturing of GWT transducers [20]. To date, the commercially available GWT systems designed for high-temperature inspection make use of PZT and potentially Lithium Niobate shear transducers that can operate up to 250°C [152]; still, further research has to be conducted for the development of piezoelectric transducers for higher temperatures and especially monitoring.

2.5 EMATs

EMATs are non-contact transducers that have been utilized in conventional UT for thickness measurement [153, 154] and welding inspection [155] and in GWT for inspection of moving

structures [93, 125, 156] and potentially structures under vacuum [2, 157]. They have simple design and can generate/receive all kinds of waves (bulk, Rayleigh and Lamb) without requiring either any couplant or force exerted on them. Only electrical conductive materials can be inspected by EMATs while their efficiency is dependent on the material properties of the specimen. The electric and magnetic properties of the structure under inspection can greatly affect EMAT performance; EMATs are more efficient on ferromagnetic materials like steel. They are also power-demanding, with some configurations like electromagnet EMATs requiring significantly more energy than conventional, permanent magnet EMATs do and resulting in high operating cost and bulky instrumentation. Their ultrasonic response is also lower than PZTs'—inspected lengths with EMATs are an order of magnitude smaller, making them more desirable as receivers rather than as transmitters.

Their operating principles are primarily governed by Maxwell equations describing electromagnetism and Lorentz force [158] and by magnetostrictive effect firstly stated by Joule [159]. Dobbs [160] was the first that investigated the relationship between electromagnetism and ultrasound. Based on his research Lorentz force can generate ultrasonic waves within a material. However, it was Thompson that set the foundations of EMAT research and technology. He studied the generation and detection mechanisms of EMATs for Rayleigh and Lamb waves as well as their dependency on lift-off, material properties and coil geometry [161]. Apart from Lorentz force, he also investigated in depth the effect of magnetostriction and magnetization force on EMAT ultrasonic performance [162, 163]. In 1979, Period Permanent Magnet (PPM) EMAT was introduced and analyzed by Thompson and Vasile about its potential to excite and receive Shear Horizontal wave modes, a non-trivial task for piezoelectric transducers at that time [164]. Contemporarily, Kawashima contributed further to the modeling of EMAT ultrasonic properties and the effect of coil geometry on the ultrasound generation and reception [165, 166]. Hoeller and Mohr developed the first EMAT system for guided wave testing of cylindrical structures in 1976 [131].

Since the early 1990s and onwards, many advances in the theoretical study of EMATs have been reported due to general technological progress and more particularly the increasing computational

capabilities of computers [167-176]. Ludwig *et al.* developed a finite element model that calculates the ultrasound generated by an EMAT based on all three mechanisms of ultrasound generation [177-179]. This research sheds light on the EMAT performance against variable excitation means and lift-offs, by analyzing the ultrasonic response of EMAT coil driven by a tone-burst excitation signal. However, this work has never been experimentally validated. Further research was conducted by Ogi regarding the magnetostrictive effect on the ultrasonic properties of EMATs [180] and the conclusions of this study have been only qualitatively validated by experiments. In recent years, more research has been conducted regarding EMATs for GWT. Dixon *et al.* have investigated the EMAT physics and designs for Rayleigh and Lamb waves and their defect/crack detection probabilities on metal sheets, tubular structures and rail tracks [125, 181-186]. They studied the electrical and frequency characteristics of various EMAT designs and their impact on EMAT wave mode purity and directivity mainly for Rayleigh waves [183, 187]. Supplementary to this, Wilcox *et al.* focused more on guided wave theory, wave mode purity characteristics and directivity of EMATs for Lamb wave inspection [26, 188]. The skin effect on the efficiency of EMAT transmitters was investigated by Shapoorabadi *et al.* in 2001 by means of FEA model, whose results agree well with experimental results. Rose *et al.* theoretically investigated the defect detection probabilities of an EMAT system employed on coated pipes for GWT [189, 190]. The attenuation and phase change of the wave propagating in the pipe in regards to the material properties of coating were also analyzed. To date, Ribichini's research about the magnetostriction effect on the ultrasonic performance of EMATs in 2011 is the first theoretical study regarding this topic that has been experimentally validated [27, 191].

Added to the numerical and FEA of EMAT literature presented above, a plethora of experimental studies about EMAT potential and limitations on GWT have been performed on both planar and cylindrical structures [192-204]. EMATs have been employed for numerous industrial applications like material properties measurements, on-line UT and GWT of plate-like and tubular structures operating under extreme conditions and tomography.

In 1979, Thompson *et al.* successfully developed an EMAT system for flaw detection in steam generator tubes [205] and a few years later Bottger *et al.* experimentally investigated the defect

detection capabilities of magnetostrictive EMATs exciting/receiving L(0,2) on ferrite pipes [129]. Hirao [206] has been experimentally evaluating EMATs to various applications since 1995 when he and his co-workers designed and tested an on-line EMAT system for measuring the S_0 wave velocity and subsequently the r-values in cold rolled steel sheets. GWT of gas pipelines with PPM EMATs, corrosion detection and SH-wave mode conversion nature have been studied by Hirao *et al.* [25, 207] and they have also developed new EMAT designs for line focusing and wire inspection [208, 209]. Hirao and Ogi experimentally studied the ultrasonic performance of a novel meander-line coil (periodic coil) EMAT specifically designed to be driven with chirp signals and their research resulted in an EMAT with enhanced wave mode characteristics [256]. Ribichini [27] and Wilcox [26] have also developed periodic coil EMATs with improved magnetostrictive performance and Lamb tomography efficiency respectively. Over the years several researchers have proposed methods to enhance the ultrasonic performance of permanent magnet EMATs for GWT of pipelines [194]. However, it has been the magnetostrictive EMAT technology that has received most of the scientific and industrial attention. Murayama empirically analyzed the ultrasonic properties and GWT potential of various magnetostrictive EMAT designs in 1996 [210-212] and ten years later Kwun *et al.* developed a magnetostrictive EMAT for both Lamb and SH wave modes [213]. During the last ten years, researchers have managed to optimize the shape, size and efficiency of Magnetostrictive Patch Transducers (MPT) for GWT of pipelines [214-223].

EMATs specifically designed for the inspection of complex structures, moving structures or tomography have been reported in the literature [125, 224-230]. The on-line GWT of rail tracks with the use of EMATs has been studied in depth by Dixon *et al.* [185, 186]. One of the outcomes of this research was the development of a novel EMAT design for online rail-track inspection and a technique for lift-off compensation [125, 224]. EMATs have been widely utilized with other NDT techniques like Laser Ultrasonic and EC probes, for welding inspection, thickness measurement, crack detection and defect sizing [87-96, 225-227]. Dixon *et al.* established a non-contact setup of Laser and EMAT ultrasonic for crack detection on metal sheets where guided waves are generated via laser and are detected by EMATs [91-93]. Non-contact tomography and 2D imaging has been achieved with the use of omnidirectional EMATs specifically designed for tomography purposes [188, 228-230]. In 2005, Wilcox *et al.* designed and tested an EMAT array exciting S_0 for Lamb

wave tomography of large areas on plate-like structures [188] and in 2007, Hutchins *et al.* accomplished a multi-mode guided wave tomography for defect detection and tomographic reconstruction of plates with the use of EMATs [228]. Recently, Huang *et al.* designed and tested a novel omnidirectional EMAT for ultrasonic Lamb wave tomography of defects in metallic plates that comprises a permanent magnet and a contra-flexure coil [229].

The potential use of EMATs at high-temperature environments has been investigated since 1991 when Idris *et al.* have designed and tested a water-cooled EMAT that can obtain ultrasonic signals up to 1000 °C for thickness measurements [231]. A Nd-Fe-B permanent magnet, a printed circuit board (PCB) spiral coil, a 0.5mm thick layer of mica and a cooling system were the main parts of this EMAT. Steel, Cu 10.2% Sn alloy and Al 4.86% Si alloy were tested. The ultrasound was introduced to the specimen via a Q-switched Nd:YAG laser and the EMAT was utilized as a detector. The EMAT was exposed to the heat source for as much time as it needed for the signal to be recorded and then it was removed. Oil- and air-cooled EMATs have been also designed and reported to operate efficiently for thickness measurements at high temperatures for short periods [232-234]. In 2011 Hernandez *et al.* have designed an electromagnet EMAT for thickness measurement up to 600 °C for short time periods without any cooling [235]. The EMAT comprised a pulsed electromagnet designed for high temperatures and an alumina-encapsulated, copper, spiral coil. The EMAT was exposed to heat for times less than two minutes, depending on the temperature of the specimen. The EMAT performance was investigated at room temperature on both steel and aluminum while at high temperatures the transducer was tested only on steel. To date, high-temperature EMATs have been developed only for thickness measurements on metal blocks and they are not suitable for GWT at high temperatures. An EMAT that can be used in GWT and withstand high temperatures for either inspection or monitoring is still required to be developed. The current study focused on the theoretical analysis and optimization of EMAT design for high-temperature GWT and on its development and experimental characterisation and evaluation.

2.6 Summary

An overview of the state-of-the-art of high-temperature NDT and mainly GWT and transducers has been presented. A literature review of the historical progress of the modeling and experimental development of EMATs for GWT and EMATs withstanding high temperatures was performed and its conclusions set the basis of the current study. The underlying physics of guided waves, ultrasonic transduction and reception mechanisms of EMATs as well as the effect of temperature on them are introduced in the following Chapter.

Chapter 3

Theoretical Background for the Design of High-Temperature EMAT

3.1 Introduction

This Chapter gives an overview of the physics underlying the guided wave propagation in solids and the effect of dispersion and temperature rise on wave propagation and interpretation of signal received. EMAT transduction and detection mechanisms are also analyzed in this Chapter. Lorentz, magnetization and magnetostriction force, are mathematically described in terms of electrostatics and elasticity theory. The main parameters that influence EMAT operation, like skin effect, lift-off and coil impedance, are studied and emphasis is given to their relationship to the ultrasonic performance of EMAT. A brief introduction to the main EMAT designs and their ultrasonic characteristics and a qualitative analysis of the effect of temperature rise on the EMAT operating parameters are also given.

3.2 Guided Waves

3.2.1 Introduction

In Chapter 2 a brief introduction to GWT was given with emphasis on its capability to inspect large structures from a single point due to low attenuation guided waves exhibit over long distances. However, guided waves are subject to dispersion. Their velocity is dependent on the geometry and material properties of the specimen and excitation frequency. The quality, resolution in time and thus interpretation of the signal received can become complicating and lead to invalid conclusions regarding the structural integrity of the specimen if dispersion is not successfully confined. Hence,

weight should be given to the analysis of the propagation mechanisms of guided waves in solids and their correlation to EMAT design.

The geometry of the specimen affects the wave propagation of guided waves; both the number of the wave modes present in a structure and their velocity differs with the shape of the specimen. An infinite number of guided wave modes can propagate inside a structure. In plate-like structures, the number of wave modes that can be present in a certain bandwidth is smaller compared to pipes. Hence, the interpretation of the signals received from plates is less complicated than that of pipes. In both cases, though, all guided wave modes apart from SH_0 in plates and $T(0,1)$ in pipes are dispersive; their velocity is dependent on the frequency-thickness product. The shape of a wave package of multiple frequencies changes as it propagates in the specimen and it can result in poor resolution and inefficiency in defect detection. Hence, wave mode purity is of great importance in GWT; GWT systems are designed to introduce ultrasound to the specimen in a manner that only one wave mode will be excited and propagate in it. Provided this, the interpretation of the signal received can provide useful information for both known and unknown features of the specimen, the SNR of the signal received is enhanced and the defect detection probability increases. The ratio of the wave mode that the system should generate to any other unwanted wave generated is a way to estimate the wave mode purity potential of a GWT system.

Guided wave modes are categorized into families based on their particle displacement format. The nomenclature of guided waves differs from planar to tubular structures, due to the different wave mode families existing in each structure. In plates, the wave modes are named based on the family they belong to, symmetric (S_x), axisymmetric (A_x), and Shear Horizontal (SH_x) and the integer x that corresponds to their order. Their order is related to their cut-off frequency. Guided waves can propagate after their cut-off frequency; S_0 , A_0 and SH_0 do not have any cut-off frequency and thus they are called fundamental wave modes. In cylindrical structures, wave modes are divided into three families; longitudinal and axisymmetric $L(n,m)$, torsional and axisymmetric $T(n,m)$ and flexural and non-axisymmetric $F(n,m)$. Integer n denotes the number of harmonic vibrations of displacement around the circumference and integer m represents the order of the wave mode.

Although the commercial GWT systems are mainly designed for pipeline inspection and they usually excite either L(0,2) or T(0,1), this study focuses on plate-like structures. Hence, emphasis is given to the physics of guided wave propagation in plates and more particularly SH₀ wave mode and the effect of temperature rise on wave propagation.

3.2.2 Guided Waves Physics

Guided waves are governed by the same partial differential, wave motion equations that bulk waves also do. However, boundary conditions are also required for a guided wave propagation problem to be solved. Assuming the conservation of the mass within an arbitrary volume of a linearly elastic solid, neglecting any external body forces and applying Newton's second law, Euler's equation of motion can be derived as shown below [236].

$$\rho \frac{\partial^2 \mathbf{u}}{\partial t^2} = \nabla \cdot \sigma_s \quad (3.1)$$

where ∇ is the vector operator, \mathbf{u} is the particle displacement vector, ρ is the density and σ_s is the stress tensor that can be also expressed in terms of tensor ϵ_s by using Hooke's law.

$$\sigma_s = \mathbf{C} \epsilon_s \quad (3.2)$$

where \mathbf{C} is the stiffness tensor. If the specimen is made of an isotropic, homogeneous, linear elastic material, the stiffness tensor can be replaced by two material constants called Lamé constants (λ, μ) and the Hooke's law becomes

$$\sigma_s = \lambda \mathbf{I} \nabla \cdot \mathbf{u} + \mu (\nabla \mathbf{u} + \mathbf{u} \nabla^T) \quad (3.3)$$

where \mathbf{I} is the identity matrix. From 3.1 and 3.3, Euler's law equation results in

$$\mu \nabla^2 \mathbf{u} + (\lambda + \mu) \nabla \nabla \cdot \mathbf{u} = \rho \frac{\partial^2 \mathbf{u}}{\partial t^2} \quad (3.4)$$

Equation 3.4 is Navier's equation of motion for an isotropic elastic medium. This vector equation can expand to a set of three scalar linear equations which cannot be directly integrated and their

solution must be assumed according to the application. If Helmholtz decomposition is used, the displacement \mathbf{u} becomes

$$\mathbf{u} = \nabla\varphi + \nabla \times \Psi \quad (3.5)$$

where φ is a compressional scalar potential and Ψ is a vector potential whose divergence is zero ($\nabla\Psi = 0$) [236]. Navier's equation finally becomes

$$\nabla \left[(\lambda + 2\mu)\nabla^2\varphi - \frac{\partial^2\varphi}{\partial t^2} \right] + \nabla \times \left[\mu\nabla^2\Psi - \rho \frac{\partial^2\Psi}{\partial t^2} \right] = 0 \quad (3.6)$$

Equation 3.6 is satisfied when both square brackets are equal to zero. The two new equations derived from the above can be used for the wave propagation analysis for both bulk and guided waves and are shown below. They are called Helmholtz differential equations.

$$\frac{\partial^2\varphi}{\partial t^2} = c_L^2\nabla^2\varphi \quad (3.7)$$

$$\frac{\partial^2\Psi}{\partial t^2} = c_S^2\nabla^2\Psi \quad (3.8)$$

Equation 3.7 describes the wave motion of the longitudinal waves and equation 3.8 governs the shear wave modes. c_L and c_S are the longitudinal and shear velocity respectively and can be calculated based on the following equations.

$$c_L = \left(\frac{\lambda + 2\mu}{\rho} \right)^{1/2} \quad (3.9)$$

$$c_S = \left(\frac{\mu}{\rho} \right)^{1/2} \quad (3.10)$$

Helmholtz equations show that the two kinds of waves that can propagate in an infinite, isotropic medium do not interact with each other, since the two equations are independent of each other. The general solutions of equations 3.7 and 3.8 are given by

$$\varphi = \varphi_0 e^{i(\mathbf{k}\cdot\mathbf{z} - \omega t)} \quad (3.11)$$

$$\Psi = \Psi_0 e^{i(\mathbf{k}\cdot\mathbf{z} - \omega t)} \quad (3.12)$$

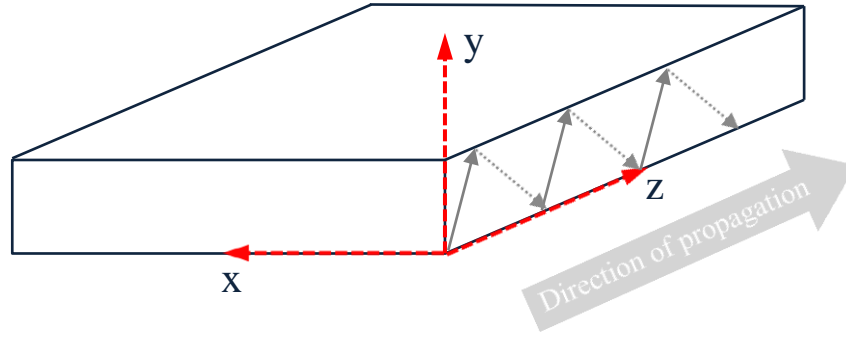


Figure 3.1. Schematic of Lamb wave propagation in an isotropic plate

where φ_0 and Ψ_0 are arbitrary initial constants, t is time, \mathbf{z} is the spatial coordinate of the wave, ω is the circular frequency and \mathbf{k}_L and \mathbf{k}_S are the longitudinal and shear wavenumber vectors respectively. The particle displacement of longitudinal waves is in the same direction with the wave propagation, while the vibration of shear waves is perpendicular to the direction of wave propagation.

As it was mentioned before, guided waves propagate either at the boundaries of a structure or within them while bulk waves propagate in infinite mediums. Hence, in guided wave theory, the wave propagation equations, presented briefly above, should be coupled with the appropriate boundary conditions so that a guided wave propagation problem will be solved. In an isotropic plate of thickness t , where the planes at $y=0, t$ are traction free boundary surfaces and the direction of wave propagation is on z axis, as Figure 3.1 shows, the unknown variables of the wave propagation problem, φ and Ψ , can be calculated if equations 3.7 and 3.8 are solved and coupled with the above boundary conditions. When it is assumed that no particle displacement but only rotations exist around y axis, *Lamb* waves propagate within the boundaries of the plate and they are described by the following simplified version of Helmutz differential equations.

$$\frac{\partial^2 \varphi}{\partial t^2} = c_L \left(\frac{\partial^2 \varphi}{\partial x^2} + \frac{\partial^2 \varphi}{\partial z^2} \right) \quad (3.13)$$

$$\frac{\partial^2 \Psi}{\partial t^2} = c_S \left(\frac{\partial^2 \Psi}{\partial x^2} + \frac{\partial^2 \Psi}{\partial z^2} \right) \quad (3.14)$$

Lamb waves comprise vertically polarized shear waves (SV) and longitudinal waves, both coupled together. The solution of the above set of equations is complicating and can only be calculated by

means of numerical models. Lamb waves are dispersive and thus their velocity is dependent on the geometry and material properties of the specimen and the frequency.

If in the same medium, the displacement in x and z -axis is assumed zero and also the scalar potential φ is ignored and set to zero, equation 3.7 vanishes and equation 3.8 becomes

$$\frac{\partial^2 \Psi}{\partial t^2} = c_s \left(\frac{\partial^2 \Psi}{\partial x^2} \right) \quad (3.15)$$

This wave equation corresponds to SH waves and its general solution can be of the same format with 3.12. Hence, if the unknown potential in 3.15 is substituted by its general solution, the unknown vector potential Ψ_0 can be expressed as below

$$\Psi_0(0) = \mathbf{A} \sin(k_y y) + \mathbf{B} \cos(k_y y) \quad (3.16)$$

where k_y is the through thickness wavenumber and is given by

$$k_y^2 = k_s^2 + k_z^2 \quad (3.17)$$

Provided the fact that stresses are related to displacement via Hooke's law, the boundary conditions can be correlated with the unknown vector potential. Again the surface planes of the plate are traction free. The full numerical analysis of this SH wave propagation problem can be found in [236] and yields the dispersive nature of SH waves modes. The phase and group velocity of SH wave modes can be calculated from the two following equations respectively.

$$c_p(ft_p) = \pm 2c_s \left(\frac{ft_p}{\sqrt{4(ft_p)^2 - l^2 c_s^2}} \right) \quad (3.18)$$

$$c_g = c_s \sqrt{1 - \frac{(l/2)^2}{(ft_p/c_s)^2}} \quad (3.19)$$

where l is an integer from zero to infinity, f is frequency, t_p is thickness and c_s is the velocity of bulk shear wave. The integer l determines the number of SH wave modes existing in a band of frequencies; there are infinite SH wave modes as the product of frequency and thickness reaches

infinity. SH_0 is the only non-dispersive guided wave and its velocity remains constant and equal to that of bulk shear wave; as it can be confirmed by solving equation 3.18 for l equal to zero. For any non-zero, positive value of l , the phase velocity of SH wave modes varies with frequency and thus all the rest wave modes apart from SH_0 are dispersive. Consequently, the shape of a wave packet containing multiple frequencies alters as the wave propagates, resulting in a complicating signal interpretation. The root of the denominator of equation 3.18 gives the cut-off frequency of the l - order wave mode; below this frequency the wave does not propagate. Only SH_0 does not have any cut-off frequency and thus it can propagate at any frequency. As the product of frequency-thickness increases, the phase velocity of all wave modes converges to the velocity of SH_0 . The entire multi frequency wave-packet travels with a velocity equal to group velocity. The dispersion curves of a 3mm thick steel plate are depicted in Figure 3.2, as they were calculated by Disperse software [237].

As it has been already emphasized, SH_0 is non-dispersive leading to a less complicating signal interpretation when it is the only wave mode propagating in the specimen. Also, it cannot

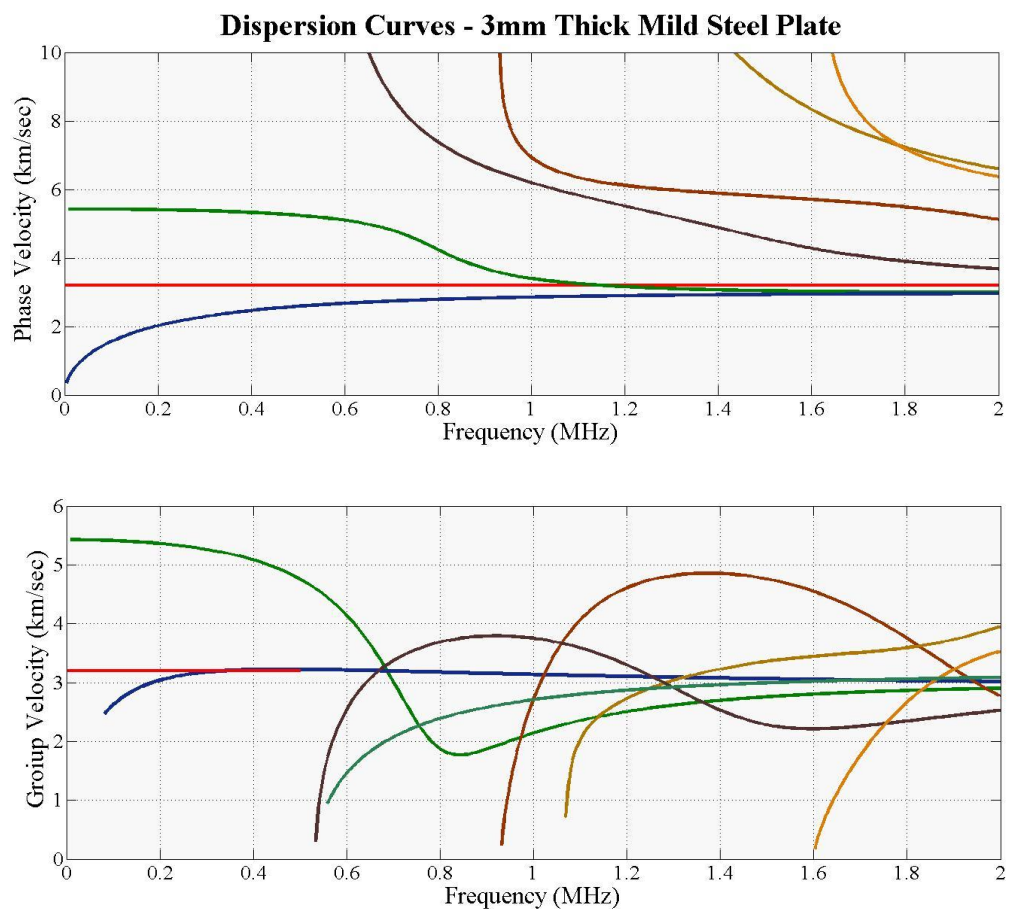


Figure 3.2. Dispersion curves of a 3mm thick steel plate

propagate in liquids due to its in-plane displacement, making the online inspection of tanks and pipes carrying liquids feasible [236]. Weld inspection and crack detection can also be accomplished with the use of SH_0 (or $T(0,1)$ in pipes) [236]. However, it has been experimentally proved that SH_0 is not as sensitive as SH_1 is to corrosion detection [192], due to its non-dispersive nature. The high sensitivity SH_0 has to axial features like longitudinal cracks can limit its efficiency in corrosion detection under support brackets, since the latter are usually axially welded on the pipe and thus reflections can be generated from the welds resulting in false indications of structural discontinuities [116]. Consequently, each wave mode is suitable for a specific number of applications. This study focuses on crack detection at both room and high temperatures and therefore SH_0 wave mode is one of the main aspects of this research.

3.2.3 Temperature Rise Effect

Wave velocity can also change due to temperature variations [238, 239]. Temperature increase leads to thermal expansion of the specimen and alternation of its density and elastic properties. The density ρ and Young's modulus E on steel decrease with temperature increase and they are given by the following equations respectively [240].

$$\rho = \frac{\rho_{TH}}{1 + \alpha\Delta T} \quad (3.20)$$

$$E = \left[1 + \frac{T}{2,000 \ln\left(\frac{T}{1,100}\right)} \right] E_{TH}, \quad \text{for } 20^\circ\text{C} < T \leq 600^\circ\text{C} \quad (3.21)$$

where ρ_{TH} represents density at room temperature, α denotes the linear coefficient of thermal expansion, ΔT is the temperature increase, T is temperature and E_{TH} is Young's modulus at room temperature. On the contrary, Poisson's ratio ν of steel increases with temperature rise, as the following equations show [240].

$$\nu = 3.78 \cdot 10^{-5} T + 0.283, \quad \text{for } 20^\circ\text{C} < T \leq 450^\circ\text{C} \quad (3.22)$$

$$\nu = 9.2 \cdot 10^{-5} T + 0.259, \quad \text{for } T > 450^\circ\text{C} \quad (3.23)$$

Consequently, the wave velocity of longitudinal and shear bulk wave, c_L and c_S , change with temperature, since both are directly related to the three aforementioned material properties and thus the phase and group velocity of Lamb and SH wave modes also change. As a result, the ultrasonic response of the specimen alters with temperature increase yielding useful information regarding its structural state and thermal properties. Nevertheless, the temperature should be kept stable or temperature compensation should be also accomplished during the signal interpretation so that reliable conclusions can be made regarding the structural integrity of the specimen.

The SNR of the signal received at room and high temperatures, the wave purity characteristics, the length of inspection and the defect detection probabilities of GWT system vary for different applications due to the physics of guided waves, but also to the ultrasonic characteristics of the transducers used. The following subsection analyses the GWT potential of EMATs and presents their capabilities at room and high temperatures.

3.3 EMAT Transduction

EMATs comprise permanent magnet or electromagnet, for providing a static magnetic field, and a coil driven by alternating current. The coil shape and size and the magnet configuration determine the wave mode purity and ultrasonic characteristics of EMAT design. Depending on the magnetic and electric properties of the specimen, EMAT performance alters. When an electrically conductive, non-ferromagnetic material, is in proximity to an EMAT, Lorentz force is the dominant mechanism for the generation and detection of ultrasound. Whereas, in ferromagnetic materials, Lorentz, magnetization and magnetostriction force contribute to ultrasound generation/reception. The EMAT design and its operating conditions as well as the magnetic properties and condition of the specimen define which mechanism will preponderate each time. Hence, the EMAT operation on ferromagnetic materials can be more efficient but also its analysis can be more complicating compared to that on paramagnetic materials.

In both cases, the electromagnetic coupling between the EMAT and the specimen is governed by Maxwell's equations (including Faraday's and Ampère's law), as they are shown below [158].

$$\nabla \cdot \mathbf{D} = \rho_q \quad (3.24)$$

$$\nabla \cdot \mathbf{B} = 0 \quad (3.25)$$

$$\nabla \times \mathbf{E} = -\frac{\partial \mathbf{B}}{\partial t} \quad (3.26)$$

$$\nabla \times \mathbf{H} = \mathbf{J} + \frac{\partial \mathbf{D}}{\partial t} \quad (3.27)$$

where \mathbf{D} is the electric displacement, ρ_q is the charge density, \mathbf{B} is the magnetic field, \mathbf{E} is the electric field, \mathbf{H} is the magnetic field strength and \mathbf{J} is the current density. Additionally to these, the constitutive equations accompany the above mathematical framework.

$$\mathbf{J} = \sigma \mathbf{E} \quad (3.28)$$

$$\mathbf{B} = \mu_0(\mathbf{H} + \mathbf{M}) \quad (3.29)$$

where σ is the electric conductivity, \mathbf{M} represents the magnetization and μ_0 is the magnetic permeability of free space. Equations 3.24 to 3.29 calculate the electromagnetic interaction between the EMAT and the specimen. The mechanical equilibrium of the specimen after it has been subjected to electromagnetism generated by EMAT, can be determined by its electromagnetic properties and solid mechanics. The physics underlying the forces exerted on a conductive material after an electromagnetic wave is introduced to the latter are further analysed in the following subsection.

3.3.1 Lorentz Force

Based on Ampere's and Faraday's law, as they are mathematically described by equations 3.27 and 3.26 respectively, the alternating current \mathbf{J} applied to the coil generates a dynamic magnetic field that in its turn induces a mirror alternating current (eddy current - \mathbf{J}_e) on the surface of the specimen. The particles of eddy current interact with the magnetic flux density yielding a body force, Lorentz force, given by the following equation.

$$\mathbf{F}_L = q(\mathbf{E} + \mathbf{v} \times \mathbf{B}) \quad (3.30)$$

where \mathbf{F}_L is Lorentz force, q is the electric charge, \mathbf{E} stands for electric field, \mathbf{v} represents the velocity of a single charged particle and \mathbf{B} is the overall magnetic field. If the specimen does not macroscopically undergo additional electric charges, then equation 3.30 can be simplified to:

$$\mathbf{F}_L = q(\mathbf{v} \times \mathbf{B}) \quad (3.31)$$

From a microscopic perspective, the electrons on the surface of the sample experience a Coulomb force due to the electric field induced on the specimen from the coil and they also are subjected to Lorentz force due to the presence of magnetic field. Therefore, the equation of motion for an electron is given by [235]:

$$m \frac{d\mathbf{v}_e}{dt} = -e(\mathbf{E} + \mathbf{v}_e \times \mathbf{B}) - \frac{m\mathbf{v}_e}{\tau} \quad (3.32)$$

where m is electron mass, \mathbf{v}_e represents mean velocity of an electron and τ is the mean time required for electron-ion collision. If the mean velocity of electron remains constant, then equation 3.32 becomes

$$-e(\mathbf{E} + \mathbf{v}_e \times \mathbf{B}) = \frac{m\mathbf{v}_e}{\tau} \quad (3.33)$$

For a given volume of n_e and N_i electron and ion density respectively, the body force per unit volume yielded on ions due to scattering of electrons and transfer of momentum to ions can be calculated as below [235]:

$$\mathbf{F}_L = N_i Z_i (\mathbf{E} + \mathbf{v}_i \times \mathbf{B}) + n_e \left(\frac{m\mathbf{v}_e}{\tau} \right) \quad (3.34)$$

where Z_i and \mathbf{v}_i are the charge and velocity of an ion. Provided that the specimen is neutrally charged and also the velocity of ions can be considered negligible compared to that of electrons, equation 3.34 can be further simplified to equation 3.35 in which the term $-n_e e \mathbf{v}_e$ is equal to eddy current density.

$$\mathbf{F}_L = -n_e e \mathbf{v}_e \times \mathbf{B} \quad (3.35)$$

Finally, Lorentz force is the product of the eddy current density and the overall magnetic flux density on the surface of the specimen, as equation 3.36 shows.

$$\mathbf{F}_L = \mathbf{J}_e \times (\mathbf{B}_{st} + \mathbf{B}_{dyn}) \quad (3.36)$$

where \mathbf{J}_e is eddy current density, \mathbf{B}_{st} and \mathbf{B}_{dyn} represent the static and dynamic magnetic field respectively. Both the static magnetic field provided by the magnets and the dynamic magnetic field generated by the coil contribute to Lorentz force generation. The former can affect Lorentz force mechanism more than the latter. Although the impact of the dynamic magnetic field on force generation is relatively smaller compared to that of the static field, still it is not negligible after a specific threshold of current amplitude. The frequency components of the resultant force are also related to the frequency characteristics of eddy current and magnetic fields. Lorentz force associated with the dynamic magnetic field has double the frequency compared to that generated due to the static magnetic field.

As it has been already mentioned, Lorentz force is the dominant transduction/reception mechanism of EMATs when they are employed on paramagnetic materials like aluminum or stainless steel. Two additional mechanisms are present in ferromagnetic materials, magnetization and magnetostriction.

3.3.2 Magnetization Force

Magnetization force (\mathbf{M}) ensues when a ferromagnetic material is subject to an external magnetic field and is present both on the surface and in the bulk of the sample, as the following equation also attests [27].

$$\mathbf{M} = \int_V \nabla^*(\mathbf{M} \cdot \mathbf{H})dV + \frac{1}{2}\mu_0 \int_S \mathbf{nM}_n^2 dS \quad (3.37)$$

where \mathbf{n} is the unit vector normal to the sample surface, \mathbf{M}_n stands for the normal to surface component of Magnetization and \mathbf{M} is Magnetization force. The first integrand of this equation represents Magnetization force, while the second is related to electromagnetic fields that are present only on the surface of the sample and thus it can be neglected.

The impact of Magnetization on the ultrasonic performance of EMATs was firstly investigated by Thompson [162] and it has been further studied in [163]. It was proved that waves generated under

Magnetization are of similar amplitude and out of phase with those generated by Lorentz force when the bias magnetic field is tangential to the sample surface. Subsequently, the overall generation of ultrasound is limited and thus Magnetization can be neglected. On the contrary, magnetostriction can significantly influence EMAT performance on ferromagnetic materials under certain conditions and therefore the following subsection outlines its underlying physics.

3.3.3 Magnetostriction

Magnetostriction occurs in ferromagnetic materials under the presence of an external magnetic field, since the dipoles of the ferromagnetic domains of the former tend to align to the orientation of the latter, resulting in elastic strain. The dynamic magnetic field generated by EMAT coil can lead to a time-varying elastic strain and wave generation. The elastic, electric and magnetic properties of the specimen, as well as the orientation and magnitude of the static against dynamic magnetic field of EMAT, can alter the ultrasonic wave generation efficiency of magnetostriction.

The magnetostrictive constitutive equations are non-linear and can be expressed in an analogous fashion with piezoelectricity, as it is shown below [27].

$$\epsilon_s = S^H \sigma_s + \mathcal{D} \mathbf{H} \quad (3.38)$$

$$\mathbf{B} = \mathcal{D}^T \sigma_s + \mu^\sigma \mathbf{H} \quad (3.39)$$

where ϵ_s and σ_s are the strain and the stress tensors, S is elastic compliance matrix measured under constant magnetic field, \mathcal{D} is the magnetostriction matrix (magneto-mechanical coupling) and μ is permeability at constant stress. Considering that the bias magnetic field of EMATs is much larger than the dynamic magnetic field, their operating point on the magnetostriction curve does not alter significantly, allowing the assumption that the EMAT operating area on magnetostriction curve is linear. Additionally to this, the hysteresis effect can also be neglected for further simplification of the analysis. Hence, the set of equations 3.38 and 3.39 can be decomposed into their static and dynamic components where the analysis of the latter can yield more valuable information [27].

Given the above hypotheses, the magnetostrictive strain generated in all directions is directly proportional to magnetostriction matrix \mathcal{D} . The magneto-mechanical coefficients are calculated via

magnetostriction curve and therefore, they are related to bias magnetic field in a non-linear manner. Once, the bias magnetic strength is known and relatively larger than that of dynamic field, the number of magneto-mechanical coefficients needed for the calculation of the magnetostriction strain, decreases significantly and leads to a less complicating magnetostriction analysis. Otherwise, both the amplitude and the direction of the total magnetic field alters resulting in a more complex magnetostriction matrix and analysis.

It has been reported that magnetostriction can contribute more compared to Lorentz force for specific EMAT designs, ferromagnetic materials and operating conditions [27]. Apart from bias magnetic strength and material properties of specimen, the frequency of excitation current and skin effect can also influence the amplitude of magnetostriction [27]. However, this research focuses on the performance of EMATs on paramagnetic materials and therefore the magnetostriction effect is not further studied in the following Chapters.

3.4 EMAT Reception

As ultrasound has been generated and wave propagates in the sample, the motion of particles (atoms) under the presence of a magnetic field can result in an electric field, as it is attested below.

$$\mathbf{E} = \frac{\partial \mathbf{u}}{\partial t} \times \mathbf{B} \quad (3.40)$$

If this occurs in the vicinity of an EMAT receiver, the current on the surface of the specimen generates an alternating magnetic field that induces eddy current on the EMAT coil. Hence, the ultrasound can be detected by the EMAT and based on the Time of Flight (ToF) of each wave mode/reflection, the structural integrity of the specimen can be assessed. The voltage detected on the edges of the coil is proportional to the wave velocity, as Dixon *et al.* have mathematically proved that EMATs operate as particle velocity sensors [153].

It has been well documented that EMATs operate more efficiently as receivers rather than as transmitters [87-96]. The high power requirements of EMAT transmitters, combined with their lower GWT performance compared to other technologies like piezoelectric transducers, limit their

efficiency and utilization as actuators. On the contrary, EMATs have been successfully employed as detectors along with EC probes for enhanced thickness measurements and defect sizing [225-227]. A typical non-contact setup that several researchers have established for different applications comprises laser as ultrasound transmitter and single or multiple EMATs for reception [87-96]. In these experiments, EMATs have been applied for both conventional UT and GWT of either moving or high-temperature structures. The coil shape and size, as well as the magnet polarization and arrangement, define the wave mode and directivity of EMAT. Therefore, a brief overview of the main EMAT designs follows.

3.5 EMAT Designs

The shape, size and material properties of coil as well and magnets affect greatly the EMAT performance and applicability. Many an EMAT design has been reported in the literature over the years [27], but in this section, only the main EMAT configurations and their ultrasonic characteristics are presented. The four main coil shapes are spiral, racetrack, meander and butterfly, are shown in Figure 3.3. Combined with corresponding magnet configuration, the six most widely utilized EMAT designs are developed [27]. Depending on the application, EMAT design alters and therefore, EMATs for bulk waves (conventional UT) differ from those for guided waves (GWT).

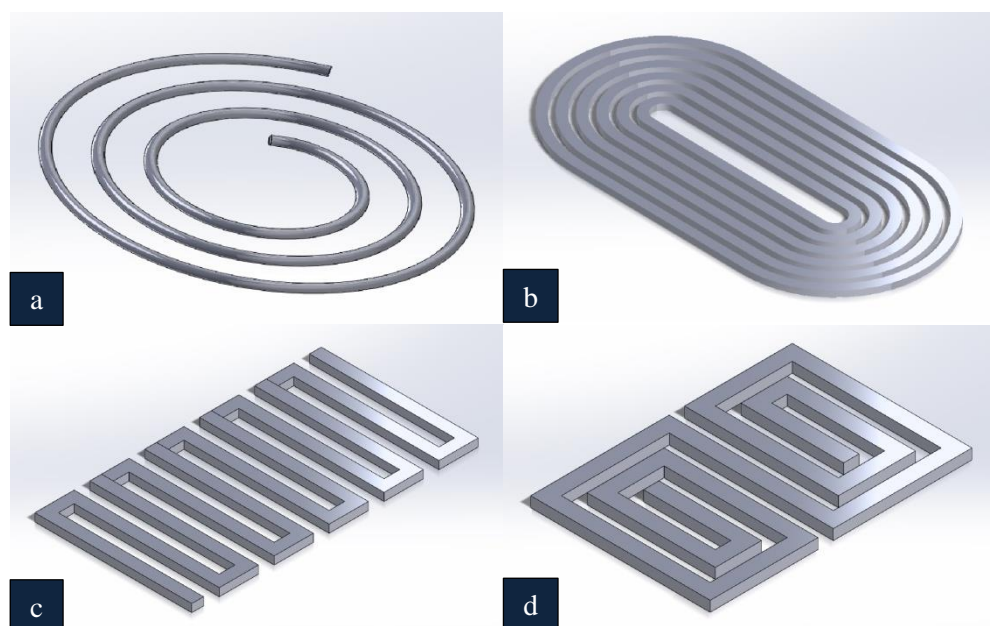


Figure 3.3. EMAT coil (a) spiral (b) racetrack (c) meander (d) butterfly

However, the former have successfully been employed for generating Lamb waves as well [167]. The main three configurations for bulk waves are the spiral (or pancake), racetrack and butterfly coil EMATs, while meander coil EMAT can be utilized for bulk, Rayleigh and Lamb waves. PPM EMAT has been successfully employed in GWT for SH wave modes excitation/reception and magnetostrictive EMATs have been also documented for their GWT potential.

As the name implies, spiral coil EMATs are composed of a flat spiral-shaped coil and normal to the sample surface magnetic field (Figure 3.4 a). Therefore, they can generate radially polarized shear waves in all directions around the coil, rendering them omnidirectional. However, the magnetic field is never completely normal to the sample surface; a substantial part of the magnetic lines is tangential to the specimen surface and can result in the generation of longitudinal waves as well; arising questions about the wave purity characteristics of this EMAT design especially on paramagnetic materials. In ferromagnetic materials, though, a destructive interference between Lorentz and magnetization mechanism occurs leading to a significant energy loss in longitudinal wave propagation. It is a suitable candidate for thickness measurement and defect detection applications using conventional UT and it has been also reported for ultrasonic Lamb wave tomography [188, 228, 229], due to its omni-directivity.

When the orientation of both the electric and magnetic field change simultaneously, the orientation

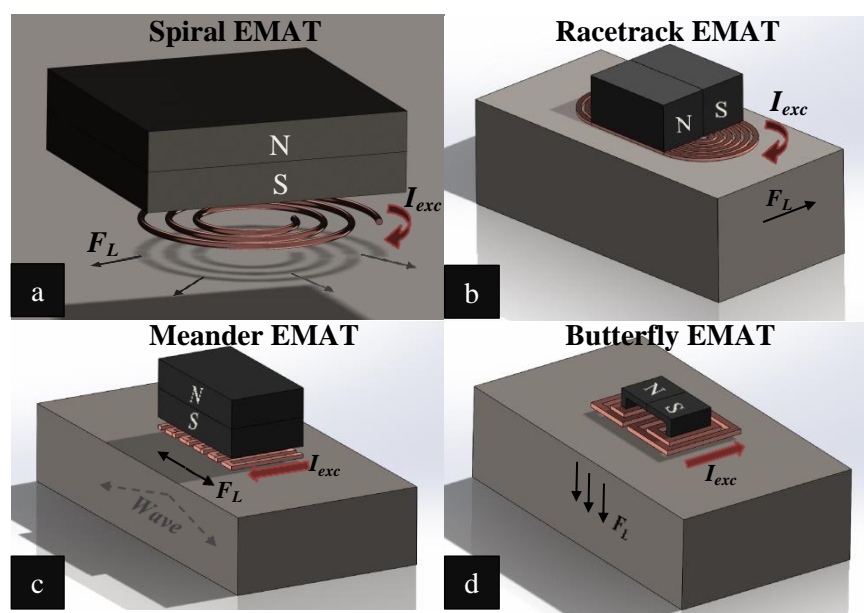


Figure 3.4. EMAT designs (a) spiral EMAT (b) racetrack EMAT (c) meander EMAT (d) butterfly EMAT

of the resultant force remains constant. Racetrack coil EMAT design relies on this principle, as it is illustrated in Figure 3.4 b. The racetrack coil comprises two limbs of straight wire lines with opposite current orientation. The magnetic field interfering with the electric field of each limb is of alternating orientation as well. As a result, linearly polarized shear waves propagate in the bulk of the specimen. An alternation of this EMAT design, the butterfly coil EMAT is composed of a butterfly coil, shown in Figure 3.3 d, and a tangential to the sample surface magnetic field, as Figure 3.4 d demonstrates. Still the wave generated is linearly polarized, however, this EMAT configuration excites longitudinal waves.

EMATs with meander coil can be applied in both conventional UT and GWT, since they can excite bulk, Rayleigh and Lamb waves, if the orientation of the magnetic field is perpendicular to the sample, as Figure 3.4 c also shows. Especially bulk waves are generated at an angle and thus they propagate obliquely in the specimen. The wavelength of the wave generated is equal to double spacing within the limbs of the coil (or equal to its pitch). The meander coil has been also cited to have been used in conjunction with arrays of magnets of alternating polarization [27]. This configuration permits the excitation/reception of angled SH wave modes.

An established and widely deployed EMAT design in NDT industry is the PPM EMAT, since many applications can avail of its capability to excite/receive SH wave modes [155, 194]. PPM EMATs consist of two arrays of magnets of alternating polarization and a racetrack coil, as Figure 3.5 depicts. The orientation of Lorentz force alternates for adjacent magnets resulting in SH displacement. The orientation of the electric and the magnetic field of one EMAT side is

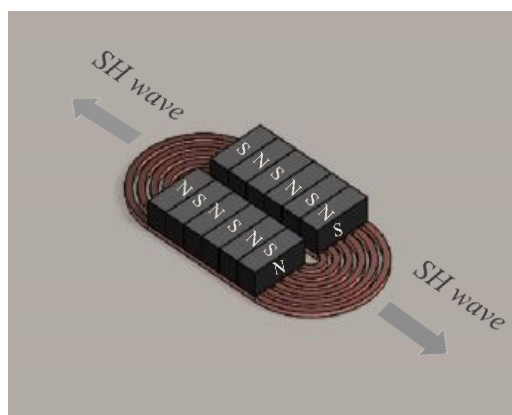


Figure 3.5. PPM EMAT

supplementary to the other side, similarly to racetrack EMAT for bulk waves. Therefore, the force generated on both sides has the same orientation and SH displacement doubles. The SH wavelength equals to the pitch of magnets, in other words, the distance between two adjacent magnets of the same polarization. Hence, the operating frequency of PPM EMAT is strictly fixed due to its design; however, the frequency of the excitation current applied to the coil can alter the frequency characteristics of EMAT and result in a narrow operating bandwidth. SH_0 wave mode is notably attractive in GWT due to its non-dispersive nature and thus PPM EMAT is equally critical. This research focuses on SH_0 and therefore the high-temperature EMAT design has a PPM configuration.

Magnetostrictive EMATs (Magnetostrictive Patch Transducers – MPT) is another EMAT technology that is mainly deployed on ferromagnetic materials, since its operation relies only on magnetostriction. Several MPT configurations have been reported in the literature for GWT of both plates and pipes [214, 223] and can excite/receive all the essential wave modes for GWT like S_0 and A_0 for plates and $L(0,1)$, $L(0,2)$ and $T(0,1)$ for pipes. Another EMAT design whose operating principles avail of only magnetostriction, consists of meander coil within a tangential magnetic field. In this case, the bias magnetic field is parallel to the current and thus no Lorentz force is generated. The shear strain resulted by magnetostriction leads to the excitation of SH wave modes. A more detailed overview of this design can be found in the literature [27].

Apart from the wave mode purity, EMAT design has been optimized in terms of ultrasonic efficiency and specifications of applications. Dixon *et al.* have developed an EMAT design that eliminates the eddy current losses on the magnets with the use of a ferrite sheet between the coil and the magnets [241]. The same researcher has reported a novel EMAT design for online rail-track inspection with the use of a spring-like mechanism for lift-off stabilization [125]. Impedance matching is another critical part of the EMAT instrumentation that is required for the optimization of the energy transfer to and from the EMAT. The next section analyzes the parameters that limit EMAT efficiency and also presents methods that can be followed for the tackling of these challenges.

3.6 Electromagnetic Losses

The GWT performance of EMATs is considered lower compared to that of piezoelectric transducers. The electromagnetic losses due to skin effect, impedance mismatch between the instrumentation and EMAT as well as the EMAT and the specimen and lift-off variations moderate the efficiency of EMATs. A brief analysis of the above issues is followed.

3.6.1 Skin Effect

Although the elastic wave generated by an EMAT can travel all through the bulk of the specimen, the electromagnetic wave introduced to the latter cannot penetrate its depth and thus their electromagnetic coupling is spatially restrained to the specimen surface. Based on Faraday's law, the electromagnetic wave launched by an EMAT on the surface of a sample is given by [235]:

$$\nabla \times (\nabla \times \mathbf{E}) = -\frac{\partial}{\partial t} (\nabla \times \mathbf{B}) \quad (3.41)$$

The above equation can be simplified with the use of vector identity, shown below (equation 3.42), and by taking into account that the sample remains neutrally charged, as equation 3.43 shows.

$$\nabla \times (\nabla \times \mathbf{E}) = -\nabla^2 \mathbf{E} + \nabla(\nabla \cdot \mathbf{E}) \quad (3.42)$$

$$\nabla^2 \mathbf{E} = \frac{\partial}{\partial t} (\nabla \times \mathbf{B}) \quad (3.43)$$

The term on the left-hand side of the above equation can be expressed as follows.

$$\nabla^2 \mathbf{E} = \mu_0 \mu_r \sigma \frac{\partial \mathbf{E}}{\partial t} + \mu_0 \mu_r \varepsilon_0 \varepsilon_r \frac{\partial^2 \mathbf{E}}{\partial t^2} \quad (3.44)$$

where μ_r , σ and ε_r is the magnetic permeability, electrical conductivity and relative permittivity of specimen and ε_0 is the permittivity of free space. Given that $\sigma \gg \omega \varepsilon_0 \varepsilon_r$, the second term in the right hand side of equation 3.44 can be omitted. Hence, equation 3.44 reduces to

$$\nabla^2 \mathbf{E} = \frac{\partial^2 \mathbf{E}}{\partial z^2} \quad (3.45)$$

From equations 3.44 and 3.45, the differential equation for the propagation of the electromagnetic wave inside the sample is derived as:

$$\frac{\partial^2 \mathbf{E}}{\partial z^2} = \mu_0 \mu_r \sigma \frac{\partial \mathbf{E}}{\partial t} \quad (3.46)$$

The attenuation of the wave as it propagates in the bulk of the specimen can be measured by skin depth which is given below.

$$d = \sqrt{\frac{2}{\mu_0 \mu_r \sigma \omega}} \quad (3.47)$$

where d is the skin depth and ω is the angular frequency. Finally, the electromagnetic wave propagating inside the sample can be described in terms of skin effect as equation 3.48 shows.

$$\mathbf{E}_z = \mathbf{E}_{z0} e^{i(\omega t)} e^{-(1+i)\left(\frac{z}{d}\right)} \quad (3.48)$$

where \mathbf{E}_z represents the electric field at z depth inside the bulk of the specimen and \mathbf{E}_{z0} is the electric field at the surface of the sample.

The electromagnetic attenuation inside a conductive material is directly related to the frequency of the electromagnetic wave and the material properties of the specimen. As the frequency of the electromagnetic wave increases, the penetration depth decreases. Similarly, good electrical conductors tend not to allow the electromagnetic wave to propagate in their thickness, as well as highly ferromagnetic materials, like iron, also do. Hence, the electromagnetic coupling between the EMAT and the specimen gets spatially confined within the surface of the specimen and the EMAT coil wires and limits EMAT efficiency. EMAT coils of large wire diameter tend to suffer from skin effect and thus experience electromagnetic losses, resulting in lower EMAT performance. As the electromagnetically active area of both EMAT and specimen is restricted due to skin effect, the current flowing in the coil and the electromagnetic energy introduced to the specimen decreases. The EMAT impedance, and more particularly its mutual inductance with specimen, alters with magnetic properties of specimen and skin effect and consequently EMAT performance differs with material properties of sample.

3.6.2 Impedance – Electrical Circuit

The shape, size and materials properties of EMAT coil as well as its interaction with magnets and specimen affect the overall EMAT impedance. Assuming that an EMAT that is not in proximity with any conductive material operates as a single coil, its impedance can be modeled as Figure 3.6 depicts. The shape, size, wire diameter and magnetic permeability of the coil have a direct impact on its self-inductance, L_{coil} . The parasitic capacitance formed within the turns of the coil, C_p , as well as the resistivity of the wire, R_{coil} , contribute to coil impedance. The equivalent impedance of the electrical circuit presented in Figure 3.6 is given below.

$$Z_{coil} = \frac{1 + j\left(1 - \frac{\omega^2}{\omega_R^2}\right) \frac{\omega L_{coil}}{R_{coil}} - \omega C_p R_{coil}}{\left(1 - \frac{\omega^2}{\omega_R^2}\right)^2 + (\omega C_p R_{coil})^2} R_{coil} \quad (3.49)$$

$$\theta_{coil} = \tan^{-1}\left(\left(1 - \frac{\omega^2}{\omega_R^2}\right) \frac{\omega L_{coil}}{R_{coil}} - \omega C_p R_{coil}\right) \quad (3.50)$$

$$\omega_R = \frac{1}{\sqrt{L_{coil} C_p}} \quad (3.51)$$

where ω_R represents the resonant angular frequency. For low parasitic capacitance, the impedance maximizes at the resonant angular frequency. For frequencies lower than the resonant, the phase is positive and the real part of the impedance increases with frequency increase. Whereas, when the angular frequency is larger than the resonant frequency, the phase becomes negative and the real part still increases with frequency increase.

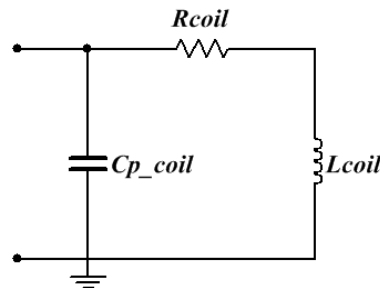


Figure 3.6. Equivalent electric circuit of EMAT coil

The above schematic does not take into account the eddy current losses the coil experiences due to the electromagnetic coupling between itself and the magnet. The alternating dynamic magnetic field generated by the coil induces eddy current on the magnets as well. This eddy current causes eddy current losses back to the coil. Nevertheless, when the EMAT is employed on a specimen, these electromagnetic losses derived from the destructive interference between the coil and the magnets can be neglected. A more substantial electromagnetic issue the EMAT coil experiences is the skin effect. Based on the analysis given in the Section 3.5.1, the electromagnetic wave applied to EMAT coil from the power generator (pulser instrumentation) does not necessarily propagate through the entire cross section of the coil. The high-frequency current driven to the coil in conjunction with relatively large diameter coil of EMAT transmitter, can result in skin effect and lessening of the electromagnetism launched by the EMAT. Hence, EMAT receiver coils are usually composed of small diameter wires (0.2mm), while EMAT transmitter coils are of relatively large wire diameter, and are driven by low-frequency current. Additionally, the material selection for the coil is of great importance again due to skin effect. Both the resistivity and the magnetic permeability of the wire can affect the skin depth and thus copper has been reported as a suitable candidate for the coil manufacturing.

When the EMAT is in good proximity with a conductive material, its performance alters since it interacts with the specimen and its impedance changes accordingly. The electromagnetic coupling established between the EMAT and the specimen lead them to operate as a transformer, as Figure 3.7 shows. In Figure 3.7 a the EMAT transmitter is modeled as primary winding and the specimen as secondary, while Figure 3.7 b shows that EMAT receiver operates as secondary winding and the specimen as primary. In either case, both coil windings experience electromagnetic losses due to their resistance, magnetic flux leakage and parasitic capacitance. These parameters are strongly related to the magnetic and electrical properties (permittivity, permeability, and electrical conductivity) of EMAT and specimen.

The self-inductance of the coil of an EMAT transmitter can be decomposed into the primary, leakage and mutual inductance, when the EMAT is employed on a sample. The primary leakage (L_{coil}) denotes the portion of magnetic flux launched by EMAT that has not been coupled with the

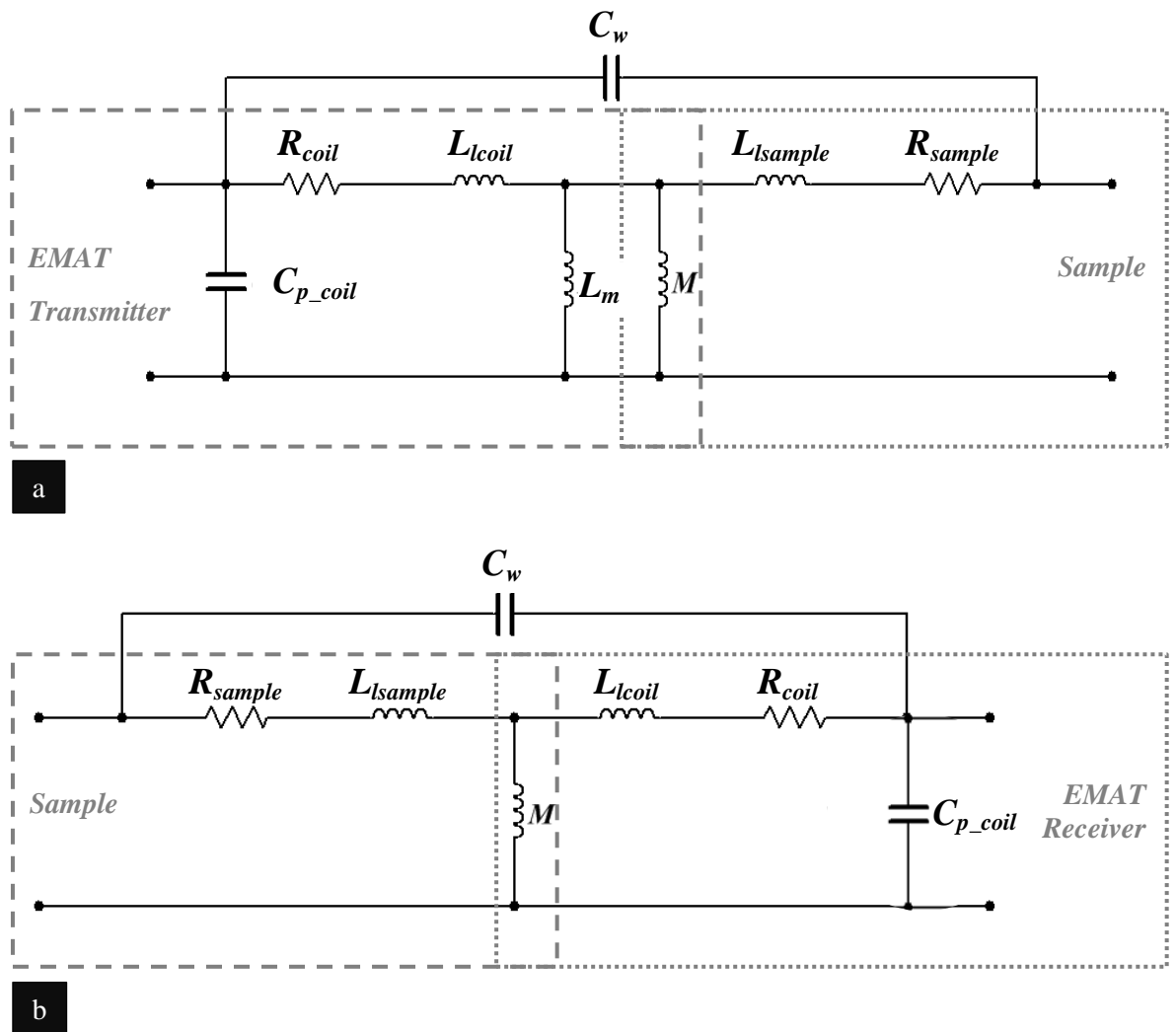


Figure 3.7. Equivalent electric circuit of (a) EMAT transmitter and sample (b) sample and EMAT receiver specimen. The mutual inductance (M) characterizes the strength of the electromagnetic coupling between the EMAT and the specimen and as soon as it is established, the electromagnetic wave is introduced to the specimen and causes the wave generation. The electromotive force produced in the sample induces eddy current losses (L_m) to the EMAT transmitter coil almost instantaneously with the wave generation. The time required for the electromagnetic wave to be detected back by the transmitter coil is significantly smaller than the duration of a pulse of a typical ultrasonic wave generated by an EMAT. Hence, the equivalent inductance of an EMAT transmitter, while it is deployed on a conductive material, is given by the following equation.

$$L_{eq} = L_{lp} - L_M + M \quad (3.52)$$

Depending on the material properties of the specimen, the mutual inductance and the eddy current losses on the EMAT coil vary. It has been experimentally proved that the equivalent inductance of

the coil of an EMAT transmitter decreases with the presence of a conductive material and more particularly, its decrease is greater when the sample is made of a paramagnetic material compared to ferromagnetic [242]. On the other hand, when the EMAT operates as a receiver, the equivalent inductance of the receiver coil is equal to secondary leakage and mutual inductance. No eddy current losses are induced to the coil and therefore EMATs can operate more efficiently as receivers rather than as transmitters. Nevertheless, the magnetic properties of specimen can affect the inductance of the coil of an EMAT receiver and its efficiency, since the mutual inductance is directly correlated to the magnetic permeability of the specimen.

However, in both cases, part of the energy transmitted to EMAT coil dissipates as heat due to the resistance of wire (R_{coil}). Low resistance conductive materials are, therefore, used for the manufacturing of an EMAT coil like copper, silver, platinum and constantan. The parasitic capacitance between the EMAT and specimen (C_w) is attributed to the dielectric medium in between them which can lead to an increase of electrical noise, a drop of the SNR and of the overall EMAT efficiency. The relative permittivity of the dielectric material present between the EMAT and specimen like air and lift-off are the main parameters that can affect parasitic capacitance. For given material properties and EMAT geometry, lift-off increase leads to capacitance drop. Alternatively, it has been experimentally shown that an autotransformer connection between the EMAT and the specimen can drop the noise level and increase the amplitude and the SNR of the signal received [151]. More particularly, the connection/interaction between the EMAT and the specimen is differential, since one induces to the other alternating, differential mode current of almost the same amplitude. Transformers perform in a similar way and they also suffer from common mode noise; in real transformers, a small capacitance links the primary to the secondary winding and also performs as a path for the common mode current across the transformer. As a result, in both cases, the common mode current flows to the ground via the parasitic capacitance and thus no current flows to the EMAT coil/specimen or secondary winding. Nevertheless, an autotransformer acts as a high-value parallel impedance that does not attenuate the differential current significantly but presents zero impedance to the common mode signals by shorting them to ground potential [151]. Autotransformers have smaller resistance and leakage reactance compared to conventional two winding transformers; therefore, the former is more

efficient than the latter [151]. Hence, if we presume that the interaction between the EMAT and the specimen is equivalent to a transformer and we connect them so as to perform as an autotransformer, then the common mode noise should be canceled and the EMAT receiver would work more efficiently. In this case, the alternating, differential mode current will be induced in the EMAT coil and the signal received will have an enhanced SNR and valid information will be retrieved from it. The autotransformer connection is also more robust resulting in the increase of the amplitude of the "wanted" signal. If an extra layer of stainless steel is attached to EMATs, touching both the EMAT housing and the specimen, then a common ground connection (autotransformer) is established. Figure 3.8 shows the equivalent electrical circuit of the EMAT/specimen connection.

As far as the impedance of the specimen is concerned, its resistance and inductance can be calculated based on the eddy current density induced on its surface and the impact of the skin effect on it. As the electromagnetic wave launched by the EMAT attenuates quickly inside the sample, the electromagnetic coupling between the EMAT and the specimen mainly occurs on the surface of the specimen. The resistance the specimen shows against the electromagnetic wave propagation can be calculated as if a conductive material of length L and width W was subjected to a current density given by [235]:

$$\mathbf{j}_z = \mathbf{j}_{z0} e^{i(\omega t)} e^{-(1+i)\left(\frac{\pi}{d}\right)} \quad (3.53)$$

The total eddy current is equal to the integral of the eddy current density for infinite depth and over the entire width of the sample, as it is shown below:

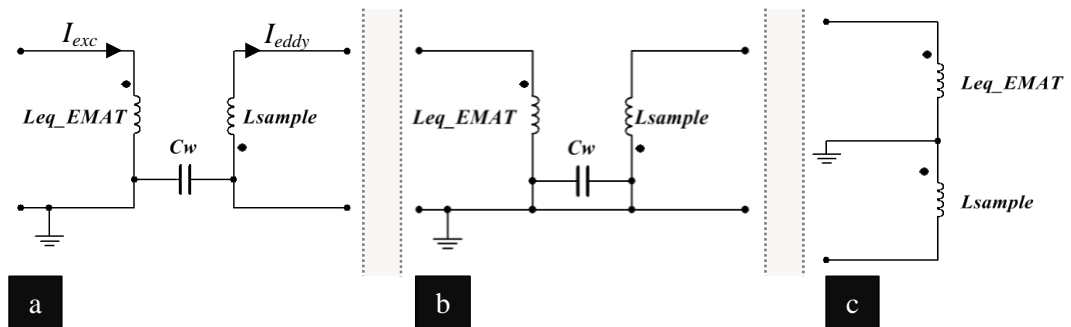


Figure 3.8. Electric circuit (a) EMAT/specimen transformer connection (b) autotransformer connection (c) autotransformer connection without parasitic capacitance

$$I_e = W \int_0^\infty j_z dz = j_{z0} e^{i(\omega t)} W \frac{d}{i+1} \quad (3.54)$$

The impedance on the surface of the sample can be calculated as the ratio of the applied voltage on the surface to the eddy current along the length of the sample, as it is shown below:

$$Z_{sample} = \frac{V}{I} = (1 + i) \frac{\rho_r L}{Wd} = (1 + i) \frac{\rho_r L}{W \left(\sqrt{\frac{2}{\mu_0 \mu_r \sigma \omega}} \right)} = e^{i\left(\frac{\pi}{4}\right)} \frac{L}{W} \sqrt{\mu_0 \mu_r \rho_r \pi f} \quad (3.55)$$

where ρ_r denotes the resistivity of the sample. The above equation 3.55 exhibits that the real and imaginary part of impedance on the surface of the sample are equal and thus its resistance and reactance are equal and dependent on the magnetic permeability and resistivity of the specimen as well as the frequency of excitation current. Also, the average eddy current over the entire thickness of the sample is of $\frac{3\pi}{4}$ phase lag compared to the excitation current on the EMAT coil, provided the fact the eddy current has at least a phase lag of $\frac{\pi}{2}$ compared with the excitation current [235].

Impedance analysis is of great importance in EMAT technology and signal interpretation. Variations in EMAT impedance can alter its efficiency, the SNR and amplitude of the signal received and can lead to invalid information regarding the structural integrity assessment of the specimen. Impedance matching between the EMATs and the instrumentation is required for the enhancement of the EMAT performance, since a portion of the electromagnetic losses can be eliminated. Impedance also varies with lift-off and thus their relationship is critical as well and analyzed further in the next subsection.

3.6.3 Lift-off

Based on impedance analysis performed in the previous subsection, the distance between the EMAT and the specimen, lift-off, alters the EMAT impedance, its electromagnetic coupling with the sample and finally its ultrasonic efficiency. As lift-off increases, the electromagnetic coupling between the EMAT and the specimen dwindles and the equivalent impedance of EMAT increases, since the eddy current losses decrease. When the EMAT is relatively away from any conductive material, its equivalent impedance is equal to its self-inductance, as no electromagnetic interference

occurs. Consequently, lift-off variations cause impedance alternations and finally changes in the signal received. This can result in misleading observations regarding the structural integrity of the sample under inspection and therefore lift-off should be kept stable during the inspection or lift-off compensation techniques should be developed.

Lift-off has been experimentally shown to affect the frequency characteristics of the excitation current applied to the coil and thus the frequency response of Lorentz force and the resultant ultrasonic wave [242]. The duration of the excitation current in a spiral coil that is in good proximity to an aluminum sample increases with lift-off increase and therefore, the Lorentz force produced is of larger duration as the lift-off increases. The ultrasound generated is also of lower frequency. In the same research, it has been cited that the lift-off response of an EMAT varies with regards to its coil shape. Spiral EMATs exhibit higher sensitivity to lift-off variations compared to linear coils. Further research was conducted by Morrison *et al.* regarding the ToF of S_0 against lift-off for different EMAT coil shapes, confirming that ToF of S_0 change as a predictable function of lift-off, hence, if the lift-off of the transducers is known at the time of measurement the absolute ultrasonic ToF may be determined. [224]. Thus, lift-off compensation can be accomplished either by measuring the inductance of the EMAT receiver or the spread of the excitation pulse on the EMAT transmitter or by analyzing the frequency content and ToF of the signal received.

The electromagnetic losses and mechanisms described above refer to room temperature operating environment. As temperature rises, the material, electric, magnetic and thermal properties of EMAT and specimen alter resulting in further changes in the electromagnetic coupling between the EMAT and the specimen and the impedance of the former. The development of a high-temperature EMAT requires the study of its performance at high temperatures and the impact of temperature increase on its electromagnetic potential and impedance.

3.7 Temperature Effect

As it was mentioned in the Section 3.2.3, temperature increase affects the material properties of the specimen resulting in wave velocity variations and changes in ToF of waves. Additionally to this,

the electric and magnetic properties of specimen and EMAT components like the relative permittivity, magnetic permeability and electrical resistivity, also alter with temperature. The magnetic leakage and mutual inductance, skin effect and resistance of both alter with temperature.

Equation 3.56 shows that the electrical resistance of any conductive material increases with temperature rise, implying that additional electromagnetic losses can be noticed on both EMAT coil and specimen due to resistance increase.

$$R(T) = R_0 (1 + \alpha \Delta T) \quad (3.56)$$

where R represents the electrical resistance in temperature T , R_0 denotes the electrical resistance at room temperature, α is the temperature coefficient of resistance and ΔT is temperature difference from room temperature. EMAT coil specifically designed to withstand high temperatures should be made of a low resistance conductive material that also possesses relatively small temperature coefficient, like constantan.

The parasitic capacitance between EMAT and specimen can alter with temperature due to changes in permittivity. Especially, in cases where the EMAT coil is embedded into ceramics, the permittivity of both air and ceramic influence parasitic capacitance. The thickness of ceramic can also function as additional lift-off between EMAT and specimen and drop in parasitic capacitance. Similarly, the parasitic capacitance within the turns of coil alters with temperature rise accordingly to the material surrounding the coil. Ceramic embedded coils experience larger capacitance at room temperature compared to bare coils due to larger permittivity ceramic materials possess compared to air. The relationship between relative permittivity of ceramic material and temperature determines the capacitance trend against temperature rise. Unlike resistance, relative permittivity does not change with temperature in the same manner in all materials. Hence, no universal mechanism in terms of specimen material can be formed for the calculation of EMAT parasitic capacitance.

The way magnetic permeability changes with temperature both in EMAT coil and specimen determines the alterations in self-inductance of EMAT coil, magnetic leakage, mutual, and eddy current inductance with temperature rise. Similarly to relative permittivity, prior knowledge of the

relationship between magnetic permeability and temperature for different specimen materials is required for the estimation of the overall EMAT inductance at high temperatures. Thus, the trend of the overall EMAT inductance against temperature can differ when the EMAT is employed on mild steel as opposed to stainless steel.

Based on equation 3.47, skin depth is dependent on magnetic permeability and resistance of specimen. Therefore, its behavior over temperature increase is disproportional to that of magnetic permeability and resistance of specimen. When the resistance increases with temperature, skin depth should decrease. However, additional information regarding magnetic permeability is required for the valid estimation of the skin depth at elevated temperatures.

The MOT of EMAT components is another crucial parameters that can greatly affect the design of a high-temperature EMAT. As it has been already mentioned, the EMAT coil should be made of a low resistance and magnetic permeability material. Copper meets these specifications and thus is an ideal candidate for coil manufacturing. However, it is subjected to oxidation at elevated temperatures and therefore it cannot be utilized in a high-temperature EMAT. Alternatively, silver, platinum and constantan can be used instead of copper, since all of these materials possess relatively low resistivity, smaller temperature coefficient compared to copper and melting point above 950°C. Especially, the former two exhibit similar characteristics, with platinum having smaller resistivity but slightly larger temperature coefficient than constantan. Nevertheless, platinum is also more expensive compared to constantan whose temperature coefficient is the lowest among all the four materials, making it the most suitable candidate for the manufacturing of high-temperature EMAT coil. Additionally, thermal insulation should be also applied on the coil structure for impeding the heat transfer to it without though affecting the electromagnetic coupling between the EMAT and the specimen. Ceramics are widely employed for thermal insulation and some types do not interact electromagnetically with the component they are applied on, like alumina.

Temperature rise also influences the performance of permanent magnets. The MOT of Nd-Fe-B is only 200°C, restricting its use in high-temperature EMAT technology. High Curie magnets can be used instead. SmCo and Alnico possess MOTs of 300°C and 500°C respectively, however, the

magnetic field they generate is weaker than Nd-Fe-B. Alnico also gets demagnetized easily in magnetic fields of opposite polarity and should not be employed in a PPM EMAT. EMATs designed for GWT should possess high magnetic capabilities, for maximum electromagnetic coupling with the specimen. The wave generated in the specimen must propagate long distances, requiring more energy to be introduced to the specimen compared to thickness measurements. Nd-Fe-B magnets are the strongest, but cannot be utilized at high temperatures without a cooling system so that their temperature remains below their MOT.

3.8 Summary

In this Chapter, the propagation mechanisms of guided waves in solids and main parameters that affect it were outlined and linked to EMAT design. The operating principles of EMATS were also explained. All three mechanisms of ultrasonic transduction and reception, Lorentz, magnetization and magnetostriction force, were mathematically analyzed. A brief overview of the main EMAT designs for both bulk and guided waves was given emphasizing on the wave purity characteristics of each design. The parameters that limit the ultrasonic performance of EMATs were also outlined. An analysis of skin effect, EMAT impedance and lift-off for both room and high temperatures was accomplished. The challenges of the designing of a high-temperature EMAT were also introduced, manifesting the importance of material selection and estimation of optimum operating conditions.

The following Chapter presents the methodology followed for the determination of the optimum EMAT design for SH excitation/reception at elevated temperatures. FEA models for the wave purity characteristics of PPM EMAT at room and high temperatures were carried out. Thermal and CFD simulations for the material selection and estimation of the optimum operating conditions, thermal potential and limitations of the final EMAT design were also performed. The theoretical results and their analysis are presented in the following Chapter.

Chapter 4

Numerical Simulation of High Temperature EMAT

4.1 Introduction

In this Chapter, the methodology and results obtained from coupled electromagnetic and mechanical FEA regarding the ultrasonic signal response of a PPM EMAT against temperature rise are summarized. The wave mode purity characteristics of a standard room temperature PPM EMAT attached on a stainless steel plate were investigated via Comsol software at room and high temperatures, by solving only the operating equations related to Lorentz force. The conclusions made out of this analysis were utilized as a benchmark for the design of the high-temperature EMAT. Thermal and CFD analysis was also performed for the material selection and optimization of the high-temperature EMAT design. Transient thermal simulations were accomplished for the estimation of the optimum coil design and its thermal insulation against its lift-off limitations. CFD analysis calculating the most suitable operating conditions for the water cooled EMAT was conducted for both short (at 500°C) and long term (at 250°C) inspection purposes.

4.2 Wave Propagation FEA

4.2.1 FEA Model Overview

In the previous Chapter, the physics underlying guided wave propagation in solids and the main operating principles of EMATs were described. The analytical solution of the equations given can yield useful information regarding the final output of EMATs only for simple geometries and when specific assumptions have been made for simplification purposes. To date, numerical models have been widely utilized for calculating accurately the response of complicating structures under the presence of different physical phenomena. FEA (alternatively called Finite Element Method – FEM) was adopted in the present study for the estimation of the electromagnetic and ultrasonic

interaction between a PPM EMAT and a stainless steel plate. Commercial software, Comsol Multiphysics [243], was used for solving the partial differential equations governing electromagnetism and continuum mechanics coupled together. Custom constitutive equations can also be used for the investigation of more complicating problems such as magnetostriction. All the above render this package appropriate for the estimation of the electromagnetic coupling between PPM EMAT and stainless steel plate and their ultrasonic response.

In this current research, the EMAT is studied regarding its ultrasonic signal response and wave purity characteristics mainly on paramagnetic materials and more particularly stainless steel. Based on the EMAT theory analyzed in the previous Chapter, Lorentz force is the dominant transduction and reception mechanism on paramagnetic materials and thus it is the only force taken into consideration in the implementation of the numerical model. The static magnetic module computes the magnetic flux density \mathbf{B}_{st} generated by the arrays of permanent magnets and the dynamic electromagnetic module is utilized for the calculation of the magnetic flux of the dynamic magnetic field \mathbf{B}_{dyn} produced by the coil and eddy current density \mathbf{J}_e induced on the plate given the excitation current. After the calculation of these three quantities, Lorentz force can be directly estimated based on equation 3.13 and used as a load input to the mechanical module that simulates the guided wave propagation (ultrasonic signal) in the plate.

Several researchers have followed the same approach for calculating the electromagnetic/mechanical interaction between EMAT and sample [27, 174, 175, 179, 181]. However, in most cases, the EMAT configuration was simpler than that of PPM EMAT and also the temperature effect on the above problem was not taken into account, since only room temperature models have been developed so far. Therefore, there were still challenges to be overcome for the successful and meaningful execution of the model, such as the mesh size and number of elements of a 3D simulation against computational limitations and temperature effect consideration over complexity of the mathematical/physics problem. Along with the above challenges, skin effect can also affect the computational complexity of the FEA model. Nevertheless, it has been shown that in metals Lorentz force mechanism is not greatly affected by the skin effect phenomenon, since only the spatial distribution of eddy current alters with skin

depth while the overall eddy current density induced in the sample remains constant [27]. Hence, skin effect can be neglected in the FEA model for both magnets and sample.

The FEA model was developed to solve the mathematical framework described by equations 3.1-3.6 as if the electric field \mathbf{E} and magnetic field \mathbf{B} were related to a scalar potential V and a Magnetic Vector Potential (MVP) \mathbf{A} , as given below.

$$\mathbf{E} = -\nabla V - \frac{\partial \mathbf{A}}{\partial t} \quad (4.1)$$

$$\mathbf{B} = \nabla \times \mathbf{A} \quad (4.2)$$

The two new quantities can be retrieved from the following set of equations that are a simplified version of Ampère's law and its divergence respectively.

$$\sigma \frac{\partial \mathbf{A}}{\partial t} + \nabla \times (\mu_0^{-1} \nabla \times \mathbf{A} - \mathbf{M}) - \sigma \mathbf{v} \times (\nabla \times \mathbf{A}) + \sigma \nabla V = \mathbf{J}_{exc} \quad (4.3)$$

$$-\nabla \cdot \left(\sigma \frac{\partial \mathbf{A}}{\partial t} - \sigma \mathbf{v} \times (\nabla \times \mathbf{A}) + \sigma \nabla V - \mathbf{J}_{exc} \right) = 0 \quad (4.4)$$

where \mathbf{v} is the velocity in the conductor (which can be equal to the velocity of electrons \mathbf{v}_e) and \mathbf{J}_{exc} denotes the density of excitation current. All the above constitute the mathematical problem addressed to the electromagnetic solver and its solution yielded the Lorentz force distribution generated in the plate.

After the electromagnetic analysis and the calculation of Lorentz force, the elastic problem and guided wave propagation were performed under the principle of virtual work. Based on this theory, the overall, internal virtual work equals to the overall virtual work derived from external forces and thus the total energy stored remains constant. The mechanical solver calculated the displacement \mathbf{u} generated due to Lorentz force by coupling together all the wave propagation equations described in Chapter 2.

4.2.2 FEA Model Implementation

The configuration of PPM EMAT directly affects the frequency characteristics of the wave mode generated into the specimen and therefore, prior knowledge of the ultrasonic specifications the EMAT should meet are required for its design. The frequency and subsequently the wavelength of the wave mode introduced to the sample are related to the minimum defect size the ultrasonic system needs to detect. The wavelength should be smaller than double the minimum defect size. In GWT, low-frequency waves, from 20 to 100 kHz, are usually introduced into the structure under inspection due to their low attenuation over long distance. However, their relatively large wavelength limits the size of defect that can be detected. The pitch of PPM EMAT determines the wavelength of the wave mode generated and thus the size of the magnets affects the frequency characteristics of the EMAT. Nevertheless, the size of magnet influences its magnetic strength if it is assumed that its density remains constant and therefore PPM EMATs are usually designed for relatively high-frequency GWT, 150-500 kHz. In this study, a 10mm long crack is the minimum defect detection requirement and the EMAT was designed to excite/receive SH_0 of 12mm wavelength.

The EMAT is primarily developed for the inspection/monitoring of structures made out of stainless steel, since stainless steel is extensively used for the construction of critical components operating at elevated temperatures. Pipelines, tanks and absorber tubes are made out of stainless steel in solar thermal industry [2]. Provided that the shape and thickness of the structure under inspection determines the complexity of the GWT signal interpretation, this EMAT is mainly designed for thin, plate-like structures. The dispersion curves of a 3mm thick, 316L stainless steel plate of 8000 Kg/m^3 density, 195GPa Young's modulus and 0.285 Poisson ratio, have been calculated via Disperse commercial software and are shown in Figure 4.1. This figure shows that the optimum operating frequency for SH_0 excitation for a 12mm pitched PPM EMAT is 256kHz. S_0 and A_0 can also be present though. The red circles in Figure 4.1 and Table 4.1 show at which frequency SH_0 , S_0 and A_0 can be excited by a 12 pitched PPM EMAT and their phase velocity at these frequencies.

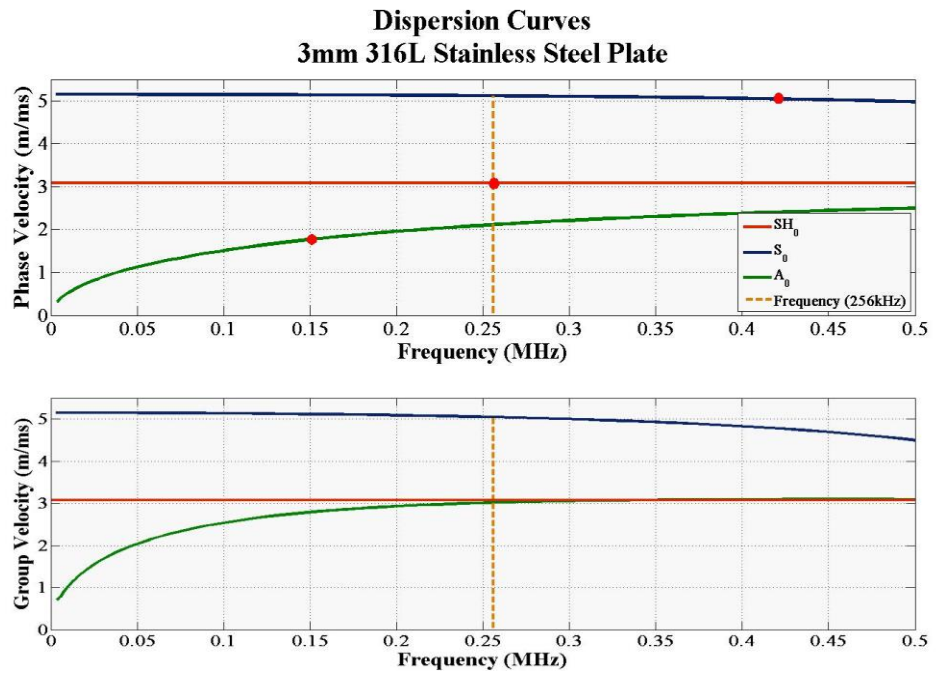


Figure 4.1. Dispersion curves of a 3mm thick 316L stainless steel plate

Hence, an EMAT designed for 12mm wavelength SH_0 should be driven with AC current of 256kHz frequency. At this frequency though, SH_0 and A_0 have the same group velocity. As a result, both wave modes can be excited/received from the EMAT simultaneously resulting in a more complicated signal, since A_0 is dispersive at this frequency. Nevertheless, the orientation of the displacement of each wave mode is different; SH_0 has an in-plane displacement while A_0 has an out of plane displacement as well. Thus, the wave mode, and more particularly the displacement, the PPM EMAT is sensitive to needs to be investigated via FEA for both room and high temperatures.

Table 4.1 Frequency and Velocity of S_0 , A_0 and SH_0 for a 12mm magnet pitch PPM EMAT

Dispersion Curves		
Wave Mode	Frequency (kHz)	Phase Velocity (m/s)
SH_0	256	3080
S_0	420	5040
A_0	146	1750

As the temperature of the specimen increases, its material, electric and magnetic properties alter, resulting in variations in the velocity and attenuation of the propagating wave mode. Young's modulus and density of the specimen decrease with temperature increase, while Poisson ratio increases. These changes result in the velocity drop of bulk shear and longitudinal waves and the decrease of the phase and group velocity of SH_0 , A_0 and S_0 as well, as it was discussed in subsection 3.7. Table 4.2 and Table 4.3 summarize the phase and group velocity of SH_0 , S_0 and A_0 respectively at 256 kHz from room temperature up to 500°C with a step of 100°C. Hence, as the temperature rises and the wave velocity decreases, any reflections received by the EMAT will be shifted in time. The electrical resistance and permeability of 316L stainless steel also change with temperature increase.

Table 4.2 Phase Velocity of S_0 , A_0 and SH_0 for various temperatures

Phase Velocity at 256kHz						
Wave	20	100	200	300	400	500
Mode	(°C)	(°C)	(°C)	(°C)	(°C)	(°C)
SH_0	3080	3052	3001	2924	2808	2621
S_0	5118	5076	5003	4888	4699	4384
A_0	2110	2102	2079	2041	1992	1896

Table 4.3 Group Velocity of S_0 , A_0 and SH_0 for various temperatures

Group Velocity at 256kHz						
Wave	20	100	200	300	400	500
Mode	(°C)	(°C)	(°C)	(°C)	(°C)	(°C)
SH_0	3080	3052	3001	2924	2808	2621
S_0	5047	5006	4928	4807	4604	4277
A_0	3013	2994	2950	2885	2779	2609

The electrical resistance increases while permeability decreases with temperature rise; leading to electromagnetic losses, lessening of the strength of the electromagnetic coupling between the EMAT and the specimen and finally attenuation and amplitude drop of the signal received at high temperatures. Table 4.4 summarizes the values of density, Young's modulus, Poisson ratio and electrical resistivity of 316L stainless steel for room and high temperatures, as they were calculated based on [142] and used in the FEA model. The way permeability changes with temperature is strongly dependent on the composition of the metal and therefore no universal formula can be retrieved from literature for its calculation. Similarly, permittivity alters with temperature rise strictly dependently on the material composition. Therefore, the model does not take into account any variation caused in permeability and permittivity due to temperature changes. In the same manner, the resistance of the EMAT coil and permeability of the magnets change with temperature, however, the model investigates the effect of temperature on EMAT/specimen interaction only for inspection purposes. It is assumed that the EMAT is exposed to heat for short period of time where no significant changes can be observed on EMAT impedance and the electromagnetic energy it generates as temperature increases. Consequently, the results obtained from the FEA model can only provide a qualitative idea of the EMAT/specimen interaction at high temperatures.

Table 4.4 Material properties over temperature rise

Material Properties						
Material Properties	20	100	200	300	400	500
	(°C)	(°C)	(°C)	(°C)	(°C)	(°C)
Density	8000	7967	7895	7783	7635	7453
(Kg)						
Young's Modulus	195	190	183	172	156	133
(GPa)						
Poisson Ration	0.285	0.286	0.290	0.294	0.298	0.30
Resistivity	17.2	23.1	30.5	37.9	45.3	52.7
(nΩm)						

Provided that EMAT for GWT at high temperatures has never been studied before, the FEA model calculates the ultrasonic signal performance of a typical PPM EMAT design at ambient and high temperatures. This analysis focuses on the wave mode purity and temperature limitations of the existing EMAT technology and can be utilized as a benchmark for the design of the high-temperature PPM EMAT. Two arrays of six Nd-Fe-B magnets each were simulated as shown in Figure 4.2 a, b. Each magnet has 15mm width, 5 mm depth, 5mm height and Magnetization of 750kA/m. The direction of their magnetic flux is on the z-axis and the distance between them is 1mm. Due to computational limitations, the copper coil has been simplified and designed as two rectangular blocks of 35mm width, 15mm depth and 0.4mm height each. The AC current driven to the coil is a 3 cycle, Hanning windowed sinusoidal wave of 20A amplitude and of 256kHz central frequency along the x-axis. The orientation of the excitation current flowing inside one rectangular coil limb is opposite to the orientation of the current inside the other limb. The EMAT has a lift-off of 0.6mm from the specimen, which is a square 316L stainless steel plate of 3mm thickness and 1000mm length. A rectangular air block encapsulated the entire configuration, both EMAT and plate, providing electromagnetic coupling of EMAT and specimen. The external sides of that block are magnetically insulated.

The above configuration should yield an in-plane wave mode (x-y plane) propagating in y-axis, since the magnetic field is primarily in z-axis and eddy current on x-axis. The frequency response of racetrack coil is broadband and thus only the magnets arrangement and the frequency of the AC current can affect the frequency response of PPM EMAT. The pitch of the magnets is 12mm and equal to the wavelength of SH_0 at 256 kHz. The wavelength of the wanted wave mode directly

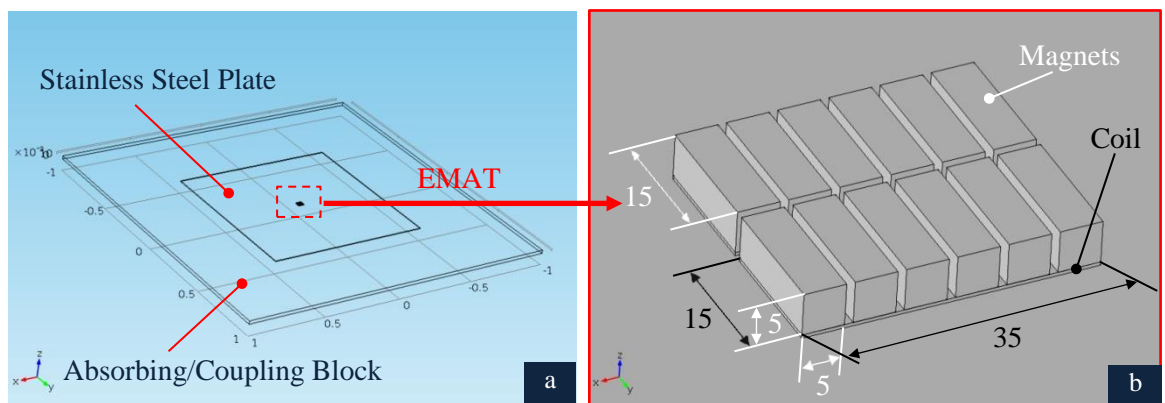


Figure 4.2. (a) Comsol FEA model configuration (b) EMAT configuration

affects the mesh element size and computational requirements of the model. It is well documented that the maximum mesh element size should not exceed the tenth fraction of the wavelength of the wanted wave mode [27]. The smaller the element size, the higher accuracy and resolution can be obtained. However, the time required for the simulation to be completed and its computational requirements increase greatly with the element size decrease, while the resolution of the final results plateaus after a certain element size. Thus, the optimum element size should be defined in terms of model resolution against computational limitations. Additionally, the element size is not only calculated based on the wavelength of the wave mode the EMAT is designed to excite/receive. According to guided wave theory, numerous, additional wave modes can propagate simultaneously with the wave mode the EMAT is to generate/detect. The dispersion curves of the 3mm thick stainless steel plate show that at 256kHz, S_0 and A_0 wave modes can also be present and propagate either at the same or different angle with SH_0 . Although, the phase velocity of each wave mode is distinctly different from the others, the group velocity of A_0 is slightly smaller than that of SH_0 , indicating that both wave modes can have the same ToF. This can result in mode conversion, complicating signal interpretation and invalid conclusions. However, both S_0 and A_0 exhibit an in– and out–of–plane displacement by contrast with SH_0 that propagates only in–plane. This feature can be selected for the wave mode purity analysis performed via FEA. In this case, the mesh element size should be calculated based on the smallest wavelength of the potentially propagating wave modes. Therefore, the maximum mesh element size is equal to the tenth fraction of A_0 wavelength at 256 kHz and is equal to 0.1mm. Finally, the relatively small mesh element size in conjunction with the large dimensions of the specimen render the model computationally demanding. As a result, any further refining of the element size resulted in the unsuccessful completion of the simulation based on the available computational resources and thus its optimum mesh element size equals to 0.8mm.

4.2.3 FEA Results and Discussion

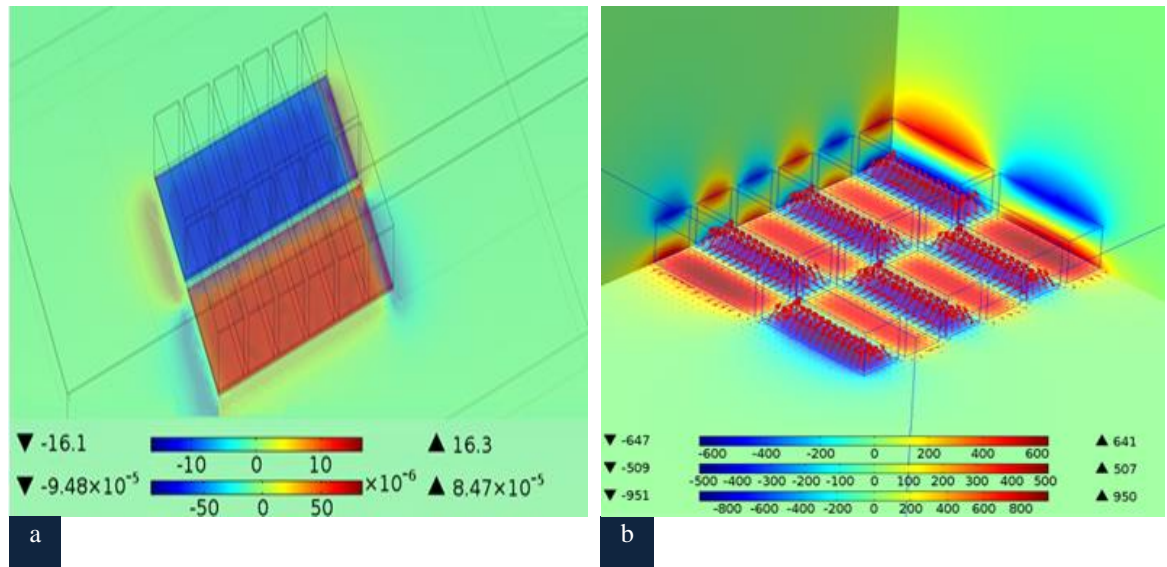


Figure 4.3. (a) Excitation/Eddy current distribution at 11µsec (b) Magnetic Flux Distribution (MSP)

Figure 4.3 shows the excitation/eddy current at 11µsec and the static magnetic flux distribution respectively. Both the electric and the magnetic field are uniformly distributed. The orientation of the eddy current alters between the two sides of the coil and it is on the x-y plane; the first label refers to excitation current density and the second to eddy current (A/m^2). The orientation of the magnetic field alters as it is depicted in Figure 4.3 b; it is mainly on the z-axis and its maximum strength is observed at the center of each magnet separately, as it is expected. The labels correspond to Magnetic Scalar Potential (MSP) in y – z, x – z and x – y plane respectively (T). Thus, the Lorentz force generated should mainly result in an in-plane displacement (x – y plane). Figure 4.4 shows how in- and out-of-plane displacement are related to coordinate system of the model. In the rest of thesis, any citation of in- and out-of-plane displacement will be in accordance with Figure 4.4. A probe was placed 30cm away from the EMAT at 0° angle from the direction that SH_0 amplitude is expected to maximize. At this angle, SH_0 propagates in x – y plane, while S_0 and A_0 have z and x component. Any displacement in the y-axis in this direction is a strong indication of SH_0 propagation whilst z displacement refers to both S_0 and A_0 depending on the ToF. The displacement in x-axis can be the result of both SH_0 and A_0 . Hence, the probe obtained the displacement on y and z-axis, as they can be used for the wave mode distinction. Figure 4.5 shows that the y displacement (blue line) maximized at 98 µsec while the z displacement (green line) maximized at 100 µsec. The ToF of the former matched with the wave velocity of the SH_0 , as it

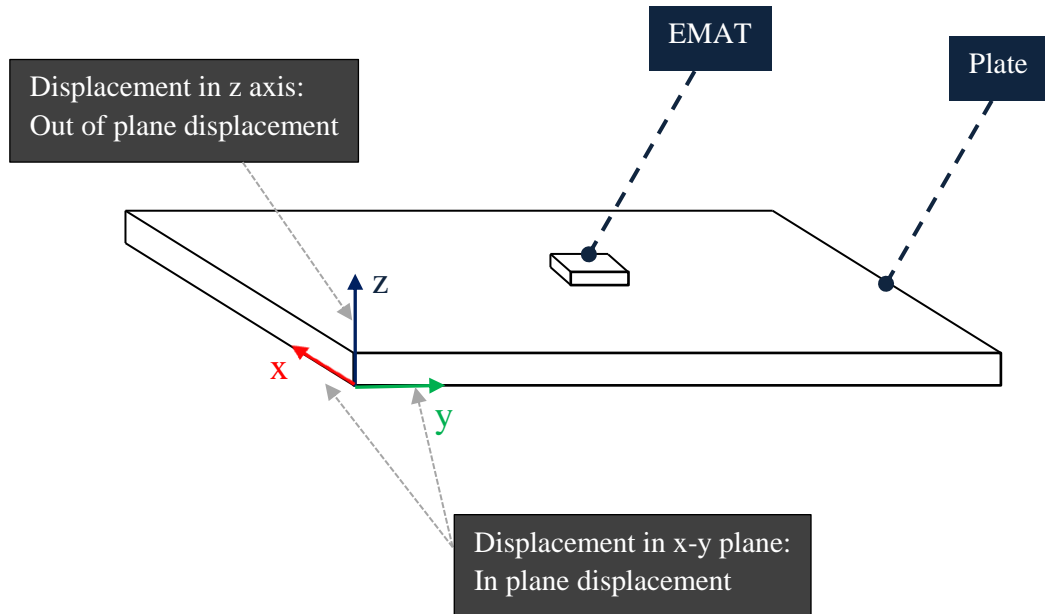


Figure 4.4. Schematic of coordinate system and displacement orientation

was calculated from the dispersion curves, while the latter could be A_0 . No S_0 reflections were noticed at this angle.

The three polar plots shown in Figure 4.6 and 4.7 individually provide more information regarding the wave purity characteristics and beam spread of this EMAT design. Each presents how the normalized x, y and z displacement at 59 μsec and 97 μsec respectively altered all around the transducer in 30 cm distance from its center. Thirty-six reception points were evenly distributed along the circumference of this circle. The ultrasonic signal response of the EMAT was symmetrical in all axis, since no imperfections were attributed to the EMAT design. Although, the largest displacement generated by the EMAT propagated in the y-axis at 0° angle with SH_0 velocity, indicating that most of the energy introduced to the specimen resulted in SH_0 wave mode

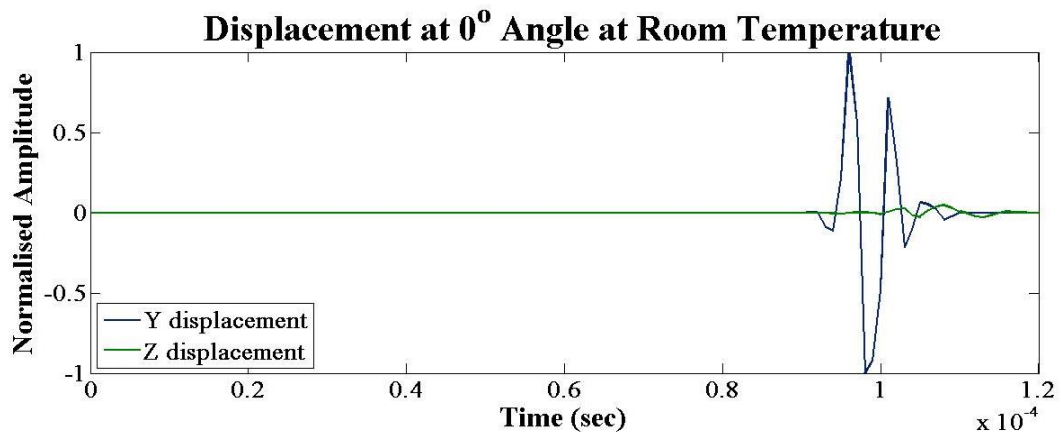


Figure 4.5. Y and Z displacement at 0° angle

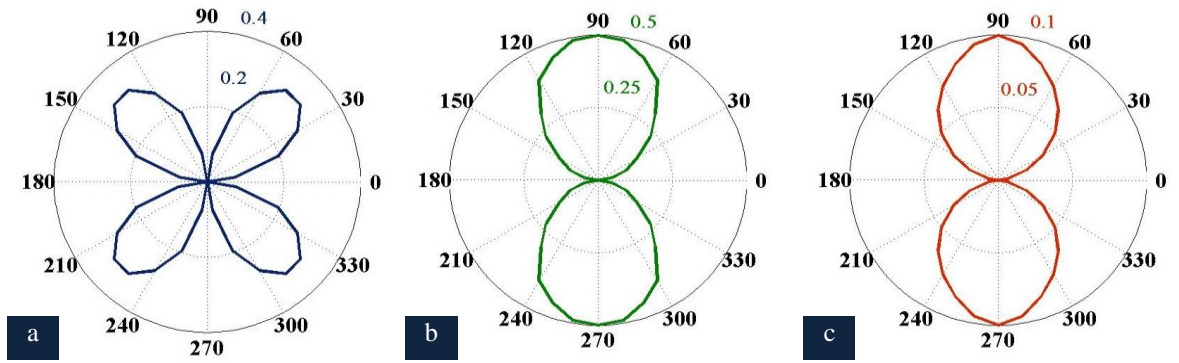


Figure 4.6. Displacement of S_0 wave mode at a) x, b) y and c) z axis

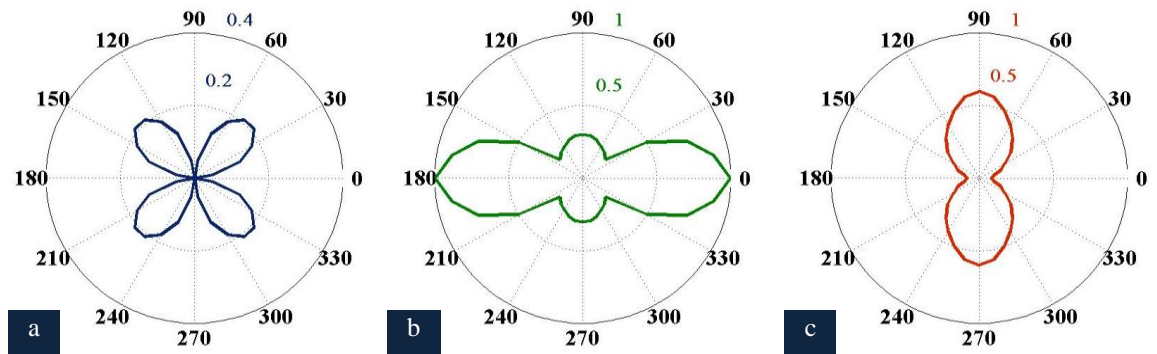


Figure 4.7. Displacement measure at 97 μsec a) x, b) y and c) z axis

propagating at the right angle, portion of the energy resulted in out-of-plane displacement in various angles and propagating with both S_0 and A_0 velocity. The maximum out-of-plane displacement (z-axis) was observed at 90° angle from the SH_0 direction. At this point, the out-of-plane energy traveled with both S_0 and A_0 velocity and its amplitude is considerable to x and y components. Nevertheless, a considerable y displacement was noticed at this angle as well. At 90° angle, both Lamb waves propagated in y-axis and their particle oscillation was noticed on both z and y-axis. As a result, both observations led to the conclusion that S_0 and A_0 can be excited by this EMAT configuration at 256 kHz and especially at 90° their amplitude maximizes. Nevertheless, the out-of-plane displacement was smaller compared to the in-plane and especially at 0° where y displacement maximized, the out-of-plane displacement minimized. Consequently, most of the energy transmitted to the sample resulted in an in-plane displacement propagating with SH_0 velocity and maximizing at 0° , with a beam spread of 35° . This confirms that PPM EMAT is suitable for SH_0 , however, other wave modes can be present at various angles leading to poor wave purity characteristics.

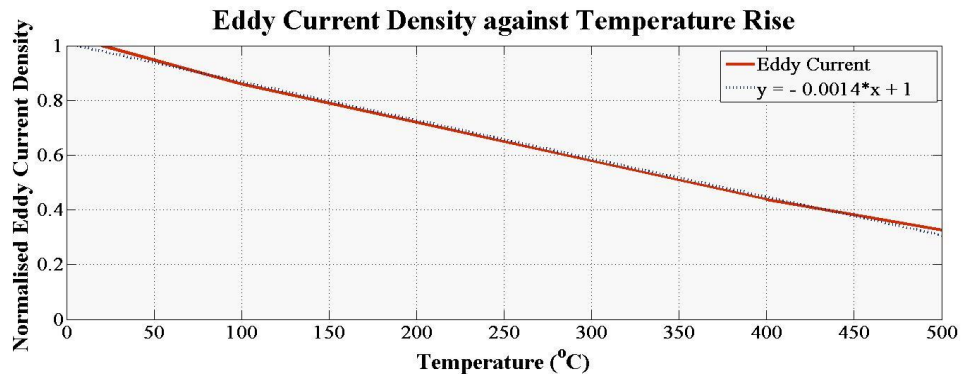


Figure 4.8. Eddy current density against temperature rise

The same FEA model was implemented for the theoretical evaluation of the ultrasonic signal response of PPM EMAT at high temperatures, as it was described before. Figure 4.8 shows how the total eddy current density induced on the plate altered with temperature rise, from 20°C up to 500°C with 100°C step. The results were normalized to the eddy current density calculated for room temperature. As it was expected, the eddy current density decreased with temperature rise substantially (drop rate of 16% per 100°C), as the electrical resistance of copper increased significantly with temperature increase and thus electromagnetic losses occurred. However, the eddy current distribution did not alter with temperature rise, since the electrical resistance changed with temperature uniformly through the entire volume of the plate and the skin effect was not taken into consideration. No changes were noticed on the magnetic field flux introduced on the surface of the sample, since the magnetic permeability of the sample remained constant in all simulations. However, it is known that magnetic permeability dwindles with temperature rise. Therefore, more information regarding the magnetic behavior of the material against temperature is required, so that a more accurate FEA model will be developed.

Figure 4.9 demonstrates the effect of temperature rise on the amplitude of the ultrasonic signal of the simulated configuration. In more details, Figure 4.9 a shows how y displacement corresponding to SH_0 measured at 0° angle dropped with temperature, since the out-of-plane displacement at this angle was significantly smaller than y component and can be neglected. All amplitude measurements were taken in regards to the effect of temperature rise on ToF. The amplitude dropped quadratically with temperature rise due to the eddy current behavior at high temperatures. Still, was in plane displacement more than 20% of its initial value at 500°C, indicating that the current EMAT technology can withstand high temperatures. Figure 4.9 b depicts the normalized y

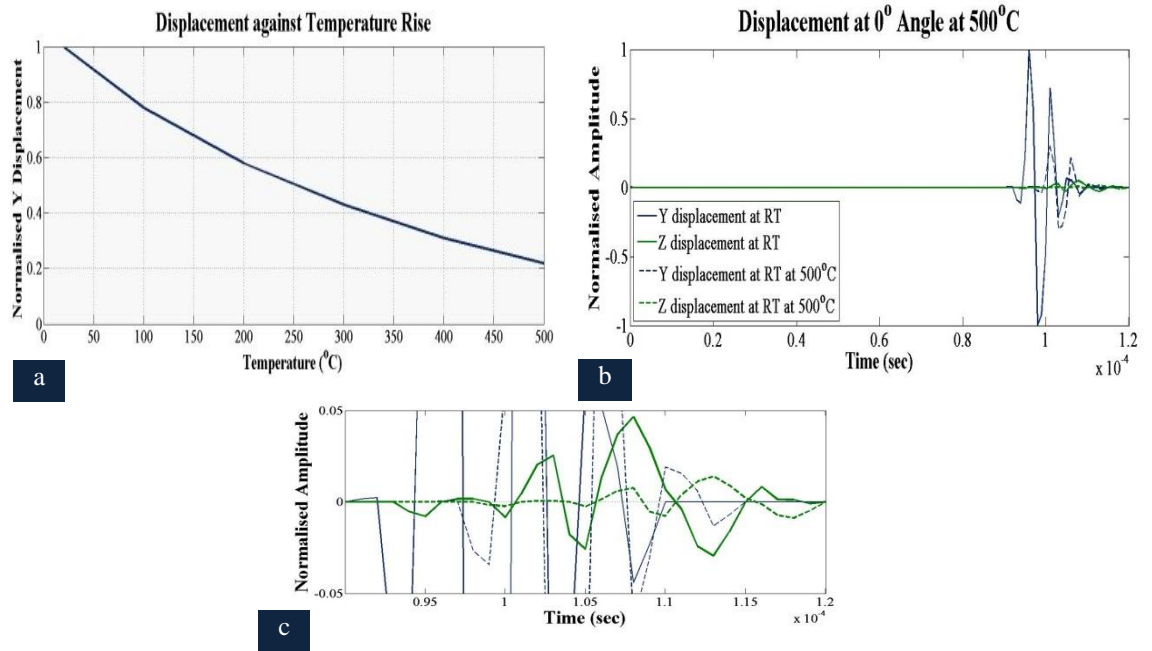


Figure 4.9. (a) Y displacement against temperature rise (b) Displacement at 0° angle at 500°C (c) Out-of-plane displacement at room temperature and 500°C (zoom)

and z displacement at room temperature and 500°C; both the in- and out-of-plane displacement decreased with the same rate. However, the temperature effect was more noticeable in out-of-plane displacement due to its relatively small amplitude compared to in-plane even at room temperature. The in-plane displacement decreased, but it was not negligible and it also shifted in time. However, the magnetic losses due to temperature rise were not taken into consideration and therefore a considerable divergence between the theoretical and experimental results is expected regarding the high-temperature performance of the existing EMAT technology. Despite this, any divergence between the theoretical and experimental results due to magnetic losses can still be counterbalanced with the thermal insulation and optimization of the EMAT design. The high-temperature EMAT should be designed so that its electromagnetic losses will be minimized over temperature and thus its experimental evaluation can still validate the above theoretical results. Moreover, the displacement dropped at the same rate in all axis around the EMAT, since the eddy current and Lorentz force distribution did not alter with temperature rise. Hence, the ratio of the maximum in-plane to maximum out-of-plane displacement remained the same over temperature rise, resulting in poor wave mode purity characteristics. However, the out-of-plane displacement decreased so greatly at 500°C compared to room temperature (71.7%) that it can be neglected, as shown in Figure 4.9 c.

The above analysis sheds light to the wave mode purity characteristics of PPM EMAT transmitter when it is employed on a stainless steel plate, as it shows that not only in-plane but also out-of-plane displacement can be generated at various angles all around the transducer. The ToF of out-of-plane displacement matches with both S_0 and A_0 velocity, while the in-plane propagates with SH_0 velocity. Consequently, the FEA model partially agrees with literature, since this EMAT configuration is suitable for SH_0 generation, but can also introduce S_0 and A_0 wave modes in the specimen at both room and high temperatures. Similarly to this, shear piezoelectric transmitters also experience poor wave mode purity characteristics [158], although their operating principles and specifications are different from those of EMATs. This indicates that the wave mode purity limitations both transducer technologies experience are due to guided wave physics. The spatial distribution of the force generated into the specimen determines the plane of particle oscillation. Hence, the EMAT transmitter produces Lorentz force of a particular spatial distribution that results in SH_0 at a specific direction, but also S_0 and A_0 .

The guided wave analysis of a stainless steel plate with the same material properties at room temperature and dimensions and under the same excitation/displacement with those simulated in the coupled electromagnetic/mechanical FEA model was conducted. An FEA model calculating the guided wave propagation of the above configuration was implemented in Abaqus commercial software [244]. A single point of excitation was introduced to the plate, corresponding to a single pair of alternated polarization EMAT magnets. The displacement introduced into the middle of the plate was of the same frequency with Lorentz force calculated previously, but of more cycles, 10 cycles. Due to computational limitations and symmetrical nature of the wave propagation problem, only one-quarter of a 30cm radius circle all around the excitation point was simulated. Nineteen reception points were used all around the arc. The polar plots in Figure 4.10 and Figure 4.11 summarize the results obtained from this analysis. Figure 4.10 a-c show the x, y and z displacement at 59 μ sec respectively and corresponding to S_0 and Figure 4.10 a-c presents x, y and z displacement at 97 μ sec. Both figures matched well with Figure 4.6 and 4.7. In both cases in- and out-of-plane displacement was generated at various angles, where the y displacement maximized at 0° and the z displacement at 90° . Hence, the energy introduced to the specimen by the EMAT was of a specific pattern that unavoidably resulted in the generation of multiple wave modes inside

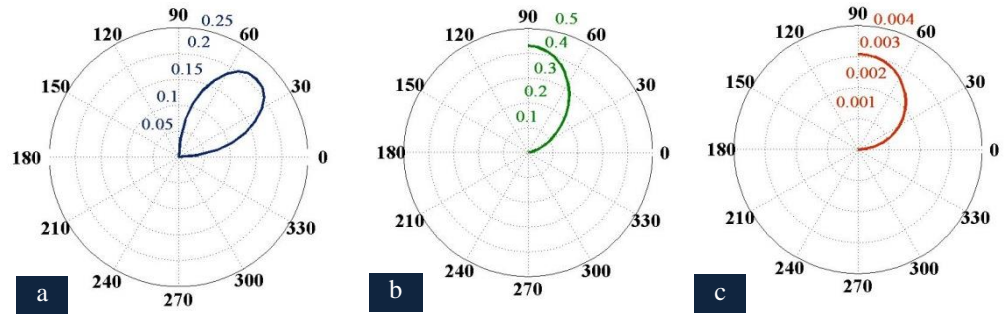


Figure 4.10. Displacement of S_0 wave mode at a) x, b) y and c) z axis

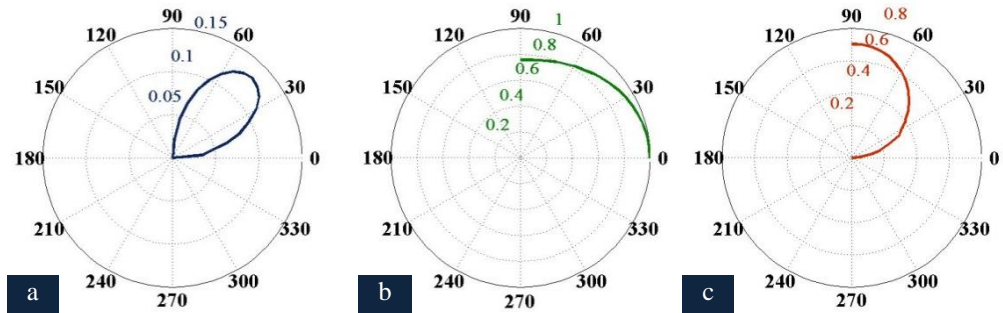


Figure 4.11. Displacement measured at 97 μsec a) x, b) y and c) z axis

the structure, due to the mechanics of the latter. Nevertheless, the EMAT is sensitive to only one particular force/displacement distribution in a certain direction, which is strongly related to its design. Thus a PPM EMAT receiver can only detect an in-plane displacement regardless of the total number of propagating wave modes.

At high temperatures, the theoretical results demonstrate that the temperature effect on the material and electric properties of the specimen can greatly influence the electromagnetic interaction between the EMAT and the specimen and their ultrasonic output signal, even if the electromagnetic and thermal properties of the EMAT remain constant. A PPM EMAT transmitter designed for room temperature can generate ultrasound to the sample even up to 500°C. However, the signal received at a 30cm distance from the center of the transducer was weak (80% drop), although the temperature effect on electromagnetic properties of the specimen was partially evaluated. Provided the fact that the magnetic properties of the sample also change with temperature increase and can result in further degradation of the electromagnetic coupling between EMAT and specimen, the ultrasonic performance of a room temperature EMAT can be lower than what was already theoretically estimated. The high-temperature EMAT should be designed to compensate for greater

electromagnetic losses than those calculated by the FEA model. Also, the EMAT should be designed so that its electromagnetic properties will not alter significantly with temperature rise and therefore its thermal response should be maintained constant as the temperature increases. As a result, a careful study regarding the material selection and optimum thickness of any thermal insulation applied on the EMAT was conducted, so that the EMAT would be thermally insulated efficiently and also its ultrasonic performance would not degrade significantly at high temperatures. A cooling system should also be incorporated in the EMAT design, so that its thermal properties would remain constant with temperature rise. Any electromagnetic divergence between the high-temperature EMAT design and the already existing technology observed at room temperature should be compensated as the temperature increases and could be also counterbalanced by providing additional power to the EMAT. The FEA model calculated the ultrasonic performance of a PPM EMAT designed for room temperature as it was driven by less power than its typical requirements and thus extra power could be also provided to the high-temperature EMAT, if it was needed. Consequently, a thermal and CFD analysis is of great importance for the material selection and estimation of the optimum EMAT design and its operating conditions at high temperatures.

4.3 Transient Thermal Simulations

The high-temperature EMAT was designed so that the temperature of the coil and the magnets remain below their MOT. Given that the coil is directly exposed to heat and its spacing from the magnets is usually less than 1 mm, its cooling becomes a challenge. No cooling system can be easily designed to efficiently cool down the coil without affecting the specimen. Conductive materials, with MOT higher than 500 °C, can be used for the manufacturing of the coil, like constantan. In spite of its relatively large resistivity ($49 \cdot 10^{-8} \Omega \text{ m}$) compared to copper ($1.68 \cdot 10^{-8} \Omega \text{ m}$ and $4.29 \cdot 10^{-3}/^\circ\text{C}$ temperature coefficient of resistivity), constantan possesses a small temperature coefficient of resistivity ($3 \cdot 10^{-5}/^\circ\text{C}$) attributing its enhanced electromagnetic performance at high temperatures. The low amplitude ultrasonic signal constantan coil EMAT generates at room temperature should be compensated with temperature rise. Therefore, an experimental investigation of the above was also performed along with impedance analysis at both room and high

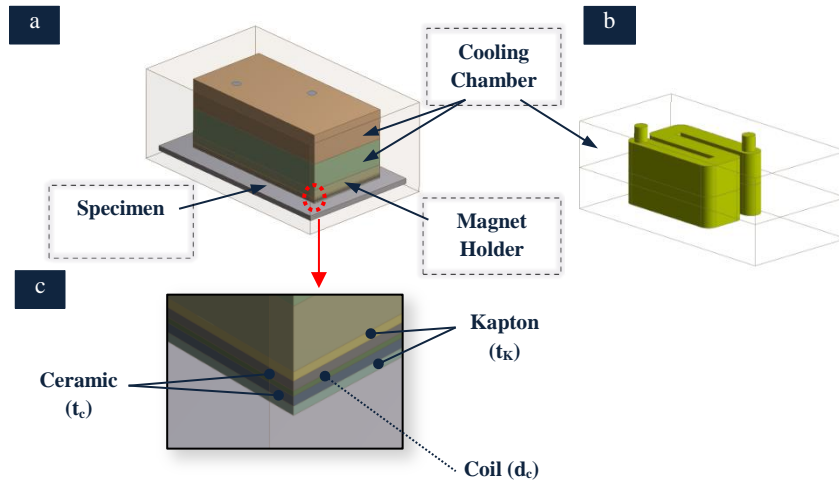


Figure 4.12. Thermal EMAT model (a) entire EMAT design (b) cooling chamber (c) Coil structure

temperatures. Thermal insulating materials should be also added to the coil to impede the heat transfer from the specimen. However, EMATs are very sensitive to lift-off variations, since the electromagnetic coupling strength between the EMAT and the specimen decreases with lift-off. Consequently, the thickness of any material added to the coil should be as small as possible so that both the coil will be efficiently protected from the heat and the electromagnetic coupling will be maximized. The optimum thickness of the thermal insulation was investigated via thermal simulations.

FEA was used for the thermal evaluation of a simplified EMAT design. Only the main parts of the EMAT were modeled, including the cooling, the magnets/magnet holder and the coil structure. The housing of the EMAT was made of brass, which possesses high thermal conductivity and melting point compared to aluminum and stainless steel transducer housings. A rectangular box of 3 mm thickness of 316 L stainless steel was modeled as the specimen/heat source. Figure 4.12 shows the geometry analyzed in Ansys commercial software using its Transient Thermal module [245]. In all simulations, the EMAT was in full contact with the specimen so the results correspond to the severest thermal conditions. The EMAT components are denoted in Figure 4.12 a and the cooling chamber in Figure 4.12 b. A detailed image of the coil is given in Figure 4.12 c. The coil was made of constantan and was encapsulated in alumina between two layers of Kapton.

Alumina was selected for the thermal encapsulation of the coil, due to its relatively high specific heat capacity (minimum value of 0.45 J/g K) and dielectric constant (99% alumina of 9 dielectric constant). Thus, it is an excellent candidate for the thermal and electrical insulation of the coil. However, its high dielectric constant can increase the capacitance of the EMAT and limit the ultrasonic signal performance of the transducer. During the first set of simulations, the optimal thickness of alumina substrate was calculated in regards to the thermal properties and lift-off/ultrasonic limitations of the EMAT. The temperature of the specimen was set to 100 °C with no active cooling. No Kapton encapsulated the coil whose diameter/thickness (d_c) was fixed at 0.4 mm. The thickness of the alumina layers (t_c) was increased gradually in simulations from zero with a step of 0.25 mm until the thermal response of the EMAT essentially plateaued. The maximum thickness was 1 mm due to lift-off limitations. The time needed for the coil (t_{max_coil}) and magnets ($t_{max_magnets}$) temperature to maximize did not increase significantly for alumina thickness exceeding 0.75 mm, as Figures 4.13 and 4.14 show. Figure 4.13 a,b show the temperature increase of the coil and magnets for 0.75 and 1 mm thick alumina layers respectively. In Figure 4.14, the green and orange solid lines show how the normalized time required for the coil and the magnets temperature to reach their maximum (t_{norm_coil} , $t_{norm_magnets}$) converged with ceramic thickness. Equation 4.5 gives t_{norm_coil} and $t_{norm_magnets}$ was calculated in the same manner, where i is the step in ceramic thickness increase. The blue and red dashed lines in Figure 4.14 present how the normalized Lorentz force amplitude drops with lift-off for stainless steel and steel, respectively, based on equations 4.6 and 4.7, respectively, where G is the lift-off and D_p refers to the pitch of the PPM

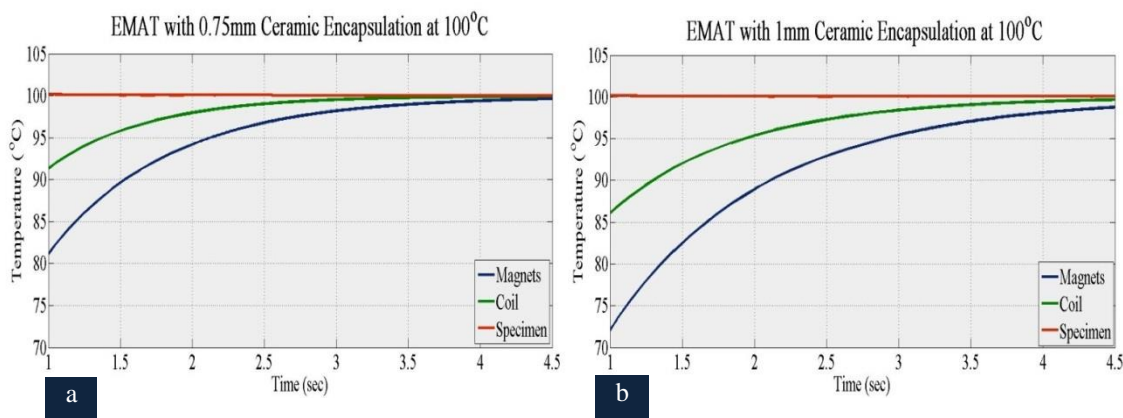


Figure 4.13. Temperature gradient of alumina encapsulated coil (a) 0.75mm alumina thickness (b) 1mm alumina thickness

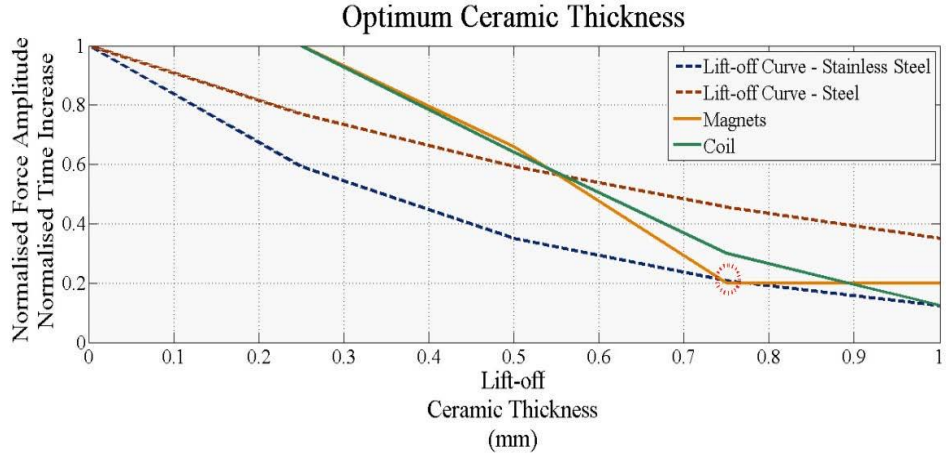


Figure 4.14. Optimum ceramic thickness graph

EMAT.

$$t_{norm_coil} = \frac{t_{max_coil\ i} - t_{max_coil\ i+1}}{t_{max_coil\ i}}, i = 1,2,3 \quad (4.5)$$

$$F_{L_stainless\ steel} = e^{\frac{-12\pi}{GD\rho}} \quad (4.6)$$

$$F_{L_steel} = e^{\frac{-4\pi}{GD\rho}} \quad (4.7)$$

Figure 4.14 shows that $t_{norm_magnets}$ plateaued and t_{norm_coil} dropped with smaller rate after 0.75 mm ceramic thickness. Consequently, any further ceramic thickness increase would not improve significantly the thermal response of EMAT over time. The ceramic thickness can also affect the amplitude of ultrasonic signal response of EMAT, since it increases its lift-off. When the ceramic thickness is 0.75 mm, Lorentz force decreases to 20% and 45% of its maximum for stainless steel and steel, respectively. When the ceramic thickness increases to 1 mm, Lorentz force in stainless steel is less than 20% of its maximum, making the EMAT inefficient for GWT. Hence, the minimum thickness of each alumina layer should be chosen as 0.75 mm. Regardless of the ceramic thickness, the time needed for the EMAT components to reach maximum temperature, whilst the EMAT was heated up to 100°C, was of the order of only a few seconds (5 seconds). Hence, additional thermal insulation was needed to extend the maximum operating temperature and time of the EMAT.

Kapton possesses large specific heat capacity (1 J/g K) and thus it can impede the heat transfer from the specimen to the EMAT coil over time more efficiently than alumina. It also exhibits

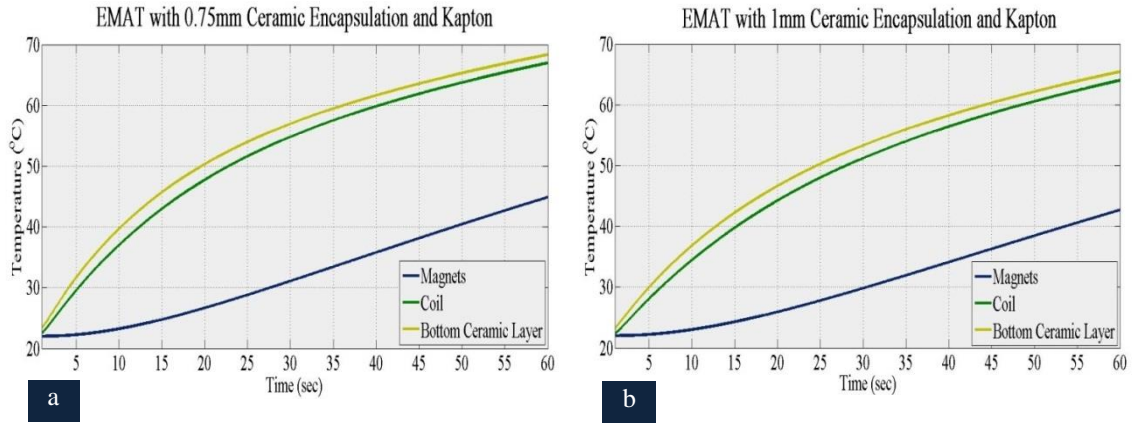


Figure 4.15. Temperature gradient of Kapton and alumina encapsulated coil (a) 0.75mm alumina thickness (b) 1mm alumina thickness

strong electrical insulating characteristics. However, its MOT is 400°C and therefore it can limit the thermal response and MOT of the transducer. Further simulations were performed with two Kapton layers in place. The alumina thickness increased from 0.75 mm to 1 mm in 0.25 mm steps with a Kapton layer (t_k) of 1 mm and a specimen held at 100 °C. Figure 4.15 a (0.75 mm alumina) and Figure 4.15 b (1.0 mm alumina) show the temperature increase of the bottom ceramic layer, the coil and the magnets for the fully encapsulated EMAT. The response of all three components did not change significantly with the ceramic layer thickness, indicating that a 0.75 mm thick alumina encapsulation is suitable for this design. However, the trend of magnet temperature was affected; both the first and second derivatives of the magnet response changed compared to Figure 4.13, explained by the double insulation of the magnet compared to the coil, with two layers of alumina and Kapton inhibiting heat transfer. When both Kapton and 0.75 mm thick alumina encapsulation were used and the EMAT was heated for 1 min, the temperature of the coil and the magnets reached only 67 °C and 45 °C, respectively. These encouraging results indicate that this EMAT design can potentially withstand even higher temperatures. Thus, its higher temperature response was also investigated.

In the final thermal simulations, the EMAT design (coil encapsulated with 0.75 mm thick alumina and two layers of Kapton) was tested up to 500 °C. No active cooling was used and the temperature of the specimen increased from 100 °C to 500 °C. Table 4.5 summarizes the temperature of the coil and the magnets with the EMAT heated for 1 min. The results show that alumina and Kapton can

be used for thermal insulation of the coil and magnets, since the temperature of the EMAT components remained well below their MOT.

The current thermal analysis resulted in the optimum EMAT design in terms of transient thermal properties. The EMAT was designed so that the time required for the maximum heat to be transferred to it would be maximized without any active cooling. The material properties and thickness of the thermal insulation added to the coil to limit the heat transfer were selected and calculated so that the EMAT would be efficiently insulated thermally up to 500°C and the electromagnetic losses would be also eliminated. The results obtained show that a Kapton and alumina encapsulated constantan coil can withstand high temperatures (500°C) for short period of time (1 min), since the coil and magnet temperature did not exceed their MOT during the first minute of operation. Thus, the current design can be utilized for inspection purposes. Nevertheless, in this analysis the thermal properties of the EMAT did not plateau over time and especially, at 500°C the temperature of the magnets was relatively close to their MOT and it could exceed it, as the operating time increased. Therefore, further CFD simulations were carried out, in which the active cooling was also evaluated, for the enhancement of the thermal properties of the EMAT over time.

Table 4.5. Thermal properties of EMAT based on transient thermal analysis

Specimen	Temp./°C				
	100	200	300	400	500
Coil	66.4	123.4	180.3	236.7	294.4
Magnets	43.9	72.1	100	129.2	156.5

4.4 CFD Analysis

4.4.1 Water Cooled EMAT for Inspection

Based on the EMAT theory and GWT specifications outlined in Chapter 3, the electromagnetic coupling between the EMAT and the specimen in GWT should be as strong as possible so that the length of inspection will be maximized. Given that the EMAT is driven by the largest electrical supply that is currently available and its design permits the optimum thermal and electrical performance of its coil, its magnetic potential should be also optimized over temperature rise. The EMAT must be designed so that both Nd-Fe-B and SmCo magnets can be successfully utilized up to 500°C. Consequently, the temperature of the magnets should be constantly maintained below the MOT of Nd-Fe-B (200°C). Thermal insulation of the coil will increase the time required for energy to be transmitted to the magnets but excess thermal energy can lead them to break down. The heat must, therefore, be removed via a cooling system designed into the EMAT. A CFD analysis in Ansys software using its Fluid Flow (Fluent) module was performed. The EMAT was theoretically evaluated regarding its thermal response over time. Optimal flow velocity and inlet temperature of the coolant were identified and the effect of the cooling medium on the performance of the cooling system was also investigated.

In the first set of simulations, the optimum coolant flow velocity was calculated. The duration of the coolant being inside the cooling chamber and exposed to heat affects the amount of thermal energy it absorbs. The temperature of the coolant increases with time, reducing its temperature difference with the heat sink until eventually, this is too small to dissipate sufficient heat. The optimum flow velocity must, therefore, be calculated. In these simulations, water with inlet temperature of 10 °C was used as coolant. The density, specific heat capacity, thermal conductivity and viscosity of water were, respectively, 998 kg/m³, 4182 J/kg·K, 0.6 W/m·K and 0.001 Pa·s. The temperature of the specimen was held at 500 °C and the EMAT was in total contact with the specimen for 5 mins. The water flow velocity was increased in the simulations from 1 m/s to 9 m/s in steps of 2 m/s. Figure 4.16 a demonstrates how the maximum and minimum temperature of the coil and the magnets dropped with increasing flow velocity after 5 mins of heat exposure. The minimum temperature of the magnets decreased dramatically. It dropped below 200 °C at a flow velocity of only 3 m/s showing that flow velocity has a major influence on EMAT efficiency. The optimum flow velocity for this system in terms of power requirement was 3 m/s since higher flow velocities would require more electrical power. However,

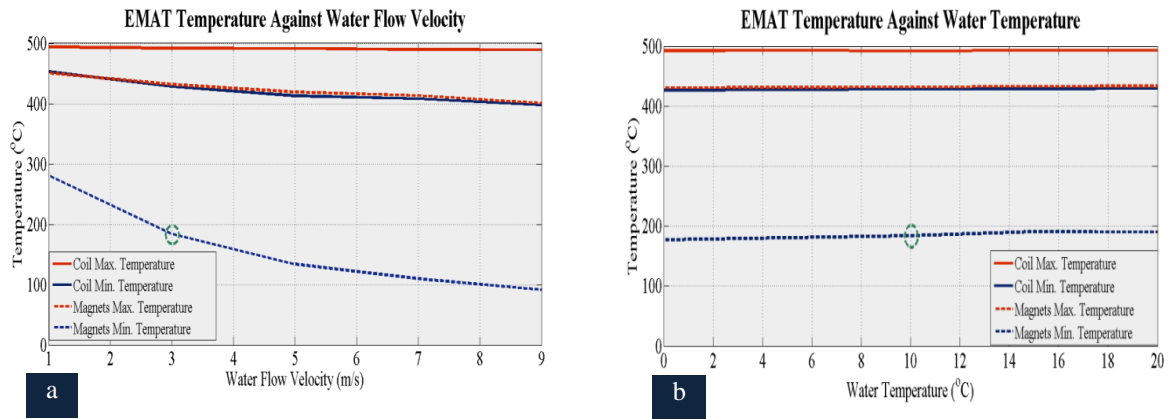


Figure 4.16. (a) EMAT temperature against coolant flow velocity (b) EMAT temperature against coolant temperature

it should be highlighted that the thermal response of the EMAT did not plateau after 5 mins of operation. This can complicate the EMAT performance for monitoring purposes, since the temperature of its components may exceed their MOT after 5mins.

A parameter that could also affect the efficiency of the system is the temperature of the coolant entering the cooling area. In further simulations, the water flow velocity was kept at 3 m/s and its temperature increased from 0 °C to 20 °C in steps of 5 °C. The balance of the components was held at 25 °C. Figure 4.16 b shows how the maximum and the minimum temperature of the coil and the magnets changed with the water temperature after 5 mins of operation. No significant changes were observed in any of the four temperatures as the coolant temperature increased. Thus, this parameter cannot be used to control the performance of the cooling system. An optimum coolant temperature of 10 °C can be freely chosen since the minimum temperature of the magnets was below 200 °C and no additional equipment is required to cool the water.

Figure 4.17 a shows the temperature gradient of the main EMAT components when the EMAT was heated up to 500°C for 5 mins under its optimum operating conditions, as they were calculated previously. It is apparent that the size and position of the cooling chamber affect the temperature gradient of the coil and the magnets. The area below the cooling chamber was efficiently cooled while areas further away from the cooling chamber and closer to the cooling outlet experienced higher temperatures. However, the size and position of the cooling chamber were directly affected by BNC connector position. Space was needed for the electrical components of the EMAT to be safely positioned without the overall size of the EMAT exceeding 100 mm. A design with wider

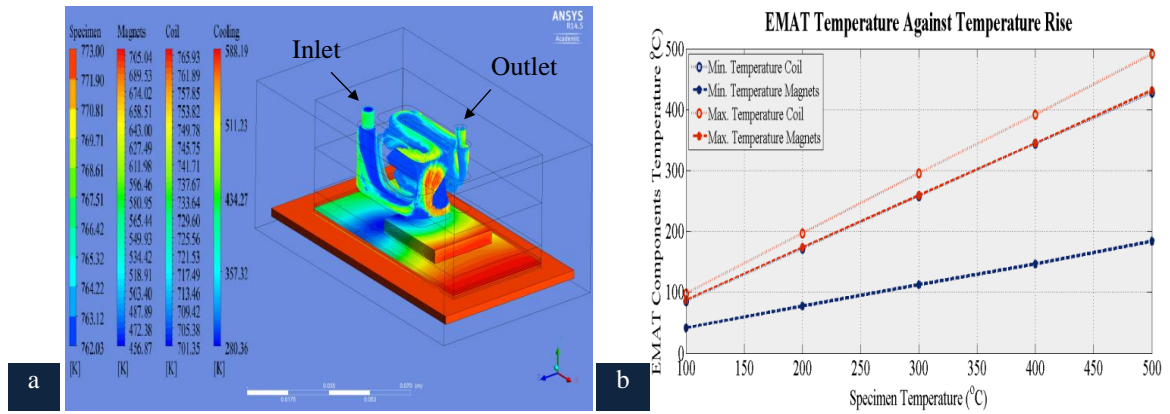


Figure 4.17. Water cooled EMAT (a) temperature gradient of EMAT components at 500°C (b) temperature of EMAT components against temperature rise.

cooling chamber could cool the critical EMAT components more efficiently but may result in a bulkier EMAT. Figure 4.17 b summarizes the results obtained when the aforementioned model was evaluated from 100 °C to 500 °C in steps of 100 °C. In all cases, the minimum temperature of the main two EMAT components did not exceed their MOT, indicating that this EMAT design under the specified conditions can withstand high temperatures for at least 5 mins. Nevertheless, the maximum temperature of the magnets exceeded their MOT when the specimen temperature exceeded 250 °C, and the maximum water temperature exceeded 100 °C. However, these temperatures occurred in a small area and the short time required for the water to circulate in the cooling chamber means the water will not evaporate. These observations, though, can limit the operating time of the EMAT at high temperatures.

4.4.2 Oil Cooled EMAT for Inspection

The material properties of the cooling medium—heat capacity, thermal conductivity, freezing point and viscosity—affect the performance of the cooling system, its thermal efficiency and limitations. Water and oil have been widely used as coolants for transformers and EMATs. A thermal analysis was performed for an oil-cooled EMAT. The density, specific heat capacity, thermal conductivity and viscosity of the oil used in the model are respectively 890 kg/m³, 1860 J/kg·K, 0.126 W/m·K and 0.06 Pa/s. Flow velocity was 3 m/s and the temperature of oil as it entered the cooling chamber was 10 °C while the rest of the EMAT components were at 25 °C. The temperature of the specimen was held at 500 °C with the EMAT in contact. Under these conditions,

the oil did not cool the magnets as efficiently as water; the minimum temperature of the magnets exceeded 200 °C within 5 mins of operation. However, optimum operating parameters change with the coolant and since it was simulated under the optimum conditions for water, the thermal performance of the oil-cooled EMAT was low. The temperature of oil can be below zero, if a refrigerator is used, however, this results in complicated and costly instrumentation. The oil cooled EMAT design was simulated again with an oil temperature of -10 °C and the flow velocity was set to 3 m/s and then 9 m/s. Table 4.6 summarizes the results retrieved from the three case studies for the oil cooled EMAT; neither flow velocity nor temperature significantly improved the oil system's efficiency.

Oil has a smaller heat capacity and thermal conductivity than water and less time is required for its temperature to increase. The viscosity of oil also impedes its circulation inside the cooling chamber. Hence, the temperature difference between coil and heat sink was smaller compared to that with water-cooling, resulting in lower efficiency. The cooling system must be re-designed to improve the thermal response of the oil cooled EMAT. Magnets and coil can be in a single chamber through which cooling oil flows. Oil is a minor fire hazard. It may also attenuate and alter the magnetic field and its dielectric constant alters with temperature. Further research with oil is necessary. Water is safer but its higher freezing point limits cooling efficiency.

Table 4.6. Temperature of oil cooled EMAT against flow velocity and oil temperature

	Flow	Coolant	Coil	Max.	Coil	Min.	Magnets Max.	Magnets Min.
Medium	Velocity	Temperature	Temperature		Temperature		Temperature	Temperature
	m/s	°C	°C		°C		°C	°C
Oil	3	10	497		482.9		480	421.1
Oil	3	-10	496.8		482.2		479.1	417.9
Oil	9	-10	496.1		480.4		477.2	413.4
Water	3	10	491.8		428.1		431.8	183.6

Consequently, a water-cooled EMAT with Kapton and ceramic encapsulated coil can withstand high temperatures for short period (less than 5 mins) based on theoretical analysis and can potentially be used for high-temperature inspection. However, during this operating period of 5 mins, the thermal response of the EMAT did not plateau. This indicates that further changes may be required for this EMAT to be maintained thermally stable over long periods of time. Additional analysis for the evaluation of the thermal potential and limitations of the current EMAT design in terms of long term operation at high temperatures was performed. The optimum operating conditions and MOT of this EMAT against high temperatures over time (> 5 mins) were identified.

4.4.3 Water Cooled EMAT for Long Term Inspection

The FEA model presented in the previous subsection was utilized for the thermal analysis of the current EMAT design over long-term operation as well. The EMAT was heated up to 500°C for 15 mins under the optimum operating conditions calculated previously and the results were unsatisfactory. Similarly, when the temperature of the specimen decreased from 500°C to 250°C with 50°C step, the temperature of the magnets remained above 200°C after 15 mins of thermal exposure. As a result, the operating conditions had to be re-calculated and selected based on the steady state thermal response of the EMAT.

Since the flow velocity can greatly affect the thermal response of the EMAT, the long-term thermal properties of the transducer were estimated, as it was heated up to 500°C for at least 15 mins and the flow velocity increased from 3 m/s to 30 m/s with 2 m/s step. In all cases, the temperature of the magnets exceeded their MOT. Hence, no variations in the flow velocity of the coolant can significantly enhance the thermal performance of this EMAT design for long term operation at 500°C.

Given the above limitations of this transducer design and the fact that the currently available high-temperature GWT monitoring systems operate up to 200°C, the EMAT was re-evaluated regarding its thermal properties over time at 250°C. The effect of flow velocity on the thermal performance of EMAT was investigated again. The EMAT was heated up to 250°C for 60 mins incrementally. The flow velocity was increased with a step of 2 m/s from 3 m/s to 15 m/s when finally the minimum

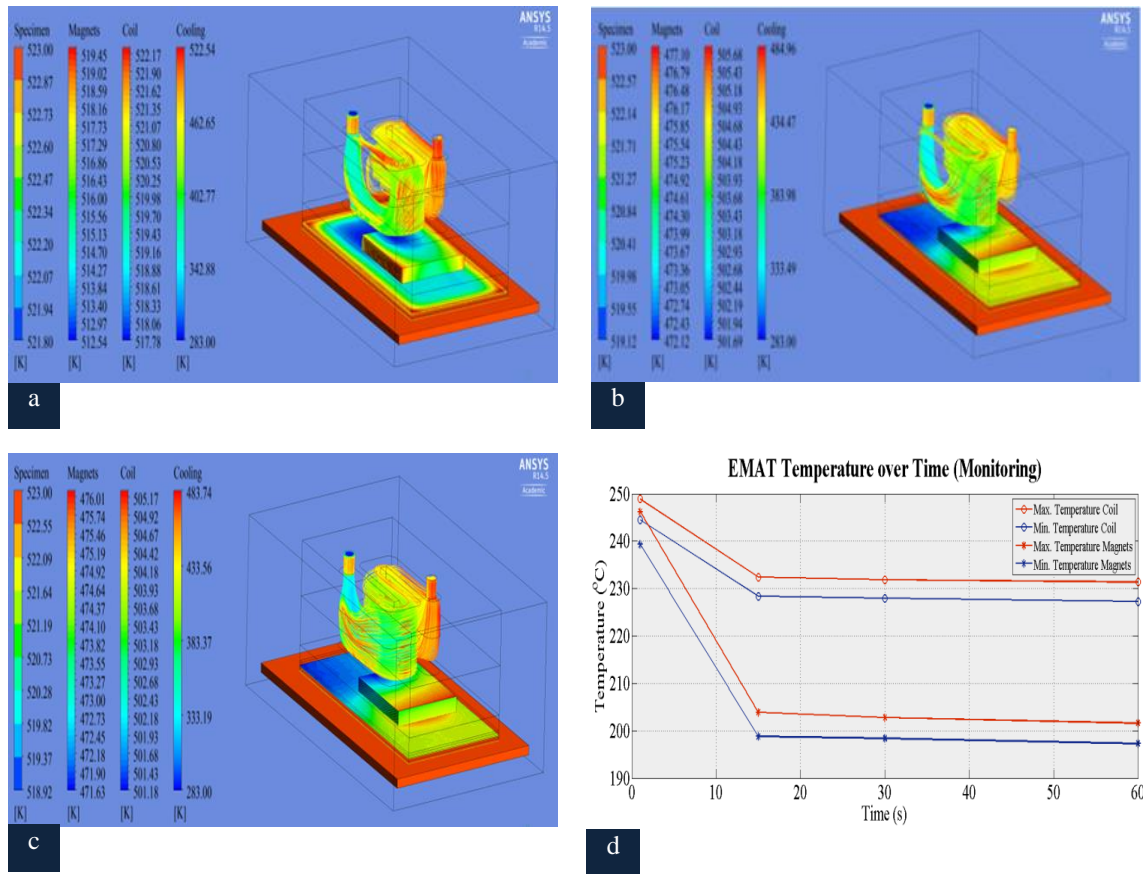


Figure 4.18. Temperature gradient of EMAT at 250°C after (a) 1min (b) 15mins (c) 30mins (d) coil and magnets temperature against operating time

temperature of the magnets essentially plateaued below 200°C over time. Figure 4.18 depicts how the temperature gradient of the EMAT altered over time and how the temperature of the EMAT components converged as the operating time increased. Figure 4.18 a-c show the temperature gradient of the EMAT at 250°C at 1 min, 15 mins and 30 mins of thermal exposure respectively, while Figure 4.18 d demonstrates how the temperature of the EMAT components dropped over time. The results obtained show that the current EMAT design required 15 mins of operation at 250°C so that the temperature of its components and more particularly its magnets would drop below their MOT and be kept constant. Especially, after 30 mins of operation, the temperature gradient of the EMAT did not alter and its thermal properties constantly met its design requirements. Similarly to previous results (Section 4.4.1), the parts of the components that are under the cooling chamber or closer to its inlet were more efficiently cooled down over time.

Consequently, this EMAT operating under the aforementioned conditions was thermally stable for at least 60 mins, whilst the minimum temperature of its essential components did not exceed their

MOT. Hence, it can be potentially employed for the GWT monitoring or long-term inspection of structures operating up to 250°C.

4.4.4 Summary

This Chapter focuses on the theoretical investigation of the wave mode purity characteristics of PPM EMAT configuration and its ultrasonic signal potential and limitations at high temperatures. FEA models were implemented for the calculation of the electromagnetic response of a room temperature EMAT attached to a stainless steel plate and their ultrasonic interaction. The results obtained from this study show that this EMAT configuration can excite SH_0 waves in the right direction according to the literature. However, S_0 and A_0 can propagate in various angles and especially in 90° angle from the SH_0 direction.

The same configuration was studied regarding its ultrasonic performance at high temperatures. This analysis showed that the currently existing EMAT technology can withstand up to 500°C, since valid information was retrieved from the model up to this temperature. However, the signal received is significantly weak and the effect of temperature rise on essential components and properties of EMAT and specimen were not taken into consideration. Consequently, the model provides a qualitative idea of the performance of the already existing technology at high temperatures. The high-temperature EMAT should be designed to counterbalance larger electromagnetic losses that those calculated.

Thermal and CFD analysis was also performed regarding the material selection, optimization of EMAT design and calculation of its optimum operating conditions against temperature rise. A detailed study of the coil structure, thermal insulation and the thickness of each material was conducted in terms of optimum thermal and ultrasonic signal properties of the EMAT. A water – cooled EMAT with constantan coil encapsulated in alumina and Kapton was investigated regarding its thermal response over time up to 500°C. The flow velocity of the coolant was proved to greatly affect the thermal properties of the transducer, on the contrary to its inlet temperature, whilst the current design can effectively withstand high temperatures with the use of water and not oil. The

final EMAT design successfully met its thermal specifications up to 500°C for short period of time (5 mins) and up to 250°C for one hour of heat exposure. The temperature of the main EMAT components remained below their MOT in both cases, indicating that the current design has the potential to successfully operate at high temperatures.

The following Chapter outlines the methodology followed for the experimental validation of the aforementioned theoretical analysis. A commercial PPM EMAT designed for room temperature was evaluated regarding its ultrasonic signal potential and limitations at room and high temperatures. The effect of autotransformer connection on the SNR and ultrasonic performance of the EMAT was also experimentally investigated. The results obtained constructed a benchmark for the experimental evaluation of the water cooled EMAT. The water cooled EMAT was developed and characterized regarding its impedance and wave mode purity characteristics.

Chapter 5

Design and Characterization of Water Cooled EMAT

5.1 Introduction

Due to limited development of high temperature EMAT, the limitations of the existing EMAT technology for this application should be experimentally investigated and utilized as a benchmark for the characterization of the water cooled EMAT. A system of commercial PPM EMATs [163] was evaluated regarding its ultrasonic signal performance and defect detection potential at room and high temperatures, up to 180°C, with and without shielding (autotransformer connection). The results of this evaluation are summarized in this Chapter. A GWT system of two water-cooled EMATs was developed and tested regarding its ultrasonic potential and limitations at room temperature. An experimental comparison between the two EMAT systems and designs was accomplished. The experimental validation of the ultrasonic FEA study presented in the previous Chapter was also accomplished. Impedance analysis and wave mode purity characterization via vibrometry tests were also performed and presented in this Chapter.

5.2 Existing Technology

5.2.1 Room Temperature Ultrasonic Evaluation

A pair of commercial PPM EMATs with the exact same design with the configuration studied in the previous Chapter was experimentally evaluated regarding its defect detection capabilities at room temperature. An experimental validation of the effect of autotransformer connection on the SNR of the signal received and the overall ultrasonic performance of the EMAT system was also performed. The effect of power input and lift-off on the performance of EMATs was investigated.

The EMATs were composed of racetrack, copper coil of 0.315mm wire diameter and two arrays of six Nd-Fe-B magnets each with 12mm pitch. They were designed for room temperature SH inspection. They were employed on the specimen in a pitch-catch configuration with 30 cm distance between them. A square, 316L stainless steel plate of 1,25m length and 3mm thickness was tested. Both defect free and areas with defects were tested. Five defects of different length and mass loss each were introduced to the specimen with 10cm distance from each other. The defect tested was 10mm long and of 66.6% mass loss and was placed in the middle of the distance between the two EMATs. Ritec RAM 5000 SNAP pulser/receiver [246] was used for driving the EMAT transmitter with a 7 cycle, Hanning windowed pulse of 256 kHz frequency. It was also used for amplifying the signal received with a gain of 80dB and filtering it within the bandwidth of 10 kHz and 20 MHz. The signal was finally collected, averaged and recorded in an oscilloscope.

The effect of the voltage difference between the EMATs and the specimen on the quality of the signal received was investigated. An additional thin, stainless steel cover was placed all around the transducers, touching both the EMATs housing and the specimen, for establishing a common ground connection (shielding) between them. In this manner, the electrical connection between the EMATs and specimen can be regarded as autotransformer. Four case studies were investigated; defect free and a defective area, with and without shielding (autotransformer connection). The influence of lift-off on EMAT response was investigated from zero to 1mm lift-off with a step of 0.1mm. A study regarding the power supply requirements of these EMATs was also accomplished by gradually decreasing the power output of Ritec with a step of 5% starting from its maximum power level (5000 Watts) and stopping at 20% of its maximum power where no useful information could be retrieved anymore from the signal received.

Figure 5.1 a shows the signal received from the defect-free area when the EMATs and the specimen did not have any common ground connection (shielding). The first reflection is the signal transmitted from the transmitter to the receiver and the other three are coming from the edges of the plate. In this case, the noise level was high and the amplitude of all the reflections was relatively low compared to the noise level, resulting in a low SNR (8dB). Figure 5.1 b shows the signal received when the defect was tested without the EMATs being shielded. Similarly to the previous

figure, the signal transmitted and the three reflections from the edges of the plate are obvious, but their amplitude was relatively small compared to the noise level. Additionally, no reflections from the defect were noticed, resulting in poor EMAT defect detection potential. Figure 5.2 a presents the signal received when the EMATs tested the defect-free area and they were shielded. The amplitude of the reflections increased three times, the noise level decreased and as a result, the SNR increased more than six times (52dB). Likewise, the signal shown in Figure 5.2 b, which corresponds to the ultrasonic signal response of shielded EMATs on the defect, exhibited higher SNR (35dB) than that of the signal shown in Figure 5.1 b. This time, both defect reflections were successfully detected and led to significantly enhanced defect detection EMAT capabilities.

The results obtained agree with theory presented in Chapter 3 where it was firstly mentioned that an autotransformer connection between EMAT and specimen (shielding) can result in SNR improvement and enhanced the ultrasonic performance of an EMAT system, due to the noise cancellation. The electromagnetic coupling between the specimen and the EMATs was proved to be weak when they were connected as a two winding transformer. The electromagnetic losses between the EMATs and the specimen were greater than in a conventional two winding transformer, since no ferrite connected the EMATs and the specimen. The air between them increased the noise level and lessened the electromagnetic coupling. When the EMAT/specimen connection performed as an autotransformer, the noise level decreased and the amplitude of the ultrasonic signal increased. Less common mode noise interfered with the EMAT receiver and thus more current was induced in the coil. Consequently, the voltage difference between the EMAT and

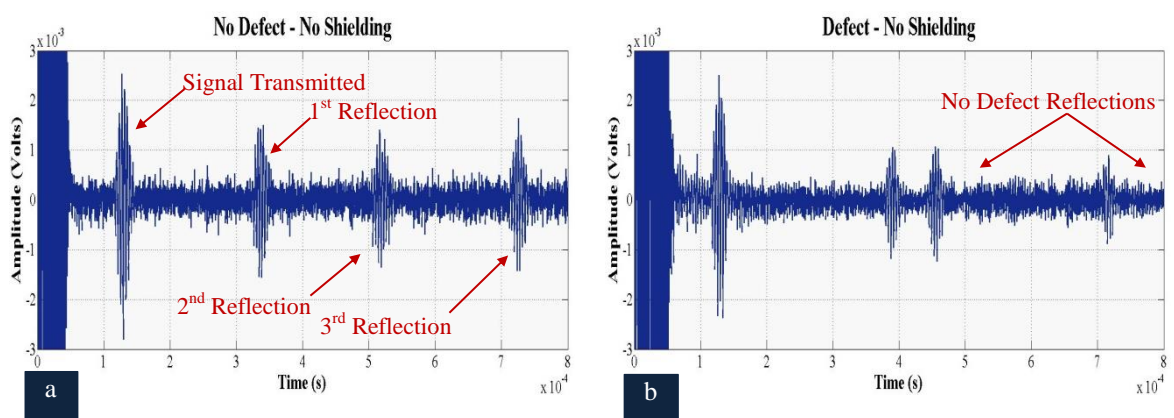


Figure 5.1. (a) Signal received from defect free area without shielding (b) Signal received from defect without shielding

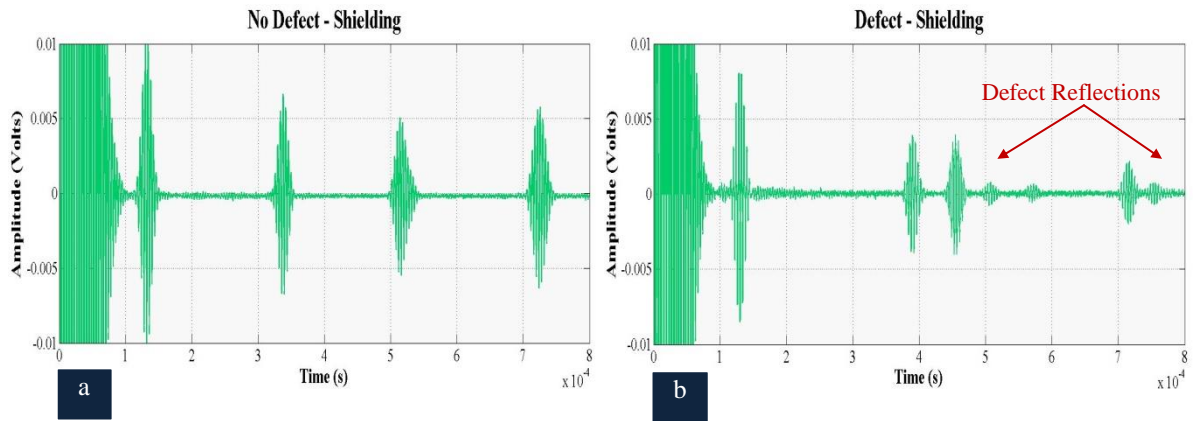


Figure 5.2. (a) Signal received from defect free area with shielding (b) Signal received from defect with shielding the specimen affects significantly the quality of the signal received and when there is no voltage difference and both components are connected to ground, the probability of defect detection increases greatly. Therefore, all ultrasonic results presented below correspond to shielded EMAT systems.

The results obtained also confirm that the frequency selected based on the size defect and the dispersion curves was suitable for the detection of 10mm long defect. The ToF of the reflections matched with the SH_0 velocity, as it was calculated from the dispersion curves. The experimental results agreed with literature based on which PPM EMAT receivers are sensitive to SH_0 . However, still it cannot be confirmed that the EMAT transmitter did not excite multiple wave modes that were not detected by the EMAT receiver.

The blue line in Figure 5.3 shows how the normalized amplitude of the signal transmitted changed with respect to lift-off. It decreased almost exponentially and especially when lift-off was equal to 1mm no reflections coming from the edges of the plate were noticed, arising questions about the maximum length of inspection that can be achieved under these conditions. As a result, this EMAT

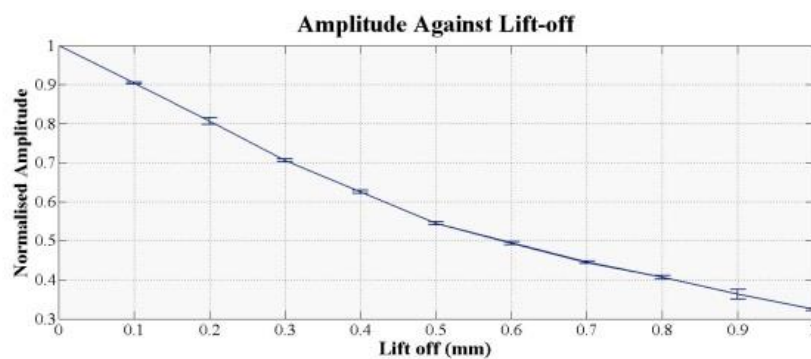


Figure 5.3. Room temperature PPM EMAT: Amplitude against lift-off

configuration can be efficiently employed for GWT with less than 1 mm lift-off from the specimen. EMAT for GWT exhibit higher lift – off limitation compared to EMAT designed for other applications [242]. A parameter that influences its performance against lift-off is the impedance of the coil. The impedance changes with lift-off as well as with the material properties of the specimen. The self – inductance of the coil decreases with lift-off decrease, while the mutual inductance between the EMAT and specimen increases. Both lead to variations in the overall impedance of the coil. Additionally, the parasitic capacitance between the transducer and the plate alters with lift-off and contributes further to impedance changes. A detailed analysis of the EMAT impedance against several operating parameters including lift-off follows in the next subsection. At this point, it should be highlighted that lift-off increase results in impedance variations that should be counterbalanced with the use of impedance matching circuit.

An experimental evaluation of this system regarding its power requirements was also conducted. The power level decreased gradually from 100% to 20% with a step of 5%; as no useful information could be retrieved from the signal received when the power level was smaller than 20%. Figure 5.4 shows how the normalized amplitude of the signal transmitted increased with power supply increase. It can be observed that the amplitude increased almost linearly. Similarly, with lift-off, the impedance of the coil affects the power requirements of EMAT system. If the pulser/receiver unit drives the EMAT transmitter through an output resistor, the impedance of the coil should be equal to the output impedance of the pulser unit, so that the voltage drop in the coil will be minimized. Therefore, impedance matching is always required, so that the coil is driven with the maximum power possible and strong signals are obtained. Nevertheless, the power requirements of EMAT transducers remain high, leading to the conclusion that EMATs are more

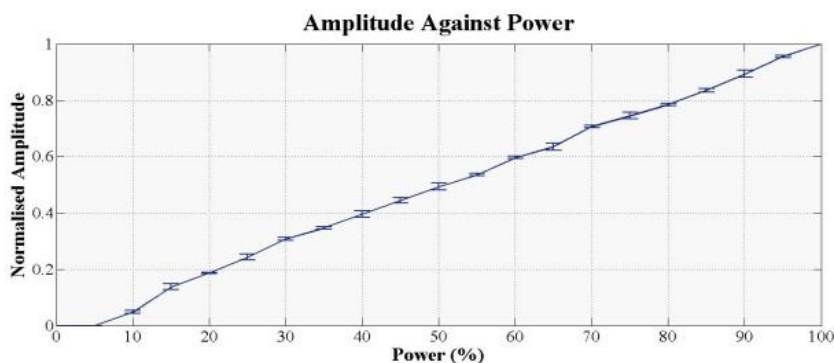


Figure 5.4. Room temperature PPM EMAT: Amplitude against power supply

efficient as receivers rather than transmitters in terms of power requirements.

5.2.2 High-Temperature Ultrasonic Evaluation

According to the literature, high-temperature EMATs have been designed so far only for thickness measurements [231-235] and thus, an EMAT that can withstand high temperatures and be suitable for GWT is still required. An approach for that would be the material selection and calculation of the optimum operating conditions for the development of a novel high-temperature EMAT for GWT. However, a benchmark for the experimental evaluation of the new EMAT is also needed. Thus, further study regarding the high-temperature performance of the already existing EMAT technology for GWT had to be conducted prior to the design of the new EMAT.

The room temperature EMAT system was tested from ambient temperature to 180°C with a step of 10°C. The two EMATs were tested only up to 180°C, because their ultrasonic signal response had worsened significantly at this temperature and any further temperature increase would possibly cause a serious and irreversible damage to them. The EMATs were continuously exposed to heat with zero lift-off for 15 minutes and were employed again in a pitch-catch configuration of 30 cm distance and with the 10mm long defect in the middle, as shown in Figure 5.5. A three phase heating unit manufactured by STORK [247] was utilized for the temperature rise of the specimen. This set of experiments was conducted three times. Figure 5.6 a-d show the signal received at room temperature, 60°C, 100°C and 180°C respectively. In the signal obtained at room temperature both



Figure 5.5. High temperature experimental set-up (a) EMATs attached upon specimen (b) electrical instrumentation - RITEC (c) thermal instrumentation

the reflections from the plate edges and the first two reflections from the defect were clear. However, it is obvious that the amplitude of the signal received diminished greatly after 60°C, since the signal transmitted and the second reflection coming from the plate decreased 25% and 75% respectively at 60°C. Especially, at 100°C and 180°C the second reflection of the plate edge was hardly noticed. The divergence in the impact of temperature rise on different reflections is due to the non-uniform heating of the specimen. There were areas whose temperature was largest than others and therefore the temperature rise effect was more noticeable on the reflections propagating to them. Similarly, the amplitude of the defect reflections decreased greatly after 60°C (98%) and no valid information could be retrieved at 100°C and 180°C. Both observations lead to the conclusion that the current EMAT technology cannot be efficiently employed at elevated temperatures, since both the inspection of length and the defect detection potential deteriorated greatly after 60°C. The industrial applicability of the transducers becomes questionable for temperatures higher than 100°C. In all cases, all reflections shifted in time, as it was expected. However, due to imperfections in the experimental setup and more especially in the mechanism used for the heating of the plate, the area inspected was not uniformly heated up and therefore the reflections did not exhibit the same shifting in time. The third reflection from the plate shifted more

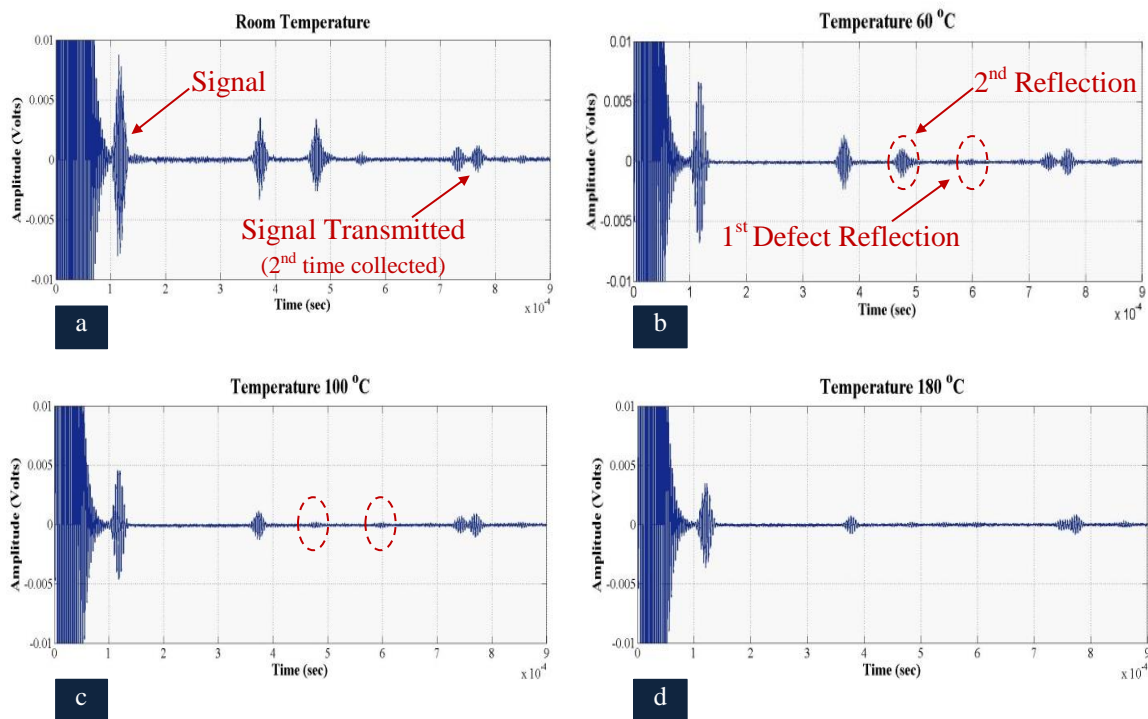


Figure 5.6. Signal received at (a) room temperature (b) 60°C (c) 100°C (d) 180°C

in time compared to the signal transmitted when it was received for the second time, as it can be noticed in Figure 5.6 d, and it could lead to complicating signal interpretation.

Figure 5.7 shows how the amplitude of the signal transmitted decreased with temperature rise; it is clear that the amplitude decreased almost linearly with temperature rise. However, the amplitude of the signal transmitted in 30°C and 40°C was slightly larger than that at room temperature in the area marked in red in Figure 5.7. Also, the amplitude error altered with temperature rise. A reason for that can be the ground connection between the EMAT and the specimen. The thermal conductivity of stainless steel is low and therefore the specimen was not heated up uniformly. As a result, the plate deformed and the mechanical connection between the EMAT ground and the specimen altered with temperature rise due to the gradient of the bend. This mechanical/electrical connection influenced significantly the amplitude of the signal transmitted and thus it can be the reason for the amplitude increase at 30°C and 40°C. Based on the conclusions made from the previous figure, the EMAT performance started decreasing substantially at 60°C and its industrial reliability and applicability started being questionable after 100°C. Although the amplitude of the signal transmitted was still 75% and 56% of its maximum value at 60°C and 100°C respectively, still the overall energy propagating at these temperatures was not enough for the reliable structural integrity assessment of the sample. Hence, the room temperature EMATs cannot be used for the inspection or monitoring of high-temperature structures (>100°C). However, the performance of a new EMAT system specifically designed for GWT at high temperatures (>200°C) should be compared with that of this room temperature EMAT system up to 100°C.

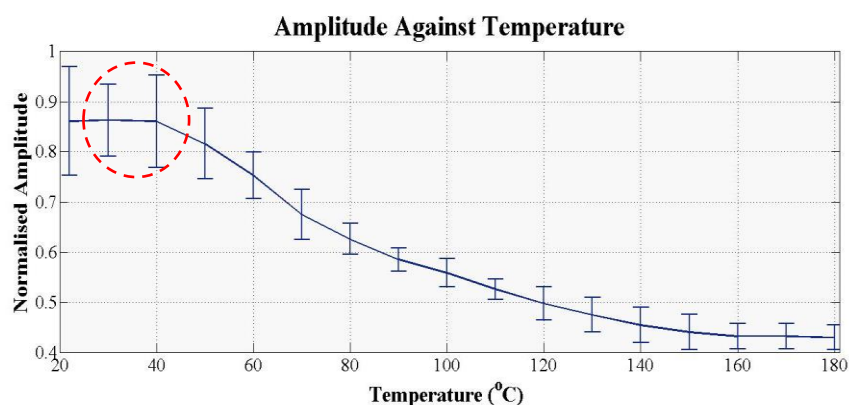


Figure 5.7. Room temperature PPM EMAT: Amplitude against temperature rise

5.3 Water Cooled EMAT for High-Temperature GWT

5.3.1 EMAT Design

The water cooled EMAT was designed and manufactured based on the numerical simulations carried out in Chapter 4 and is shown in Figure 5.8. All housing components were made of brass and both Nd-F-B and SmCo magnets were used and arranged in a PPM configuration. The CAD design and dimensions (mm) of the EMAT are shown in Figure 5.8 a whilst the final EMAT prototype is depicted in Figure 5.8 b. Figure 5.9 a shows the racetrack coil without either alumina or Kapton encapsulation, while Figure 5.9 b depicts the underside view of the constantan coil, as it was encapsulated in alumina within two Kapton layers and a thermocouple. The coil was hand wound, since the current Printed Circuit Board (PCB) technology does not allow the manufacturing of a PCB constantan coil fully encapsulated in alumina and Kapton that can operate up to 500°C. The wire diameter was 0.4 mm and the thickness of each alumina layer was 0.8 mm. The Kapton layer was 0.1 mm thick and its melting point was 400 °C. If a single Kapton layer of this thickness was not thermally efficient for impeding the heat transfer, more layers could be added to the structure until the total thickness of Kapton encapsulation was 1 mm at each side. Care had to be taken when the temperature exceeded 350 °C, since the melting point of Kapton is 400 °C.

The EMAT was designed so that the coil could be replaced easily and coils of different shape and/or material could be connected to the rest of the transducer. Thus, the coil was firstly designed so that its ends would be connected to crimp connectors that allowed it to be easily disconnected from the rest of the housing. Additionally, only one end of the coil was needed to be connected to

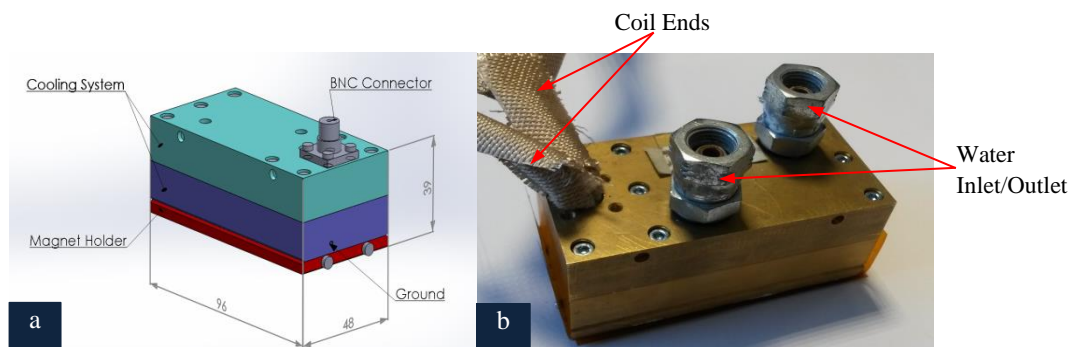


Figure 5.8. (a) EMAT design and dimensions in mm (b) EMAT prototype

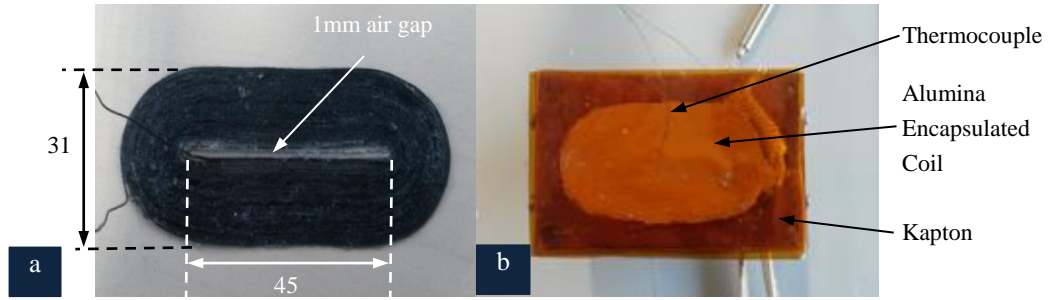


Figure 5.9. (a) Constantan Coil (b) Alumina & Kapton encapsulated coil (in mm)

the signal carrier, while the other end could be directly attached to the housing of the transducer and establish the ground connection. Thus, an extra hole was designed on the housing of the transducer for the mechanical attachment of the wire on it, as Figure 5.8 a shows. However, no crimp connectors withstanding up to 500°C for continuous operation are currently available. Therefore, this approach can be followed for EMATs designed for lower temperatures like 250°C. Alternatively, the coil ends were extended so that a commercial BNC connector, whose MOT was below 500 °C, could be used and placed further away from the heat source.

The experimental characterization of the new EMAT in terms of its impedance and wave purity profile was conducted. The results obtained are outlined in the following sections.

5.3.2 Impedance Analysis

The EMAT was firstly evaluated regarding its impedance under several conditions. As it was mentioned in Chapter 3, the impedance of EMAT alters with and without the presence of specimen as well as with magnets, coil structure, lift-off and temperature. Therefore, a detailed study regarding the impedance profile of the new EMAT prototype was performed prior to its ultrasonic evaluation and was also correlated to the latter.

As it was cited in both Chapter 3 and 4, constantan suffers from larger resistivity ($49 \cdot 10^{-8} \Omega\text{m}$) compared to copper, resulting in larger EMAT impedance and possibly limited ultrasonic performance, if the two coils are identical. Additionally, given that eddy current induced on the magnets attached onto the coil results in the appearance of eddy current on the coil and further impedance drop, hence the EMAT impedance was measured with and without magnets. Alumina encapsulation also is expected to influence the EMAT impedance and especially its phase, since

alumina can alter the inter-winding capacitance of the coil. Agilent 4294A impedance analyzer [248] was utilized for the impedance measurements. A racetrack, copper coil of 0.4mm wire diameter and 30 turns and identical constantan coil were tested. Two arrays of six Nd-Fe-B magnets each were attached onto constantan coil for the evaluation of magnets effect on coil impedance. The impedance of the water cooled EMAT with alumina encapsulated, constantan coil was finally measured, when the EMAT was not in proximity of any electrically conductive material. Table 5.1 summarizes the results obtained from the preliminary EMAT impedance analysis. The results matched with theory, since the impedance of constantan coil was larger compared to copper coil and especially its resistance was three orders of magnitude larger. The magnets reduced the overall impedance and inductance of the coil, due to eddy current, but the ceramic encapsulation attributed lift-off between the coil and the magnets and led to eddy current reduction, inductance increase and capacitance decrease. The magnets effect was noticeable, but it was partially tackled with the use of ceramics that eliminated the inter-winding capacitance as well. Nevertheless, the impedance analysis shows that the EMAT cannot operate as an ideal inductor and substantial electromagnetic losses can occur if an impedance matching circuit is not utilized between the EMATs and the pulser/receiver unit. The effect of the electromagnetic properties of the specimen on EMAT impedance was also experimentally studied. The EMAT impedance was measured when the transducer was attached onto 316L stainless steel and mild steel plate with the lift-off being increased from 0 mm up to 1.5mm with 0.5mm step. Table 5.2 and 5.3 outline the

Table 5.1 Preliminary EMAT impedance analysis at room temperature

Case	Impedance	Resistance	Inductance	Capacitance
	(Ω)	(Ω)	(μ H)	(pF)
Copper Coil	61 \angle 90.9	0.014	37.3	41.7
Constantan Coil	70.7 \angle 60.2	19.8	35.3	94
Magnets & Constantan Coil	36.4 \angle 45.9	25.4	13.6	40
EMAT (Air)	35.1 \angle 51.78	21.5	15.4	26.2

Table 5.2 EMAT impedance against material properties of specimen at room temperature

Material	Impedance	Resistance	Inductance	Capacitance
	(Ω)	(Ω)	(μH)	(pF)
Air	35.1 \angle 51.78	21.5	15.4	26.2
Mild Steel	32.72 \angle 43.29	24.2	11.3	93.2
316L Stainless Steel	28.29 \angle 41.5	21.4	10.4	51.4

Table 5.3 EMAT impedance against lift-off at 256 kHz at room temperature

Material	Lift-off	Impedance	Resistance	Inductance	Capacitance
	(mm)	(Ω)	(Ω)	(μH)	(pF)
Mild Steel	0	32.72 \angle 43.29	24.2	11.3	93.2
	0.5	32.9 \angle 44.6	23.6	12	66
	1	33 \angle 45.79	23.3	12.5	54.19
	1.5	33.3 \angle 46.8	22.9	13	45.15
Stainless Steel	0	28.29 \angle 41.5	21.4	10.4	51.4
	0.5	29.4 \angle 43.9	21.3	11.4	39.8
	1	30.33 \angle 45.6	21.2	12.14	34.65
	1.5	31 \angle 46.8	21.3	12.7	32

results obtained from this part of the impedance analysis. As it was expected, the EMAT impedance and inductance decreased with the presence of electrically conductive materials and especially with paramagnetic material. The eddy current losses occurred due to the presence of specimen resulted in inductance drop, whilst in ferromagnetic materials, this drop was counterbalanced by the relatively large mutual inductance between the EMAT and the specimen.

Nevertheless, the capacitance was greater when the EMAT was attached onto mild steel compared to stainless steel. Consequently, the EMAT should perform more efficiently when it is attached to mild steel, as literature also confirms [242]. However, the noise level can be also higher due to larger parasitic capacitance. Moreover, lift-off increase led to impedance and inductance increase and parasitic capacitance drop. As the distance between the EMAT and specimen increased the mutual inductance between them dropped and the EMAT tended to operate as an inductor instead of a transformer. Thus, the EMAT impedance converged to EMAT self-inductance as lift-off increased. Capacitance is a critical quantity that greatly affects the EMAT performance, since it contributes to losses. The above measurements shed light on the effect of various parameters on the overall EMAT impedance, including its total capacitance. Additional measurements were taken regarding the parasitic capacitance between the EMAT and the specimen for both mild steel and stainless steel as the lift-off increased. The parasitic capacitance was larger when the EMAT was attached onto mild steel compared to stainless steel and it lessened with lift-off increase, as it is shown in Table 5.4.

The EMAT impedance was also measured at high temperatures. The analysis was performed from

Table 5.4 Parasitic capacitance between EMAT and specimen (room temperature)

Material	Lift-off	Parasitic Capacitance
	(mm)	(pF)
Mild Steel	0	50
	0.5	45.4
	1	42.25
	1.5	40
Stainless Steel	0	46.49
	0.5	41.98
	1	38.48
	1.5	36.25

ambient temperature up to 250°C with 50°C step on stainless steel and mild steel at 0 mm and 1mm lift-off. The experiments were conducted three times. Figure 5.10, 5.11 and 5.12 show how the normalized EMAT resistance, inductance and capacitance altered respectively with temperature rise for stainless steel and mild steel at 0mm and 1mm lift-off. As it was expected, resistance increased linearly with temperature and it was larger when the EMAT was employed on mild steel compared to stainless steel. Similarly, inductance increased with temperature in a linear fashion. Although no universal formula linking the magnetic permeability of either stainless steel or mild steel and temperature is available, all four inductance quantities followed the same trend. EMAT inductance increased when the transducer was employed on mild steel due to the stronger electromagnetic coupling between them. However, as the temperature rose the electromagnetic coupling between the EMAT and the sample lessened and their mutual inductance decreased. A Large part of the electromagnetic energy produced by the EMAT was not transferred to the specimen and their transformer connection weakened with temperature rise. Consequently, the EMAT coil tended to operate as a mere inductor as temperature increased, instead of the primary winding of a transformer, and its inductance converged to its self-inductance value, as it is shown in Figure 5.11. EMAT capacitance also increased with temperature rise and altered with material properties of the specimen. As Table 5.3 also confirms, EMAT capacitance doubled when the transducer was attached with no lift-off on mild steel compared to stainless steel and remained larger at 1mm lift-off as well. From all the above, the overall EMAT impedance increased with temperature rise and could result in deterioration of the ultrasonic performance of EMAT at high temperatures and drop of the SNR of the signal received. Nevertheless, in all cases the percentage of increase of all these electric values did not exceed 15%, indicating that although the amplitude of the signal received will be noticeably reduced as temperature rises, still the EMAT will manage to operate at least up to 250°C.

The wave purity characterization of the new PPM EMAT is equally important to its impedance analysis. Thus, its detailed vibrometry evaluation was performed and analyzed in the following section.

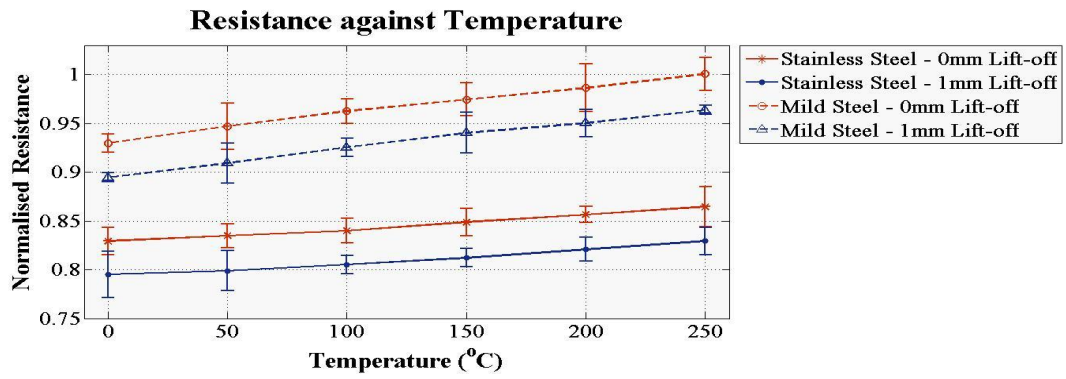


Figure 5.10. Resistance against temperature rise

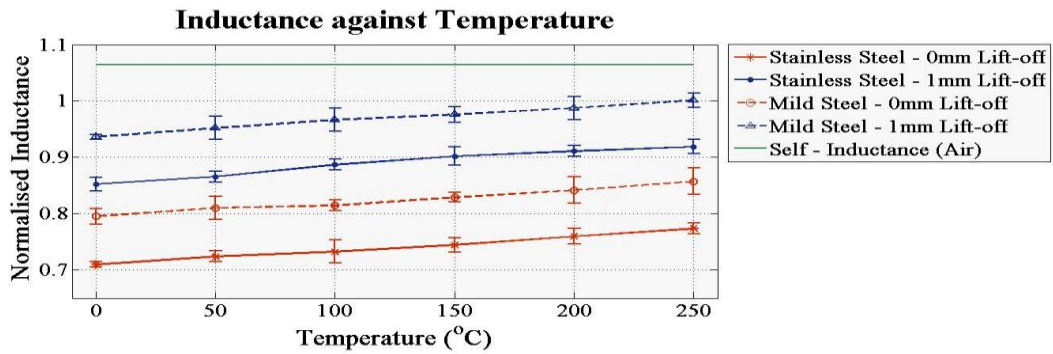


Figure 5.11. Inductance against temperature rise

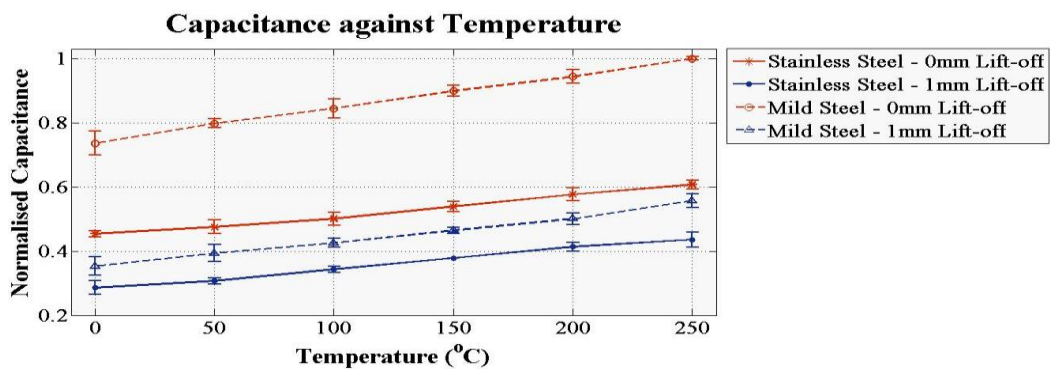


Figure 5.12. Capacitance against temperature rise

5.3.3 Wave Mode Purity Characterization

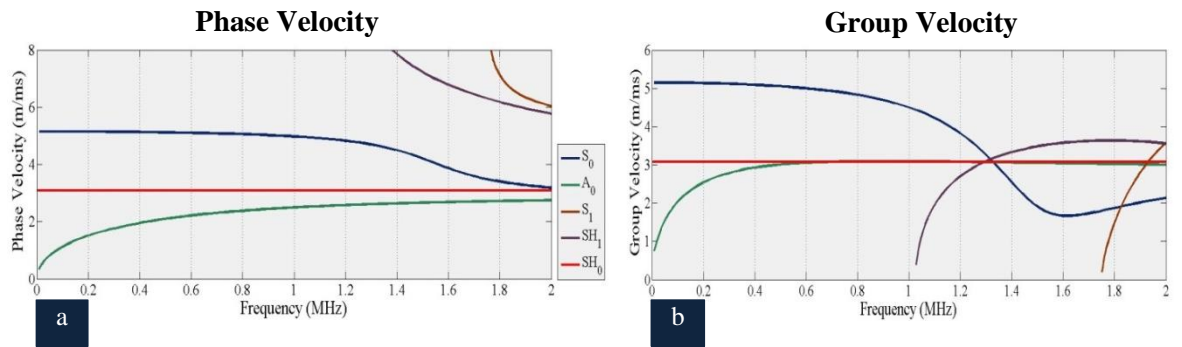
In Chapter 4 a theoretical analysis regarding guided wave propagation and wave mode purity properties of PPM EMAT was presented. Based on this, PPM EMATs are suitable for excitation of SH_0 , however, their wave mode purity characteristics are poor. S_0 and A_0 wave modes can also be

excited and propagate in several angles. The transducers designed for GWT should desirably exhibit high wave mode purity characteristics so that the signal interpretation will be simpler and result in accurate and reliable conclusions. Hence, a wave mode purity experimental characterization of PPM EMAT was required prior to its ultrasonic evaluation.

Laser Doppler Vibrometry (LDV) is an NDT technique that allows the accurate measurement of vibrations occurring on samples whose surface is highly reflective and can be scanned by lasers. It is an optical technique whose function relies on Doppler effect as most of the optical techniques also do, like interferometry. A laser beam is split into two, reference and test beam, where the latter directs to the specimen. The test beam scatters and a portion of it reflects back to the vibrometer. Both beams are finally collected by a photo-detector and analyzed regarding their phase difference which can result in the estimation of the velocity of any vibration or wave propagating in the specimen. LDV has been utilized in several scientific fields and industries, like medical, automotive and acoustics [249-254]. In the current study, LDV was used for the wave purity characterization of the water cooled, PPM EMAT.

Based on the FEA results presented in Chapter 4, PPM EMAT can generate in-plane and out-of-plane displacement propagating in several angles, with S_0 , A_0 and SH_0 velocity. Especially, in a 3mm thick stainless steel plate, it is relatively perplexing to clearly discriminate SH_0 and A_0 even at 0° where only SH_0 is expected to propagate, due to the small difference between SH_0 and A_0 group velocity. However, dispersion curves alter with plate thickness and more particularly they shift to the right with thickness decrease as Figure 5.13 confirms. As a result, the difference in SH_0 and A_0 group velocity increases with plate thickness decrease. Hence, the wave mode purity characterization of the EMAT was performed for stainless steel plates of variant thickness. Moreover, the FEA model introduced in the previous Chapter, took into consideration only Lorentz force while in ferromagnetic materials, like mild steel, magnetostriction also occurs and can alter the wave mode purity profile of the transducer. Thus, the EMAT was characterized regarding its wave mode purity against the material properties of the specimen as well. Any divergence between the results obtained from stainless steel and mild steel and between the experimental and theoretical values derived from the contribution of magnetostriction in wave generation.

1.5mm thick Stainless Steel Plate



0.5mm thick Stainless Steel Plate

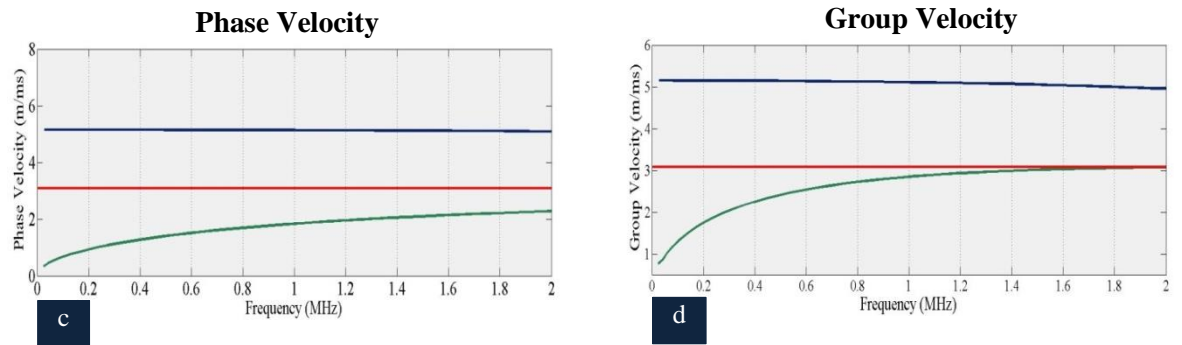


Figure 5.13. Dispersion curves (a) phase velocity of 1.5 mm thick stainless steel plate (b) group velocity of 1.5 mm thick stainless steel plate (c) phase velocity of 0.5 mm thick stainless steel plate (d) group velocity of 0.5 mm thick stainless steel plate

A 3D scanning laser vibrometer manufactured by Polytec [255] was utilized for the measurement of the wave displacement generated by the water cooled, PPM EMAT. This type of vibrometer can estimate the velocity of the wave propagating in all three coordinates and it can automatically scan entire areas of single target – points. The EMAT was evaluated regarding its wave purity characteristics on both stainless steel and mild steel. Three square, 316L stainless steel plates of 1m length and thickness of 3mm, 1.5mm and 0.5mm respectively and a square, mild steel plate of 1m length and 3mm thickness were inspected. Figure 5.14 shows the experimental setup used. The EMAT was employed in the middle of the plate and was driven by Ritec RAM 5000 SNAP with 10 cycle, 256 kHz AC current pulse of 30A. As the EMAT was designed specifically for a 3mm thick, 316L stainless steel plate, a full wave mode purity profile was obtained when the transducer was employed on this plate. Therefore, the vibrometer scanned a circular area of 65 reception points evenly distributed in 30cm distance from the center of EMAT with 5° angle between the points. As it is obvious in the figure, seven points are missing in the bottom arc of the circular scanning area, due to the vertical EMAT holder. Therefore, no information about the wave propagation at this area could be retrieved from the experimental results and it should be assumed that the EMAT

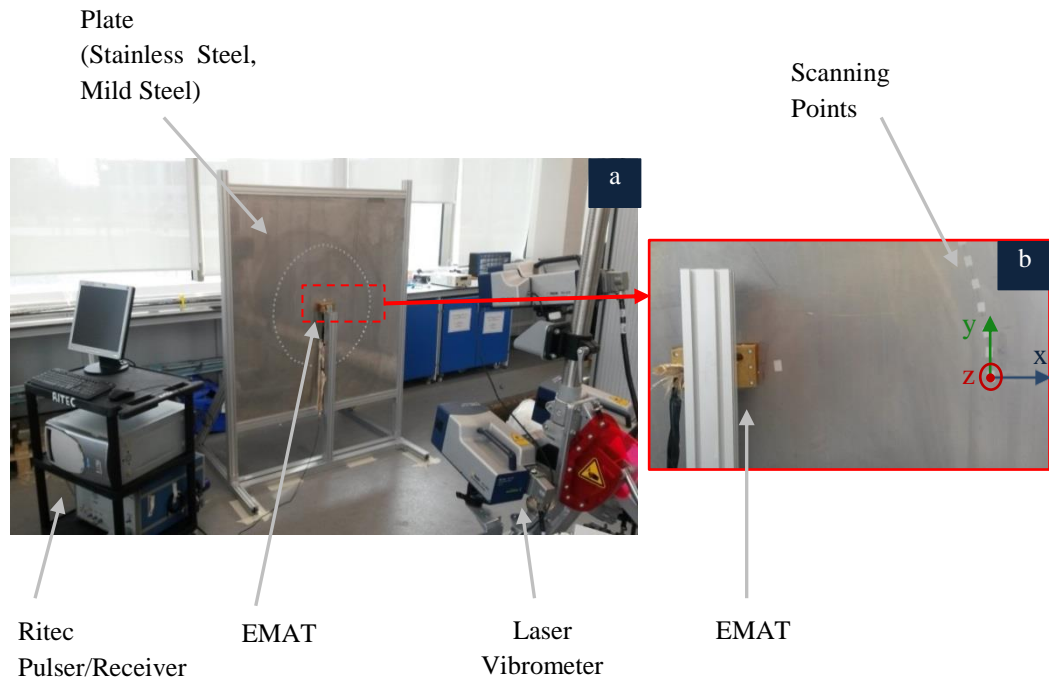


Figure 5.14. (a) Experimental setup of vibrometry tests (b) zoom in to EMAT and scanning area

performance was approximately symmetrical. Based on this assumption, in the rest of experiments, the area of interest that the lasers scanned was only the top right quarter of the circle. This simplification allowed reduction of time required for the completion of the experimental procedure, while still cogent comparisons and conclusions could be made out of this analysis with no resolution decrement.

The polar plots shown in Figure 5.15 a-c represent how the x, y and z displacement generated by PPM EMAT in 3mm thick stainless steel plate altered respectively all around the transducer, as they were received at 59 μsec and the polar plots in Figure 5.15 d-f show the same quantities measured at 97 μsec . Although the trend in all polar plots did not fully match with that the theoretical values followed (Figure 4.6 and 4.7), still the results matched overall. The largest portion of the energy introduced to the plate yielded in-plane displacement whose amplitude maximized at 180° and 0° in y-axis when it was gated at 97 μsec , as Figure 5.15 e shows. This indicates that the transducer mostly generated in-plane displacement propagating with SH_0 velocity at the same angle SH_0 was expected to propagate. However, EMAT response was not fully symmetrical, since the amplitude of y displacement was not the same at 0° and 180° . As it was expected any imperfections attributed to the coil during its manufacturing resulted in the non-symmetrical ultrasonic signal performance of the EMAT. However, a considerable y displacement

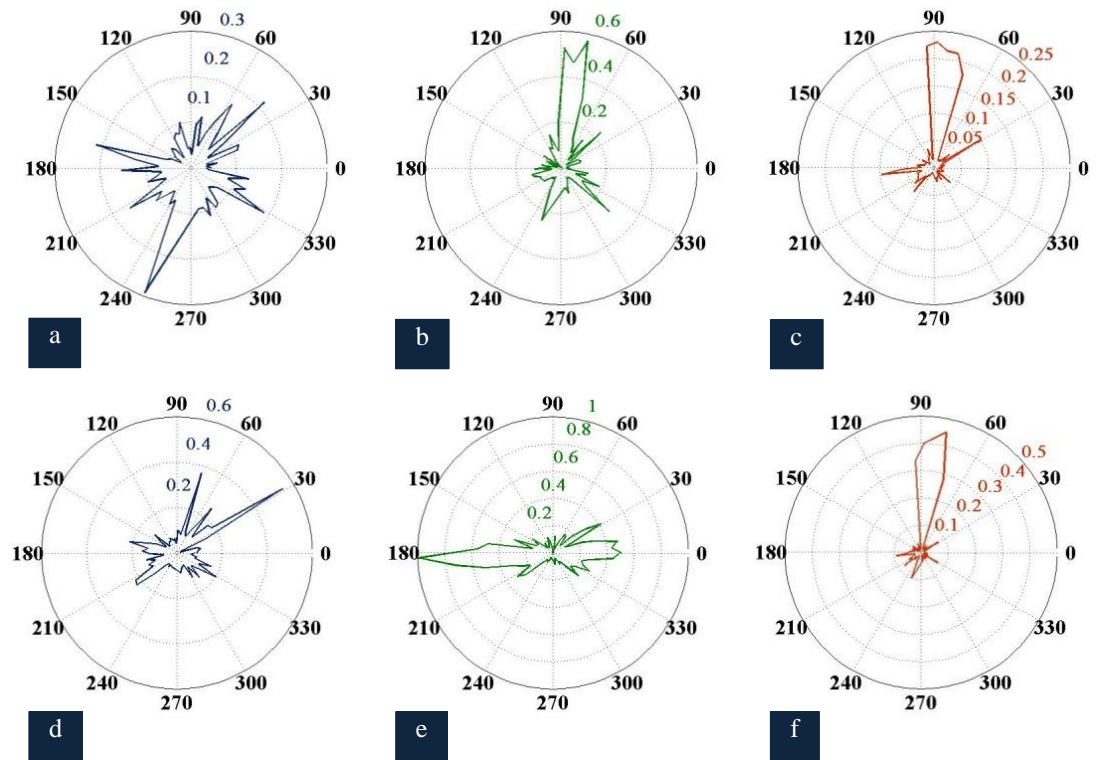


Figure 5.15. Wave mode purity plots for 3mm stainless steel plate. Displacement in (a) x axis (b) y axis (c) z axis at 59 μ sec (d) x axis (e) y axis (f) z axis at 97 μ sec

was detected at 90° at 59 μ sec as well and is shown in Figure 5.15 b, denoting that S_0 wave mode was also generated. In all cases, the z component of displacement maximized at 90° (Figure 5.15 c and f) as the FEA results also show and its amplitude was comparable to that of y component. As a result, both S_0 and A_0 were propagating simultaneously with SH_0 . By contrast with the y and z displacement components, no clear conclusions were retrieved from the x component in Figure 5.15 a and f. Although its maximum was noticed approximately between 30° and 60° , partially matching with the FEA results, no information was obtained regarding the discrimination of A_0 from SH_0 . In all cases, the experimental values agreed with the theoretical results, apart from the z component of the S_0 displacement whose measured amplitude was approximately double the value obtained from FEA in section 4.2.3.

Figure 5.16 a-d depict the x, y and z displacement received at 180° plotted all together and each one individually. Although the noise level was relatively high at x and z-axis, there were still two reflections coming at 59 μ sec and 97 μ sec in both cases, denoting S_0 and A_0 propagation, whose amplitude, though, was considerably lower than that of the y displacement gated at 97 μ sec and corresponding to SH_0 . Despite the reflection gated at 97 μ sec in z-axis, that could correspond to A_0

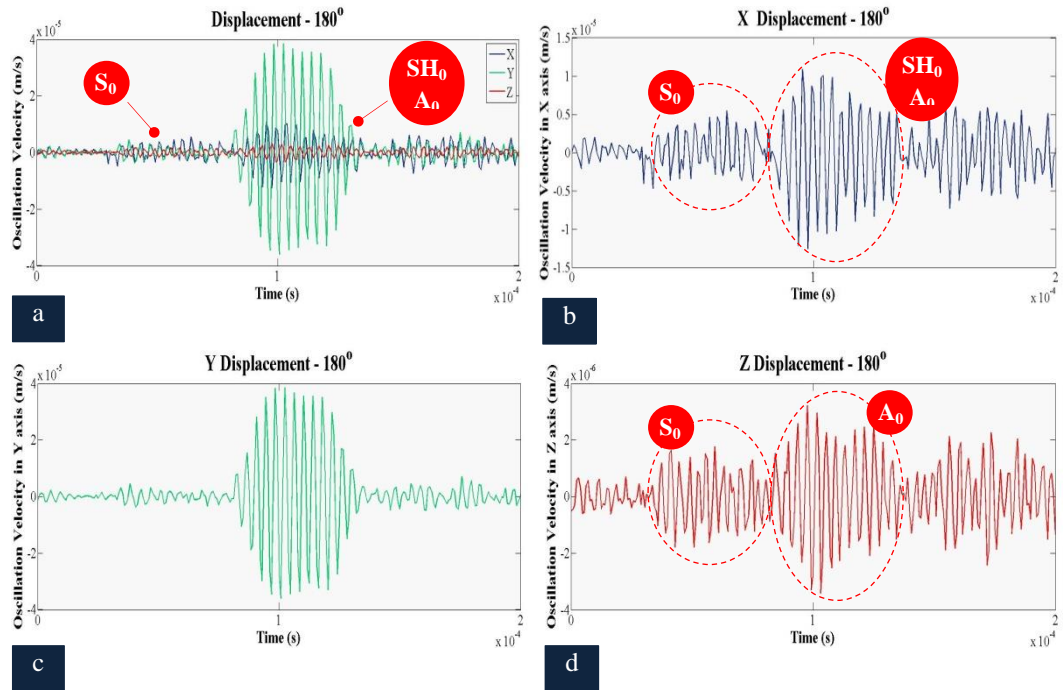


Figure 5.16. Displacement at 180° in 3mm thick stainless steel plate in (a) all axes (b) x axis (c) y axis (d) z axis

wave mode, still no cogent conclusions could be made regarding A_0 propagation. Consequently, the EMAT mainly generated SH_0 [25, 27], as it is also stated in the literature. However, out-of-plane displacement was also excited and propagated with S_0 velocity and possibly A_0 velocity as well, resulting in the poor wave mode purity characteristics of this EMAT configuration. Further experimental investigation was conducted for final quantification of the possibility of this EMAT to excite A_0 wave mode as well. The following results show the wave mode purity properties of the same EMAT as it was attached onto thinner stainless steel plates of 1.5mm and 0.5mm thickness.

As it has been already mentioned, dispersion curves shift to the right with thickness decrease resulting in larger difference in the group velocity between SH_0 and A_0 . As their velocity difference increases, it becomes more likely for A_0 to be distinctly received and distinguished from SH_0 . Table 5.5 summarizes the phase and group velocity of SH_0 , S_0 and A_0 against plate thickness at 256 kHz. Figure 5.17 a-c, d-f and g-i show how the x, y and z displacement received at 58 μ sec, 97 μ sec and 111 μ sec respectively changed from 0° to 90° when the EMAT was attached to 1.5 mm thick stainless steel plate. Similarly, Figure 5.18 a-c, d-f and g-i depict the same quantities when the EMAT was employed on 0.5 mm thick stainless steel plate and were measured in time accordingly. In both cases, the transducer operated in a similar manner and the results matched with both the theoretical and experimental values obtained from the 3mm thick stainless steel. The largest portion

Table 5.5 Phase and group velocity against plate thickness at 256 kHz

Thickness (mm)	Phase Velocity (m/s)			Group Velocity (m/s)		
	SH ₀	S ₀	A ₀	SH ₀	S ₀	A ₀
0.5	3080	5041	1100	3080	5147	1900
1.5	3080	5145	1648	3080	5128	2680
3	3080	5118	2110	3080	5047	3013

of the energy transferred to the specimen led to the appearance of in-plane displacement propagating at the same angle and velocity with SH₀. On contrary to the experimental results obtained from 3mm thick stainless steel plate, all three wave modes were clearly distinguished and no overlapping occurred as the plate thickness decreased, as Figure 5.19 and 5.20 also show. The displacement corresponding to S₀ presented the same spatial characteristics regardless of the thickness of the plate and the amplitude of its y and z component maximized at 90° whilst x component was mainly present between 30° and 70°. Although, the y component of SH₀ displacement maximized at 0° and considerable displacement was also observed at x-axis as well at the same angle, oscillations were noticed at x and y-axis from 30° to 60°. Despite the clear distinction of all three wave modes, still A₀ must have affected SH₀ propagation, due to its dispersive nature. A portion of A₀ energy interfered with SH₀, resulting in vibrations in all three directions propagating with SH₀ velocity but at a different angle from that SH₀ was expected to propagate. Nevertheless, the out-of-plane displacement remained significantly lower compared to y displacement and thus it can be neglected. Moreover, the y and z component of A₀ reflection followed the same trend with S₀ and maximized at 90°, while its x displacement appeared within 30° and 70°. Especially when the EMAT was attached on the 0.5 mm thick plate, x and y displacement corresponding to A₀ was noticed below 30° as well. However, both S₀ and A₀ displacement exhibited greatly smaller amplitude compared to SH₀ in all three coordinates (at least one order of magnitude), when the EMAT was attached on the thinner plate. Therefore, the wave

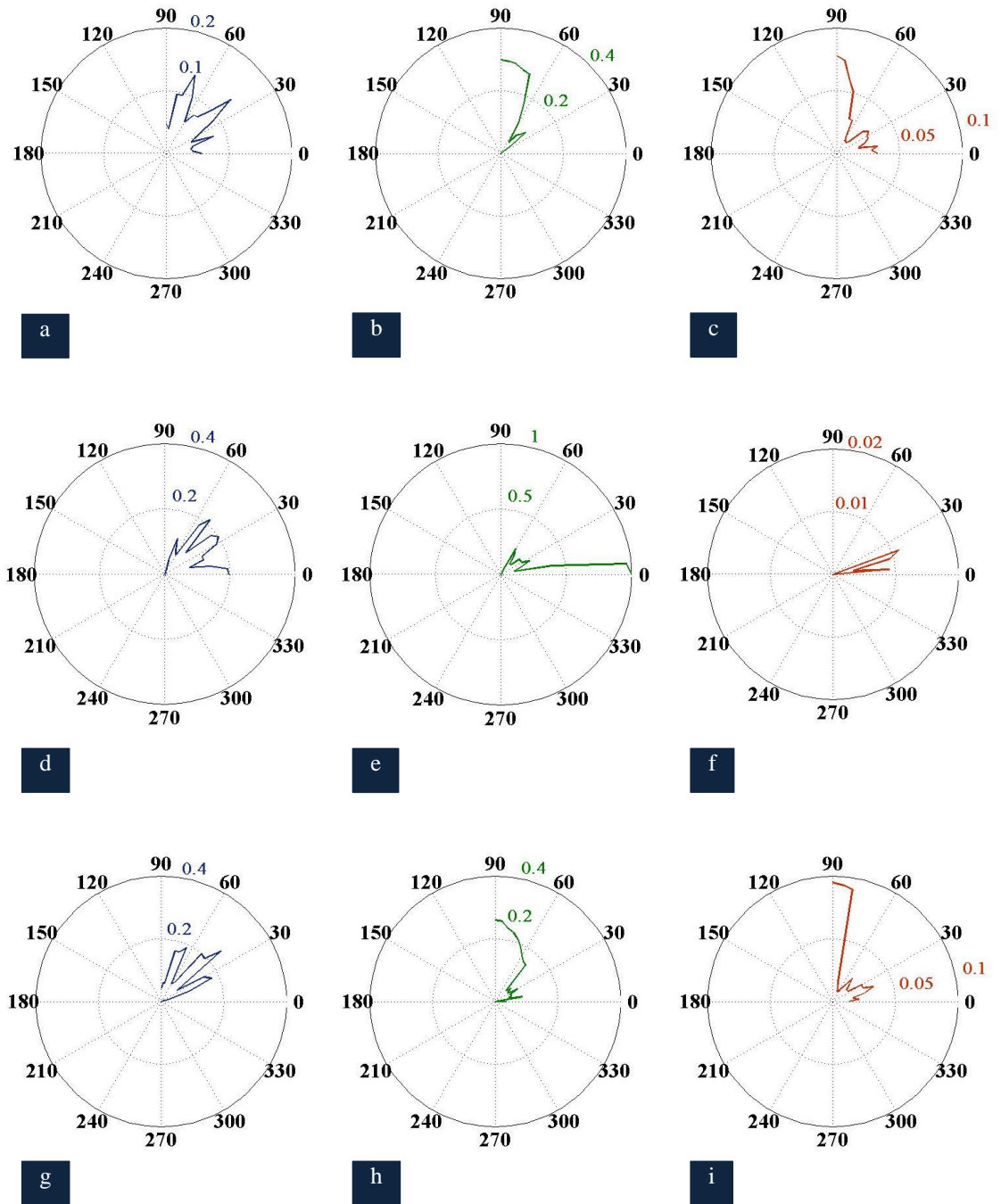


Figure 5.17. Displacement generated in 1.5 mm thick stainless steel plate in (a) x axis (b) y axis (c) z axis received at 58 μsec (d) x axis (e) y axis (f) z axis received at 97 μsec (g) x axis (h) y axis (i) z axis received at 111 μsec .

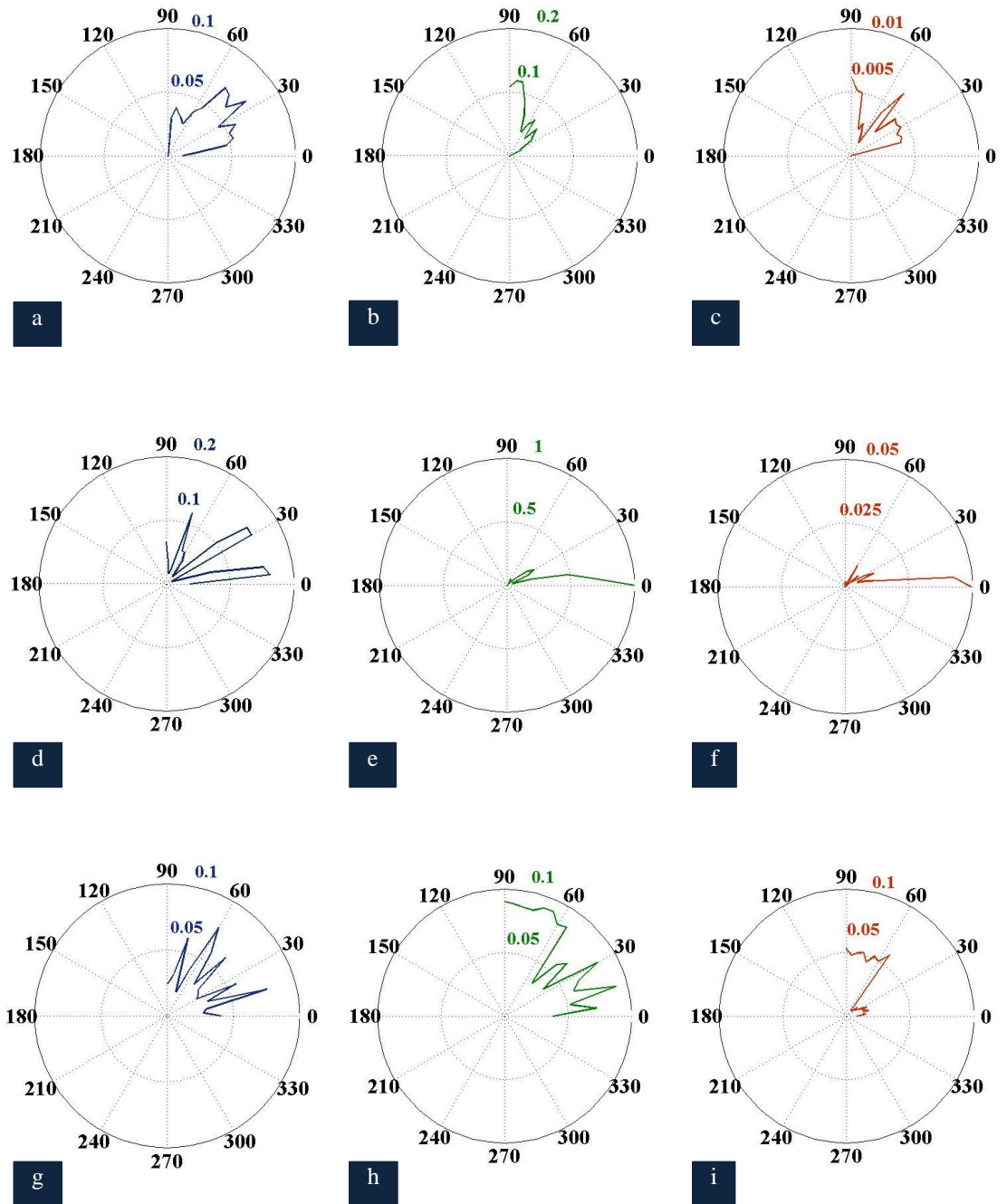


Figure 5.18. Displacement generated in 0.5 mm thick stainless steel plate in (a) x axis (b) y axis (c) z axis received at 58 μ sec (d) x axis (e) y axis (f) z axis received at 97 μ sec (g) x axis (h) y axis (i) z axis received at 158 μ sec.

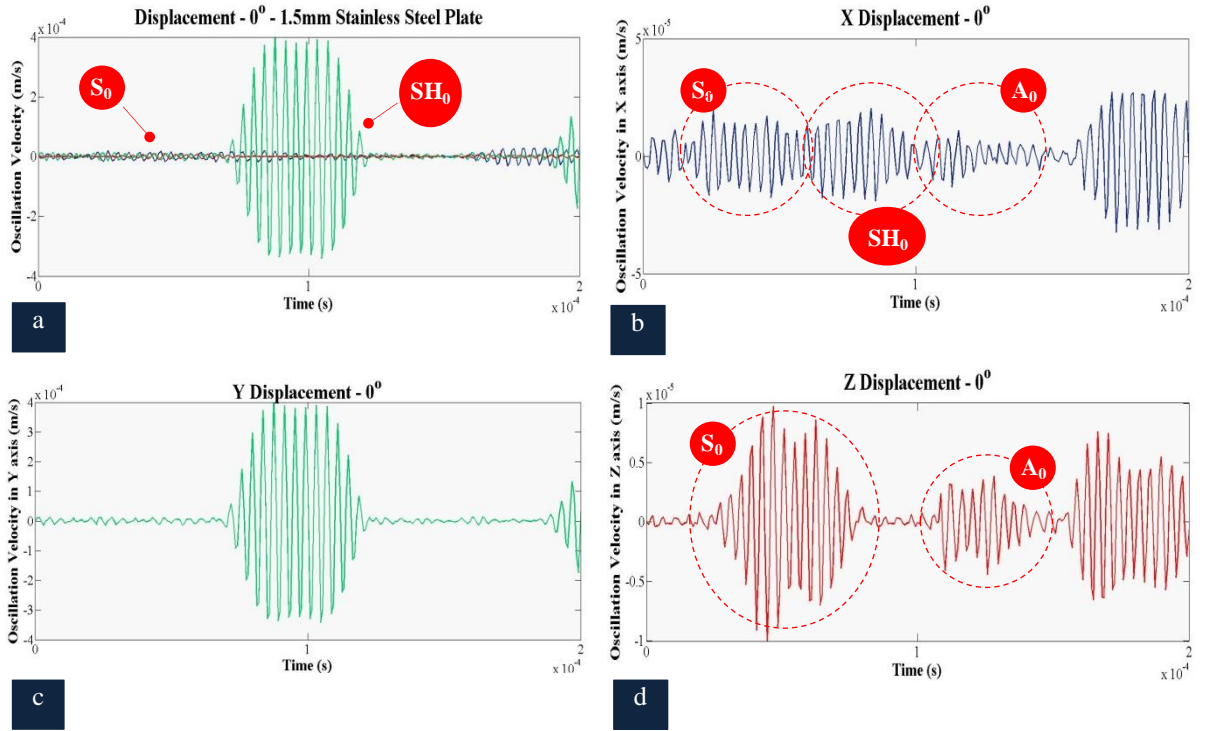


Figure 5.19. Displacement at 0° in 1.5 mm thick stainless steel plate in (a) all axes (b) x axis (c) y axis (d) z axis

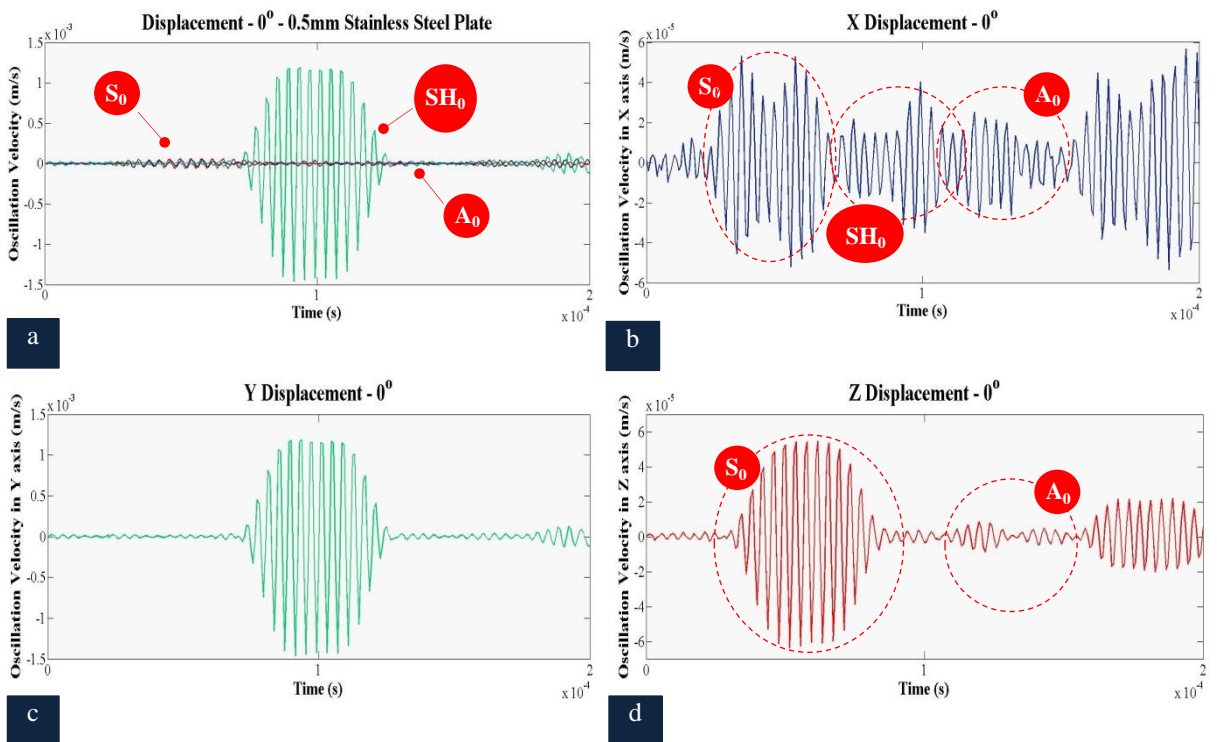


Figure 5.20. Displacement at 0° in 0.5 mm thick stainless steel plate in (a) all axes (b) x axis (c) y axis (d) z axis

mode purity properties of EMAT did not alter significantly with plate thickness decrease and it was proved that most of the energy introduced to the sample resulted in SH_0 . Still the ratio of in-plane to out-of-plane displacement, the amplitude of all displacements and the SNR became greater with thickness decrease and resulted in slightly higher and more refined wave mode purity characteristics as the thickness of the plate decreased. Finally, the experimental values agreed with FEA results and confirmed that firstly, Lorentz force is the dominant excitation mechanism in stainless steel. PPM EMAT generates a certain pattern of Lorentz force that causes the excitation of SH_0 at 0° and unavoidably S_0 and A_0 at 90° due to guided wave physics and their dispersive nature.

The experimental results demonstrated previously shed light on the wave purity characteristics of PPM EMAT when it is employed on paramagnetic materials, like stainless steel, where the dominant transduction mechanism is Lorentz force. However, in ferromagnetic materials, like mild steel, magnetostriction also occurs and dominates after a certain frequency. Magnetostriction is not related to eddy current and magnetic field density in a linear function. On the contrary, the magnetic state of the specimen also affects it. Therefore, FEA models are usually developed for calculating its amplitude and spatial distribution. However, the current study does not focus on magnetostriction and therefore it was not taken into consideration in the theoretical analysis presented in Chapter 4.

Given the fact that the magnetostriction effect could not be predicted by the FEA models presented in Chapter 4, the analysis of the experimental results obtained from the wave mode purity characterization of the EMAT on mild steel could not be fully performed based on the FEA models. On the contrary, the experimental analysis had to rely on the differences between the experimental results from stainless steel and mild steel. Provided that the results yielded by the coupled electromagnetic/mechanical and the wave propagation FEA matched and were also experimentally validated, the FEA model developed in Abaqus could be utilized again for the estimation of wave propagation in mild steel. Any divergence between the FEA results and the experimental characterisation of the EMAT on mild steel would be due to magnetostriction and it could be used for the qualitative quantification of the latter.

This FEA analysis was expected to yield similar results to those obtained from the wave propagation analysis on stainless steel, since material properties of mild steel do not differ greatly from those of stainless steel. The polar plots shown in Figure 5.21 a-c and d-f represent how the x, y and z displacement received at 56 μsec and 93 μsec respectively altered from 0° to 90° . As it was expected, no significant differences were noticed between the two theoretical case studies. The trend all displacements followed in mild steel did not differ from that in stainless steel. Hence, the experimental values retrieved from the EMAT characterisation on mild steel should match with those corresponding to stainless steel and any discrepancies between them would be caused due to magnetostriction effect.

Again, the group velocity of SH_0 and A_0 are almost equal, not permitting the direct measurement of A_0 displacement from the experimental results and thus impeding the signal interpretation. Nevertheless, the signals presented in Figure 5.22 provide more information about the wave purity profile of EMAT on mild steel, as it depicts the displacement generated at 0° in all coordinates

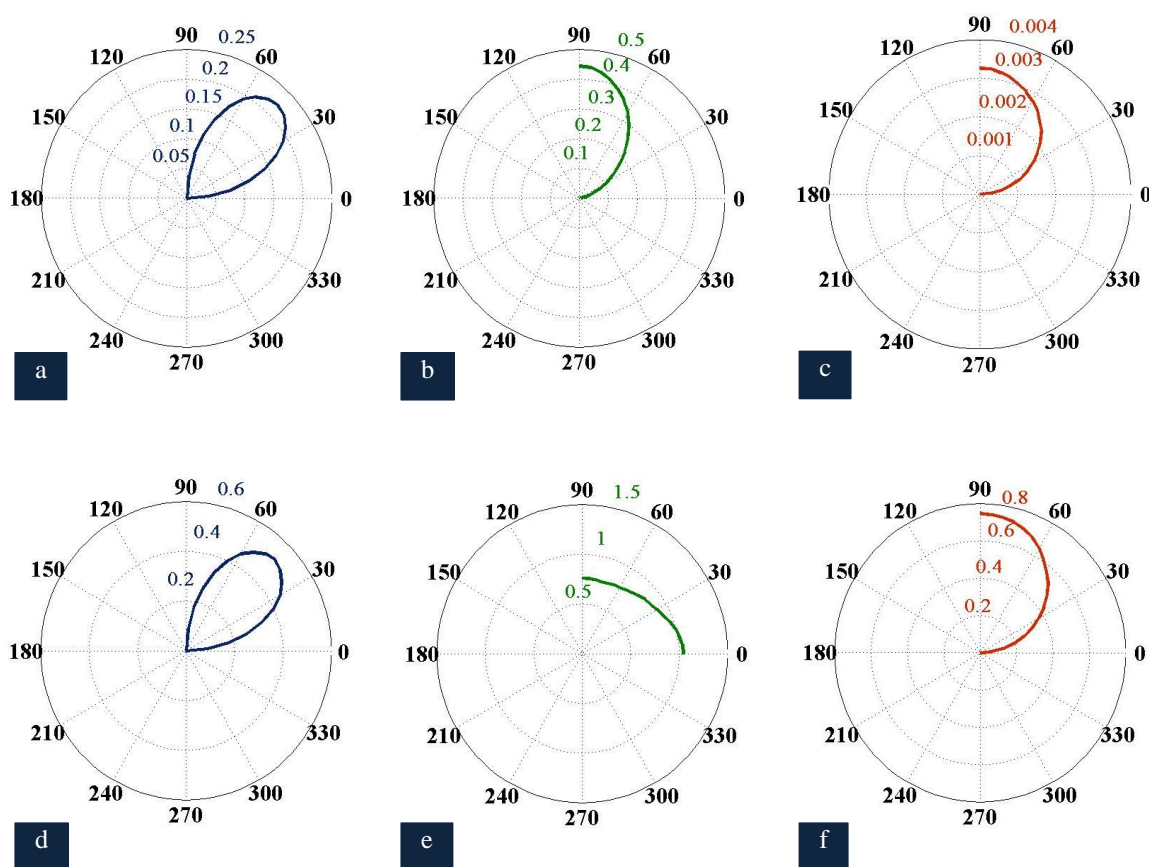


Figure 5.21. FEA results for wave propagation in 3mm thick mild steel plate in (a) x axis (b) y axis (c) z axis received at 56 μsec (d) x axis (e) y axis (f) z axis received at 93 μsec

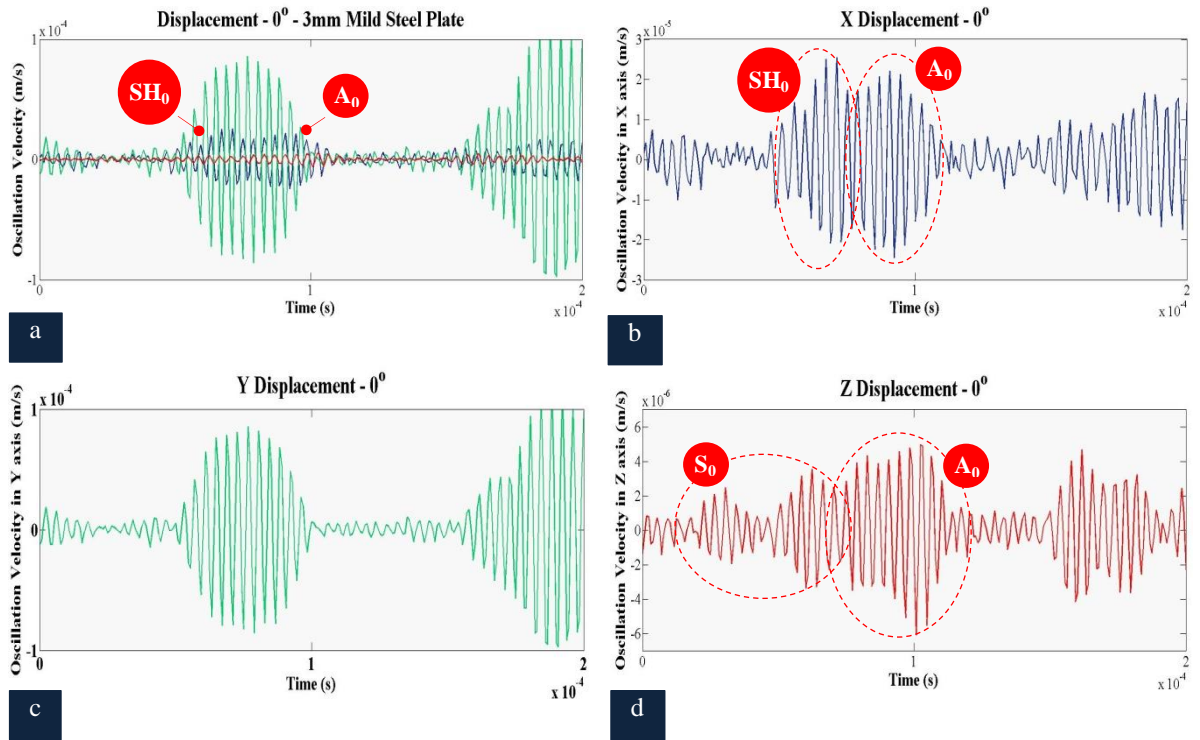


Figure 5.22. Vibrometry results. Displacement at 0° in 3 mm thick mild steel plate in (a) all axis (b) x axis (c) y axis (d) z axis

together and in each one separately. Although in the y-axis there was clearly only one reflection propagating with SH_0 velocity and confirming the suitability of this configuration for SH_0 excitation, still in the x-axis there were two reflections overlapping and exhibiting a stretched profile that is due to dispersion. This indicates the presence of A_0 and it is reinforced by the existence of out-of-plane displacement propagating with both S_0 and A_0 velocity, as Figure 5.22 d shows. However, these observations could not be used for the measurement of A_0 amplitude, since the signal interpretation became more complex as the angle increased and therefore only two groups of displacements were measured through the experimental results.

Figure 5.23 a-c and d-f show how the x, y and z displacement received at 56 μsec and 93 μsec respectively changed from 0° to 90° when the EMAT was attached to the 3 mm thick mild steel plate. The experimental results presented many similarities with FEA results. The largest in oscillation amplitude was noticed at 0° in the y-axis propagating with SH_0 velocity, whilst y displacement was also observed at 90° with almost 80% smaller amplitude than SH_0 and propagating with S_0 velocity. Out-of-plane displacement was detected at both 56 μsec and 93 μsec in several angles with its maxima being at approximately 90° . In both cases the out-of-plane amplitude was significantly smaller than the in-plane displacement (two orders of magnitude) and

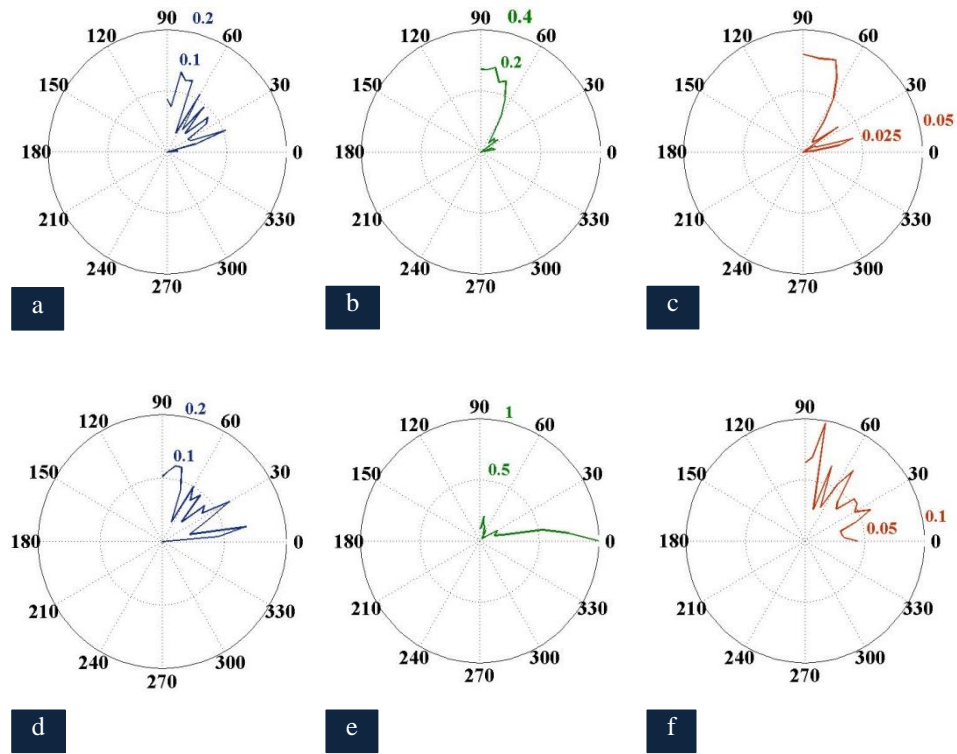


Figure 5.23. Vibrometry results. Displacement generated in 3 mm thick mild steel plate in (a) x axis (b) y axis (c) z axis received at 56 μ sec (d) in x axis (e) y axis (f) z axis received at 93 μ sec.

it can be negligible. However, its spatial distribution differed from one case to the other. Although the out-of-plane displacement of S_0 maximised at 90° as FEA and stainless steel results showed, the z displacement received at 93 μ sec and potentially corresponding to A_0 , presented a considerable spatial distribution from 0° to 30° that did not match with the theoretical results or the wave mode purity profile of EMAT on stainless steel. Nevertheless, the main discrepancy between the theoretical and experimental results could be found in x displacement which was not detected only within 30° and 60° as the FEA model had estimated but also around 80° where its amplitude was also maximum. The same observation was made when the experimental results from mild steel were compared with those from stainless steel. Both divergences are related to A_0 wave propagation. The overlapping occurred between SH_0 and A_0 complicated the amplitude measurements and caused uncertainties to the results shown. Despite this discrepancy, the wave mode purity profile of PPM EMAT did not alter greatly in regards to the material properties of the specimen. In both stainless steel and mild steel, the EMAT excited SH_0 , but also S_0 and A_0 in different angles. Hence, special care should be taken when EMAT transmitters are combined with other transducer technologies that can detect multiple wave modes. On the contrary, instrumentation systems based on EMAT transduction and reception should not suffer from low

wave mode purity characteristics, since the EMAT receivers are not particularly sensitive to unwanted wave modes. Hence, the experimental evaluation of the ultrasonic potential of the water cooled EMAT at room temperature was accomplished and presented in the following section.

5.3.4 Room Temperature Ultrasonic Evaluation

As it has been outlined in the previous sections, the design of the water cooled PPM EMAT was optimized in terms of thermal properties against ultrasonic limitations. Although a careful material selection and design were performed allowing the above, still the ultrasonic signal response of the new EMAT will differ from that of a typical room temperature EMAT. Based on the impedance analysis presented already, the ultrasonic performance of the new EMAT is expected to be lower compared to that of the existing EMAT technology for room temperature. Nevertheless, any divergence between the two EMAT designs should be noticed within a small range of temperatures. The new EMAT was designed so that its performance will be compensated with temperature increase and also withstand higher temperatures than the MOT of existing EMAT transducers, 100°C. Hence, a comparison between the room temperature and water cooled EMATs had to be firstly conducted at ambient temperature.

Two pairs of each EMAT design, with Nd-Fe-B magnets, were employed on a 3mm thick stainless steel plate at a defect-free area in a pitch-catch configuration. In both cases, the distance between the transmitter and the receiver was 30cm. An eight cycle, 256kHz, Hanning modulated, AC current pulse of 30A was driven to both transmitters via Ritec, whilst the signal received was amplified with 80 dB gain, filtered with a low and high pass filter of 20MHz and 10kHz cut off frequencies respectively (averaged of 1024 signals). Figure 5.24 a, b shows the signal received from the room temperature (commercial) and the water cooled EMAT respectively at ambient temperature. As it was expected the amplitude of the signal received by the new EMAT system was significantly smaller compared to the room temperature EMATs. The amplitude of the signal transmitted dropped ten times when the water cooled EMATs were employed on stainless steel. The electromagnetic losses due to the impedance mismatch between the new EMATs and the power generator and the large resistance of constantan coil resulted in its relatively low ultrasonic

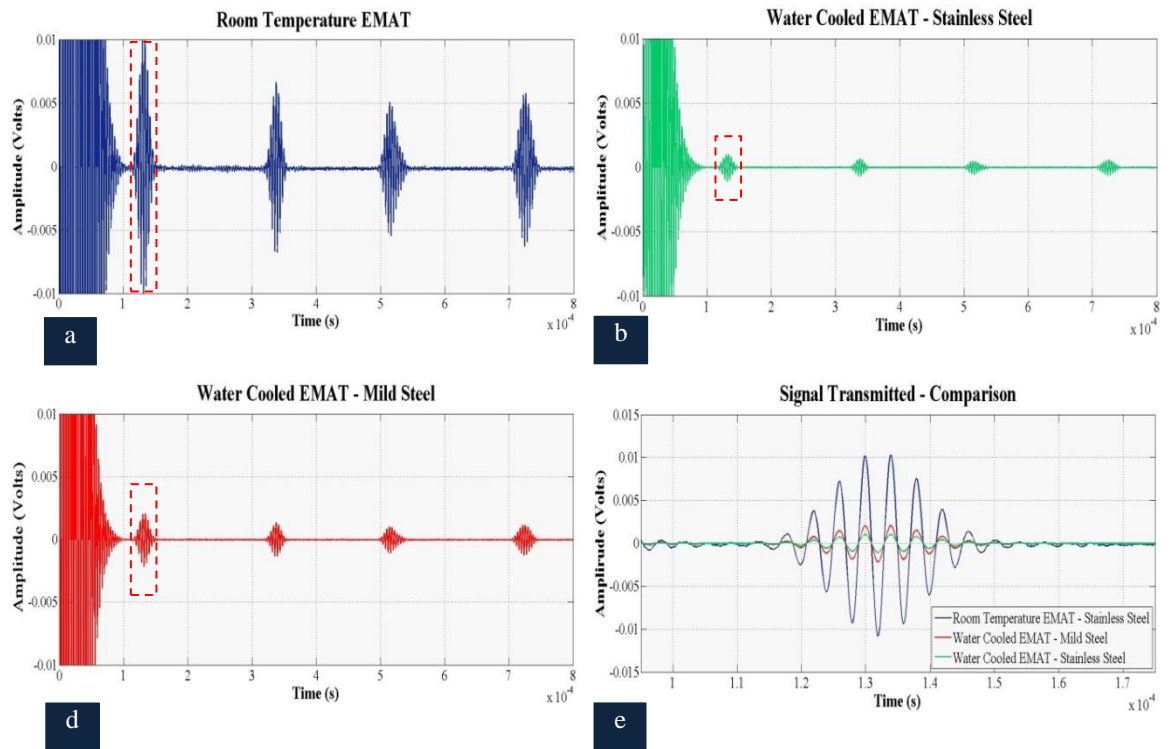


Figure 5.24. Signal received from (a) room temperature EMAT on stainless steel (b) water cooled EMAT on stainless steel (c) water cooled EMAT on mild steel (d) amplitude difference

response. Yet, the new EMAT system managed to detect all first four reflections, indicating that it can transmit enough energy to the specimen for the inspection of at least two meters. The SNR of the signal received in both cases did not alter and remained large (50dB) permitting the detection of reflections propagating up to two-meter distance.

Additionally, the new EMAT system was evaluated regarding its response to the material properties of the specimen. The new transducers were employed upon a 3mm thick mild steel plate in a pitch-catch configuration with 30cm distance between them. The signal received is shown in Figure 5.24 c. Although the amplitude of the signal received doubled when the EMATs were employed on mild steel compared to stainless steel, still their response was lower than that of the room temperature EMATs. Figure 5.24 d shows how the amplitude of the signal transmitted altered in all three cases. Similarly to stainless steel, the SNR of the signal received from mild steel was high, enhancing the ultrasonic potential of the new EMAT system. Nevertheless, its relatively low ultrasonic signal response rises questions regarding its lift-off limitations and power requirements.

The EMATs were tested against lift-off increase. Figure 5.25 shows that the amplitude of the signal transmitted dropped almost exponentially with lift-off increase, likewise room temperature

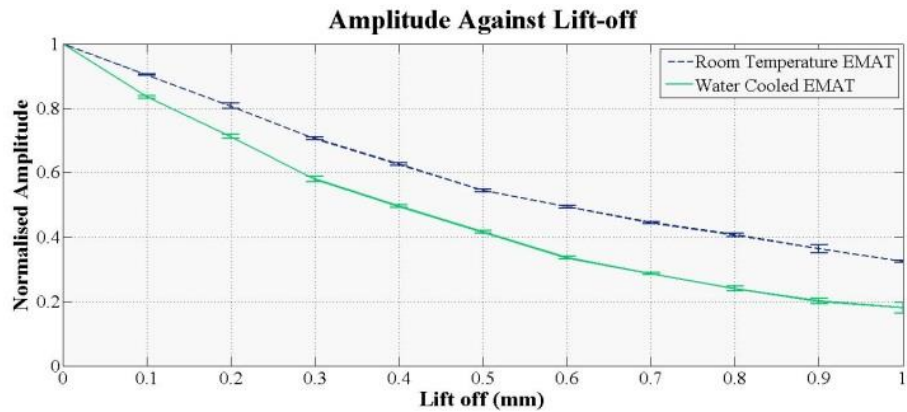


Figure 5.25. Water cooled EMAT - Amplitude against lift-off

EMATs. However, its decrease rate was larger. At 1mm lift-off, the amplitude dropped by 80%, whilst the amplitude of the signal transmitted by the room temperature EMATs at the same lift-off was more than 20% of its maximum. Despite the slightly larger lift-off limitations the new EMATs exhibited compared to the existing technology, they can still be efficiently utilized up to 1mm lift off. These results are encouraging, since lift-off increase directly enhances the thermal response of the transducer and subsequently can beneficially affect its ultrasonic properties at high temperatures as well. Although, the ultrasonic performance of the new EMAT was relatively weak against lift-off at ambient temperature, at high temperatures lift-off increase will result in an increase of the time needed for the maximum thermal energy to be transferred to the EMAT. This can assist in the compensation of ultrasonic signal response of the EMAT against temperature rise.

An experimental comparison between the new EMAT design and the existing technology regarding their power requirements was also accomplished. The power generated by RITEC was incrementally decreased with a step of 5% of its maximum, as the new EMATs were attached on a 3mm thick stainless steel plate. The maximum magnitude of AC current generated by Ritec at its 50 Ω output impedance was 30 A. The EMAT transmitter was connected to the power generator without any impedance matching between them leading to voltage drop and lessening of the ultrasonic response of the EMAT system. Nevertheless, the trend the normalized amplitude of the signal transmitted followed is related to power change and not to the absolute value of power. The results obtained corresponded to the severest operating conditions of EMATs in terms of power supply and also matched with the experimental setup followed when the room temperature EMATs were tested. Figure 5.26 demonstrates that both EMAT systems were similarly dependent on power

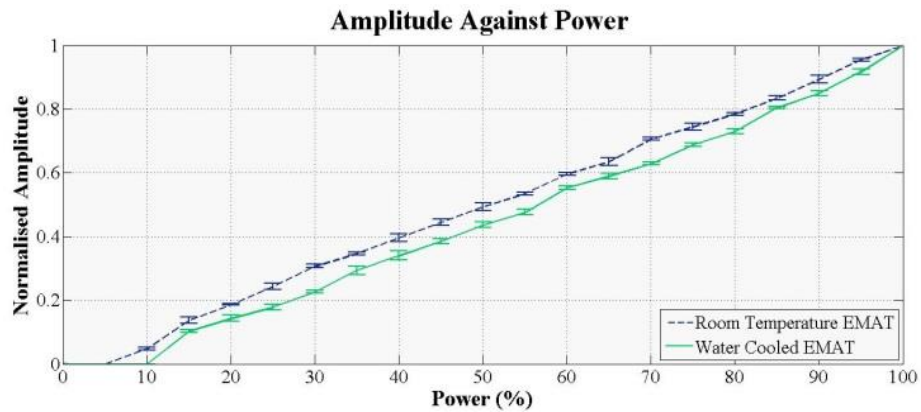


Figure 5.26. Water cooled EMAT - Amplitude against power

input. The amplitude of the signal transmitted dropped almost linearly in both cases, while the water cooled EMAT was approximately 5% more power demanding than copper coil EMAT. The difference in their power requirements is strongly related to their impedance difference and more particularly to their coil resistance. Based on impedance analysis, the constantan coil possessed larger electrical resistance than copper and therefore was further incompatible with the power generator and experienced larger electromagnetic losses. However, its temperature coefficient of resistivity was significantly smaller than that of copper resulting in its enhanced ultrasonic signal performance at high temperatures, as it will be outlined in the following Chapter.

5.3.5 Summary

This Chapter presents the results obtained from the experimental evaluation of the existing EMAT technology designed for room temperature GWT as it was tested at high temperatures. It was found that copper coil PPM EMAT cannot operate efficiently at temperatures higher than 100°C and therefore an alternative EMAT was designed to successfully withstand at elevated. A water cooled EMAT was developed based on the thermal and CFD analysis outlined in the previous Chapter. All the technical details concerning its design and manufacturing challenges were summarized. The new EMAT was characterized regarding its impedance against the material properties of the specimen, lift-off and temperature rise. As it was expected, the new EMAT possessed larger impedance and resistance compared to copper coil EMAT that can limit its ultrasonic response at ambient temperature but also stabilize it at higher temperatures. The theoretical analysis about the wave mode purity profile of PPM EMAT on stainless steel was experimentally validated.

Vibrometry tests conducted on stainless steel plates of variant thickness and mild steel and revealed that this configuration is suitable for SH_0 wave mode excitation. However, a considerable displacement corresponding to both S_0 and A_0 was also detected resulting in the poor wave mode purity characteristics of PPM EMAT. Finally, the new EMAT was evaluated regarding its ultrasonic signal potential and limitations at room temperature. Its ultrasonic response was lower than that of a room temperature EMAT, however, its lift-off limitations and power requirements matched with those of the copper coil EMAT.

The new EMAT is expected to exhibit greater thermal and ultrasonic properties at high temperatures in comparison to the currently available EMAT technology designed for room temperature GWT. Thus, its experimental evaluation against material properties of the specimen, lift-off and power input and temperature rise was also conducted. The results collected from this experimental procedure are summarized in the following Chapter.

Chapter 6

High Temperature Experiments

6.1 Introduction

The water cooled EMAT was finally evaluated regarding its high-temperature performance against various operating conditions. Both Nd-Fe-B and SmCo magnets were utilized and compared in terms of their impact on the ultrasonic signal performance of the EMAT at both room and high temperatures. Specimen material properties, lift-off, power input, temperature rise and operational time at high temperatures are the parameters the EMATs were tested against. The EMATs were evaluated on both ferromagnetic and paramagnetic materials up to 500°C for short period of time (<1min) and 250°C over time. The results obtained from this experimental procedure are presented and analyzed in this Chapter as well as the final conclusions about the high-temperature performance of the water cooled PPM EMAT.

6.2 High-Temperature Experiments – Short Term Exposure

Both Nd-Fe-B and SmCo water cooled EMAT systems were tested regarding their GWT potential and limitations up to 500°C for short period of heat exposure. Both systems were composed of separate EMAT transmitter and receiver. Stainless steel and mild steel were the materials the two EMAT systems were evaluated on against lift-off and power input at high temperatures. Their ultrasonic and thermal response was analyzed and compared with the theoretical values obtained from FEA analysis and thus an experimental validation of the theoretical study presented in Chapter 4 was also accomplished.

6.2.1 Experimental Set-up

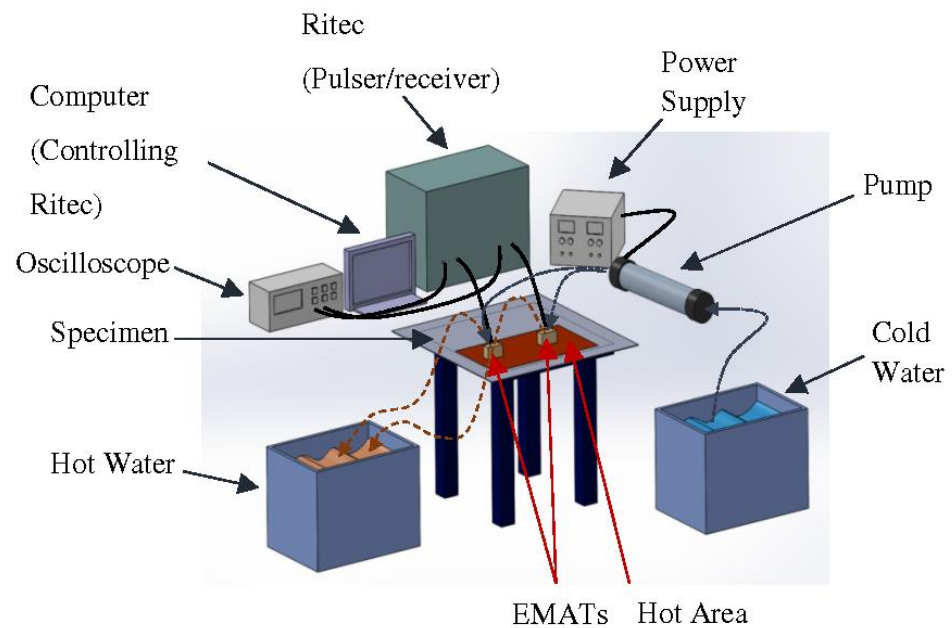


Figure 6.1. Experimental setup for high temperature experiments

The experimental setup shown in Figure 6.1 was developed for the high-temperature evaluation of the high-temperature EMAT systems. They were employed in a pitch-catch configuration with 30 cm between the transmitter and receiver on a defect-free area with no lift-off. A square, 316 Ti stainless steel plate of 1.25 m edge length and 3 mm thickness and a square mild steel plate of 1 m edge length and 3 mm thickness were used as specimens. The EMAT transmitter was driven by Ritec RAM 5000 SNAP with a 5 cycle pulse of 256 kHz on stainless steel and a 10 cycle pulse of the same frequency on mild steel. The excitation pulse was Hanning windowed when the EMATs were attached to stainless steel, while no Hanning window was applied on the excitation pulse when steel was tested. The EMAT receiver was also connected to Ritec so that the raw signal could be amplified with 80 dB gain and filtered with high and low-pass filters of 10 kHz and 20 MHz cut-off frequencies respectively. The filtered signal was collected, averaged and recorded with a 2-channel Agilent oscilloscope. A pump (D5 Photon 170 Pump Combo) was used for circulating the water in the two EMATs with a flow velocity of 3 m/s while the temperature of the cold water was 10 °C. The specimen was heated up by a heat treatment module manufactured by STORK. The module was connected to four ceramic pads, which were composed of high grade sintered alumina ceramic beads and nickel chrome core wires. The pads were driven with high current by the module and the thermal energy generated via the nickel chrome wires was transmitted to the specimen. The temperature of the specimen, the EMAT coil, the magnets and the water outlet of

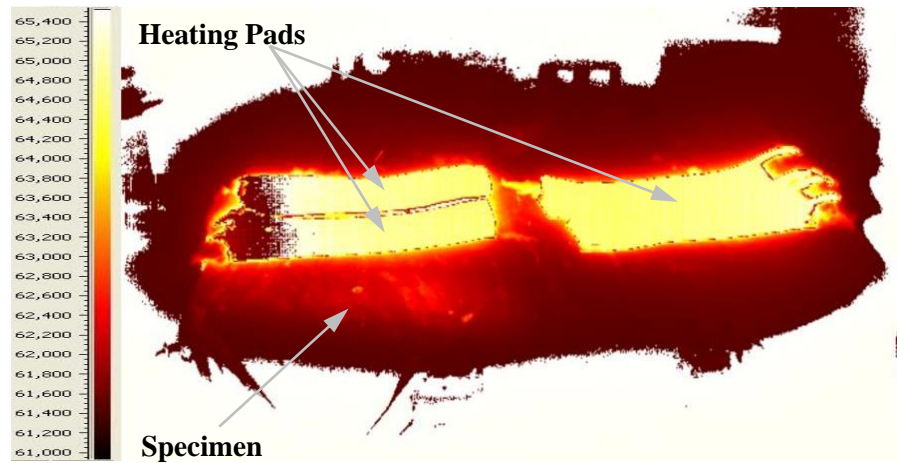


Figure 6.2. Thermal picture of the experimental setup used for the heating up of the specimen (500°C)

the cooling chamber were monitored by a 4-channel thermo-logger. The thermocouples attached to the coil and the magnets were placed on the area underneath the cooling chamber where the temperature would minimize based on the simulations presented in section 4.4.1.

The thermal conductivities of both stainless steel and steel are low (16 and 50 W/m·K respectively at room temperature) and thermal energy introduced to a certain area of the plates cannot readily diffuse throughout the entire specimen volume. Figure 6.2 depicts the thermal image of the specimen as it was heating up via the heating modules. Only the area underneath the heating pads was heated up efficiently since luminance maximized only in those areas. Bending of the specimen also occurred due to the temperature variation on the specimen volume. Thus, divergences were expected in the time shift of reflections traveling in areas of different temperature. As soon as the heating pads were removed from the plates, the temperature of the area of inspection decreased quickly. Testing done at high temperatures for only short times (less than a minute for each target temperature) and the experiments were conducted three times for each EMAT system. The temperature of the heating pads was increased from ambient to 700 °C and the maximum temperature of the area below the pads was 600 °C. With the pads removed and the EMATs placed with zero lift-off on the defect-free, heated area, the specimen temperature was 500 °C. The ultrasonic signal response and the temperature of the coil and magnets were recorded from 500 °C down to ambient temperature in steps of 50 °C.

6.2.2 EMAT Performance against Material of Specimen

The signals received from the above experimental procedure when both EMAT systems were tested on stainless steel and mild steel with no lift-off are shown in the following figures. In each graph, the blue signal corresponds to the Nd-F-B EMAT system and the red signal to SmCo system. All figures present the signal transmitted and the three reflections coming from the edges of the plate. Figure 6.3 a-c illustrate the ultrasonic signals recorded when the EMAT was tested on a steel plate at room temperature, 250 °C, and 500 °C, respectively, and Figure 6.3 d shows how the amplitude of the signal transmitted decreased with temperature for all the three experimental sets. Figure 6.4 shows the results obtained when the EMATs were attached to stainless steel. Figure 6.4 a–c show the ultrasonic signal at room temperature, 250 °C and 500 °C and Figure 6.4 d presents how the amplitude of the signal transmitted decreased with temperature on stainless steel.

As expected the EMATs performed better on steel than on stainless steel due to the stronger electromagnetic coupling. The amplitude of the signal received for steel was an order of magnitude larger than stainless steel. Nevertheless, both EMAT systems managed to perform efficiently up to 500°C on both materials. Compared to the high-temperature ultrasonic response of a conventional, room temperature PPM EMAT system as it was studied in detail in Chapter 5, the new EMAT systems operated up to 500 °C, while the conventional could hardly be employed up to 100 °C. In all cases, the amplitude transmitted at 500°C was more than 20% of its maximum as well as all four reflections were noticeable. These encouraging observations lead to the conclusion that both water cooled EMAT systems can successfully be employed for GWT inspection up to 500°C.

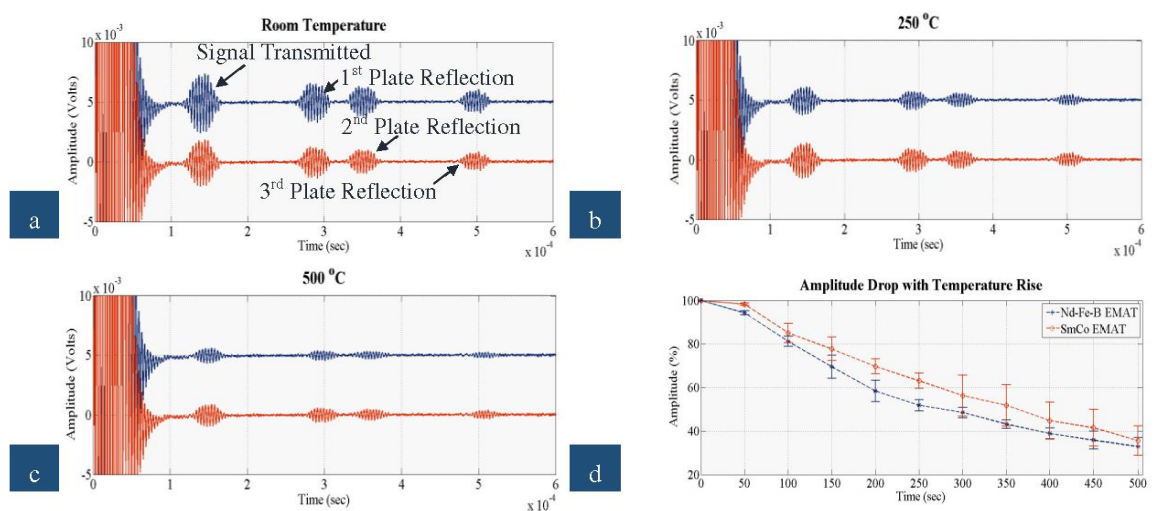


Figure 6.3. Signal received from both EMATs on mild steel at (a) room temperature (b) 250°C (c) 500°C (d) amplitude against temperature

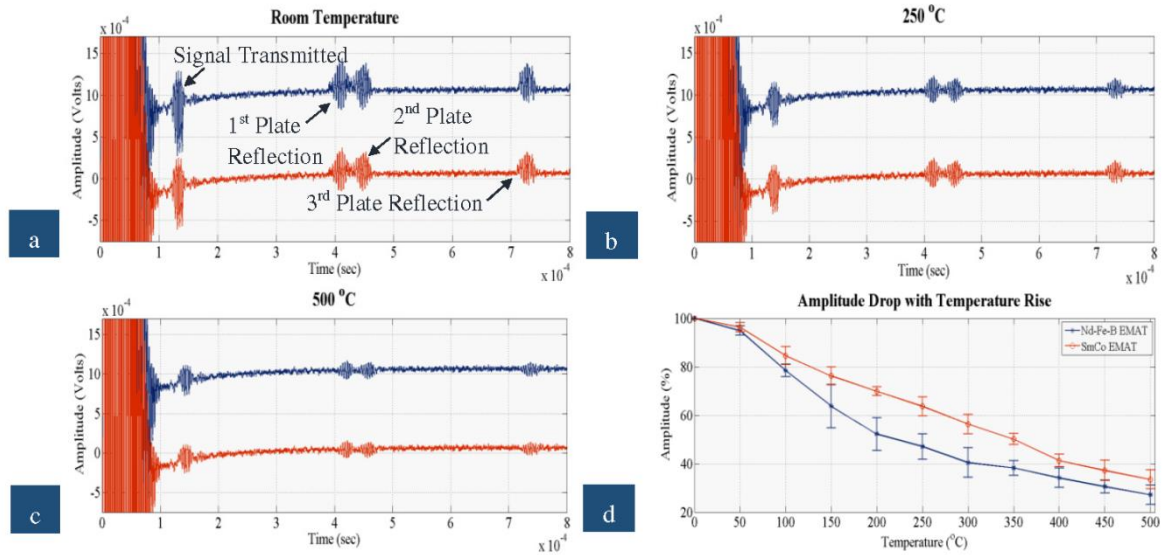


Figure 6.4. Signal received from both EMATs on stainless steel at (a) room temperature (b) 250°C (c) 500°C (d) amplitude against temperature

On both materials, SmCo EMATs were more efficient in terms of amplitude decrease against temperature rise, compared to Nd-F-B. At room temperature, the amplitude of the Nd-F-B EMATs was approximately 20% larger than that received by the SmCo. Regardless of the material tested, the performance of the Nd-F-B EMATs fluctuated slightly from 200 °C to 350 °C, indicating that over this range the temperature of the magnets must have reached the MOT of Nd-F-B. The amplitude drop with Nd-F-B was slightly larger (less than 10%) when stainless steel was inspected due to weaker electromagnetic coupling with the specimen. The amplitude of the signal received with SmCo EMATs dropped at a constant rate as temperature rose, especially on stainless steel, and its amplitude drop over the entire temperature range was smaller than with Nd-F-B. All this indicates that the temperature of the magnets was close to the MOT of Nd-F-B, especially from 200 °C to 500 °C, resulting in the stable performance of the SmCo EMATs and the fluctuating performance of the Nd-F-B EMATs. The cooling system appeared efficient for both types of magnet, since ultrasonic signals were obtained over the entire temperature range and the SNR did not deteriorate with temperature rise. Nevertheless, SmCo EMAT managed to withstand better high temperatures and its amplitude was larger at high temperatures compared to Nd-F-B.

Based on the dispersion curves of stainless steel and steel plate, the velocity of SH_0 equals 3080 and 3203 m/s, respectively. Thus, ToF of the reflections shown in the graphs matched the velocity of SH_0 ; ToF of all four reflections was increased by 30 μ s pulse duration. As a result, it is experimentally demonstrated that although PPM EMAT transmitter generated multiple wave

modes including SH_0 , the EMAT receiver detected only SH_0 at both room and high temperatures, as it was expected. An EMAT system does not suffer from poor wave mode purity, however, a system composed of an EMAT transmitter and a receiver sensitive to multiple wave modes is likely to detect more wave modes than only SH_0 at both room and high temperatures. In addition, all four reflections shifted in time as temperature increased, as expected. No differences in time shift of four reflections were noticed.

Figure 6.5 shows how the temperature of the EMAT coil and magnets changed with the temperature of the specimen. The red dashed and blue dotted curves denote the calculated minimum temperature of the coil and the magnets from the CFD simulations presented in Chapter 4 and shown in Figure 4.16 b. The red circles and blue stars are the measured temperature of the coil and the magnets and the error bars depict the temperature variation in the three experimental sets. The experimental values agreed with theory, excepting the measured temperature of the magnets at 100 °C, which was approximately twice the theoretical value. During the experiments, the specimen temperature decreased gradually after reaching 500 °C, while in the simulations the temperature was held at a certain target value (varying from 100°C to 500°C). Therefore, it is likely the EMAT and its housing maintained a portion of the thermal energy absorbed at 500 °C until it was dissipated by the cooling system. The time needed for the maximum energy to be dissipated was larger than the time needed for the temperature of the specimen to decrease to 100 °C (15 mins). Therefore, the temperature of the EMAT did not drop with the calculated rate and the largest discrepancy between theoretical and experimental values was observed at 100 °C. Nevertheless, the thermal model can be used for the analysis of EMATs when the temperature of the specimen remains constant; during online inspection/monitoring the temperature of the specimen usually stays constant or changes only slightly (maximum 10°C change [2]).

The cooling system, the material selection (constantan coil, SmCo magnets) and the optimum operating conditions can significantly improve the EMAT ultrasonic signal response at high temperatures. The new EMAT can efficiently be employed for GWT up to 500 °C for short operational time (< 1 min) and can be potentially utilized for inspection of absorber tubes and other

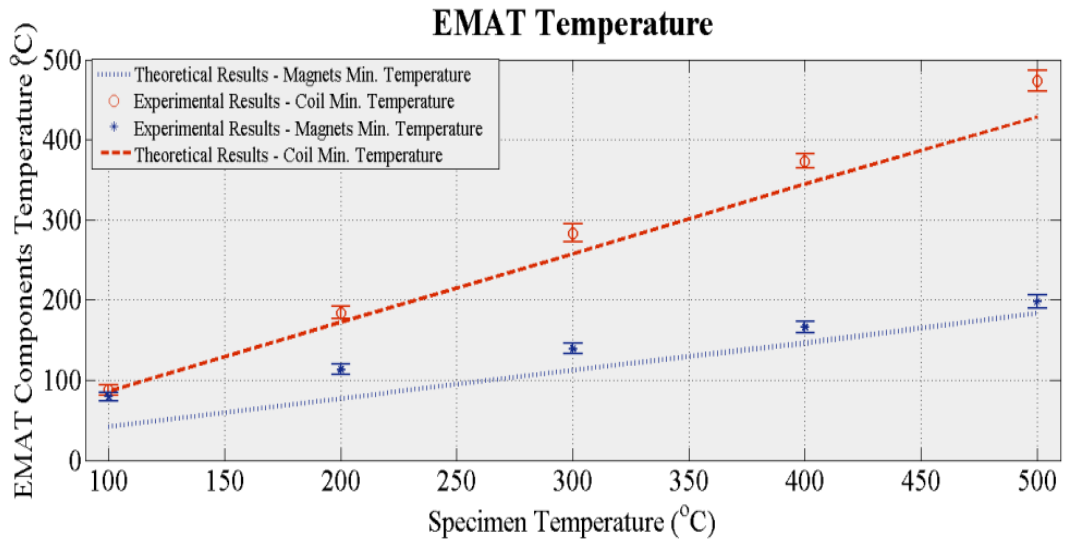


Figure 6.5. Temperature of EMAT components: measured and estimated values

conducting, paramagnetic, high-temperature objects. Further experimental investigation of the limitations and potential of the EMAT against lift-off and power input was also conducted at high temperatures.

6.2.3 Lift-off Limitations

The effect of lift-off on the ultrasonic performance of EMATs at high temperatures was experimentally studied. As it was cited in previous Chapters, EMATs are significantly sensitive to lift-off and both the room and high-temperature PPM EMAT exhibited exponential amplitude drop with lift-off increase at room temperature. Nevertheless, any increase in the distance between the EMAT and the specimen enhances the thermal properties of the former and can prolong its operational time at elevated temperatures. Hence, both water cooled EMAT systems were evaluated regarding their GWT potential against lift-off on both stainless steel and mild steel up to 500°C.

The experimental procedure remained the same and so the specimen was firstly heated up to 600°C when the heating pads were removed and the EMATs were attached on it with 0.5mm and 1mm lift-off sequentially. Signals were recorded from 500°C down to ambient temperature with 50°C steps. Figure 6.6 demonstrates how the amplitude of the signal transmitted by Nd-Fe-B EMATs dropped with temperature rise for 0mm, 0.5mm and 1mm lift-off on mild steel and stainless steel.

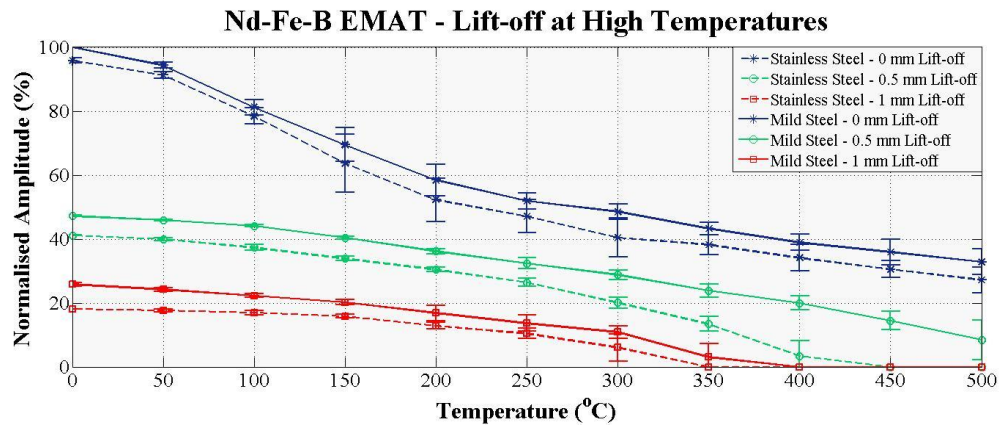


Figure 6.6. Nd-Fe-B EMAT: Amplitude against lift-off at high temperatures

The solid blue, green and red lines correspond to amplitude drop on mild steel at 0 mm, 0.5 mm and 1mm lift-off respectively, whilst the dashed lines refer to amplitude drop on stainless steel for the same lift-off values. As expected, the EMATs operated more efficiently on mild steel than stainless steel regardless of lift-off or temperature. The largest discrepancy in EMAT ultrasonic response between the two materials was noticed at 0.5 mm lift-off. The amplitude dropped with a higher rate on stainless steel after 350°C and it decreased greatly (less than 5%) at 400°C. With mild steel, the amplitude decreased at constant rate till 500°C, where its value was relatively high (10%) according to the operating conditions. The MOT varied with lift-off as well. In all cases MOT was larger than 200°C, which is the MOT of Nd-Fe-B magnets, indicating that cooling system kept magnets temperature below their MOT. Nevertheless, lift-off affected significantly the electromagnetic coupling between the EMAT and the specimen as temperature rose and limited their efficiency and MOT. As the electromagnetic coupling was weak and amplitude was relatively low at room temperature when there was lift-off, any thermal energy transferred to the EMATs had a greater impact on their ultrasonic response compared to no lift-off, regardless of the performance of the cooling system. Thus their efficiency was more limited. Although the rate of amplitude drop was smaller as lift-off increased due to more efficient heat dissipation via the cooling system, the ultrasonic signal degradation was more noticeable with lift-off increase due to originally low electromagnetic coupling. In all cases, the EMATs operated efficiently, with amplitude more than 10%, up to 300°C and their response was essentially stable up to this temperature for 0.5 mm and 1mm lift-off. As a result, MOT decreased as lift-off increased, but it still remained larger than 200°C. Their stable ultrasonic performance against lift-off up to 300°C is also encouraging

regarding the potential of the Nd-Fe-B EMAT system for long-term inspection up to 250°C. In addition, the range of error increased with temperature rise and lift-off. As the EMATs were directly exposed to heat with no distance from the specimen, their thermal and subsequently ultrasonic properties changed quickly and thus variations in the amplitude of the signal received were greater compared to those with lift-off. The ultrasonic performance of EMAT system varied with temperature rise when non-contact measurements were taken and the error range became greater after 300°C. Hence, Nd-Fe-B EMAT system can be successfully utilized up to 500°C (depending on specimen material) and 300°C with lift-off. Both ferromagnetic and paramagnetic materials can be inspected successfully, with greater success on ferromagnetic.

Figure 6.7 shows how the amplitude of the signal transmitted by SmCo water cooled EMAT system dropped with temperature for varying lift-off. Again, the solid blue, green and red line correspond to amplitude drop on mild steel at 0 mm, 0.5 mm and 1 mm lift-off, while the dashed lines refer to stainless steel. Similarly to Nd-Fe-B EMATs, the amplitude of the signal received by SmCo system from mild steel was 5-10% larger than that of stainless steel. The amplitude decreased with the same rate with both systems when non-contact measurements were taken. However, MOT of SmCo EMAT against lift-off was larger, although it decreased as the lift-off distance increased. The amplitude at 500°C at 0 mm and 0.5 mm lift-off was larger than that of Nd-Fe-B EMATs at the same temperature. The ultrasonic performance of SmCo EMATs was less than 10% after 400°C and equaled to zero at 500°C when lift-off maximized. Again, no amplitude variations were noticed within a large temperature range, from ambient temperature up to 400°C, reassuring further the long-term inspection potential of this system design. The error range was

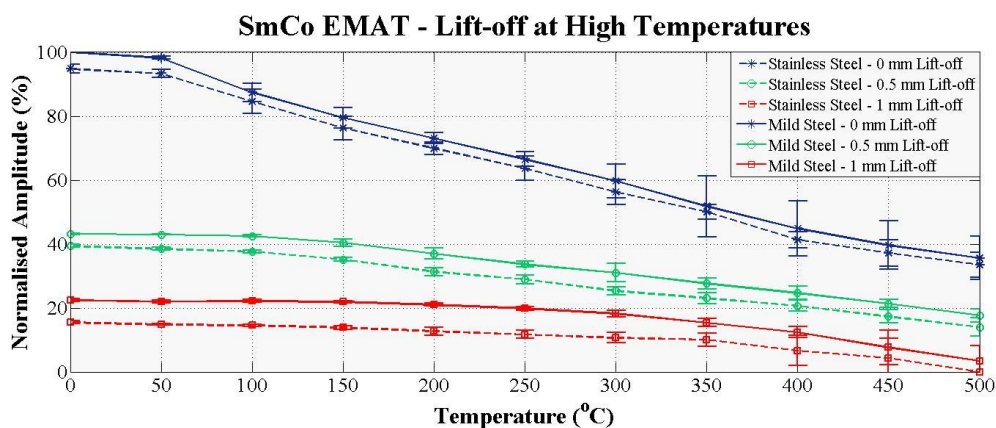


Figure 6.7. SmCo EMAT: Amplitude against lift-off at high temperatures

greater when no distance existed between the transducers and the test piece due to the greater effect of temperature rise on EMATs performance as well as when temperature increased and lift-off measurements were taken. Consequently, this system can withstand up to 500°C at 0 mm and 0.5 mm lift-off and 400°C for 1 mm lift-off.

Both EMAT systems can operate at least up to 300°C regardless of lift-off. The cooling system managed to extend their MOT by at least 100°C under the severest conditions in terms of lift-off for both mild and stainless steel. The ultrasonic signal response of both EMAT systems was stable for a large range of temperature on both materials indicating their long-term inspection capabilities up to 250°C.

6.2.4 Power Requirements

The EMAT systems were also tested regarding their power requirements at high temperatures. Due to limitations of the experimental setup, simplification steps were taken. The temperature of specimen decreased from 500°C down to ambient at a high rate and therefore not enough time was given for the thorough investigation of their power requirements at high temperatures. The temperature effect on EMAT performance was studied only for four power levels, 100%, 75%, 50% and 25% of maximum power Ritec can drive to the EMAT (5000 Watt on 50 Ω output resistance without load). The minimum power requirements of both EMAT systems were found in terms of temperature rise. The EMATs were tested on stainless and mild steel with no lift-off. Figure 6.8 a, b demonstrate how the normalized amplitude of the signal received by Nd-Fe-B EMAT dropped with temperature rise for all four power levels on mild and stainless steel respectively. The temperature effect was more noticeable on stainless steel, since the amplitude decreasing rate was higher compared to mild for all four power levels as well as no ultrasonic response was obtained at 500°C for power less than 100% of Ritec power. Likewise, lift-off limitations, although the cooling system maintained EMAT temperature below 200°C, nevertheless the amplitude on stainless steel was 15% smaller than that on mild steel at room temperature. As a result, the temperature effect was greater as the power input decreased. The Nd-Fe-B EMAT

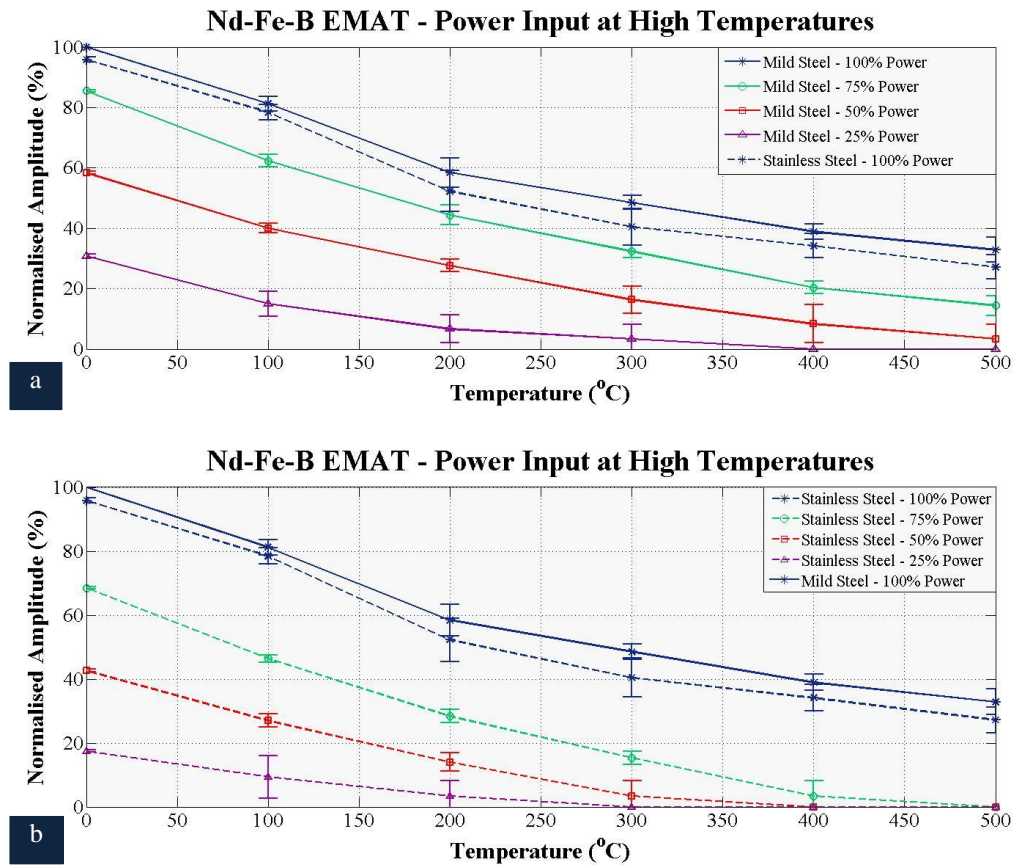


Figure 6.8. Nd-Fe-B EMAT: Amplitude against power input at high temperatures on (a) mild steel (b) stainless steel

system can successfully inspect mild steel up to 450°C and stainless steel up to 250°C with more than 50% power of Ritec.

Figure 6.9 a, b shows the ultrasonic performance of SmCo EMAT system against power input variations up to 500°C on mild and stainless steel respectively. As with lift-off evaluation, SmCo EMATs suffered from low magnetic strength and ultrasonic signal properties at room temperature that degrade linearly with power decrease. However, their larger MOT and advanced performance at high temperatures compared to Nd-Fe-B magnets allowed the compensation of their large power requirements. SmCo EMATs managed to operate efficiently up to 500°C on mild steel and 300°C on stainless steel for power more than 50% (Ritec). As expected, their amplitude decreasing rate was smaller compared to Nd-Fe-B water cooled EMAT system against temperature rise regardless of their power input level, resulting in their superior high-temperature performance in terms of power requirements.

Both designs operated satisfactorily up to 500°C for short period (less than 1 min) against lift-off and power input variations. The cooling system maintained EMAT temperature below 200°C,

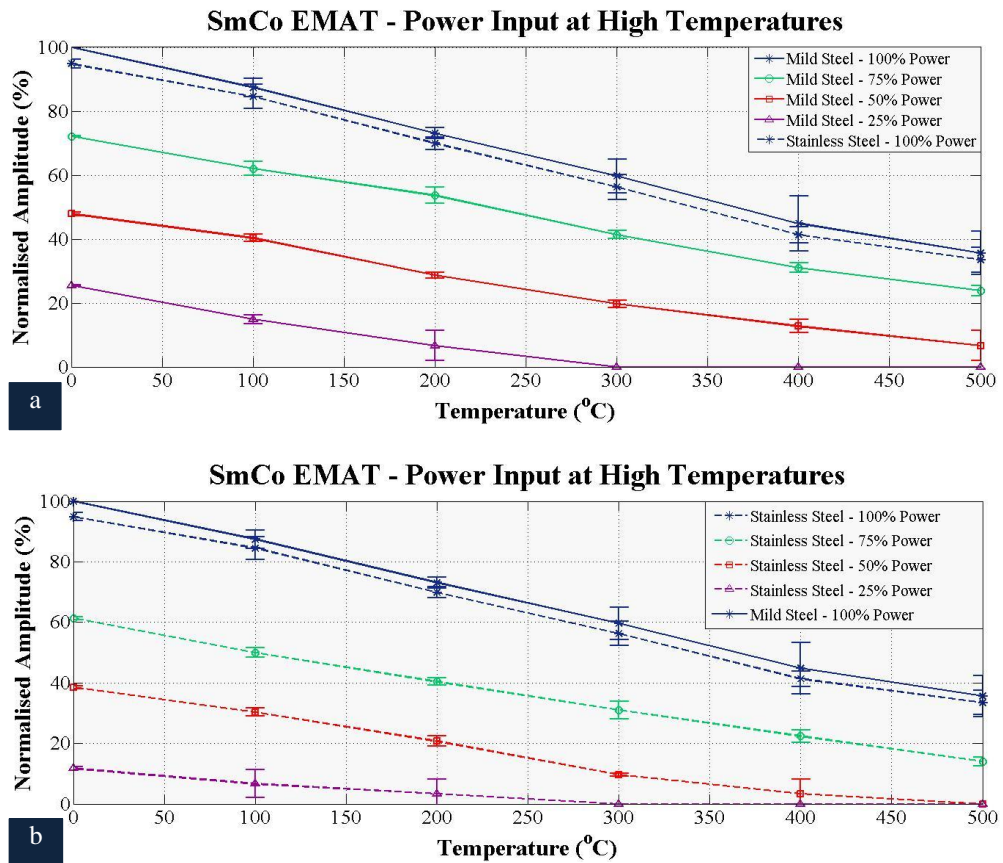


Figure 6.9. SmCo EMAT: Amplitude against power input at high temperatures on (a) mild steel (b) stainless steel

meeting the design requirements and agreeing well with the theoretical results. Despite the room temperature limitations each design experienced, still was their MOT extended by at least 100°C under their severest operating conditions. SmCo EMATs exhibited better thermal and ultrasonic signal properties up to 500°C compared to Nd-Fe-B, confirming their suitability for this application.

6.3 High-Temperature Experiments – Long Term Exposure

In the previous section, the maximum time the transducers were exposed at elevated temperatures was relatively short. The EMATs were employed at each target temperature for less than a minute. Thus, they were further assessed regarding their operational time at high temperatures. Based on FEA analysis presented in Chapter 4, the water cooled EMAT could not operate up to 500°C for more than 5mins. On the contrary, the theoretical results show that long-term operation could be achieved at lower temperatures. Hence, both EMAT systems were tested regarding their long-term

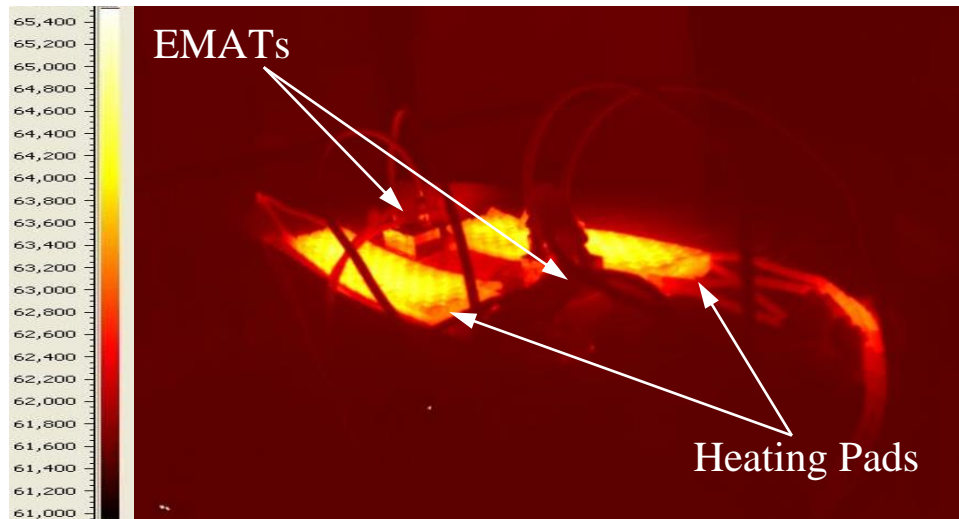


Figure 6.10. Thermal photo of experimental setup for the EMAT evaluation about long term inspection at 250°C

inspection capabilities up to 250°C and a comparison between the theoretical and experimental results was accomplished.

The transducers were tested on both materials with maximum power input and no lift-off. The experimental setup remained the same, however, the procedure followed for the heating up of the plate and the stabilization of its thermal properties over time was slightly different from that described in the previous section. The EMAT system was employed in pitch catch on the plate and the heating pads were placed on their sides. A thermocouple monitored the temperature of the area between the transducers. Heating pads temperature kept on increasing till the specimen temperature reached 250°C. The distance between the pads and the EMATs varied over the duration of the experiments so that the temperature of inspected area was kept stable. Figure 6.10 shows the thermal photo of the experimental setup at 250°C. The low thermal conductivity of both materials resulted in the overheating of the area underneath the heating pads, as the figure depicts. The EMATs were exposed to heat for three hours. The experimental procedure was time restricted due

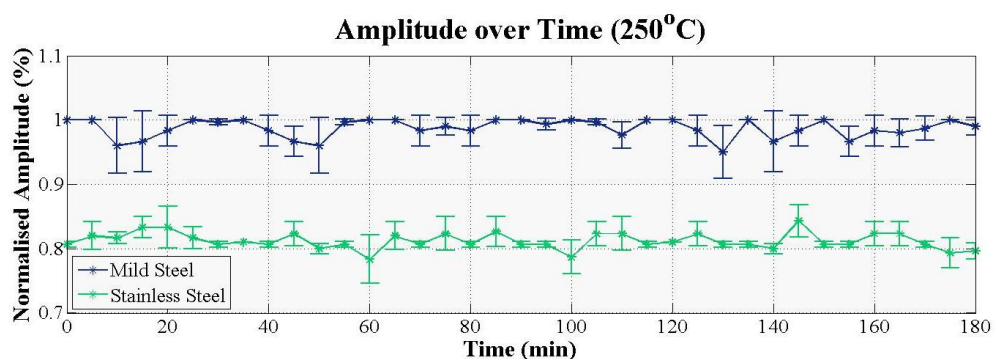


Figure 6.11. Nd-Fe-B EMAT: Amplitude over time at 250oC

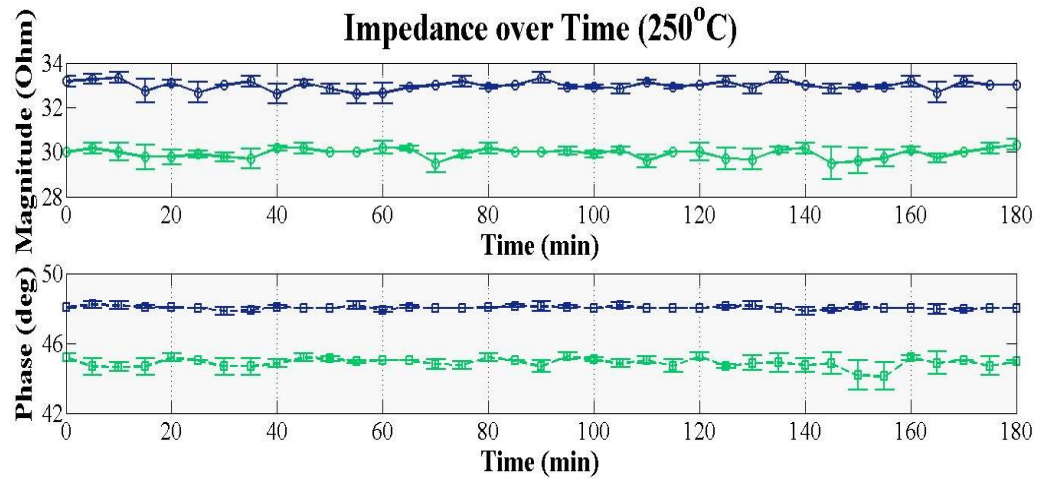


Figure 6.12. Nd-Fe-B EMAT: Impedance over time at 250oC (a) Magnitude (b) Phase

to health and safety reasons.

The ultrasonic response of the system was continuously recorded every five minutes. Figure 6.11 shows how the normalized amplitude of the signal transmitted by Nd-Fe-B EMATs at 250°C for both mild and stainless steel changed over time for three hours. The blue line corresponds to amplitude change for mild and green line to stainless steel. Figure 6.12 demonstrates the impedance change over time at the same temperature, as it was measured (calculated) via an electric circuit measuring EMAT voltage and current (through a 0.1Ω resistor in series with EMAT). The solid blue and green line refer to impedance magnitude on mild and stainless steel respectively and dashed lines to phase. Both figures show that the ultrasonic signal and electrical properties of the EMAT system did not alter significantly over time. The Nd-Fe-B EMATs managed to operate at 250°C continuously for three hours and the variations observed in the amplitude of the signal transmitted were due to small changes in the temperature of the specimen. The experimental results validated the FEA results and the operating time was larger than one hour. Figure 6.13 a, b show the signal obtained at 250°C at the first minute of operation (inspection purposes) and after three hours of uninterrupted operation respectively on stainless steel. Likewise, the amplitude of the signal transmitted, the SNR and the length of inspection did not deteriorate over time neither did time shift alter. The overall ultrasonic performance of Nd-Fe-B EMATs maintained stable for three hours and no indications were found about any potential break down of the system after three hours of operation at 250°C. Consequently, this EMAT design can be utilized for long-term inspection of structures operating up to 250°C. However, further experimental investigation is required regarding

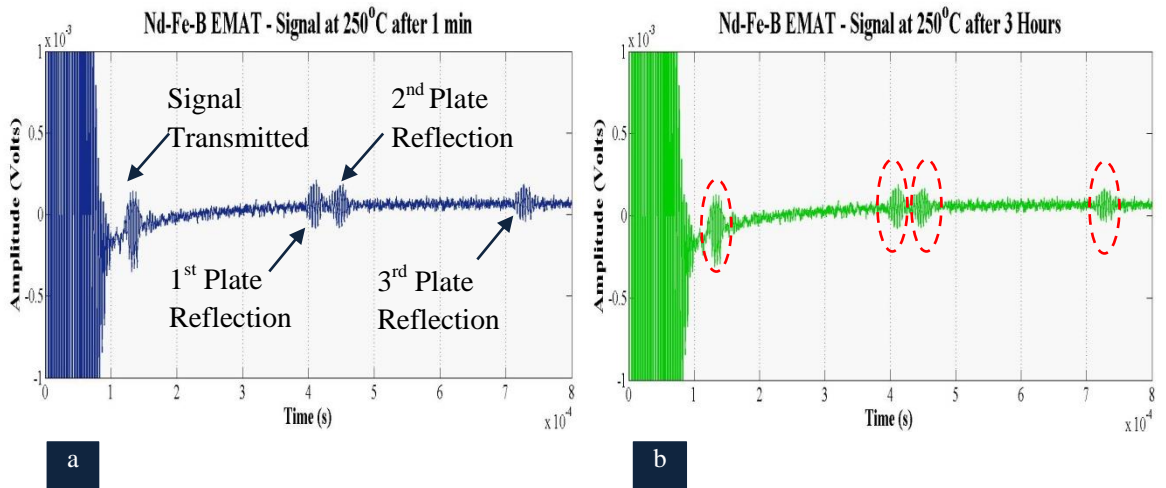


Figure 6.13. Nd-Fe-B EMAT: Signal received at 250°C after (a) 1 min (b) 3 hours operation

its ultrasonic and thermal performance over longer period of time (days) so that its monitoring potential and limitations are found.

SmCo EMATs were also tested regarding their ultrasonic performance at 250°C over time. Figure 6.14 demonstrates how the amplitude of the ultrasonic signal altered with time. Again, no significant variations were noticed and the system operated efficiently and continuously for three hours. However, SmCo possesses higher $M\dot{O}T$ than 250°C and therefore the long-term inspection potential of the system could be also investigated at higher temperatures than 300°C. Hence, it was also tested at 350°C for three hours. Similarly, with 250°C, the transducers managed to operate efficiently, as shown in Figure 6.15, 6.16 and 6.17. Despite the expected amplitude drop at 350°C, the ultrasonic performance of the EMATs remained stable for three hours on both materials. However, some amplitude variations were still noticed. The range of variation was large and they occurred more frequently compared to lower temperature performance. On the contrary, no

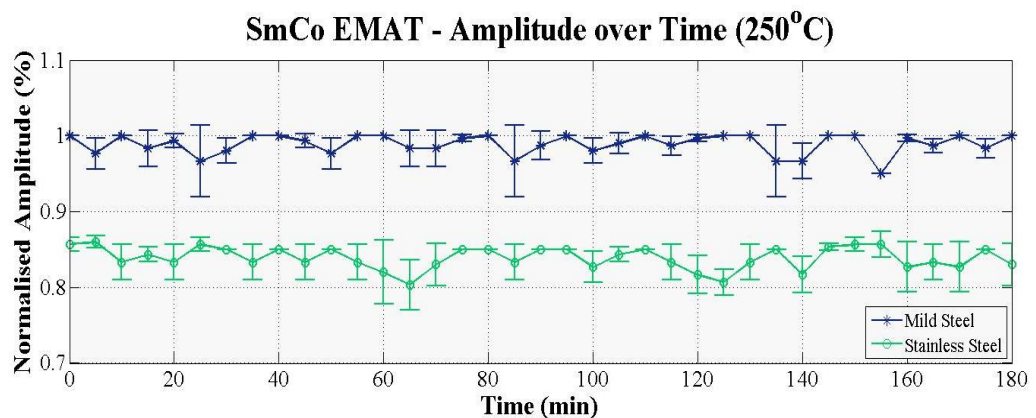


Figure 6.14. SmCo EMAT: Amplitude over time at 250°C

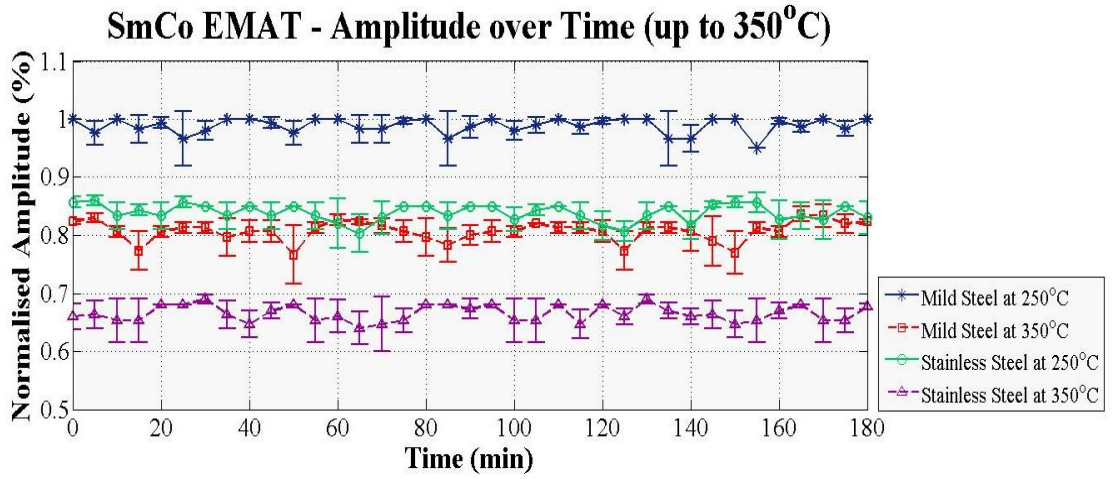


Figure 6.15. SmCo EMAT: Amplitude over time 250°C and 350°C

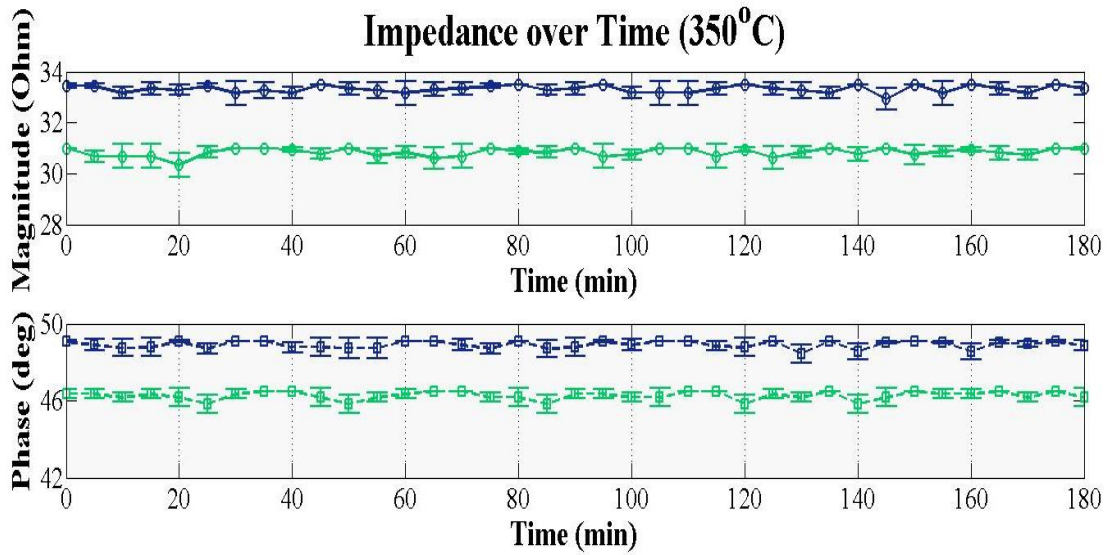


Figure 6.16. SmCo EMAT: Impedance over time at 350°C

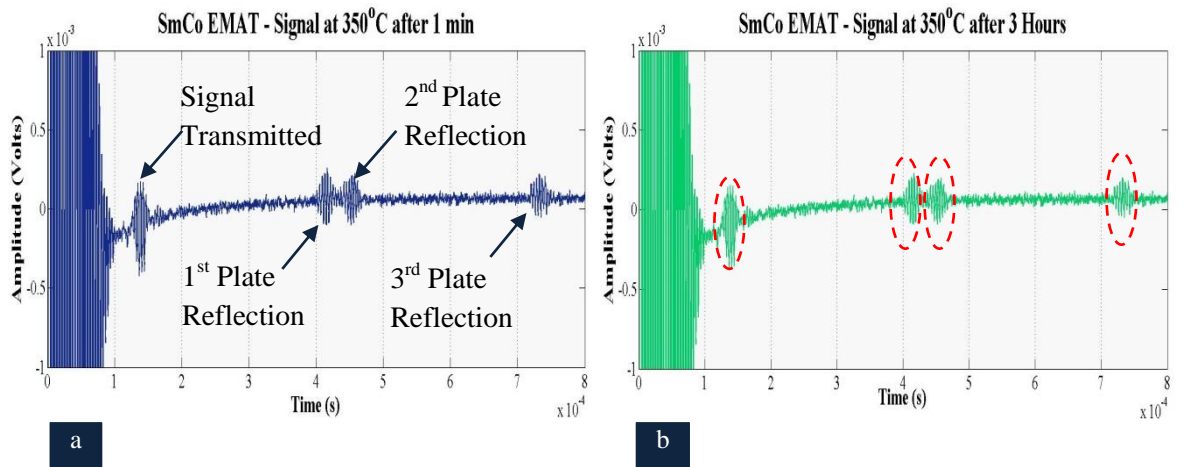


Figure 6.17. SmCo EMAT: Signal received at 350°C after (a) 1 min (b) 3 hours operation

significant changes were observed in its impedance (see Figure 6.16). The ultrasonic signals presented in Figure 6.17 provided evidence that SmCo EMAT system managed to generate and detect SH_0 without a drop in SNR or drop length of inspection at 350°C for three hours. The cooling system continuously dissipated adequate heat and maintained EMAT temperature below 300°C, extending MOT and operational time of the system. As a result, SmCo EMATs can be deployed for long-term inspection of both ferromagnetic and paramagnetic materials at elevated temperatures (350°C).

Both EMAT systems can successfully be employed for long-term inspection up to 250°C and especially SmCo can operate efficiently over time up to 350°C. Hence, SmCo EMATs exhibit superior high-temperature performance for both short and long term inspection compared to Nd-Fe-B EMAT system. Consequently, they are more suitable for GWT at elevated temperatures. Nevertheless, Nd-Fe-B can be also utilized at high temperatures, since the cooling system can maintain its temperature below its MOT. The thermal and CFD analysis were experimentally validated and the experimental values agree with theoretical results. Thus, reliable FEA models for the accurate design and calculation of EMAT thermal response has been established.

6.4 Summary

This Chapter outlines the results obtained from the experimental evaluation of both Nd-Fe-B and SmCo water cooled EMATs at high temperatures. The EMAT systems were tested against various operating parameters including specimen material, lift-off, power input, temperature and operational time. They were employed on mild and stainless steel. Their ultrasonic signal and thermal properties were recorded, analyzed and compared with theoretical values obtained from FEA analysis presented in Chapter 4, hence an experimental validation of theoretical study was accomplished.

Both EMAT systems were successfully employed up to 500°C for short period of time. SmCo EMAT system exhibited better high-temperature performance compared to Nd-Fe-B EMATs. Lift-off increase and power input decrease limited their MOT. However, the cooling system managed to

dissipate adequate thermal energy so that MOT of both systems could be extended by at least 100°C. The measured thermal properties of EMATs agreed with theoretical values calculated from the thermal and CFD study. In addition, they were evaluated regarding their operational time at high temperatures. Likewise, inspection at high temperatures, both designs operated efficiently up to 250°C for three hours continuously and especially SmCo performed successfully up to 350°C. As a result, the latter showed enhanced high-temperature performance compared to the former for both short and long term heat exposure, indicating SmCo's suitability for high-temperature applications.

Two water cooled EMAT systems were thoroughly evaluated regarding their high-temperature capabilities and limitations. Both performed efficiently up to 500°C for short heat exposure and 250°C for continuous operation, also validating the thermal and CFD FEA models presented in Chapter 4.

Chapter 7

Conclusions and Recommendation for Future Work

7.1 Thesis Review

A new high-temperature Electromagnetic Acoustic Transducer (EMAT) for guided wave inspection of plates has been designed, developed and experimentally evaluated.

Based on the literature review presented in Chapter 2, various Non-Destructive Testing techniques, including Acoustic Emission, Eddy Current, Thermography, Optical techniques, laser and conventional Ultrasonic Testing, have been successfully applied at least up to 300°C with shortcomings, though, like qualitative results, sensitivity to noise and laboratory use. Guided Wave Testing is an emerging NDT method that has been widely employed for the structural assessment of large structures in oil/gas, nuclear and solar thermal industry. Its efficiency at elevated temperatures is directly associated with the high-temperature performance of the transducers utilized. Although the dominant technology of transducers for GWT is piezoelectric, EMAT is an attractive candidate for applications where non-contact measurements are needed. Despite the numerous theoretical and experimental studies about EMATs since 1972, only recently did researchers develop and test EMATs for high temperatures. Still, in some of these cases, EMATs are employed in conjunction with laser generators at high temperatures and in all of them only wall thickness measurements were monitored. It is, therefore, desirable to develop an EMAT system suitable for high-temperature GWT of plates. The work described in this thesis demonstrated the systematic approach taken to develop and test of a water-cooled EMAT for GWT of plates up to 500°C.

The theoretical basis that was required for the implementation of the FEA models and analysis of both theoretical and experimental results was described in Chapter 3. The three mechanisms of ultrasound transduction and detection that EMAT operation relies on were outlined and emphasis

was given to Lorentz force, as it dominates in paramagnetic materials. The main EMAT designs for both conventional UT and GWT and their ultrasonic properties were presented and emphasis was given to Period Permanent Magnet configuration and its suitability for SH_0 excitation/detection. It was also stressed that various operating parameters like skin effect, impedance mismatch and lift-off can cause electromagnetic losses and limit EMATs efficiency. Likewise, temperature also degrades EMAT performance and thus detailed study was conducted regarding the thermal limitations and potential of the water-cooled EMAT and their relationship with the rest of the operating parameters.

This led to the development of a Finite Element Analysis model for the prediction of the ultrasonic response of a room temperature PPM EMAT on stainless steel plate at both room and high temperatures. The steps and simplifications followed for the successful and meaningful execution of the model were described in Chapter 4. The wave mode purity characteristics of this EMAT were calculated as well as the temperature effect on them and the overall EMAT performance. This 3D analysis intended to investigate the limitations of the existing EMAT technology at high temperatures and perform as a benchmark for the design of the high-temperature EMAT. Thermal and Computational Fluid Dynamics FEA simulations were also accomplished for the material selection, EMAT design optimization and estimation of the optimum operating conditions. The EMAT was designed so that its thermal properties were maximized and its electromagnetic losses were minimized. The optimum flow velocity, temperature inlet and material properties of coolant were calculated via CFD analysis for short and long term heat exposure, as well as the operational time of EMAT at elevated temperatures.

An experimental evaluation of the limitations of the existing PPM EMAT technology was also carried out and summarized in Chapter 5. Room temperature EMATs were tested regarding their defect detection capabilities, lift-off limitations, power requirements and high-temperature performance. An empirical method for the enhancement of SNR of signal received was also established. The water-cooled EMAT was designed, manufactured and evaluated its operating characteristics. Its impedance analysis against various parameters, including lift-off, specimen material and temperature, was performed. Thorough experimental validation of the FEA study

about the wave mode purity profile of PPM EMAT was carried out via vibrometry tests; the EMAT transmitter was characterized in terms of its wave mode profile against plate thickness and material properties. Therefore, the effect of magnetostriction on EMAT wave mode properties was also studied. Finally, the EMAT was tested regarding its ultrasonic response at room temperature and compared to existing technology. Its performance on both paramagnetic and ferromagnetic materials was obtained as well as its lift-off limitations and power requirements at room temperature.

The final experimental validation of the theoretical study and evaluation of high-temperature response of the water-cooled EMAT were portrayed in Chapter 6. Two water-cooled EMATs were tested up to 500°C for short and long term operation. In both cases, ultrasonic signals were successfully obtained at all target temperatures and the thermal properties of both transmitter and receiver matched with the theoretical values calculated by FEA study. The effect of lift-off increase and power input decrease on the thermal and subsequently, ultrasonic properties of both EMAT types was also investigated. All the above was conducted on both mild and stainless steel. Finally, the EMATs were assessed regarding their long term operation at lower temperatures. They were exposed for three hours at 250°C and they both managed to operate efficiently for the entire duration of the experimental procedure.

7.2 Thesis Findings

Main findings from Chapter 4 related to the theoretical study of EMAT technology at room and high temperatures in terms of its ultrasonic and thermal properties are listed below.

7.2.1 EMAT model for room and high temperatures

A 3D FEA model for the prediction of the ultrasonic performance of room temperature PPM EMAT at room and high temperatures (500°C) was implemented in commercial software. Simplifications were performed regarding the temperature effect on the EMAT/specimen system. Only the impact of temperature rise on the material and electrical properties of specimen were

simulated, thus addressing the problem where the EMAT is employed only for inspection purposes on already heated areas.

The results obtained were encouraging, revealing that the amplitude drop of a room temperature EMAT ensued by the material and electrical variations due to temperature rise up to 500°C is not dramatically large. Weak signals can be obtained up to 500°C. However, the results obtained to give a qualitative idea of the ultrasonic response of room temperature EMAT, since critical information linked to temperature effect could not be obtained and imported into the model. Thus, further deterioration of the signal amplitude and quality is expected. Still, can it be used as a benchmark for the design of high-temperature EMATs for GWT, since any further deterioration of EMAT performance can be counterbalanced by power input increase till the latter meets the maximum power values that are currently available.

Moreover, the model shed light to the wave mode characteristics of PPM EMAT. Despite SH_0 , it was found that out-of-plane displacement propagating with both S_0 and A_0 velocity can be also detected in a different angle than SH_0 . Temperature effect did not alter the results and thus both the ratio of in-plane to out-of-plane displacement and directivity remained the same. This finding is of significant importance, since transducers designed for GWT should preferably exhibit high wave mode purity. Excitation of multiple wave modes leads to complicating signal interpretation and potentially invalid conclusions regarding the structural integrity of the test object. Nevertheless, the above requires a system that both excites and detects multiple wave modes. Based on an ultrasonic model implemented for the study of the wave propagation in stainless steel plate regardless of the excitation means, which is usually used for the estimation of the ultrasonic response of piezoelectric transducers, it was found that guided wave physics cause the above problem. Consequently, EMATs, likewise piezoelectrics, generate a force of particular spatial distribution that unavoidably results in the excitation of multiple wave modes due to guided wave physics. However, EMAT receivers are still sensitive to one particle displacement pattern, determined by their design, and therefore to a single wave mode. An EMAT transmitter/receiver system does not suffer from low wave mode characteristics, however, systems composed of EMAT transmitter and detector sensitive to multiple wave modes is very likely to collect complicating

signals whose analysis cannot provide meaningful information about the structural state of specimen.

7.2.2 EMAT thermal and CFD model

A transient thermal model for the calculation of thermal properties of EMAT up to 500°C without active cooling was developed. Due to limited space all around EMAT coil, no active cooling can be designed for the efficient temperature control of coil. Instead, a detailed study regarding its thermal insulation was performed, as any material added to coil structure for impeding heat transfer would increase lift-off and limit the electromagnetic coupling between EMAT and specimen. Thus, a careful material selection that would eliminate thermal energy transferred to coil per time unit and also would not affect the electromagnetic properties of EMAT was accomplished. The optimum thickness of each material that would permit the maximization of thermal properties of EMAT and elimination of its electromagnetic losses was calculated. A constantan coil encapsulated in 0.75mm thick alumina envelope inside two Kapton layers of 1mm thickness each presented the best thermal response over time. The maximum operational time of this EMAT design without active cooling up to 500°C under the severest operating conditions is equal to one minute. Therefore, CFD analysis was also carried out for the calculation of the appropriate operating parameters of the cooling system for the thermal stabilization of EMAT at high temperatures over time.

Given that EMATs for GWT should introduce strong electromagnetic waves to the test object, their magnetic strength must be as large as possible. Nd-Fe-B is the strongest type of magnets, however, their MOT is only 200°C. Alternatively, SmCo possesses MOT of 300°C, but its magnetic strength is lower than that of the former. Hence, the cooling system should dissipate adequate thermal energy to maintain the temperature of magnets below 200°C. The optimum flow velocity and inlet temperature of a water cooled EMAT employed up to 500°C for 5 minutes were estimated. The thermal potential of an oil-cooled EMAT was also investigated, however, the current design cannot benefit from the low freezing point and high thermal conductivity of oil and results in its low thermal response compared to water. On the contrary, the water – cooled EMAT was proved that it can be also utilized for long term operation up to 250°C under appropriate operating conditions.

Both the thermal and CFD model implemented for the estimation of EMAT thermal properties at high temperatures over time can provide crucial information for the design of a high-temperature EMAT. Scrupulous research on the parameters, including materials and fluid dynamics, that affect the thermal response of EMATs can be performed and lead to the design of transducers that can successfully withstand high temperatures and also meet their operational requirements.

The findings from Chapter 5 are related to the evaluation of the existing EMAT technology at high temperatures and the room temperature characterization of the water-cooled EMAT and are reported below.

7.2.3 Limitations of existing GWT EMATs - Mechanism for SNR enhancement

As no EMAT for GWT at high temperatures was designed before, the limitations of the existing EMAT technology for GWT had to be explored firstly. Two copper coil PPM EMATs with Nd-Fe-B magnets and no active cooling were assessed regarding their defect detection capabilities, lift-off limitations and power requirements at room temperature and also tested up to 180°C. Their defect detection potential on stainless steel plate was relatively low due to their weak electromagnetic coupling with specimen and high noise level. However, an empirical method for the enhancement of SNR of signal received was established. Based on the operating principles of EMAT as they were outlined in Chapter 3, the interface of EMAT and specimen performs as a two winding transformer. If EMATs are attached on specimen in an autotransformer configuration, the noise level drops and SNR of the signal received increases. The experimental evaluation of the above revealed that room temperature EMATs employed on stainless steel plate without shielding/autotransformer connection exhibit 8dB SNR, whilst with shielding it rises to 52dB. This remarkable SNR enhancement agrees with the theory presented in Chapter 3 and increased significantly the defect detection capabilities of the existing EMAT technology.

Therefore, the high-temperature experiments were conducted with the EMATs being shielded. Yet, did their performance degrade significantly after 100°C, since their length of inspection was limited from meters to centimeters, resulting in their questionable industrial applicability at high-

temperature environments. Consequently, the development of the water – cooled EMAT was a necessity.

7.2.4 Experimental validation of model - Wave mode purity of PPM EMAT

The coupled electromagnetic/mechanical FEA model showed that PPM EMAT transmitter excited multiple waves, SH_0 , A_0 and S_0 . The experimental assessment of validity of the model was accomplished via vibrometry tests. The water cooled PPM EMAT transmitter was tested regarding its wave mode purity on stainless and mild steel. A circular area of 30cm radius from the center of EMAT was scanned. It was found that most of the energy introduced to specimen resulted in- plane displacement propagating with SH_0 velocity at right angle. However, noticeable out-of-plane vibration was also detected whose amplitude maximized in 90° angle from SH_0 direction. Out-of-plane displacement was observed at times that correspond to both S_0 and A_0 .

As a result, the experimental results are aligned with the theoretical values and confirm the low wave mode purity characteristics of PPM EMAT. As it was also highlighted previously, PPM EMAT transmitters can excite multiple wave modes, however, when they operate as a receiver, they are sensitive to one wave mode.

7.2.5 Water cooled PPM EMAT – Room temperature characterization

Apart from its wave mode purity, the water cooled EMAT was tested against its lift-off limitations and power requirements and compared to that of a room temperature EMAT. As it was expected, its performance at room temperature is inferior to that of existing technology. Its special design gives it the advantage to show advanced performance at high temperatures compared to room temperature designs. As a result, its thermal insulation and material selection cause electromagnetic losses that are noticeable at room temperature and render it less efficient at ambient temperature in comparison with a room temperature EMAT. Again, its efficiency depends on the material properties of the specimen, since it is greater on mild steel than stainless steel.

Its impedance analysis also confirms all the above, as it was measured against various operating conditions. The large resistivity constantan possesses resulted in larger resistance of water cooled

EMAT and its efficiency drop compared to copper coil, room temperature EMAT. Also, its impedance varied with material properties of specimen, lift-off and temperature. Especially with temperature rise, EMAT impedance increased, since the electromagnetic coupling between the EMAT and the specimen lessens and the EMAT tends to perform as a real inductor instead of a transformer. The results retrieved from impedance analysis were fully aligned to the theory that describes EMAT and specimen interaction as a two winding transformer.

The findings presented in Chapter 6 are related to the high-temperature performance of water cooled EMAT and are listed below.

7.2.6 Water cooled PPM EMAT – High-temperature performance

Two types of water cooled EMATs were tested at high temperatures. Both Nd-Fe-B and SmCo EMATs were employed in a pitch-catch configuration on stainless and mild steel plate. They were assessed regarding their inspection capabilities up to 500°C. Both their ultrasonic and thermal properties were recorded and revealed that both EMATs can operate efficiently up to 500°C short period of time (less than a minute). Nd-Fe-B shows rapid amplitude drop after 200°C and it keeps on fluctuating up to 500°C. On the other hand, SmCo exhibits stable performance over the entire temperature range and its amplitude decreasing rate is smaller compared to that of Nd-Fe-B. As a result, SmCo appears more suitable for high-temperature GWT, although both can be employed up to 500°C. The temperature of EMAT components was also monitored and agrees with the values calculated from the FEA model, confirming the validity of the thermal and CFD analysis.

Despite the destructive effect lift-off has on the ultrasonic performance of EMAT, it can enhance the thermal properties of the transducer, since it increases the time required for the maximum heat to be transferred to the probe. The experimental investigation of the impact of lift-off on EMAT performance up to 500°C was carried out. MOT of EMAT decreased with lift-off increase. However, both EMAT systems managed to operate at least up to 300°C regardless of lift-off and specimen material. Again, SmCo showed superior performance, since its response was satisfactory and stable up to 400°C for all lift-off values. Likewise, power input decrease resulted in MOT

dwindling. Nevertheless, Nd-Fe-B EMAT withstood up to 450°C and 250°C on mild and stainless steel respectively under the lowest power input, while SmCo operated up to 500°C and 300°C.

The EMATs were also assessed in regard to their long-term inspection potential at high temperatures. Based on FEA results, the EMAT can operate at 250°C for at least one hour. Hence, the EMAT systems were exposed at 250°C for three hours. Again, both EMATs managed to operate continuously up to that temperature for the entire duration of the experimental procedure. Nevertheless, MOT of SmCo EMAT is larger than 250°C and thus its response was expected. Hence, it was evaluated again for its operational time at 350°C. Similarly, with before, the EMAT performed satisfactorily at this temperature as well. The cooling system successfully maintained the temperature of both EMATs below their MOT, ensuring their stable performance for at least three hours. Apart from the ultrasonic response of the system, the EMAT impedance was also recorded. No fluctuations were observed during the experimental procedure and thus no indications of potential break down of the system after three hours of continuous operation can be found. The experimental results match with the FEA values and actually they are even more encouraging, since the operating time is larger than one hour.

7.3 Suggestions for Future Work

The successful validation of all three FEA models implies the substantial validity of the theoretical basis they rely on and the importance of their results. However, any discrepancy observed between the theoretical and experimental values can be sheared further, if additional critical information is imported in the models. The ultrasonic response of EMAT at high temperatures can be simulated in more detail, if the temperature effect on all material, electrical and magnetic properties of EMAT and specimen is taken into account. Further information regarding the relationship between temperature rise and magnetic properties of the specimen are required for the enhancement of accuracy of the model. Moreover, a more scrupulous research about the potential and constraints of an oil-cooled EMAT at high temperatures should be conducted. The thermal and CFD models can be utilized for this research. However, the EMAT should be re-designed, so that it will benefit from the low freezing point and high thermal conductivity of oil and also counterbalance the higher

viscosity and life hazard risk oil possesses compared to water. The same tools can be used for the investigation of the maximum operating time the current EMAT design or any future high-temperature EMAT up to 250°C. Amendments on the current EMAT design and more especially its cooling system may be required for the extension of its operational time and thus its monitoring potential at high temperatures. Attention must be also paid on the impedance variations of EMAT at high temperatures and the need for an impedance matching network for the stabilization of its performance at temperature changes. Impedance matching and filtering of signals received are also required for the further enhancement of EMAT performance. A more in-depth study about PPM EMAT design and its wave mode purity profile is necessary to be performed. A novel EMAT configuration that will allow the elimination of the unwanted wave modes as soon as they are generated is required. This study can be further validated with EMATs for other wave modes, like S_0 and A_0 . Experimental research of the potential and limitations of the current study for pipe inspection/monitoring should also be investigated in near future. Finally, an EMAT that will be theoretically and experimentally validated regarding its long-term inspection potential (over days of continuous operation) at high temperatures and its industrial applicability for monitoring of high-temperature structures is needed.

References

- [1] A. Poullikkas, “Economic analysis of power generation from parabolic trough solar thermal plants for the Mediterranean region—A case study for the island of Cyprus,” *Renewable and Sustainable Energy Reviews*, vol. 13, p. 2474–2484, 2009.
- [2] Papaelias, M.; Cheng, L.; Kogia, M.; Mohimi, A.; Kappatos, V.; Selcuk, C.; Constantinou, L.; Gómez Muñoz, C.Q.; Garcia Marquez, F.P.; Gan, T.H. Inspection and structural health monitoring techniques for concentrated solar power plants. *Renew. Energy* **2015**, *85*, 1178–1191.
- [3] T. Scrubbs, “The role of NDE in the life management of steam turbine rotors,” *Insight*, vol. 46, no. 9, p. 529-532, 2004.
- [4] S. Guillot, A. Faïka, A. Rakhmatullina, V. Lambert, E. Verona, P. Echegut, C. Bessadaa, N. Calvet, X. Py, “Corrosion effects between molten salts and thermal storage material for concentrated solar power plants.,” *Applied Energy*, vol. 94, p. 174–181, 2012.
- [5] R.J. Ditchburn, S.K. Burke, C.M. Scala, “NDT of welds: State of the art,” *NDT&E International*, vol. 29, no. 2, p. 111-117, 1996.
- [6] S.D. Kenny, K. Stamps, P. Crowther, “Development of NDT technique and inspection for detection and sizing of thermal fatigue cracking in steam pipework bores of flexibly operated coal-fired power stations,” *Insight*, vol. 45, no. 2, p. 125-126, 2003.
- [7] S. Baby, T. Balasubramanian, R.J. Pardikar, “Ultrasonic study for flaw detectability in ferritic butt welds at high temperatures,” *Insight*, vol. 45, no. 1, p. 87-91, 2003.
- [8] J. Johnson, K. Kim, S. Zhang, D. Wu, X. Jiang, “High temperature acoustic emission sensing tests using a Yttrium calcium oxyborate sensor,” *IEEE Transactions on Ultrasonics, Ferroelectrics, and Frequency Control*, vol. 61, no. 5, p. 805-814, 2014.
- [9] T. Kasuya, T. Okuyama, N. Sakurai, H. Huang, T. Uchimoto, T. Takagi, Y. Lu, T. Shoji, “In-situ eddy current monitoring under high temperature environment,” *International Journal of Applied Electromagnetics and Mechanics*, vol. 20, p. 163-170, 2004.

- [10] R.J. Dewhurst, C. Edwards, A.D.W. McKie, S.B. Palmer, "A remote laser system for ultrasonic velocity measurement at high temperatures," *Journal of Applied Physics*, vol. 63, no. 4, p. 1225-1227, 1988.
- [11] R.J. Dewhurst and Q. Shan, "Modelling of confocal Fabry-Perot interferometers for the measurement of ultrasound," *Measurement Science and Technology*, vol. 5, no.6, 655, 1994.
- [12] S. Gongtian, L. Tao, "Infrared thermography for high-temperature pressure pipe," *Insight*, vol. 49, no.3, p.151-153, 2007.
- [13] F.B. Cegla, A.J.C. Jarvis, J.O. Davies, "High temperature ultrasonic crack monitoring using SH cracks," *NDT&E International*, vol. 44, p. 669-679, 2011.
- [14] I.A. Victorov, "Rayleigh and Lamb waves," Plenum Press, New York, 1970.
- [15] P. Cawley, D. Alleyne, "The use of Lamb waves for the long range inspection of large structures," *Ultrasonics*, vol. 34, p. 287-290, 1996.
- [16] D.C. Worlton, "Ultrasonic testing with Lamb waves," *Non Destructive Testing*, vol. 15, p. 218-222, 1957.
- [17] P. Wilcox, M. Lowe, P. Cawley, "The effect of dispersion on long range inspection using guided waves," *NDT&E International*, vol. 34, p. 1-9, 2001.
- [18] A. Demma, P. Cawley, M. Lowe, A.G. Roosenbrand, B. Pavlakovic, "The reflection of guided waves from notches in pipes: a guide for interpreting corrosion measurements," *NDT&E International*, vol. 37, p. 167-180, 2004.
- [19] D. Alleyne, P. Cawley, "The excitation of Lamb waves in pipes using dry coupled piezoelectric transducers," *Journal of Nondestructive Evaluation*, vol. 15, p. 11-20, 1996.
- [20] R.C. Turner, P.A. Fruierer, R.E. Newnham, T.R. Shrout, "Materials for high temperature acoustic and vibration sensors: A review," *Applied Acoustics*, vol. 41, p. 299-324, 1994.
- [21] R. Kažys, A. Voleišis, B. Voleišienė, "High temperature ultrasonic transducers: Review," *ULTRAGARSAS Journal*, vol. 63, p. 7-17, 2008.

- [22] B. Tittman, D. Parks, O. Zhang, “High temperature piezoelectrics—A comparison,” In Proceedings of the 13th International Symposium on Nondestructive Characterization of Materials (NDCM-XIII), Le Mans, France, 20–24 May 2013.
- [23] R.B. Thompson, “Physical principles of measurements with EMAT transducers,” In *Ultrasonic Measurement Methods*; Thurston, R.N., Pierce, A.D., Eds.; Academic Press: London, UK, 1990, p. 157–200.
- [24] R.B. Thompson, G.A. Alers, M.A. Tennison, “Application of direct electromagnetic Lamb wave generation to gas pipeline inspection,” In Proceedings of the IEEE Ultrasonic Symposium, New York, NY, USA, 4-7 Oct 1972, p. 91–93.
- [25] M. Hirao, H. Ogi, “An SH-wave EMAT technique for gas pipeline inspection,” *NDT&E International*, vol. 32, p. 127-132, 1999.
- [26] P. Wilcox, M. Lowe, P. Cawley, “The excitation and detection of Lamb waves with planar coil electromagnetic acoustic transducers,” *IEEE Transactions on Ultrasonics, Ferroelectrics, and Frequency Control*, vol. 52, p. 2370-2383, 2005.
- [27] R. Ribichini, Modelling of Electromagnetic Acoustic Transducers. Ph.D. Thesis, Department of Mechanical Engineering, Imperial College University, London, UK, 2011.
- [28] Beattie, G. “Acoustic emission principles and instrumentation,” *Journal of Acoustic Emission*, vol. 2, no. 12, p. 95-128, 1983.
- [29] A. Nair, C.S. Cai, “Acoustic emission monitoring of bridges: Review and case studies,” *Engineering Structures*, vol. 32, p. 1704-1714, 2010.
- [30] P. Runow, “The use of acoustic emission methods as aids to the structural integrity assessment of nuclear power plants,” *International Journal of Pressure Vessels and Piping*, vol. 21, p. 59-69, 1985.
- [31] P. Bently, “A review of acoustic emission for pressurized water reactor applications,” *NDT International*, vol. 14, p. 329-335, 1981.
- [32] C. Scruby, H. Wadley, “An assessment of acoustic emission for nuclear pressure vessel monitoring,” *Progress in Nuclear Energy*, vol. 11, no. 3, p. 275-297, 1982.
-

- [33] J.A. Steel and R.L. Reuben, "Recent developments in monitoring of engines using acoustic emission," *Journal of Strain Analysis for Engineering Design*, vol. 40, no. 1, p. 45-57, 2005.
- [34] J. Hensman, R. Mills, S.G. Pierce, K. Worden, M. Eaton, "Locating acoustic emission sources in complex structures using Gaussian processes," *Mechanical Systems and Signal Processing*, vol. 24, no. 1, p. 211-223, 2010.
- [35] H. Noma, T. Tabaru, M. Akiyama, N. Miyoshi, T. Hayano, H. Cho, "High temperature acoustic emission sensing using aluminum nitride sensor," *Journal Acoustic Emission*, vol. 25, p. 107-114, 2007.
- [36] S. Zhang, X. Jiang, M. Lapsley, P. Moses, T.R. Shroud, "Piezoelectric accelerometers for ultrahigh temperature applications," *Applied Physics Letters*, vol. 96, 2010.
- [37] G. Salazar, K. Kim, S. Zhang, X. Jiang, "Piezoelectric accelerometer for high temperature (1,300°C) sensing," In Proceedings of the SPIE Smart Structures and Materials and Nondestructive Evaluation and Health Monitoring, San Diego, CA, USA, 11 March 2012.
- [38] P. Marin-Franch, T. Martin, D. Tunnicliffe, D. Das-Gupta, "PTCa/PEKK piezo-composites for acoustic emission detection," *Sensor and Actuators A*, vol. 99, p. 236-243, 2002.
- [39] K.E. Holbert, S. Sankaranarayanan, S.S. McCready, "Response of lead metaniobate acoustic emission sensors to gamma irradiation," *IEEE Transactions on Nuclear Science*, vol. 52, p. 2583-2590, 2005.
- [40] K. Kirk, C. Scheit, N. Schmarje, "High temperature acoustic emission tests using lithium niobate piezocomposite transducers," *Insight Non Destructive Testing and Condition Monitoring*, vol. 49, p. 142-145, 2007.
- [41] S. Momon, M. Moevus, N. Godin, M.R. Mili, P. Reynaud, G. Fantozzi, G. Fayolle, "Acoustic Emission and lifetime prediction during static fatigue tests on ceramic – matrix – composite at high temperatures under air," *Composites: Part A*, vol. 41, p. 913-918, 2010.
- [42] R. Hou, D. Hutson, K.J. Kirk, Y.Q. Fu, "AIN thin film transducers for high temperature non – destructive testing applications," *Journal Applied Physics*, vol. 111, 2012.

- [43] E. Baziw, "Real-time seismic signal enhancement utilizing a hybrid Rao-Blackwellized particle filter and hidden Markov model filter," *IEEE Geoscience and Remote Sensing Letter*, vol. 2, no. 4, p. 418-422, 2005.
- [44] Q. He, J. Wang, F. Hu, F. Kong, "Wayside acoustic diagnosis of defective train bearings based on signal resampling and information enhancement," *Journal of Sound and Vibration*, vol. 332, no. 21, p. 5635-5649, 2013.
- [45] J.J. González de la Rosa, R. Piotrkowski, J.E. Ruzzante, "Higher order statistics and independent component analysis for spectral characterization of Acoustic Emission signal in steel pipes," *IEEE Transactions on Instrumentation and Measurement*, vol. 56, no. 6, p. 2312-2321, 2007.
- [46] S. Grondel, C. Delebarre, J. Assaad, J.P. Dupuis, L. Reithler, "Fatigue crack monitoring of riveted aluminum strap joints by Lamb wave analysis and acoustic emission measurement techniques," *NDT&E International*, vol. 35, no. 3, p. 137-146, 2002.
- [47] F. Santos, M. Vaz, J. Monteiro, "A new set-up for pulsed digital shearography applied to defect detection in composite structures," *Optics and Lasers in Engineering*, vol. 42, no. 2, p. 131-140, 2004.
- [48] E.A. Zarate, E.G. Gustodio, C.G. Treviño-Palacios, R.R. Vera, H.J. Puga-Soberanes, "Defect detection in metals using electronic speckle pattern interferometry," *Solar Energy Materials and Solar Cells*, vol. 88, no. 2, p. 217-225, 2005.
- [49] C. Garnier, M.L. Pastor, F. Eyma, B. Lorrain, "The detection of aeronautical defects in situ on composite structures," *Composite Structures*, vol. 93, no. 5, p. 1328-1336, 2011.
- [50] S. Schedin, G. Pedrini, H.J. Tiziani, A.K. Aggarwal, M.E. Gusev, "Highly sensitive pulsed digital holography for built-in defect analysis with a laser excitation," *Applied Optics*, vol. 40, no. 1, p. 100-103, 2001.
- [51] Z. Sodnik, H.J. Tiziani, "Photothermal interferometry for nondestructive subsurface defect detection," *Optics Communications*, vol. 58, no.5, p. 295-299, 1986.

- [52] S.H. Tung, M.H Shih, W.P. Sung, "Development of digital image correlation method to analyze crack variations of masonry wall," *Sadhana*, vol. 33, no. 6, o. 767-779, 2008.
- [53] D. Corr, M. Accardi, L.G. Brady, S. Shah, "Digital image correlation analysis of interfacial debonding properties and fracture behavior in concrete," *Engineering Fracture Mechanics*, vol. 74, no. 1-2, p. 109-121, 2007.
- [54] C.A. Calder and W.W. Wilcox, "Noncontact material testing using laser energy deposition and interferometry," *Materials Evaluation*, vol. 38, no. 1, p. 86, 1980.
- [55] O.J. Løkberg, J.T. Malmo, G.Å. Slettemoen, "Interferometric measurements of high temperature objects by electronic speckle pattern interferometry," *Applied Optics*, vol. 24, no.19, p. 3167-3172, 1985.
- [56] J.T. Malmo, O.J. Løkberg, G.Å. Slettemoen, "Interferometric testing at very high temperatures by TV holography (EPSI)," *Experimental Mechanics*, vol. 28, no. 3, p. 315-321, 1988.
- [57] J.S Lyons, J. Liu, M.A. Sutton, "High-temperature deformation measurements using digital-image correlation," *Experimental Mechanics*, vol. 36, no. 1, p. 64-70, 1996.
- [58] J.G. Martin, J.G. Gil, E.V. Sánchez, "Non-destructive techniques based on Eddy Current testing," *Sensors*, vol. 11, no. 3, p. 2525-2565, 2011.
- [59] N. Yusa, E. Machida, L. Janousek, M. Rebican, Z. Chen, K. Miya, " Application of eddy current inversion technique to the sizing of defects in Inconel welds with rough surfaces," *Nuclear Engineering and Design*, vol. 235, no. 14, p. 1469-1480, 2005.
- [60] A. Sophian, G.Y. Tian, D. Taylor, J. Rudlin, "Electromagnetic and eddy current NDT: A review," *Insight*, vol. 43, no. 5, p. 1-5, 2001.
- [61] M. Bentoumi, P. Aknin, G. Bloch, "On-line rail defect diagnosis with differential eddy current probes and specific detection processing," *European Physical Journal Applied Physics*, vol. 23, p. 227-233, 2003.
- [62] H. Shaikh, N. Sivaibharasi, B. Sasi, T. Anita, R. Amirthalingam, B.P.C. Rao, T. Jayakumar, H.A. Khatak, B. Raj, "Use of eddy current testing method in detection and evaluation of sensitization and intergranular corrosion in austenitic stainless steels," *Corrosion Science*, vol. 48, no. 6, p. 1462-1482, 2006.

- [63] A. Sophian, G.Y. Tian, D. Taylor, J. Rudlin, "Design of a pulsed eddy current sensor for detection of defects in aircraft lap-joints," *Sensors and Actuators A: Physical*, vol. 101, no. 1-2, p. 92-98, 2002.
- [64] B.A. Auld, J.C. Moulder, "Review of advances in quantitative eddy current nondestructive evaluation," *Journal of Nondestructive Evaluation*, vol. 18, no. 1, p. 3-36, 1999.
- [65] J. Vetterlein, H. Klümper-Westkamp, T. Hirsch, P. Mayr, "Eddy current testing at high temperatures for controlling heat treatment processes," In Proceedings of International Symposium of Non Destructive Testing in Civil Engineering 2003 (NDT-CE 2003), Berlin, Germany, 2003.
- [66] H. Klümper-Westkamp, H.W. Zoch, W. Reimche, F.W. Bach, "High temperature resistant eddy current sensor for "in situ" monitoring the material microstructure development of steel alloys during heat treatment – bainite sensor," *Procedia Engineering*, vol. 25, p. 1605-1608, 2011.
- [67] Emerson Process Management Reliability Solutions, Knoxville, TN, USA. Available online: www.emersonprocess.com/csi (accessed on 04 September 2016).
- [68] Omni Instruments Ltd, Dundee, United Kingdom. Available online: www.omniinstruments.co.uk/ (accessed on 04 September 2016).
- [69] R. Urayama, T. Uchimoto, T. Takagi, "Application of EMAT/EC dual probe to monitoring of wall thinning in high temperature environment," *International Journal of Applied Electromagnetics and Mechanics*, vol. 33, no. 3-4, p. 1317-1327, 2010.
- [70] G. Van Drunen, V.S. Cecco, "Recognizing limitations in eddy current testing," *NDT International*, vol. 17, no. 1, p. 9-17, 1984.
- [71] D.J. Titman, "Applications of thermography in non-destructive testing of structures," *NDT&E International*, vol. 34, no. 2, p. 149-154, 2001.
- [72] M.R. Clark, D.M. McCann, M.C. Forde, "Application of infrared thermography to the non-destructive testing of concrete and masonry bridges," *NDT&E International*, vol. 36, no. 4, p. 265-275, 2003.
- [73] I.G. Scott, C.M. Scala, "A review of non-destructive testing of composite materials," *NDT International*, vol. 15, no. 2, p. 75-86, 1982.
- [74] D. Bates, G. Smith, D. Lu, J. Hewitt, "Rapid thermal non-destructive testing of aircraft components," *Composites Part B: Engineering*, vol. 31, no. 3, p. 175-185, 2000.

- [75] FLIR Systems Inc., Boston, MA, USA. Available online: www.flir.com (accessed on 4 September 2016).
- [76] LumaSense Technologies INC., Santa Clara, CA, USA. Available online: www.lumasenseinc.com/ (accessed on 4 September 2016).
- [77] C. Meola, G.M. Carlomagno, L. Giorleo, "Geometrical limitations to detection of defects in composites by means of infrared thermography," *Journal of Nondestructive Evaluation*, vol. 23, no. 4, p. 125-132, 2004.
- [78] R.E. Green Jr. "Non-contact ultrasonic techniques," *Ultrasonics*, vol. 42, p. 9-16, 2004.
- [79] C.B. Scruby, R.J. Dewhurst, D.A. Hutchins, S.B. Palmer, "Quantitative studies of thermally generated elastic-waves in laser-irradiated metals," *Journal of Applied Physics*, vol. 51, no. 12, p. 6210-6216, 1980.
- [80] C.B. Scruby, L.E. Drain, "Laser ultrasonics. Techniques and applications," Adam Hilger, 1990.
- [81] J.P. Monchalín, C. Néron, J.F. Bussière, P. Bouchard, C. Padioleau, R. Héon, M. Choquet, J.D. Aussel, G. Durou, J.A. Nilson, "Laser-ultrasonics: From the laboratory to the shop floor" *Advanced Performance Materials*, vol. 5, no. 1, p. 7-23, 1998.
- [82] H. Nakano, S. Nagai, "Crack measurements by laser ultrasonic at high temperatures," *Japanese Journal of Applied Physics*, vol. 32, 1993.
- [83] S.E. Krüger, M. Lord, J.P. Mochalin, "Laser ultrasonic thickness measurements of very thick walls at high temperatures," In Proceedings of AIN conference, vol. 820, p.240-247, 2006.
- [84] T. Matsumoto, T. Nose, Y. Nagata, K. Kawashima, T. Yamada, H. Nakano, S. Nagai, "Measurement of high temperature elastic properties of ceramics using a laser ultrasonic method," *Journal of the American Ceramic Society*, vol. 84, no. 7, p. 1521-1525, 2001.
- [85] R.S. Lima, S.E. Krüger, G. Lamouche, B.R. Marple, "Elastic modulus measurements via laser – ultrasonic and knop indentation techniques in thermally sprayed coatings," *Journal of Thermal Spray Technology*, vol. 14, no. 1, p. 52-60, 2005.
- [86] A.V. Clark, S.R. Schaps, C.M. Fortunko, "A well-shielded EMAT for on-line ultrasonic monitoring of GMA welding," In Proceedings of IEEE Ultrasonics Symposium, 1991.

- [87] S. Boonsang, R.J. Dewhurst, "A highly sensitive laser/EMAT imaging system for biomedical applications," In Proceedings of Electrical Engineering Congress (IEECON), 2014.
- [88] P.R. Murray, R.J. Dewhurst, "Application of a laser/EMAT system for using shear and LS mode converted waves," *Ultrasonics*, vol. 40, no. 1-8, p. 771-776, 2002.
- [89] Z. Guo, J.D. Achenbach, S. Krishnaswamy, "EMAT generation and laser detection of single Lamb wave modes," In D.O. Thompson and D.E. Chimenti, editors, *Review of Progress in Quantitative Nondestructive Evaluation*, vol. 17, 1998.
- [90] D.A. Hutchins, D.E. Wilkins, "Elastic waveforms using laser generation and electromagnetic acoustic transducer detection," *Journal of Applied Physics*, vol. 58, p. 2469, 1985.
- [91] S. Dixon, C. Edwards, S.B. Palmer, "Laser – EMAT system for ultrasonic weld inspection," *Ultrasonics*, vol. 37, no. 4, p. 273-281, 1999.
- [92] X. Jian, I. Baillie, S. Dixon, "Steel billet inspection using laser – EMAT system," *Journal of Physics D: Applied Physics*, vol. 40, no. 5, p. 1501-1506, 2007.
- [93] S. Dixon, S.E. Burrows, B. Dutton, Y. Fan, "Detection of cracks in metal sheets using pulsed laser generated ultrasound and EMAT detection," *Ultrasonics*, vol. 51, no. 1, p. 7-16, 2011.
- [94] M. Sgarbi, V. Colla, S. Cateni, S. Higson, "Pre-processing of data coming from a laser – EMAT system for non-destructive testing of steel slabs," *ISA Transactions*, vol. 51, no. 1, p. 181-188, 2012.
- [95] S.E. Burrows, Y. Fan, S. Dixon, "High temperature thickness measurements of stainless steel and low carbon steel using electromagnetic acoustic transducers," *NDT&E International*, vol. 68, p. 73-77, 2014.
- [96] D.B. Boyd, P.D. Sperline, "Noncontact temperature measurements of hot steel bodies using an electromagnetic acoustic transducer (EMAT)," Pacific Northwest Laboratory, p. 1669-1676.
- [97] I. Baillie, P. Griffith, X. Jian, S. Dixon, "Implementing an ultrasonic inspection system to find surface and internal defects in hot, moving steel using EMATs," *Insight*, vol. 49, no. 2, p. 87-92, 2007.
- [98] C.A. Calder, E.C. Draney, W.W. Wilcox, "Noncontact measurement of elastic – constants of plutonium at elevated temperatures," *Journal of Nuclear Materials*, vol. 97, no. 1-2, p. 126-136, 1981.

- [99] C.B. Scruby, B.C. Moss, "Non-contact ultrasonic measurements on steel at elevated temperatures," *NDT&E International*, vol. 26, no. 4, p. 177-188, 1993.
- [100] M.S. Rohani, "The development of non-contact laser and EMAT ultrasound measurement systems for hot steel," PhD Thesis, University of Warwick, 1996.
- [101] I. Baillie, "The development of a laser-EMAT system suitable for on-line in the continuous casting plant – Innovation report," PhD thesis, University of Warwick, 2008.
- [102] J.R. Lee, C.C. Chia, C.Y. Park, H. Jeong, "Laser ultrasonic anomalous wave propagation imaging method with adjacent wave subtraction: Algorithm," *Optics and Laser Technology*, vol. 44, no. 5, p. 1507-1515.
- [103] R. Raisutis, R. Kazys, L. Mazeika, "Ultrasonic thickness measurement of multilayered aluminum foam precursor material," *IEEE Transactions on Instrumentation and Measurement*, vol. 57, no. 12, p. 2846-2855, 2008.
- [104] J. Krautkramer, H. Krautkramer, "Ultrasonic testing of materials," Springer – Verlag, 4th edition, 1990.
- [105] J.S. Jurvelin, T. Räsänen, P. Kolmoneus, T. Lyyra, "Comparison of optical, needle probe and ultrasonic techniques for the measurement of articular cartilage thickness," *Journal of Biomechanics*, vol. 28, no. 2, p. 231-235, 1995.
- [106] M. Krause, M. Bärmann, R. Frielinghaus, F. Kretzschmar, O. Kroggel, K.J. Langenberg, C. Maierhofer, W. Müller, J. Neisecke, M. Schickert, V. Schmitz, H. Wiggenhauser, F. Wollbord, "Comparison of pulse-echo methods for testing concrete," *NDT&E International*, vol. 30, no. 4, p. 195-204, 1997.
- [107] J.L. Rose, "Ultrasonic waves in solid media," Cambridge University Press, 1st edition, 1999.
- [108] R.J. Ditchburn, S.K. Burke, C.M. Scala, "NDT of welds: state of the art," *NDT&E International*, vol. 29, no. 1, p. 11-117, 1996.
- [109] B.L. Baikie, A.R. Wagg, M.J. Whittle, D. Yapp, "Ultrasonic inspection of austenitic welds," *Journal of the British Nuclear Energy Society*, vol. 15, no. 3, p. 257-261, 1976.

- [110] A Lhémy, P. Calmon, I. Lecoeur –Taïbi, R. Raillon, L. Paradis, “Modelling tools for ultrasonic inspection of welds,” *NDT&E International*, vol. 33, no. 7, p. 499-513, 2000.
- [111] M.G. Silk, “Changes in ultrasonic defect location and sizing,” *NDT&E International*, vol. 20, no. 1, p. 9-14, 1987.
- [112] G.J. Gruber, “Defect identification and sizing by the ultrasonic satellite – pulse technique,” *Journal of Nondestructive Evaluation*, vol. 1, no. 4, p. 263-276, 1980.
- [113] J. Zhang, B.W. Drinkwater, P.D. Wilcox, “Defect characterization using an ultrasonic array to measure the scattering coefficient matrix,” *IEEE Transactions on Ultrasonics, Ferroelectrics, and Frequency Control*, vol. 55, no. 10, p. 2254-2265, 2008.
- [114] I. Komura, T. Hirasawa, S. Nagai, J.I. Takabayashi, K. Naruse, “Crack detection and sizing technique by ultrasonic and electromagnetic methods,” *Nuclear Engineering and Design*, vol. 206, no. 2-3, p. 351-362, 2001.
- [115] P. Cawley, “Practical long range guided wave inspection – Applications to pipe and rail,” NDE 2002 predict, assure, improve, National Seminar of ISNT, Chennai, India, 5-7 December 2002.
- [116] M.J.S. Lowe, P. Cawley, “Long Range Guided Wave inspection usage – Current commercial capabilities and research directions,” Report, Department of Mechanical Engineering, Imperial College London, London, United Kingdom, 2006.
- [117] P. Wilcox, M. Evans, B. Pavlakovic, D. Alleyne, K. Vine, M. Lowe, “Guided wave testing rail,” *Insight – Non Destructive Testing and Condition Monitoring*, vol. 45, no. 5, p. 413-420, 2003.
- [118] M.J.S. Lowe, D.N. Alleyne, P. Cawley, “Defect detection in pipes using guided waves,” *Ultrasonics*, vol. 36, no. 1-5, p. 147-154, 1998.
- [119] N. Alleyne, M.J.S. Lowe, P. Cawley, “The reflection of guided waves from circumferential notches on pipes,” *Journal of Applied Mechanics*, vol. 65, no. 3, p. 635-641, 1998.

- [120] J.L. Rose, J.J. Ditri, A. Pilarski, J. Zhang, F. Carr, W.M. McNight, "A guided wave inspection technique for nuclear steam generator tubing," *Non-Destructive Testing '92*, edited by C. Hallai, P. Kulcsar, Elsevier, 2012.
- [121] Y.M. Cheong, D.H. Lee, H.K. Jung, "Ultrasonic guided wave parameters for detection of axial cracks in feeder pipes of PHWR nuclear power plants," *Ultrasonics*, vol. 42, no. 1-9, p. 883-888, 2004.
- [122] C.K. Jen, J.G. Legoux, L. Parent, "Experimental evaluation of clad metallic buffer rods for high temperature ultrasonic measurements," *NDT& E International*, vol. 33, no. 3, p. 145-153, 2000.
- [123] F.B. Cegla, J.O. Davies, "Ultrasonic crack monitoring at high temperatures using SH waves," In D.O. Thompson and D.E. Chimenti, editors, *Review of Progress in Quantitative Nondestructive Evaluation*, vol. 29, p. 980-987, 2010.
- [124] H.A. Sodano, G. Park, D.J. Inman, "An investigation into the performance of micro-fiber composites for sensing and structural vibration applications," *Mechanical Systems and Signal Processing*, vol. 18, no. 3, p. 683-697, 2004.
- [125] P.A. Petcher, M.D.G. Potter, S. Dixon, "A new electromagnetic acoustic transducer (EMAT) design for operation on rail," *NDT&E International*, vol. 65, p. 1-7, 2014.
- [126] D.C. Worlton, "Experimental configuration of Lamb waves at megacycle frequencies," *Journal of Applied Physics*, vol. 32, p. 967-971, 1961.
- [127] P.A. Doyle, C.M. Scala, "Crack depth measurement by ultrasonics: a review," *Ultrasonics*, vol. 16, no. 4, p. 164-170, 1978.
- [128] M.G. Silk, K.F. Bainton, "The propagation in metal tubing of ultrasonic wave modes equivalence to Lamb waves," *Ultrasonics*, vol. 17, no. 1, p. 11-19, 1979.
- [129] W. Böttger, H. Schneider, W. Weingarten, "Prototype EMAT system for tube inspection with guided ultrasonic waves," *Nuclear Engineering and Design*, vol. 102, no. 3, p. 369-376, 1987.
- [130] J.L. Rose, "Baseline and vision of ultrasonic guided wave inspection," *Journal Pressure Vessel Technology*, vol. 124, no. 3, p. 273-282, 2002.

- [131] W. Mohr, P. Höeller, "On inspection of thin-walled tubes for transverse and longitudinal flaws by guided ultrasonic waves. *IEEE Transactions on Sonics and Ultrasonics*, vol. 23, no. 5, p. 369-374, 1976.
- [132] D.N. Alleyne, P. Cawley, "The interaction of Lamb waves with defects," *IEEE Transactions on Ultrasonics, Ferroelectrics, and Frequency Control*, vol. 39, no. 3, p. 381-397, 1992.
- [133] D.N. Alleyne, P. Cawley, "Optimization of lamb wave inspection techniques," *NDT&E International*, vol. 25, no. 1, p. 11-22, 1992.
- [134] Plant Integrity Ltd, Great Abington, Cambridgeshire, United Kingdom. Available online: <http://www.plantintegrity.com/> (accessed on 5 September 2016).
- [135] Guided Ultrasonics Ltd, Nottingham, United Kingdom. Available online: www.guided-ultrasonics.com (accessed on 5 September 2016).
- [136] MKC NDT, Korea. Available online: <http://www.mkckorea.com/english.htm> (accessed on 5 September 2016).
- [137] K. Kim, S. Zhang, g. Salazar, X. Jiang, "Design, fabrication and characterization of high-temperature piezoelectric vibration sensor YCOB crystals," *Sensors and Actuators A*, vol. 178, p. 40-48, 2012.
- [138] PCB Piezotronics Inc., Depew, New York. Available online: www.pcb.com (accessed on 5 September 2016).
- [139] Meggitt Sensing Systems, Dorset, United Kingdom. Available online: www.endevco.com (accessed on 5 September 2016).
- [140] M.N. Hamidon, V. Skards, N.M. White, F. Krispel, P. Krempf, M. Binhank, W. Buff, "High temperature 434Mhz surface acoustic wave devices based on GaPO₄," *IEEE Transactions on Ultrasonics, Ferroelectrics, and Frequency Control*, vol. 53, no. 12, p. 2465-2470, 2006.
- [141] J. Thiele, M.P. Cunha, "High temperature surface acoustic wave devices: Fabrication and characterization," *IEEE Power Electronics Letters*, vol. 39, p. 818-819, 2003.
- [142] T. Aubert, J. Bardong, O. Legrani, O. Elmazria, M. Badreddine Assouar, G. Bruckner, A. Talbi, "In situ high temperature characterization of AlN based surface acoustic wave devices," *Journal Applied Physics*, vol. 114, 2013.

- [143] A. McNab, K.J. Kirk, A. Cochran, "Ultrasonic transducers for high temperature," *IEE Proceedings – Science, Measurement and Technology*, vol. 145, no. 5, p. 229-236, 1998.
- [144] A. Baba, C.T. Searfass, B.R. Tittmann, "High temperature ultrasonic transducers up to 1000°C using lithium niobate single crystal," *Applied Physics Letters*, vol. 97, 2010.
- [145] D.A. Parks, s. Zhang, B.R. Tittmann, "High temperature (>500°C) ultrasonic transducers: An experimental comparison among three candidate piezoelectric materials," *IEEE Transactions on Ultrasonics, Ferroelectrics, and Frequency Control*, vol. 60, p. 1010-1015, 2013.
- [146] X. Jiang, K. Kim, S. Zhang, J. Jognson, G. Salazar, "Review: High temperature piezoelectric Sensing," *Sensors*, vol. 14, p. 144-169, 2014.
- [147] D. Damjanovic, "Materials for high temperature piezoelectric transducers," *Ceramics, Composites and Intergrowths*, vol. 3, p. 469-473, 1998.
- [148] S.E. Burrows, K.L. McAughey, R.S. Edwards, S. Dixon, "Sol-gel bismuth titanate for high temperature ultrasound transducers," *RSC Advances*, vol. 2, p. 3678-3683, 2012.
- [149] S. Zhang, F. Yu, "Piezoelectric materials for high temperature sensors," *Journal of American Ceramic Society*, vol. 94, no. 10, p. 3153-3170, 2011.
- [150] N.D. Patel, P.S. Nicholson, "High frequency, high temperature ultrasonic transducers," *NDT International*, vol. 23, no. 4, p. 262-266, 1990.
- [151] M. Kobayashi, T.R. Olding, M. Sayer, C.K. Jen, "Piezoelectric thick film ultrasonic transducers fabricated by a sol-gel spray technique," *Ultrasonics*, vol. 39, no. 10, p. 675-680, 2002.
- [152] A. Mohimi, "High Temperature Ultrasonic Guided Wave Transducers," Ph.D. Brunel University London, London, UK, 2014.
- [153] S. Dixon, C. Edwards, S.B. Palmer, "High accuracy non-contact ultrasonic thickness gauging of aluminium sheet using electromagnetic acoustic transducers," *Ultrasonics*, vol. 39, no. 6, p. 445-453, 2001.
- [154] H. Zhang, R.L. Su, S.J. Wang, G.F. Zhai, L. Kang, "Design of bulk wave EMAT using a pulsed electromagnet," 2014 IEEE Far East Forum on Nondestructive Evaluation/Testing (FENDT), 20-23 June 2014.
- [155] P.A. Petcher, S. Dixon, "Weld defect detection using PPM EMAT generated shear horizontal ultrasound," *NDT&E International*, vol. 74, p. 58-65, 2015.

- [156] X. Zhao, V.K. Varma, G. Mei, B. Ayhan, C. Kwan, "In-line non-destructive inspection of mechanical dents on pipelines with guided shear horizontal wave electromagnetic acoustic transducers," *Transactions of the ASME*, vol. 127, p. 304-309, 2005.
- [157] M. Kogia, C. Liang, A. Mohimi, V. Kappatos, T.H. Gan, W. Balachandran, C. Selcuk, "Electromagnetic Acoustic Transducers applied to high temperature plates for potential use in solar thermal industry," *Applied Sciences*, vol. 5, p. 1715-1734, 2015.
- [158] J.C. Maxwell, "On physical lines of force," vol. 21, 1861.
- [159] J.P. Joule, "On the effects of magnetism upon the dimensions of iron and steel bars," *Philosophical Magazine, Physics of Condensed Matter, Defects and Mechanical Properties*, vol. 30, no. 199, p. 76, 1847.
- [160] E.R. Dobbs, "Electromagnetic generation of ultrasonic waves," In W.P. Mason and R.N. Thurston, editors, *Physical Acoustics*, vol. X, p. 127-189. Academic Press, New York, 1973.
- [161] R.B. Thompson, "A model for the electromagnetic generation and detection of Rayleigh and Lamb waves," *IEEE Transactions on Sonics and Ultrasonics*, vol. 20, no. 4, p. 340-346, 1973.
- [162] R.B. Thompson, "Mechanisms of electromagnetic generation and detection of ultrasonic Lamb waves in iron – nickel alloy polycrystals," *Journal of Applied Physics*, vol. 48, no. 12, 4942-4950, 1977.
- [163] R.B. Thompson, "A model for the electromagnetic generation of ultrasonic guided waves in ferromagnetic metal polycrystals," *IEEE Transactions on Sonics and Ultrasonics*, vol. 25, no. 1, p. 7-15, 1978.
- [164] C.F. Vasile, R.B. Thompson, "Excitation of horizontally polarized shear elastic waves by electromagnetic transducers with periodic permanent magnets," *Journal of Applied Physics*, vol. 50, no. 4, p. 2583-2588, 1979.
- [165] K. Kawashima, "Theory and numerical calculation of the acoustic field produced in metal by an electromagnetic ultrasonic transducer," *The Journal of the Acoustical Society of America*, vol. 60, p. 1089-1099, 1976.
- [166] K. Kawashima, "Quantitative calculation and measurement of longitudinal and transverse ultrasonic wave pulses in solid," *IEEE Transactions on Sonics and Ultrasonics*, vol. 31, no. 2, p. 83-94, 1984.

- [167] G. Zhai, T. Jiang, "Analysis of multiple wavelengths of Lamb waves generated by meander – line coil EMATs," *Ultrasonics*, vol. 54, no. 2, p. 632-636, 2014.
- [168] L. Kang, S. Dixon, K. Wang, J. Dai, "Enhancement of signal amplitude of surface wave EMATs based on 3-D simulation analysis and orthogonal test method," *NDT&E International*, vol. 59, p. 11-17, 2013.
- [169] Y. Xie, W. Yin, Z. Liu, A. Peyton, "Simulation of ultrasonic and EMAT arrays using FEM and FDTD," *Ultrasonics*, vol. 66, p. 154-156, 2016.
- [170] M.H. Rosli, R.S. Edwards, Y. Fan, "In – plane and out – of plane measurements of Rayleigh waves using EMATs for characterising surface cracks," *NDT&E International*, vol. 49, p. 1-9, 2012.
- [171] K. Hao, S. Huang, W. Zhao, S. Wang, J. Dong, "Analytical modelling and calculation of pulsed magnetic field and input impedance for EMATs with planar spiral coils," *NDT&E International*, vol. 44, no. 3, p. 274-280, 2011.
- [172] S. Wang, L. Kang, P. Xin, G. Zhai, "Characteristic research and analysis of EMATs transduction efficiency for surface detection of aluminium plate," In Proceedings of 9th International Conference on Electronic Measurement and Instruments (ICEMI '09), 16-19 August 2009.
- [173] R.J. Shapoorabadi, A. Konrad, A.N. Sinclair, "Improved finite element method for EMAT analysis and design," *IEEE Transactions on Magnetics*, vol. 37, no. 4, 2821-2823, 2001.
- [174] A.M. Hussein, "Current distribution and input impedance of a finite electromagnetic acoustic transducer," *IEEE Transactions on Magnetics*, vol. 27, no. 5, p. 4258-4261, 1991.
- [175] M. Kaltenbacher, K. Ettinger, R. Lerch, B. Tittmann, "Finite Element Analysis of coupled electromagnetic acoustic systems," *IEEE Transactions on Magnetics*, vol. 35, no. 3, p. 1610-1613, 1999.
- [176] K. Mirkhani, C. Chaggares, C. Masterson, M. Jastrzebski, T. Dusatko, A. Sinclair, R.J. Shapoorabadi, A. Konrad, M. Panini, "Optimal design of EMAT transmitters," *NDT&E International*, vol. 37, no. 3, p. 181-193, 2004.

- [177] R. Ludwig, Z. You, R. Palanisamy, "Numerical simulations of an electromagnetic acoustic transducer – receiver system for NDT applications," *IEEE Transactions on Magnetics*, vol. 29, no. 3, p. 2081-2089, 1993.
- [178] R. Ludwig, "Theoretical implementation and model predictions of a unified conservation law description of the electromagnetic acoustic transduction process," *IEEE Transactions on Ultrasonics, Ferroelectrics, and Frequency Control*, vol. 39, no. 4, p. 481-488, 1992.
- [179] R. Ludwig, X.W. Dai, "Numerical simulation of electromagnetic acoustic transducer in the time domain," *Journal of Applied Physics*, vol. 69, p. 89-98, 1991.
- [180] H. Ogi, "Field dependence of coupling efficiency between electromagnetic field and ultrasonic bulk waves," *Journal of Applied Physics*, vol. 82, 3940-3949, 1997.
- [181] X. Jian, S. Dixon, K. Quirk, K.T.V. Grattan, "Electromagnetic acoustic transducers for in – and out – of plane ultrasonic wave detection," *Sensors and Actuators A: Physical*, vol. 148, no. 1, p. 51-56, 2008.
- [182] S. Dixon, C. Edwards, S.B. Palmer, "Texture measurements of metal sheets using wideband electromagnetic acoustic transducers," *Journal of Physics D: Applied Physics*, vol. 35, no. 8, p. 816-824, 2002.
- [183] S. Dixon, S.B. Palmer, "Wideband low frequency generation and detection of Lamb and Rayleigh waves using electromagnetic acoustic transducers (EMATs)," *Ultrasonics*, vol. 442, no. 10, p. 1129-1136, 2004.
- [184] X. Jian, S. Dixon, K.T.V. Grattan, R.S. Edwards, "A model for pulsed Rayleigh wave and optimal EMAT design," *Sensors and Actuators A: Physical*, vol. 128, no. 2, p. 296-304, 2006.
- [185] R.S. Edwards, S. Dixon, X. Jian, "Characterisation of defects in the railhead using ultrasonic surface waves," *NDT&E International*, vol. 39, no. 6, p. 468-475, 2006.
- [186] S. Dixon, R.S. Edwards, X. Jian, "Inspection of rail track head surfaces using electromagnetic acoustic transducers (EMATs)," *Insight – Non Destructive Testing and Condition Monitoring*, vol. 46, no. 1, p. 326-330, 2004.
- [187] S. Hill and S. Dixon, "Frequency dependent directivity of periodic permanent magnet electromagnetic acoustic transducers," *NDT&E International*, vol. 62, p. 137-143, 2014.

- [188] P. Wilcox, M. Lowe, P. Cawley, "Omnidirectional guided wave inspection of large metallic plate structures using an EMAT array," *IEEE Transactions on Ultrasonics, Ferroelectrics, and Frequency Control*, vol. 52, no. 4, p. 653-665, 2005.
- [189] W. Luo, J.L. Rose, J.K. Velsor, M. Avioli, J. Spanner, "Circumferential guided waves for defect detection on coated pipe," In D.O. Thompson and D.E Chimenti, editors, *Review of Progress in Quantitative Nondestructive Evaluation*, vol. 25, 2006.
- [190] W. Luo, J.L. Rose, "Guided wave thickness measurement with EMATs," *Insight – Non Destructive Testing and Condition Monitoring*, vol. 45, no. 11, p. 735-739, 2003.
- [191] R. Ribichini, P.G. Nagy, H. Ogi, "The impact of magnetostriction on the transduction of normal bias field EMATs," *NDT&E International*, vol. 51, p. 8-15, 2012.
- [192] N. Andruschak, I. Saletes, T. Filleters, A. Sinclair, "An NDT guided wave technique for the identification of corrosion defects at support locations," *NDT&E International*, vol. 75, p. 72-79, 2015.
- [193] X. Zhao, V.K. Varma, G. Mei, B. Ayhan, C. Kwan, "In-line nondestructive inspection of mechanical dents on pipelines with guided shear horizontal electromagnetic acoustic transducers," *Journal Pressure Vessel Technology*, vol. 127, no. 3, p. 304-309, 2005.
- [194] Y. Wang, X. Wu, P. Sun, J. Li, "Enhancement of the excitation efficiency of a torsional wave PPM EMAT array for pipe inspection by optimizing the element number of the array based of 3-D FEM", *Sensors*, vol. 15, p. 3471-3490, 2015.
- [195] K. Zhang, P. Yi, Y. Li, B. Hui, X. Zhang, "A new method to evaluate surface defects with Electromagnetic Acoustic Transducer," *Sensors*, vol. 15, p. 17420-17432, 2015.
- [196] R. Dhayalan, V.S.N. Murthy, C.V. Krishnamurthy, K. Balasumramaniam, "Improving the signal amplitude of meandering coil EMATs by using soft magnetic flux concentrators (MFC)," *Ultrasonics*, vol. 51, no. 6, p. 675-682, 2011.
- [197] B. Dutton, S. Boonsang, R.J. Dewhurst, "A new magnetic configuration for a small in-plane electromagnetic acoustic transducer applied to laser-ultrasound measurements: Modelling and validation," *Sensors and Actuators A*, vol. 125, p. 249-259, 2006.

- [198] G.F. Zhai, B. Liu, C.R. Deng, Y.Q. Li, L. Kang, "An inspection device based on multiple Lamb wave electromagnetic acoustic transducers," In proceedings of IEEE Far East Forum on Nondestructive Evaluation/Testing (FENDT), 20-23 June 2014.
- [199] A. Boonyaprapasorn, T. Maneewarn, K. Thung – Od, "A prototype of inspection robot for water wall tubes in boiler," In Proceedings of 3rd International Conference on Applied Robotics for the Power Industry (CARPI), 14-16 October 2014.
- [200] W. Shujuan, P. Weicai, Y. Peng, L. Chao, "Research on detection method of electromagnetic ultrasonic signal based on FPGA," In Proceedings of 3rd IEEE Conference on Industrial Electronics and Applications, 3-5 June 2008.
- [201] M. Kubingi, O. Kreibich, J. Neuzil, R. Smid, "EMAT noise suppression using information fusion in stationary wavelet packets," *IEEE Transactions on Ultrasonics, Ferroelectrics, and Frequency Control*, vol. 58, no. 5, p. 1027-1036, 2011.
- [202] S.W. Lim, R.A. Shoureshi, "Advanced monitoring system for integrity assessment of electric power transmission lines," In Proceedings of American Control Conference, 14-16 June 2006.
- [203] H.J. Salzburger, "EMAT's and its potential for modern NDE – state of the art and latest applications," In Proceedings of IEEE International Ultrasonics Symposium (IUS), 20-23 September 2009.
- [204] H.M. Frost, T.L. Szabo, "Surface acoustic wave electromagnetic transducers from multiconductor flat cable," *Applied Physics Letters*, vol. 29, p. 73, 1976.
- [205] B.R. Thompson, R.K. Elsley, W.E. Peterson, C.F. Vasile, "An EMAT system for detecting flaws in steam generator tubes," In Proceedings of the ARPA/AFML, Review of Progress in Quantitative Nondestructive Evaluation, col. 13, p. 562-567, 1980.
- [206] R. Murayama, K. Fujisawa, H. Fukuoka, M. Hirao, "Development of an on-line evaluation system of formability in cold-rolled steel sheets using electromagnetic acoustic transducer (EMATs)," *NDT&E International*, vol. 29, no. 3, p. 141-146, 1996.
- [207] Nurmalia, N. Nakamura, H. Ogi, M. Hirao, K. Nakahata, "Mode conversion behaviour of SH guided wave in a tapered plate," *NDT&E International*, vol. 45, no. 1, p. 156-161, 2012.

- [208] H. Ogi, M. Hirao, T. Ohtani, "Line focusing electromagnetic acoustic transducers for the detection of slit defects," *IEEE Transactions on Ultrasonics, Ferroelectrics, and Frequency Control*, vol. 46, no. 2, p. 341-346, 1999.
- [209] T. Yamasaki, S. Tamai, M. Hirao, "Arrayed – coil EMAT for longitudinal wave in steel wires," In Proceedings of IEEE Ultrasonic Symposium, 5-8 October 1998.
- [210] R. Murayama, "Driving mechanism on magnetostrictive type electromagnetic acoustic transducer for symmetrical vertical-mode Lamb wave and for shear horizontal-mode plate wave," *NDT&E International*, vol. 34, p. 729-736, 1996.
- [211] R. Murayama, "Study of driving mechanism on electromagnetic transducer for Lamb wave using magnetostrictive effect and application in drawability evaluation of thin steel sheets," *Ultrasonics*, vol. 37, p. 31-38, 1999.
- [212] R. Murayama, S. Makiyama, M. Kodama, Y. Taniguchi, "Development of an ultrasonic inspection robot using an electromagnetic acoustic transducer for a Lamb wave and an SH-plate wave," *Ultrasonics*, vol. 42, p. 825-829, 2004.
- [213] H. Kwun, S.Y. Kim, "Magnetostrictive sensor for generating and detecting plate guided waves," *Journal of Pressure Vessel Technology*, vol. 127, p. 284-289, 2005.
- [214] Z. Liu, J. Zhao, B. Wu, Y. Zhang, C. He, "Configuration optimization of magnetostrictive transducers for longitudinal guided wave inspection in seven-wire steel strands," *NDT&E International*, vol. 43, p. 484-492, 2010.
- [215] Z. Liu, Y. Hu, J. Fan, W. Yin, X. Liu, C. He, "Longitudinal mode magnetostrictive patch transducer array employing a multi-splitting meander coil for pipe inspection," *NDT&E International*, vol. 79, p. 30-37, 2016.
- [216] Z. Liu, J. Fan, Y. Hu, C. He, B. Wu, "Torsional mode magnetostrictive patch transducer array employing a modified planar solenoid array coil for pipe inspection," *NDT&E International*, vol. 69, p. 9-15, 2015.
- [217] W. Li, Y. Cho, "Quantification and imaging of corrosion wall thinning using shear horizontal guided waves generated by magnetostrictive sensors," *Sensors and Actuators A: Physical*, vol. 232, p. 251-258, 2015.

- [218] H.M. Seung, H.W. Kim, Y.Y. Kim, "Development of an omni-directional shear-horizontal wave magnetostrictive patch transducer for plates," *Ultrasonics*, vol. 53, p. 1304-1308, 2013.
- [219] H.M. Seung, Y.Y. Kim, "Generation of omni-directional shear-horizontal waves in a ferromagnetic plate by a magnetostrictive patch transducer," *NDT&E International*, vol. 80, p. 6-14, 2016.
- [220] Y.Y. Kim, Y.E. Kwon, "Review of magnetostrictive patch transducers and applications in ultrasonic nondestructive testing of waveguides," *Ultrasonics*, vol. 62, p. 3-19, 2015.
- [221] H.W. Kim, J. K. Lee, Y.Y. Kim, "Circumferential phased array of shear-horizontal wave magnetostrictive patch transducers for pipe inspection," *Ultrasonics*, vol. 53, p. 423-431, 2013.
- [222] H.W. Kim, S.H. Cho, Y.Y. Kim, "Analysis of internal wave reflection within a magnetostrictive patch transducer for high-frequency guided torsional waves," *Ultrasonics*, vol. 51, p. 647-652, 2011.
- [223] Y.G. Kim, H.S. Moon, K.J. Park, J.K. Lee, "Generating and detecting torsional guided waves using magnetostrictive sensors of crossed coils," *NDT&E International*, vol. 44, p. 145-151, 2011.
- [224] J.P. Morrison, S. Dixon, M.D.G. Potter, X. Jian, "Lift-off compensation for improved accuracy in ultrasonic Lamb wave velocity measurements using electromagnetic acoustic transducers (EMATs)," *Ultrasonics*, vol. 44, p. 1401-1404, 2006.
- [225] T. Uchimoto, T. Takagi, T. Ichihara, G. Dodmann, "Evaluation of fatigue cracks by an angle beam EMAT-ET dual probe," *NDT&E International*, vol. 72, p. 10-16, 2015.
- [226] T. Uchimoto, P. Guy, T. Takagi, J. Courbon, "Evaluation of an EMAT-EC dual probe in sizing extent of wall thinning," *NDT&E International*, vol. 62, p. 160-166, 2014.
- [227] R.S. Edwards, A. Sophian, S. Dixon, G.Y. Tian, X. Jian, "Dual EMAT and PEC non contact probe: applications to defect testing," *NDT&E International*, vol. 39, no. 1, p. 45-52, 2006.
- [228] K.S. Ho, D.R. Billson, D.A. Hutchins, "Ultrasonic Lamb wave tomography using scanned EMATs and wavelet processing," *Nondestructive Testing and Evaluation*, vol. 22, no. 1, p. 19-34, 2007.
- [229] S. Huang, Z. Wei, W. Zhao, S. Wang, "A new omni-directional EMAT for ultrasonic Lamb wave tomography imaging of metallic plate defects," *Sensors*, vol. 14, p. 3458-3476, 2014.

- [230] Z. Wei, S. Huang, S. Wang, W. Zhao, "Magnetostriction – based omni – directional guided wave transducer for high – accuracy tomography of steel plate defects," *IEEE Sensors Journal*, vol. 15, no. 11, p. 6549-6558, 2015.
- [231] A. Idris, C. Edwards, S.B. Palmer, "Acoustic wave measurement at elevated temperature using a pulsed laser generator and an Electromagnetic Acoustic Transducer detector," *Nondestructive Testing Evaluation*, vol. 11, p. 195-213, 1994.
- [232] S.E. Burrows, Y. Fan, S. Dixon, "High temperature thickness measurements of stainless steel and low carbon steel using electromagnetic acoustic transducers," *NDT&E International*, vol. 68, p. 73-77, 2014.
- [233] S. Clarks, J. Flora, J. MacLauchlan, "High temperature Electromagnetic Acoustic Transducer (EMAT) probe and coil assemblies," D. U.S. Patent No. 5,689,070, 1997.
- [234] J. Buttram, J. Flora, "High temperature Electromagnetic Acoustic Transducer," U.S. Patent No. 6,125,706, 2000.
- [235] V.F. Hernandez, "Pulsed-electromagnet EMAT for high temperature applications," Ph.D. Thesis, The University of Warwick, 2011.
- [236] R. Carandente "Interaction between the fundamental torsional guided wave mode and complex defects in pipes," PhD thesis. Imperial College London, 2011.
- [237] B. Pavlakovic, M.J.S. Lowe, D.N. Alleyne, P. Caaley, "Disperse: A general purpose program for creating dispersion curves," In D. Chimenti and T. Thompson, editos, *Review of Progress in Quantitative Nondestructive Evaluation*, New York, 1997. Plenum.
- [238] M.B. Schulz, B.J. Matsinger, M.g. Holland, "Temperature depende of surface acoustic wave velocity on a quartz, " *Journal of Applied Physics*, vol. 41, p. 2755-2765, 1970.
- [239] M. Fukuhara, I. Yamauchi, "Temperature dependence of the elastic moduli, dilational and shear internal frictions and acoustic wave velocity for alumina, (Y)TZP and b²-sialon ceramics," *Journal of Materials Science*, vol. 28, p. 4681-4688, 1993.
- [240] A.D. Ancas, D. Gorbanescu, "Theoretical models in the study of temperature effect on steel mechanical properties," Report. Buletinul Institutului Politehnic Din Lasi, Tomul, 2006.
- [241] X. Jian, S. Dixon, "Enhancement of EMAT and eddy current using a ferrite back – plate," *Sensors and Actuators A: Physical*, vol. 136, no. 1, p. 132-136, 2007.

- [242] X. Jian, S. Dixon, R.S. Edwards, J. Morrison, "Coupling mechanism of an EMAT," *Ultrasonics*, vol. 44, p. 653-656, 2006.
- [243] Comsol, Inc., Burlington, MA, USA. Available online: <https://www.comsol.com/> (Accessed on 9 September 2016).
- [244] Dassault Systemes (Abaqus), Vélizy-Villacoublay, France. Available online: <http://www.3ds.com/> (Accessed on 9 September 2016).
- [245] ANSYS, Inc., Canonsburg, PA, USA. Available online: <http://www.ansys.com/> (Accessed on 9 September 2016).
- [246] RITEC Inc., Warwick, RI, USA. Available online: <http://www.ritecinc.com/> (Accessed on 9 September 2016).
- [247] STORK, Utrecht, Netherlands. Available online: www.stork.com/ 9Accessed on 9 September 2016).
- [248] Keysight Technologies Inc., Santa Rosa, CA, USA. Available online: <http://www.keysight.com/> (Accessed on 9 September 2016).
- [249] S. Chen, M.W. Urban, C. Pislaru, R. Kinnick, Y. Zheng, A. Yao, J.F. Greenleaf, "Shearwave dispersion ultrasound vibrometry (SDUV) for monitoring tissue elasticity and viscosity," *IEEE Transactions on Ultrasonics, Ferroelectrics, and Frequency Control*, vol. 56, no. 1, p. 55-62, 2009.
- [250] W.J. Staszewski, B.C. Lee, L. Mallet, F. Scarpa, "Structural health monitoring using scanning laser vibrometry: I. Lamb wave sensing," *Smart Materials and Structures*, vol. 13, p. 251-260, 2004.
- [251] P. Castellini, G.M. Revel, E.P. Tomasini, "Laser Doppler vibrometry: A review of advances and applications," *The Shock and Vibration Digest*, vol. 30, no. 6, p. 443-456, 1998.
- [252] A.C. Lewin, "Compact laser vibrometer for industrial and medical applications," In *Proceedings of 3rd International Conference on Vibration Measurements by Laser Techniques: Advances and Applications (SPIE)*, vol. 3411, 1 June 1998.
- [253] B. Junge, "Experiences with scanning laser vibrometry in automotive industries," In *Proceedings of 1st International Conference on Vibration Measurements by Laser Techniques: Advances and Applications (SPIE)*, vol. 377, 8 September 1990.

- [254] W.D. Arnott, J.M. Sabatier, "Laser Doppler vibrometer measurements of acoustic to seismic coupling," *Applied Acoustics*, vol. 30, p. 279-291, 1990.
- [255] Polytec Inc., Irvine, CA, USA. Available online: <http://www.polytec.com/> 9Accessed on 9 September 2016).
- [256] M. Hirao, H. Ogi, "SH-wave EMAT for chirp pulse compression," in *Electromagnetic Acoustic Transducers: Noncontacting Ultrasonic Measurements using EMATs*, New York, Springer, 2016.

↓